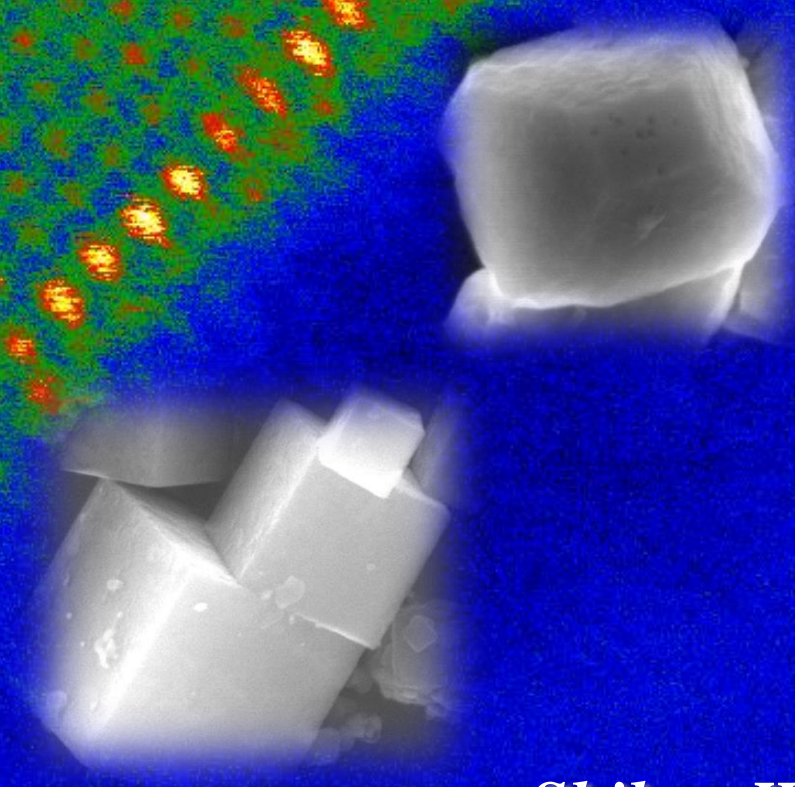


*Characterisation of Native MgO
and Its Roles in
Solidification of Mg Alloys*



Shihao Wang



Brunel
University
London

Characterisation of Native MgO and Its Roles in Solidification of Mg Alloys

A thesis submitted for the degree of
Doctor of Philosophy

by

Shihao Wang

BCAST

Brunel University London

Uxbridge, UB8 3PH

United Kingdom

7th Oct 2020

Supervision: Professor Zhongyun Fan

Doctor Yun Wang

Professor Quentin Ramasse

Abstract

Magnesium (Mg) and its alloys are becoming one of the most important structural materials in modern society. Since a refining microstructure is beneficial to nearly all aspects of properties of cast and wrought Mg alloys, grain refinement has been a major task to be tackled. Although zirconium (Zr) is currently considered as the most effective grain refiner for Al-free Mg alloys, there is not a universal grain refiner for Mg alloys yet. Recently, the native MgO particles present in Mg alloy melts have shown their ability for grain refinement in commercial purity (CP) Mg and AZ series alloys. However, the limited knowledge of the nature of native MgO and the interaction between MgO and solute inhibits the understanding of solidification process. The widespread application of native MgO particles for grain refinement of Mg alloys is therefore prevented.

In this thesis, extensive research was carried out to investigate the native MgO particles and their effect on solidification of commercial purity (CP) Mg and binary Mg alloys including Mg-Y (yttrium), Mg-Ca (calcium), Mg-Sn (tin) and Mg-Al (aluminium). The solidified structure and grain size of CP-Mg and the binary Mg alloys were assessed by TP-1 casting method, and the native MgO particles in these alloy melts were comprehensively characterised through SEM, TEM and the state-of-the-art aberration corrected STEM plus EELS. Firstly, the nature of native MgO present in the CP-Mg and the Mg alloys was well understood by comprehensive characterisation from micron-meter scale to the atomic scale. The native MgO was found to appear as liquid films that are composed of discrete MgO particles. Owing to different formation mechanisms during oxidation, two types of MgO particles differed in morphologies form. One is octahedral MgO with {111} facets and the other is cubic MgO with {100} facets. Secondly, the native MgO particles were demonstrated to act as substrates for heterogeneous nucleation of Mg, leading to significant grain refinement of CP-Mg, although they were impotent substrates in terms of the lattice misfit calculated according to the experimentally observed orientation relationships. Thirdly, elemental segregation on the surface of native MgO particles was experimentally identified in the binary Mg alloys containing Y, Ca and Sn, respectively. It is found that the structural and chemical configuration of the segregation layer formed on the MgO surface were affected by the atomic configuration of the faceting crystal planes of MgO and the specific solutes inside the melt. The potency of the native MgO particles for heterogeneous nucleation was therefore modified

Abstract

accordingly. Finally, with the knowledge of native MgO and its interaction with solute, the mechanism for grain refinement by the native MgO particles in CP-Mg and the binary Mg alloys were understood. Due to the modifiable potency of native MgO particles by the interfacial segregation, the corresponding grain initiation behaviour can be dominated by either progressive or explosive manner. The application of native MgO particles can potentially be adopted as a universal technique for grain refinement of Mg alloys.

Keywords: Mg alloys, magnesium oxide, solidification, grain refinement, electron microscopy, interfacial segregation, crystallography.

Acknowledgement

I am truly indebted to my principal supervisor, Prof. Zhongyun Fan, for offering me the such a fantastic opportunity to participate in this exciting PhD project in BCAST, Brunel University London for the last three years and a half. Continuous and invaluable supervision, mentoring and inspiration from him have set up the premise for the completion of this work. His great passion for research, the innovation and unique wisdom on considering scientific topics in a big and comprehensive vision have influenced me a lot and definitely are beneficial for my future academic career.

I would like to sincerely thank my associate supervisor, Dr. Yun Wang, for his supervision, discussions, guidance and reviews throughout this project. His knowledge and expertise in TEM and extensive experience on interfacial segregation offer me constructive suggestions during experiments and invaluable comments on interpreting the results. I am truly grateful to him for giving me the face-to-face interview in Changsha, China, June 2016.

My special acknowledgement to my associate supervisor, Prof. Quentin Ramasse, from SuperSTEM Laboratory located at Daresbury, UK. It is appreciated to have his warm concerns, endless encouragements, constructive suggestions, inspiring reviews, and professional supervisions on Cs-corrected STEM. The memorable working experience with him allowed me to see an appropriate balance that he managed among life, interest and work. A seed has been planted in my mind. I am also thankful to all colleagues in SuperSTEM Laboratory, who had provided great help on instrumental training and data analysis. Other than this, I was given a relaxed and enjoyable working experience with them, which for sure will be my dreaming working environment in the future.

The Experimental Techniques Centre (ETC) at Brunel University London is gratefully acknowledged for providing access to the experimental instruments. I would like to thank Dr. Ashely Howkins for his endless supports and helps on training and usages of TEM, SEM and FIB.

I would like to express my gratitude to my researcher development advisor, Prof. Issac Chang, and the progressive review panel committee members, Prof. Hamid Assadi and

Dr. Chamini Mendis. Their critical reviews and comments in every progressive review meeting provided great help on the project progresses.

All the colleagues in the fundamental group in BCAST are all highly appreciated, the regular knowledge sharing and discussion about solidification kept broadening and elevating my understanding in both theoretical and experimental aspect. Special thanks go to Dr. Feng Wang who unselfishly gave substantial discussions on crystallography and grain refinement, Dr. Gao Feng who kindly and patiently sheared his understanding of grain refinement through numerical modelling.

My sincere thanks go to Prof. Shouxun Ji for kindly introducing to me this exciting PhD project and Dr. Yijie Zhang for his extensive expertise on casting experiments. Dr. Jayesh Patel is acknowledged for the discussion about native MgO particles and the guidance on doing high shear melt conditioning. Dr. Kun Dou own my thanks for his great help on simulating the thermal history of Mg melt in TP-1 mould. I also wish to thank Mr Steve Cook, Mr Peter Lloyd, Mrs Samantha Melvin and all other staffs of BCAST laboratory technician team for their excellent technical support, and Mrs Susan Job, Mr Philip Saunders, Mr Matthew Ralph and Mr Philip Everett for the great administration support.

I would like to thank Prof. Rainer Schmid-Fetzer from the Clausthal University of Technology, Germany for giving me a helpful and impressive discussion on understanding the oxidation behaviour through thermodynamics and phase diagrams.

I also would like to thank my friends, colleagues and fellow postgraduate students in BCAST, Brunel University, Dr. Xinliang Yang, Dr. Yipeng Zhou, Dr. Zhongping Que, Dr. Xiangzhen Zhu, Dr. Guangyu Liu, Dr. Xixi Dong, Mrs Jiao Fang, Dr. Tungky Subroto, Ms. Susanna Venditti, Mrs Sultana Yasmin, Dr. Tuo Ye, Mr. Ewan Lordan, Mr. Qing Cai, Mr. Umar Amin for their generous help and invaluable friendship.

The financial support provided by the Engineering and Physical Sciences Research Council (EPSRC) under grant number EP/N007638/1 and the Chinese Scholarship Council (CSC) throughout my candidature are gratefully acknowledged.

I owe my deepest gratitude to my parents, my brother and sister who provided me with their unconditional love, concern and support over my studying period in UK.

List of Publications

[1] **Shihao Wang**, Feng Wang, Yun Wang, Quentin Ramasse, and Zhongyun Fan. "Segregation of Ca at the Mg/MgO interface and its effect on grain refinement of Mg alloys." In *IOP Conference Series: Materials Science and Engineering*, vol. 529, no. 1, p. 012048. IOP Publishing, 2019.

[2] **Shihao Wang**, Yun Wang, Quentin Ramasse, and Zhongyun Fan. "The Nature of Native MgO in Mg and Its Alloys." *Metallurgical and Materials Transactions A* (2020): 1-18.

Abbreviation

2DC- Two-Dimensional Compound

2D- Two Dimensional

3D-Three Dimensional

ADF- Annular Dark Field

AGS- Average Grain Size

ACW- Average columnar width

BF- Bright Field

CET- Columnar-to-Equiaxed Transition

EBSD - Electron Backscatter Diffraction

EDS- Energy Dispersive X-ray Spectroscopy

EELS- Electron Energy Loss Spectroscopy

ELNES- Energy Loss Near Edge Structure

FIB- Focus Ion Beam

HAADF- High-Angle Annular Dark-Field

HRTEM- High-Resolution Transmission Electron Microscopy

HSMC- High Shear Melt Conditioning

HS- High Shearing

HSO- High Shearing with intentional Oxidation

MAADF- Medium-Angle Annular Dark-Field

OM- Optical Microscopy

OR- Orientation Relationship

PCA-Principal Component Analysis

SAED- Selected Area Electron Diffraction

SE- Secondary Electron

SEM- Scanning Electron Microscopy

Characterisation of native MgO and its roles in solidification of Mg alloys

TEM- Transmission Electron Microscopy

XRD- X-Ray Diffraction

Table of contents

| | |
|--|------|
| Abstract | III |
| Acknowledgement..... | V |
| List of Publications | VII |
| Abbreviation..... | VIII |
| 1 Introduction..... | 1 |
| 1.1 Background | 1 |
| 1.2 Research objectives | 4 |
| 1.3 Thesis Outline | 4 |
| 2 Literature review | 7 |
| 2.1 Theoretical studies on solidification behaviour..... | 7 |
| 2.1.1 Classical nucleation theory (CNT)..... | 7 |
| 2.1.2 Adsorption model..... | 12 |
| 2.1.3 Epitaxial model | 14 |
| 2.1.4 Prenucleation..... | 16 |
| 2.1.5 Effect of solute on the growth of solid grains | 19 |
| 2.2 Theoretical models to predict grain size..... | 25 |
| 2.2.1 Free growth model | 25 |
| 2.2.2 Explosive grain initiation (EGI) model | 28 |
| 2.2.3 Interdependence model..... | 30 |
| 2.3 Evaluation of substrate potency for heterogeneous nucleation | 32 |
| 2.3.1 Turnbull's model..... | 32 |
| 2.3.2 Bramfitt's model | 33 |
| 2.3.3 Edge-to-edge matching model..... | 34 |
| 2.4 Practical methods for grain refinement of Mg alloys..... | 36 |
| 2.4.1 Zr inoculation | 36 |
| 2.4.2 Superheating..... | 37 |
| 2.4.3 Native grain refinement..... | 39 |
| 2.4.4 Carbon-based inoculation..... | 39 |

Characterisation of native MgO and its roles in solidification of Mg alloys

| | | |
|-------|--|----|
| 2.4.5 | Elfinal process-addition of FeCl ₃ | 40 |
| 2.4.6 | Theory-guided exploration of grain refiners | 40 |
| 2.4.7 | Grain refinement by MgO | 43 |
| 2.5 | The native MgO in Mg and its alloys..... | 45 |
| 2.5.1 | Oxidation in Mg and its alloys | 45 |
| 2.5.2 | The morphology of oxidation products | 47 |
| 2.6 | Manipulation of nucleation potency by elemental segregation..... | 50 |
| 2.6.1 | Elemental segregation on TiB ₂ in Al alloys | 52 |
| 2.6.1 | Interaction between substrate and solute in Mg alloys | 53 |
| 2.7 | Application of electron microscopy | 54 |
| 2.8 | Summary | 56 |
| 3 | Experimental procedure | 58 |
| 3.1 | Raw materials..... | 58 |
| 3.2 | Facilities..... | 58 |
| 3.2.1 | Furnaces and handling tools..... | 58 |
| 3.2.2 | Rotor-stator mixer | 60 |
| 3.2.3 | Pressurised filtration Device | 60 |
| 3.2.4 | TP-1 test unit..... | 61 |
| 3.3 | Casting Processes..... | 62 |
| 3.3.1 | Evaluation of grain refinement by TP-1 test..... | 62 |
| 3.3.2 | TP-1 test with intensive high shear melt conditioning (HSMC) treatment | 62 |
| 3.3.3 | TP-1 test with HSMC and controlled extra oxidation..... | 63 |
| 3.3.4 | Collection of MgO by pressurised filtration | 64 |
| 3.3.5 | Evaluation of the dispersity of native MgO | 65 |
| 3.3.6 | Collection of the oxides from melt surface | 65 |
| 3.4 | Sample preparation | 66 |
| 3.4.1 | OM samples | 66 |
| 3.4.2 | SEM samples..... | 67 |
| 3.4.3 | TEM samples | 68 |
| 3.5 | Characterisation methods..... | 70 |

| | | |
|-------|---|-----|
| 3.5.1 | Optical microscope (OM)..... | 70 |
| 3.5.2 | Scanning electron microscopy (SEM)..... | 70 |
| 3.5.3 | Transmission electron microscopy (TEM)..... | 71 |
| 3.5.4 | X-ray diffraction..... | 73 |
| 3.5.5 | Quantitative measurement..... | 74 |
| 4 | The nature of native MgO in pure Mg and Mg-9Al | 76 |
| 4.1 | Chapter overview | 76 |
| 4.2 | Results..... | 76 |
| 4.2.1 | Native MgO films/particles..... | 76 |
| 4.2.2 | Crystallography of MgO particles..... | 81 |
| 4.2.3 | Morphology of MgO particles..... | 83 |
| 4.2.4 | Size distribution of MgO particles | 86 |
| 4.2.5 | Chemical and structural configuration of MgO surface | 87 |
| 4.2.6 | Origin of {111} MgO and {100} MgO..... | 91 |
| 4.3 | Discussion | 94 |
| 4.3.1 | Formation of oxide films/particles in Mg alloys | 94 |
| 4.3.2 | Formation mechanism of {100} MgO..... | 95 |
| 4.3.3 | Formation mechanism of {111} MgO..... | 97 |
| 4.3.4 | Effect of MgO on heterogeneous nucleation and grain refinement..... | 99 |
| 4.4 | Conclusions..... | 106 |
| 5 | Interaction between Y and MgO and its effect on solidification of Mg-Y alloys . | 107 |
| 5.1 | Chapter overview | 107 |
| 5.2 | Results..... | 108 |
| 5.2.1 | Effect of Y addition on grain size | 108 |
| 5.2.2 | Native MgO particles in Mg-0.5Y | 110 |
| 5.2.3 | Structure and chemistry of Y segregation layer | 118 |
| 5.2.4 | Coarse and columnar grain due to Y ₂ O ₃ particles..... | 127 |
| 5.3 | Discussion | 130 |
| 5.3.1 | Columnar to equiaxed transition | 130 |
| 5.3.2 | Grain refinement due to Y segregation | 131 |

Characterisation of native MgO and its roles in solidification of Mg alloys

| | | |
|--------|---|-----|
| 5.3.3 | Y segregation on MgO particles | 132 |
| 5.3.4 | Mechanism underlying grain refinement | 141 |
| 5.3.5 | Poisoning effect resulting from grain initiation competition | 143 |
| 5.3.6 | Effect of substrate on solidification behaviour | 145 |
| 5.4 | Conclusions | 147 |
| 6 | Elemental segregation and its effect on solidification of Mg-Ca and Mg-Sn alloys | 148 |
| 6.1 | Chapter overview | 148 |
| 6.2 | Results..... | 148 |
| 6.2.1 | Grain size of Mg-Ca alloys without HSMC..... | 148 |
| 6.2.2 | Grain size of Mg-Ca alloys with HSMC..... | 151 |
| 6.2.3 | Grain size of Mg-Ca alloys with HSMC and oxidation..... | 153 |
| 6.2.4 | Effect of pre-cast treatments on grain size of Mg-Ca alloys..... | 155 |
| 6.2.5 | Native MgO in Mg-0.5Ca alloy | 156 |
| 6.2.6 | Ca segregation on MgO | 159 |
| 6.2.7 | Structure and chemistry of segregation layer..... | 160 |
| 6.2.8 | Strain analysis for the segregation layer by geometric phase analysis..... | 163 |
| 6.2.9 | Enhanced dispersity of native MgO due to segregation..... | 163 |
| 6.2.10 | Effect of Sn addition on grain size in Mg-Sn alloys without HSMC..... | 164 |
| 6.2.11 | Grain size of Mg-Sn alloys with HSMC..... | 167 |
| 6.2.12 | Grain size of Sn Mg-Sn alloys with HSMC and oxidation..... | 169 |
| 6.2.13 | Effect of pre-cast treatments on grain size of Mg-Sn alloys | 171 |
| 6.2.14 | Native MgO in Mg-2Sn alloy | 172 |
| 6.2.15 | Sn segregation on MgO..... | 174 |
| 6.3 | Discussion | 180 |
| 6.3.1 | Columnar to equiaxed transition (CET)..... | 180 |
| 6.3.2 | Grain refinement originated from native MgO particles..... | 185 |
| 6.3.3 | Modification of native MgO and its effect on heterogeneous nucleation | 187 |
| 6.3.4 | Mechanism for grain refinement by impotent substrate..... | 193 |
| 6.4 | Conclusions..... | 197 |

| | | |
|-----|--|-----|
| 7 | General Discussion | 199 |
| 7.1 | Morphology of native MgO particles in Mg alloys..... | 199 |
| 7.2 | Modification of MgO and its nucleation potency..... | 201 |
| 7.3 | Nucleation, grain initiation and grain refinement in Mg alloys | 203 |
| 8 | Conclusions..... | 208 |
| 9 | Future work..... | 211 |
| 10 | Appendix | 213 |
| 11 | References | 218 |

1 Introduction

1.1 Background

Since the first production of elemental magnesium (Mg) by the English scientist Sir Humphry Davy in 1808, Mg has experienced a long period before the industrialisation of its production process and practical application. Following steel and aluminium, magnesium is the third structural materials utilised commonly in today's industrial society. Its application proliferation is primarily attributed to the outstanding characteristic of its low density (1.738 g/cm^3), which is about one fourth of steel and two thirds of aluminium, being the lightest structural metallic materials in the world. This unique feature therefore offers significant opportunities for applications pursuing lightweight in industries of transportation (automotive, rail and aerospace), power tools and computer-communication-consumer (3C) products, *etc.* [1]. Besides, magnesium alloys find a promising perspective in biomedical application owing to the characteristics of biodegradability, biocompatibility and biosafety along with their mechanical properties [2].

The requirement of light weight once overwhelmed the rest drawbacks back in the 1920s, and aerospace and automobile industries widely adopted Mg and its alloys into their products until 1980s. After that a low tide appeared, their applications significantly reduced due to the poor corrosion resistance and perceived hazards with magnesium parts in the event of fire. However, owing to the technical issues being tackled through manufacturing developments, alloy design and product optimisation, the lightweight Mg and its alloys went back into the public concerns of energy and climate crisis from the 1990s. The legislation concerning the emission of greenhouse gas raises the importance of adopting light materials as alternatives for the existing heavier materials, *e.g.*, steel in most cases. In response to the current environmental and energy challenges facing modern societies, the use of Mg alloys, as the lightest class of structural materials, has become increasingly widespread in the last few decades, in particular for applications in the automotive industry [3,4]. Nevertheless, there are still several commercial and technical factors preventing the significant inroad of Mg application into the current industry that is, to date, mainly dominated by aluminium and steel.

Casting is the most practical and economical technique to produce near-net-shape Mg alloy products and raw ingots for down-stream thermal processing. This manufacturing process produces magnesium components that represent about 95% of structural Mg applications [4]. Being one of the positive characteristics in general metallic materials systems, grain refinement is essential for Mg alloys since a refined and uniform microstructure improves the materials' performance in many aspects, such as mechanical properties [5], creep resistance [6], resistance to hot tearing [7], corrosion resistance [8] and down-stream thermal processing [9,10]. A tremendous amount of research work, in aspects of the experimental and theoretical effort, has been carried out for decades to understand the solidification behaviour of metallic materials, striving to achieve grain refinement in Mg alloys.

The fundamental understanding of the solidification behaviour of metallic materials started from the classical nucleation theory [11–13]. With progress made in theoretical understandings of nucleation and growth that are the two intrinsic stages of solidification crucial for the as-cast microstructure, researchers gradually built up fundamental theories and models concerning the grain refinement, approaching the goal of engineering the solidified microstructure [14–18]. It is commonly accepted that grain refinement can be achieved when the nucleation is enhanced and the growth is restricted in a specific alloy system. Therefore, both the nucleating particles and solutes are important for grain refinement. Incorporation of these two aspects has led to numerical models that are capable of predicting and explaining most grain refinement phenomena in practical cases [17,18].

Historically, a lot of practical methods have been proposed to refine Mg and its alloys that can be classified into two groups: Al-bearing Mg alloys and Al-free Mg alloys. The grain refinement techniques used for the first group alloys include superheating [19], native grain refinement [20], carbon inoculation [21] and Elfinal process [22]. However, these methods have been abandoned due to either difficulties in practical operation in foundry or issues of detrimental impacts on the environment [23]. Recent studies were trying to explore effective and practical grain refiners for Al-bearing Mg alloys with constructive guidance on searching for potent particles to enhance heterogeneous nucleation. This brought about several candidates that have shown certain extents of grain refinement, which include Al_4C_3 , TiB_2 , TiC , SiC , AlN , Al_2Ca , ZnO and Al_2Re , *etc.* [23,24]. Unfortunately, it has to be admitted that there is not a commercial grain refiner for Al-bearing Mg alloys yet due to the issues in reliability, reproducibility and cost for the nucleating candidates mentioned above. In contrast, Mg-Zr master alloy is the

exclusively available grain refiner for Al-free Mg alloys containing little or no other poisoning elements of Mn, Fe and Si, which would form stable compounds with Zr [25–27]. A successful grain refiner with universal application for various Mg alloys is extremely hard to achieve. Due to the complexity in the melt of Mg alloys, it is difficult to find eligible particles meeting the criteria for an optimal grain refiner [24]. Given the low efficiency and high cost of Zr for grain refinement, work has been taken for decades to strive for improvements and to find alternatives. However, no effective grain refiner is available for Mg alloys yet.

As opposite to the trend to enhance nucleation, particles with a poor potency are recently found to be applicable of refining grain size through explosive grain initiation scheme [28–30]. As the dominant native oxide present in Mg alloy melt, MgO is impotent for heterogeneous nucleation due to the poor potency characterised with the large lattice misfit with Mg as well as its atomically rough surface [31]. In aspects of experiment and simulation, the native MgO particles in CP Mg and Mg-Al alloys have been found capable of refining the grain size more significantly than those potent particles [28–30]. The application of native MgO particles for grain refinement of Mg alloys following the newly proposed mechanism enlightens an alternative route to refine grain size, which is potentially an economical option satisfying the circular economy. However, the research in the solidification behaviour of Mg melts involving native MgO particles is still in a primitive stage. There remain a lot of technical and fundamental questions to be answered before the successful application in practice. For example, the knowledge about the nature of native MgO particles in Mg melts is scarce since the majority of the previous research focused on oxidation processes rather than the oxidation product itself. Therefore, the first aim of this thesis is to investigate the natural characteristics of the native MgO in Mg alloys. Their morphologies, crystallographic information, formation mechanisms, size and size distributions will be comprehensively studied to understand their effects on heterogeneous nucleation and grain initiation in Mg alloys.

It has been realised that interaction between the nucleating substrate and solutes can modify the substrate's potency through elemental adsorption [32,33] or chemical reaction on the substrate surface [34]. The possible interaction at the interface between MgO and the surrounding solutes in alloys melts is another concern of this work. With the variations in potency for nucleation, the subsequent grain initiation manner will be significantly affected, *i.e.*, in either progressive grain initiation or explosive grain initiation manner [29]. Other than this, new phases may form as the result of the reaction between substrate

and solute or between solutes. Therefore, the second objective of this thesis is to study the surface modification of MgO particles and/or newly formed particles in different binary alloy systems through advanced electron microscopy, and their consequent effects on solidification and grain refinement. On the other hand, the experimental results can be incorporated into the current fundamental theories and models, aiming to narrow the gap between theories and practice, and hopefully delivering more practical approaches for grain refinement of Mg alloys.

Although with theoretical foundation and a limited amount of experimental verifications, there is much work to be done before the universal application of native MgO particle for grain refinement in Mg alloys. This work is trying to broaden the knowledge about the nature of native MgO, elemental segregation, phase transformation, as well as the corresponding heterogeneous nucleation, grain initiation and grain refinement in various Mg alloys.

1.2 Research objectives

1. To study the morphology, size and size distribution of native MgO films/particles in Mg and its alloy melts as well as the underlying formation mechanism;
2. To investigate the interaction between solute and native MgO at the temperature above the liquidus at atomic resolution, and the consequent effect on heterogeneous nucleation;
3. To investigate the grain refinement performance of native MgO in different Mg alloys.
4. To investigate the mechanism underlying the grain refinement achieved by the application of native MgO particles in different Mg alloys.
5. To investigate different grain initiation manner in the systems containing modified MgO particles with different configurations including potency, particle size, size distribution and number density.

1.3 Thesis Outline

To start with, introduction of the research background and research objectives is presented in Chapter 1. Chapter 2 reviews the literature related to this study. It starts with

the theoretical progress in solidification that includes nucleation theories, grain growth, modelling for grain size prediction. Afterwards, the models to evaluate the nucleating potency of a substrate are reviewed as well. This is followed by a review of the practical methods for grain refinement of various Mg alloys. As a potential nucleation agent for grain refinement of Mg, MgO is reviewed in terms of its natural characteristics in Mg alloys. After that, the oxidation behaviour in Mg alloys is reviewed. Moreover, the manipulation of heterogeneous nucleation by atomic modification is summarised in terms of theory and experimental evidence, which leads to the introduction of the application of advanced electron microscopy in studying the structure and chemistry of the substrate/solid interface.

Experimental procedures and characterisation techniques used in this study are described in detail in Chapter 3.

Chapter 4 presents the natural characteristics of native MgO films/particles by microstructural examination in different scales. Based on the experimental results, the formation mechanisms of MgO films/particles and the difference in morphology are discussed in terms of thermodynamics, kinetics and crystallography. Their roles in grain refinement of Mg alloys are discussed in terms of nucleation and grain initiation.

In Chapter 5, characterisation of the interaction between native MgO and Y in Mg-0.5Y and Mg-3Y is conducted by atomic-resolution electron microscopy. The evaluation of microstructure and grain refinement in Mg-Y binary alloys with and without high shear melt conditioning (HSMC) prior to casting are provided. Discussions are made on the solidification behaviour with regard to the effect of Y interfacial segregation on heterogeneous nucleation in terms of lattice misfit, surface roughness and chemical interaction. Moreover, the correlation between the modification of native MgO particles and the grain size evolution is discussed, in an attempt to reveal the mechanism underlying either enhancing or poisoning grain refinement in Mg-Y alloys.

Chapter 6 presents the experimental results of grain structure evolution of Mg-Ca and Mg-Sn binary alloys under various melt treatments before solidification. The segregation characteristics at the MgO/Mg interface in Mg-0.5Ca and Mg-2Sn alloys are comprehensively studied by advanced electron microscopy. The corresponding nucleation potency of the native MgO particles after elemental segregation is analysed from the aspect of lattice misfit, surface roughness and chemical interaction. Application

of numerical models is applied to understand the solidification behaviour and rationalise the solidified microstructure.

In Chapter 7, general discussions are carried out in: *i*) the morphology of native MgO particles in the melts of Mg alloys (CP Mg, Mg-Al, Mg-Y, Mg-Ca and Mg-Sn alloys); *ii*) the nucleation potency manipulated by the atomic modification of nucleating substrate by deliberately selected solutes; *iii*) nucleation, grain initiation and grain refinement in Mg alloys.

Conclusions are given in Chapter 8 and it is followed by the suggestion for the future work presented in Chapter 9.

2 Literature review

In this chapter, a review of the previous theoretical studies on nucleation in the literature is presented in **section 2.1**. It contains the classical nucleation theory (**section 2.1.1**), the adsorption theory (**section 2.1.2**), the epitaxial model (**section 2.1.3**) and the prenucleation theory (**section 2.1.4**). Grain growth and effect of solute on solidification are then reviewed in **section 2.1.5**. This is followed by reviewing several numerical models (**section 2.2**), which are used to explain the grain refinement behaviour and to predict the grain size after solidification. To search for potent nucleating particles capable of achieving grain refinement, several theoretical models based on crystallographic matching principle have been proposed, which has been reviewed in **section 2.3**. After that, **section 2.4** is going through the practical grain refining techniques for Mg alloys and the associated mechanisms underlying. Despite an impotent particle for nucleating Mg grains, the native MgO has been found capable of achieving grain refinement through explosive grain initiation (EGI) (**section 2.4.7**). This raises the importance of nature of the native MgO films/particles and the corresponding oxidation behaviour of Mg alloy melts, which is reviewed in **section 2.5**. In addition, the manipulation of heterogeneous nucleation by atomic modification of the substrate surface has been reviewed in **section 2.6** from aspects of theory and experiment. Finally, the application of electron microscopy in studies of solidification under different scales is reviewed in **section 2.7**. The advanced transmission electron microscopy is essential to probe at the atomic scale the structural and chemical configuration, which are closely related to the nucleation potency.

2.1 Theoretical studies on solidification behaviour

2.1.1 Classical nucleation theory (CNT)

2.1.1.1 Homogeneous nucleation

Homogeneous nucleation means that a solid phase forms inside its own melt without any foreign substrates [11,13,35,36]. When a solid embryo forms in the melt, two contributions to the total free energy occur. One is the change of volume free energy ($v_s \Delta G_v$) and the other one is interfacial free energy ($A_{LS} \gamma_{LS}$) associated with the newly formed surface of solid (**Fig. 2.1(a)**). Assume that an embryo with radius r is solidified in the liquid, the difference in free energy for this system is given by the following equation [35].

$$\Delta G = v_s \Delta G_v + A_{LS} \gamma_{LS} = -\frac{4}{3} \pi r^3 \Delta G_v + 4 \pi r^2 \gamma_{LS} \quad \text{Eq. 2-1}$$

Where ΔG_v is the free energy difference between the solid and liquid phase, v_s is the volume of solid formed, A_{LS} is the area of the newly created liquid-solid interface, γ_{LS} is the interfacial energy associated with the newly created A_{LS} . ΔG is plotted schematically as a function of r in **Fig. 2.1(b)**, the curve first increases, reaches a maximum and then decreases. An energy barrier is required to be climbed over for nucleation, after that the resting process is energetically favoured.

There exists a *critical radius* r_{hom}^* for homogeneous nucleation upon which the embryo can spontaneously grow with the decrease of free energy and become a nucleus. While on the contrary, also driven by the reduction of free energy, the embryo will melt back when $r < r^*$. By differentiating, we can calculate the critical size [35].

$$r_{hom}^* = \frac{2\gamma_{LS}}{\Delta G_v} = \frac{2\gamma_{LS}T_m}{\Delta H_f \Delta T} = \frac{2\gamma_{LS}}{\Delta S_f (T_m - T)} \quad \text{Eq. 2-2}$$

Where T_m is the equilibrium melting temperature, ΔH_f is the latent heat of fusion while ΔS_f is the entropy of fusion per unit volume. The excess free energy of the critical nucleus can be calculated by substituting **Eq. 2-2** into **Eq. 2-1** [35].

$$\Delta G_{hom}^* = \frac{16\pi\gamma_{LS}^3}{3\Delta G_v^2} \quad \text{Eq. 2-3}$$

It is seen from this equation that the formation of an embryo with the critical size still increases the free energy of the system [13]. Overcoming the barrier of homogeneous nucleation essentially requires extra energy resulting from the fluctuation in density, atomic configurations, heat content, *etc.*

The rate of homogeneous nucleation can be derived by making the following assumptions: *i)* the concentration of nuclei with a critical number of atoms remains invariant after nucleation begins; *ii)* the addition of a single atom to critical nucleus makes it supercritical and grow rapidly. Then the concentration of nuclei I is given by [11,35]

$$I = n^* \omega^* f_{LS} \quad \text{Eq. 2-4}$$

Where ω^* is the number of atoms surrounding a critical nucleus, f_{LS} is the frequency with which atoms jump across the interface, and n^* is the number of stable nuclei being a function of temperature [35,36].

$$n^* = K_1 \exp\left(-\frac{\Delta G_{hom}^*}{k_B T}\right) \quad \text{Eq. 2-5}$$

Where the constant K_1 is related to the total number of nuclei of the solid phase [35].

While
$$f_{LS} = K_2 \exp\left(-\frac{Q_d}{k_B T}\right) \quad \text{Eq. 2-6}$$

Where Q_d is the activation energy for diffusion which is temperature independent, K_2 is a temperature-independent constant. Combining **Eq. 2-4**, **Eq. 2-5** and **Eq. 2-6** gives [35]

$$I = \omega^* K_1 K_2 \left[\exp\left(-\frac{Q_d}{k_B T}\right) \exp\left(-\frac{\Delta G_{hom}^*}{k_B T}\right) \right] \quad \text{Eq. 2-7}$$

Similar to the compensating terms of the $-v_s \Delta G_v$ and $A_{LS} \gamma_{LS}$ as temperature decreases, the nucleation rate reaches a maximum value as a result of the competition between terms of $\exp\left(-\frac{\Delta G_{hom}^*}{k_B T}\right)$ and $\exp\left(-\frac{Q_d}{k_B T}\right)$. This is schematically represented in **Fig. 2.1**. At high temperature, nucleation is suppressed by the small activation driving force. While at a lower temperature, the atomic mobility drops and then suppresses the nucleation rate.

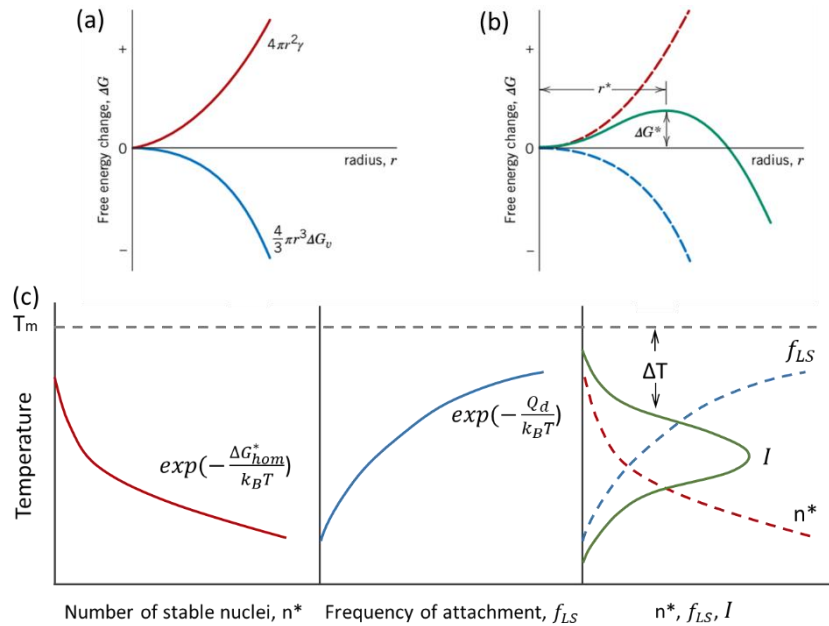


Fig. 2.1 Schematic curves of (a) volume free energy and interfacial free energy; (b) free energy versus nucleus radius; and (c) number of stable nuclei versus temperature; frequency of atomic attachment; and nucleation rate versus temperature [35].

2.1.1.2 Heterogeneous nucleation

In practice, the undercooling required for homogeneous nucleation can be extremely large. For instance, the value is 420K for nucleation of pure iron according to Kelton [12]. In a real solidification process, the undercooling is usually tens of degrees in magnitude or much less [11,12]. Rather than homogeneous nucleation, such nucleation event is more likely to be heterogeneous nucleation occurring on any possible substrates, such as fragments of crystals and inclusions including oxides particles, exogenous addition of chemicals like grain refiner, and on the mould walls [11,12]. In casting practice of metallic materials, heterogeneous nucleation is the general nucleation path happening on any possible foreign substrates during solidification. Practically, addition of inoculants to the melt prior to casting is widely applied in foundry to achieve a fine and uniform grain structure through the promotion of heterogeneous nucleation.

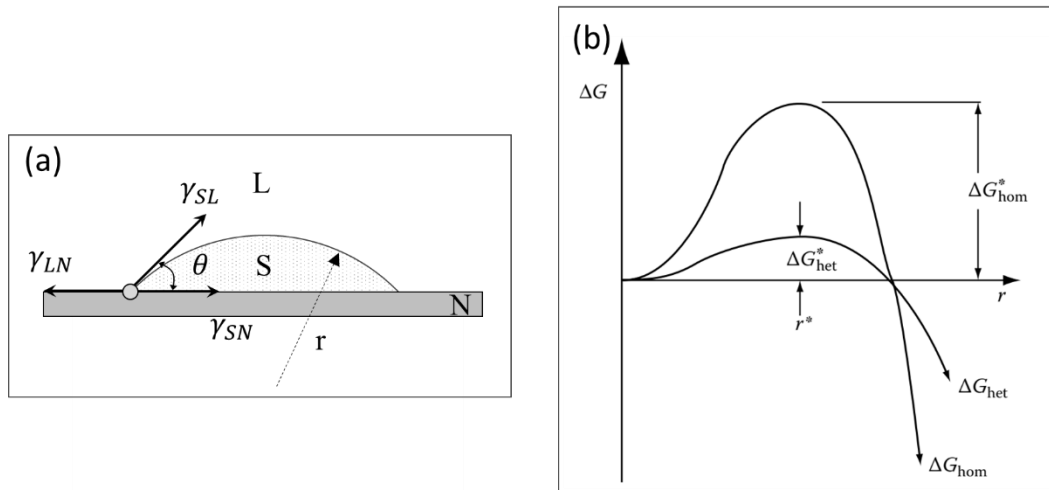


Fig. 2.2 (a) Heterogeneous nucleation of the spherical cap on a flat substrate; (b) the excess free energy of solid clusters for homogeneous and heterogeneous nucleation. Note r^* is independent of the nucleation site. Redrawn based on reference [36].

The *spherical-cap model* [13,35–37] in **Fig. 2.2(a)** schematically shows a solid embryo forms in contact with a substrate with a flat surface. For a certain volume of solid and with an assumption of isotropic interfacial tensions, the embryo shape is energetically favoured in a spherical cap requiring a minimum work of formation. As a result, a balance is achieved among the interfacial tensions in the plane of the substrate [36].

$$\gamma_{LN} = \gamma_{SN} + \gamma_{LS} \cos \theta \quad \text{Eq. 2-8}$$

Apparently, the formation of solid on the substrate is associated with the formation of the following interfaces: liquid/solid (L/S); solid/substrate (S/N); and liquid/substrate (L/N). Combining the different terms associated with interfacial free energy and the drop in free

energy associated with the formation of certain volumes of solid yields the excess free energy for the embryo formation [36].

$$\Delta G_{het} = V_s \Delta G_V + A_{LS} \gamma_{LS} + A_{SN} \gamma_{SN} - A_{SN} \gamma_{LN} \quad \text{Eq. 2-9}$$

Where V_s is the volume of the spherical cap, A_{LS} and A_{SN} are respectively the areas of the L/S and S/N interfaces, and γ_{SL} , γ_{SN} and γ_{LN} are the interfacial energies of the L/S, S/N and L/N interfaces, respectively.

Eq. 2-9 can be rewritten in terms of the wetting angle θ and the cap radius r as

$$\Delta G_{het} = \left\{ \frac{4}{3} \pi r^3 \Delta G_v + 4 \pi r^2 \gamma_{SL} \right\} f(\theta) \quad \text{Eq. 2-10}$$

The expression is the same as that of the homogeneous nucleation except for an extra term of $f(\theta)$, which is a geometric factor introduced by the presence of heterogeneous substrate.

$$f(\theta) = (2 + \cos \theta)(1 - \cos \theta)^2 / 4 \quad \text{Eq. 2-11}$$

There also exists a *critical radius* r_{het}^* for heterogeneous nucleation upon which the on-going growth of the nucleus is energetically driven by the decrease of free energy. It can be derived by differentiation of **Eq. 2-10**,

$$r_{het}^* = \frac{2\gamma_{SL}}{\Delta G_v} \quad \text{Eq. 2-12}$$

The substitution of **Eq. 2-12** into **Eq. 2-10** gives the critical nucleus free energy for the formation of a heterogeneous nucleus with critical size.

$$\Delta G_{het}^* = \frac{16\pi\gamma_{SL}^3}{3\Delta G_v^2} f(\theta) = \Delta G_{hom}^* f(\theta) \quad \text{Eq. 2-13}$$

In comparison to homogeneous nucleation (**Eq. 2-2**), the critical radius is unaffected. While the activation energy barrier against heterogeneous nucleation on a substrate gets smaller due to the introduction of the geometric factor $f(\theta)$. As the wetting angle θ decreases (**Eq. 2-11**), $f(\theta)$ decreases as well, and the corresponding ΔG_{het}^* declines (Eq. 2-13). Therefore, the wetting angle θ can be adopted as a parameter to judge the potency of a substrate, with $\theta = 0^\circ$ meaning the zero barrier for heterogeneous nucleation, while $\theta = 180^\circ$ equalling to that of homogeneous nucleation.

2.1.2 Adsorption model

In terms of thermodynamics, the spherical cap model in classical nucleation theory (CNT) has rationalized how the nucleation barrier is lowered as compared to that of the homogeneous nucleation. In the studies of solidification of liquid droplets embedded in solid bulks, the application of this model shows good fitting to the kinetics. However, it appears to break down for systems with a low nucleation undercooling. By fitting measurements based on CNT, the derived nucleation densities were found unphysical as the values are several orders less than one per droplet [32]. In certain cases where θ , $f(\theta)$ and ΔG_{het}^* approach zero, Kim and Cantor realised that the spherical cap contains only a few atomic layers in thickness when $\theta < 20^\circ$. Further drops in θ ($< 10^\circ$) make it irrational for a solid nucleus with a spherical cap. Thereafter, an *adsorption model* was postulated to evaluate the relationship between adsorption and interfacial energy. It was found that the adsorbed layer of a new crystalline phase is favourable in terms of thermodynamics, which later serves as the basis for growth.

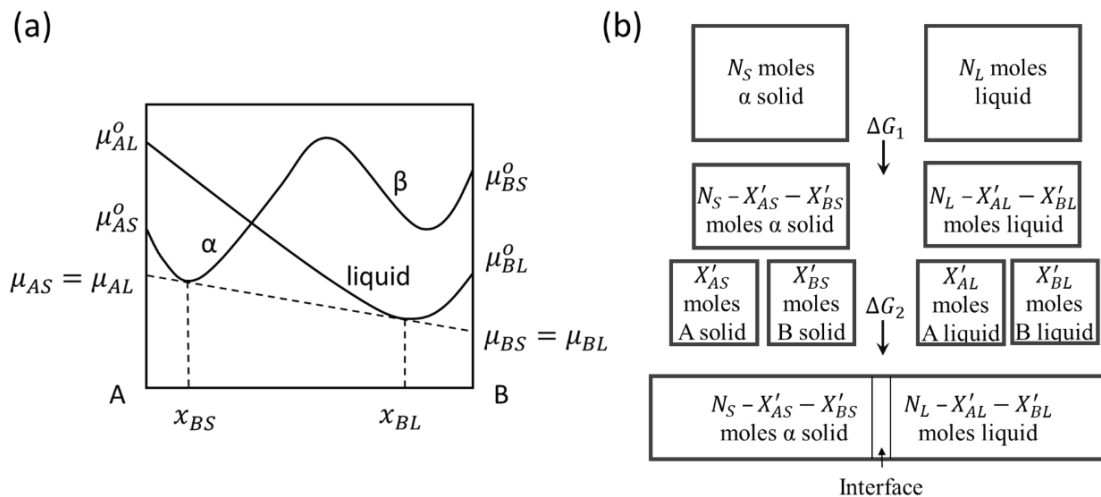


Fig. 2.3 (a) Curves of Gibbs free energy-composition for the α , β and liquid phases; (b) schematic of a two-stage virtual process illustrating the thermodynamics of constructing an α -solid interfacial monolayer. Redrawn from reference [32].

Firstly, the model is built based on binary A-B alloy systems (α for A rich solid and β for B rich solid, x_{ij} refers to the composition of i component in j phase) with simple eutectic or monotectic diagrams, where the solid and liquid have the same coordination number. A planar interface is constructed as a monolayer that is a mixture of solid A (x'_{AS}), solid B (x'_{BS}), liquid A (x'_{AL}) and liquid B (x'_{BL}) atoms, with the corresponding thermodynamics being schematically shown in **Fig. 2.3**. ΔG_1 is the change of interfacial energy due to the construction of interface by removing necessary liquid and solid atoms [32].

$$\Delta G_1 = \sum x'_{ij}(u_{ij}^o - u_{ij}) \quad \text{Eq. 2-14}$$

Where u_{ij}^o and u_{ij} are the standard state and equilibrium chemical potentials, respectively.

In the second stage, the randomly redistributed atoms in the interfacial monolayer are interacting with each other, and also with the adjacent atoms in the liquid and α solid as well. Summing the bonding energies gives the ΔG_2 [32].

$$\Delta G_2 = \sum RTx'_{ij} \ln x'_{ij} + 1/2N_o(mx'_{ij}x'_{kl}e_{ijkl} + 2nx_{ij}x'_{kl}e_{ijkl} - nx_{ij}x_{kl}e_{ijkl} - x'_{ij}e_{ij}) \quad \text{Eq. 2-15}$$

Where $i, k = A, B$, and $j, l = S, L$, e_{ijkl} is the bonding energy between an ij and a kl atom, R is the gas constant and N_o is the Avogadro's number, while m and n are fractional coordination numbers parallel and vertical to the interface. Specifically, the first term on the right is the configurational entropy of mixing the different atoms within the monolayer; term two is the bonding energy between different atoms within the interface; while the third term is the bond energy between interfacial atoms and the α solid and liquid phases; term four is the broken bond energy to from α and liquid surface to be attached at the interface; the final term is the broken bond energy from pure solid and liquid A and B.

Combination and reduction of the equation yield the molar interfacial energy γ_{ad} [32].

$$\begin{aligned} \gamma_{ad} &= \Delta G_1 + \Delta G_2 \\ &= \sum x'_{ij}(u_{ij}^o - u_{ij}) + RTx'_{ij} \ln x'_{ij} + \delta_{ij}mx'_{ij}x'_{kl}w_{ijkl} \\ &\quad + \delta_{ijkl}nx_{ij}x'_{kl}w_{ijkl} - \delta_{ijkl}nx_{ij}x_{kl}w_{ijkl} \end{aligned} \quad \text{Eq. 2-16}$$

Where $\delta_{ijkl} = 0$ when $i = k$ and $j = l$, otherwise, $\delta_{ijkl} = 1$, w_{ijkl} is the interaction parameters.

Therefore, minimization of γ_{ad} is able to determine the equilibrium interface solid fraction and composition. The interfacial monolayer changes sharply from liquid to solid that close to B in composition as the temperature decreases, acting as a catalyst for the heterogeneous nucleation of B-rich β solid. The model suggests that adsorption is

promoted by a large difference between the melting points of A and B, as well as a small difference between solid and liquid immiscibility of A and B.

2.1.3 Epitaxial model

An *epitaxial model* was proposed by Fan to describe heterogeneous nucleation on a potent substrate, whereby the mechanism follows as the layer-by-layer ordering of solid atoms onto the substrate at the atomic level [34]. As schematically shown in **Fig. 2.4(A)**, a physical model is built up to show how the liquid phase (L) nucleate on a potent substrate (N). Firstly, the random liquid atoms adsorb onto the substrate in an ordered configuration that mimics the atomic structure in the terminated crystal plane (subfigures a to b in **Fig. 2.4(A)**). Such ordering process proceeds layer-by-layer, rather than that described in CNT of forming a spherical cap (unphysically break down for a potent substrate). Such resembling initial structure is termed as *pseudomorphic solid* (PS). Nevertheless, due to the difference in lattice structure, the coherent interface (PS/N) suggest a strained growth associating with building-up of elastic strain energy within the PS layers as a function of the thickness (h). As shown in **Fig. 2.4(Ac)**, at a critical thickness (h_c) misfit dislocations are created to compensate the elastic strain energy in the PS layer, transferring the PS/N interface into a semi-coherent S/N interface. Henceforth, further growth of solid becomes strainless, entering the growth stage with curvature constrain. Before the thickness reaches h_c , the elastic strain energy is linearly proportional to h and the square of lattice misfit (f^2) between S and N [34]:

$$E_S = Bf^2h \quad \text{Eq. 2-17}$$

Where B is a function of the shear modulus and the *Poisson's* ratio. Generally, there exist several mechanisms to relief strain energy other than misfit dislocations, *e.g.*, vacancies and stacking faults. Moreover, such relaxation process might be gradual rather than a sudden trigger at h_c . However, it is noted that in this model, for simplicity, the creation of misfit dislocations is adopted as the mechanism for strain relaxation when $h = h_c$.

On the other hand, the energy of misfit dislocations is calculated as [34]:

$$E_D = 2D\delta_{re}b(\ln \frac{h_c}{b} + 1) \quad \text{Eq. 2-18}$$

Where D is a constant for the solid phase, b is the magnitude of the *Burger's* vector, and δ_{re} is the elastic strain released by the misfit dislocations. δ_{re} equals f as E_S is

completely released by E_D at $h = h_c$. If the strain relaxation is a gradual process, E_S then gradually transfer into E_D before h_c , beyond which the total energy of the pseudomorphic layer becomes constant that equal to E_D .

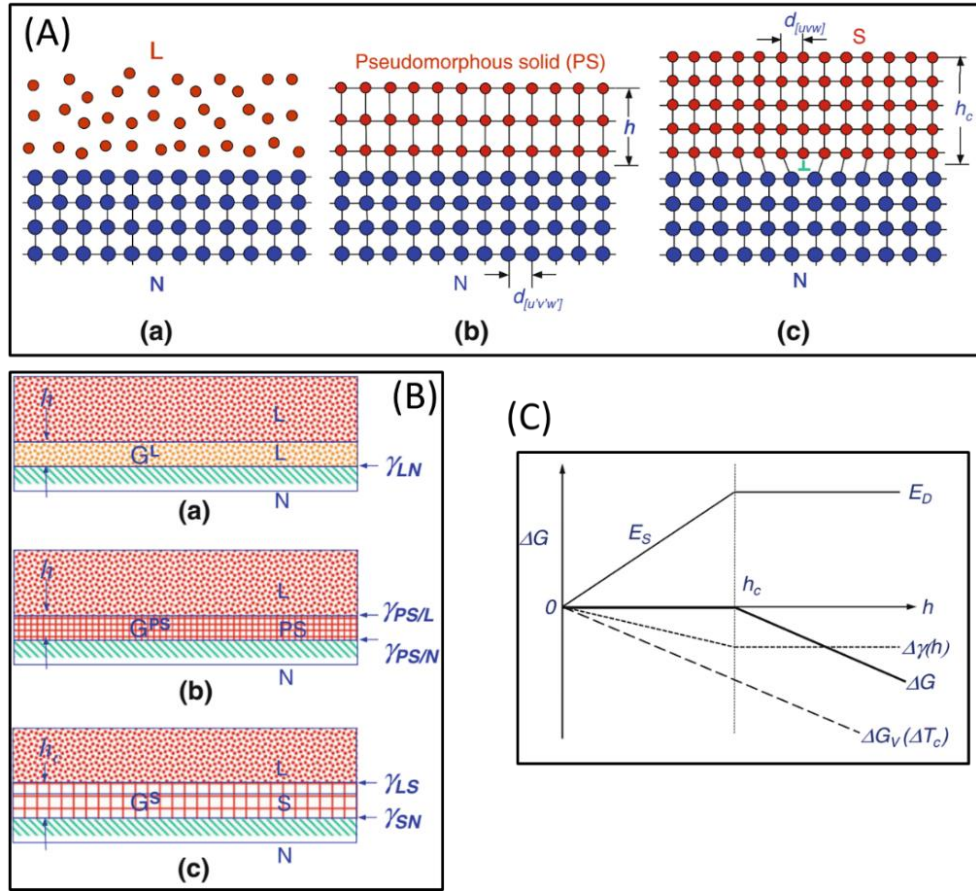


Fig. 2.4 (A) Schematic of the physical model for epitaxial model showing heterogeneous nucleation process on a potent substrate under a satisfied undercooling; (B) schematic of the energy status at the corresponding different stages; and (C) schematic illustration of the change in various energies as a function of the layer thickness. Redrawn from reference [34].

The interfacial energy status for the epitaxial nucleation process is shown in **Fig. 2.4(B)**. Among them, the formation of the S/N interface originates from PS/N interface associated with strain relaxation by dislocations, therefore γ_{SN} becomes [34]

$$\gamma_{SN} = \gamma_{PS/N}(h_c) + 2Dfb \left(\ln \frac{h_c}{b} + 1 \right) \quad \text{Eq. 2-19}$$

The total change of interface energy after epitaxial nucleation is a linear function of h during PS layer growth ($0 \leq h \leq h_c$), and becomes a constant when $h > h_c$ [34],

$$\Delta\gamma = \frac{\gamma_{LS} + \gamma_{PS/N}(h_c) - \gamma_{LN}}{h_c} h \quad \text{Eq. 2-20}$$

Fig. 2.4(C) shows the energy changes during and after the PS layer growth against the thickness h . At the h_c where PS layer has relaxed into solid phase, the free energy change per unit area is zero and can be derived as [34]

$$\Delta G = -\Delta S_v \Delta T h_c + B f^2 h_c + \Delta \gamma(h_c) = 0 \quad \text{Eq. 2-21}$$

And [34]

$$\Delta T_c = \frac{\gamma_{LS} + \gamma_{SN} - \gamma_{LN}}{\Delta S_v h_c} \quad \text{Eq. 2-22}$$

Since all the interfacial energy terms are functions of f , the critical undercooling (ΔT_{ept}) required for the formation of PS layer up to h_c is also a function of f only. Or in other words, if the $\Delta T < \Delta T_c$, heterogeneous nucleation is inhibited as the PS layer growth is unfavoured in terms of energy. Only when $\Delta T > \Delta T_c$, $\Delta G < 0$ for all h , serving as the driving force for the growth of PS layer beyond h_c . As a consequence, ΔT_c acts as a criterion for judging whether nucleation can occur or not under a ΔT . Heterogeneous nucleation is therefore a deterministic process, which is different from the stochastic event in CNT depending on the energy fluctuation in the system.

2.1.4 Prenucleation

It is well known that nucleation of a solid occurs at a certain temperature below the liquidus, forming a crystalline phase. However, atomic ordering phenomenon in the liquid close to S/L interface has been observed experimentally above the liquidus in many cases [38–40]. Theoretical calculations indicate the mechanism of a ‘hard wall’ effect, the liquid atoms near the interface packed as layers to accommodate the abrupt change in the electron density at the interface. Owing to the direct observation by advanced electron microscopy in HRTEM imaging mode, Oh *et al* revealed the atomic ordering of Al atoms of six layers at the interface between Al and α -Al₂O₃ at 850 °C, with a structure resembling that of α -Al₂O₃ [40]. A recent review by Kaplan and Kauffmann [41] suggests that the ordering structure above liquidus not only has a layering tendency perpendicular to the interface, but also has variation in the extent of ordering in each layer. Asta *et al* speculated that such layering structure is in close relationship with the subsequent heterogeneous nucleation below liquidus [42].

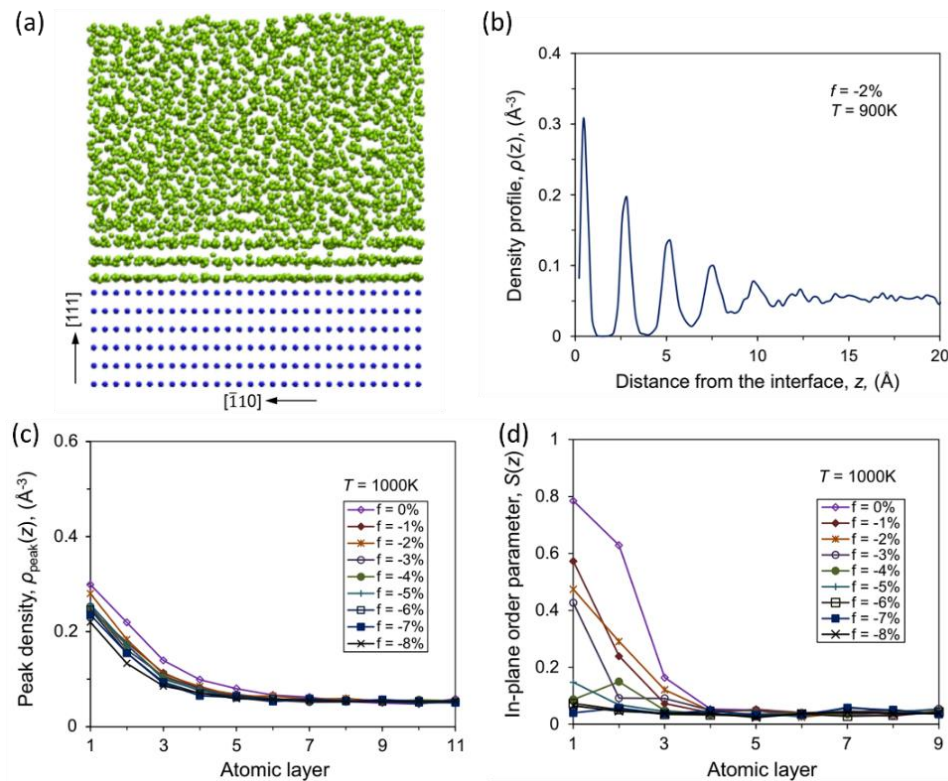


Fig. 2.5 (a) A snapshot of the simulation results, equilibrated at 900 K, for a cell with $f = -2\%$ showing the layering structure of Al liquid atoms (green) with a few atomic layers away from the substrate; (b) plot of the corresponding density profile; (c) peak density and (d) in-plane order parameter of the liquid Al atoms at the interface as a function of the number of atomic layers in the system equilibrated at 1000 K. Redrawn from reference [43].

In a system with a fixed Al solid substrate and Al liquid with fixed misfits without the interference from chemical effect, Men and Fan systematically studied the atomic ordering in the liquid adjacent to the substrate using molecular dynamics (MD) simulation [43,44]. As analogous to that of the hard-wall effect, ordering behaviour was found. Their results showed that the characteristics of the ordering have the following features (**Fig. 2.5**): *i*) the number of ordering layers perpendicular to the substrate can be extended to six layers, which are independent of the misfit, while are slightly enhanced by reducing temperature; *ii*) the in-plane ordering is substantially promoted by the reduction in misfit or temperature, while it decays as the distance away from substrate increases. Such atomic ordering phenomenon in the liquid close to the interface of substrate and liquid above liquidus is referred to as *prenucleation* [43].

As similar to the structural templating mechanism proposed in the epitaxial model where the elastic strain energy can be relaxed through the creation of dislocations [34], the first prenucleation layer, with a given misfit ($\neq 0$), also releases elastic strain energy by forming networks of Shockley partial dislocations. The atomic configuration in the

prenucleation layer varies and poses an effect on the subsequent nucleation. If the formation of the ordered structures decreases the initial lattice misfit with the nucleating solid after relaxation, the following heterogeneous nucleation will be enhanced. On the contrary, heterogeneous nucleation will be impeded if the initial lattice misfit is increased.

Another work reported by Fang *et al* studied the chemical effect on prenucleation behaviour by *ab initio* MD simulation [45]. Applying the criterion of the *heat of mixing* (ΔH^{mix}) to evaluate the chemical interaction, they artificially construct interfaces of Al/Ag, Al/W, Al/Al and Al/Cd, which have the ΔH^{mix} values of ‘-4’, ‘-2’, ‘0’ and ‘3’, respectively. For systems with negative ΔH^{mix} , the prenucleation was found to be promoted in terms of both the atomic layering and in-plane ordering. The enhancement results from the higher electron density at the interface and a higher electron transfer across the interface, which in turn freeze the atomic mobility of the liquid atoms adjacent to the substrate. Nevertheless, it is also pointed out that the contribution of chemical factor place behind that of structural factor (lattice misfit). With the realization of the importance of atomic-structure templating, the MD simulation work was extended by Jiang *et al* to study the effect of surface roughness on prenucleation [46]. As one more evidence confirming the structural templating, their results show that the surface roughness deteriorates both the atomic layering and in-plane ordering in the prenucleation layer near the substrate. In addition, The authors also found that the in-plane ordering is totally eliminated for an amorphous substrate irrelevant to the surface roughness at all, while the atomic layering in the liquid is reduced or eliminated depending on the surface roughness [46].

By now, a systematic theory has been established for prenucleation behaviour, which plays a significant role in determining the subsequent heterogeneous nucleation. Three factors have been found affecting the prenucleation: lattice misfit, chemical interaction and atomic-level surface roughness. Its application reflects in one of the recent cases about the mechanism of Zr poisoning in Al alloys inoculated with Al-5Ti-1B master alloy [47]. The presence of Zr solute results in the dissolution of Al₃Ti 2DC and the formation of Ti₂Zr 2DC instead, leading to the disappearance of the grain refinement and appearance of the coarse and columnar grain structures. The mechanism can be attributed to three factors [47]: *i*) changed misfit back to -4.2 % (TiB₂ with Ti₂Zr 2DC) from 0.09% for TiB₂ with Al₃Ti 2DC; *ii*) surface roughness due to the different sizes between Zr and Ti in the 2DC layer; and *iii*) stronger chemical interaction of Zr atoms with liquid Al than

that of Ti atoms in the Ti₂Zr 2DC layer. All the factors deteriorate the prenucleation, weakening the atomic ordering in the prenucleation layers which hinder the heterogeneous nucleation subsequently. Two extra factors other than lattice were proposed to affect heterogeneous nucleation. One other supporting example is the difference in nucleation potency for TiB₂ and AlB₂ (which are isomorphous phases) due to the difference in chemical composition [48].

2.1.5 Effect of solute on the growth of solid grains

One of the general phenomena during solidification of metallic alloys is the solute partitioning resulted from the compositional difference between solid and liquid [13,36]. Depending on the solute partitioning characteristic (k , m), solute can be either enriched or depleted at the advancing S/L interface during solidification. The actual distribution of solutes in the melt close to the S/L interface leads to a constitutional supercooled (CS) zone proceeding into the liquid, which later shows significant effect on two aspects: *i*) the growing morphology of solid grains; and *ii*) the growth rate of the solid grains. In relation to the subjects of dilute binary alloys in this work, this section will describe the development of CS zone in the first instance, and then emphasize on how the solutes affect the aspect *ii*), *i.e.*, growth restriction, which is later differently parameterized as reviewed below.

2.1.5.1 Development of constitutional supercooling zone

A simple portion of phase diagram with the idealization of straight solidus and liquidus is shown in **Fig. 2.6(a)**, the defined partition coefficient k is given as [36]

$$k = \frac{X_S}{X_L} \quad \text{Eq. 2-23}$$

Where X_S and X_L are the mole fraction of solute in the solid and liquid at the given temperature of T_2 . For an alloy X_0 under unidirectional solidification, three limiting cases will be discussed.

For case one under equilibrium solidification, whose rate is so slow that solid state diffusion allows the composition of solid and liquid to follow the solidus and liquidus lines. A typical *lever rule* can be derived [36]:

$$X_S f_S + X_L f_L = X_0 \quad \text{Eq. 2-24}$$

$$X_L = \frac{X_0}{1 + f_S(k - 1)} \quad \text{Eq. 2-25}$$

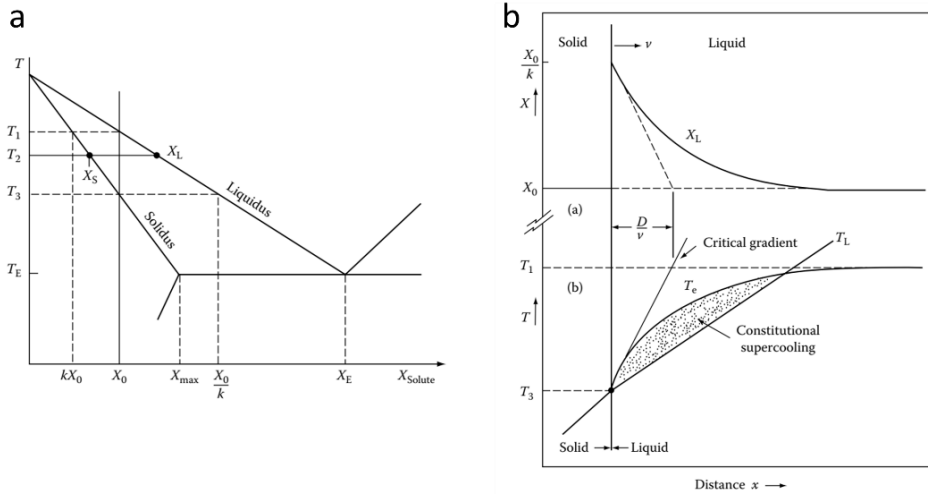


Fig. 2.6 (a) A portion of hypothetical binary phase diagram; (b) schematic illustration of the origin of constitutional supercooling (CS) ahead of a planar solidification front [36].

While for case two, where there is no diffusion at all in the solid (due to a rapid cooling rate) and perfect mixing in the liquid, solute will progressively enrich in the liquid as solidification proceeds. A balance can be made between the amount rejected solute from an infinitesimal increment of solidification, df_S , and the resulting solute increases in the liquid [36].

$$(X_L - X_S)df_S = (1 - f_S)dX_L \quad \text{Eq. 2-26}$$

Applying the boundary condition of $X_S = kX_0$ at $f_S = 0$ gives [36]

$$X_S = kX_0(1 - f_S)^{(k-1)} \quad \text{Eq. 2-27}$$

Which is known as the *non-equilibrium lever rule* or the *Scheil equation*.

In case three, it assumes that the rejected solute can only be transported away by diffusion when stirring or convection are absent in the melt. There will be a rapid building-up of solute in the liquid adjacent to the S/L interface, which equilibrates at X_0/k in steady state and decreases exponentially away from the S/L interface. A balance is created between the rate that solute diffuses down the concentration gradient and the rate of solute being rejected from the solidifying liquid [36].

$$-DC'_L = v(C_L - C_S) \quad \text{Eq. 2-28}$$

Where D is the diffusivity in the liquid, C'_L is the composition gradient at the interface, v is growing rate of S/L interface, C_L and C_S are the equilibrium concentrations of liquid and solute, respectively.

The solution of **Eq. 2-28** yields the concentration profile in the liquid [36].

$$X_L = X_0 \left\{ 1 + \frac{1-k}{k} \exp \left[-\frac{x}{(D/v)} \right] \right\} \quad \text{Eq. 2-29}$$

The resultant concentration profile X_L is shown in **Fig. 2.6(b)**, starting from X_0/k at $x = 0$ and decreasing exponentially to large distances from the interface. Correspondingly as shown in **Fig. 2.6(b)**, the equilibrium liquidus temperature (T_e) varies as well. In comparison to the actual liquid temperature (T_L) with a gradient imposed by the external heat extraction, there exists an area below its T_e . It is known as constitutional supercooling due to the correlation with compositional effects.

2.1.5.2 Growth restriction

As reviewed by StJohn *et al* [49], continuous work has been undertaken to understand the correlation between solute-segregation-induced CS zone and the final solidification grain structure. Along with studies working on its effect on stability and formation of cellular dendritic grains, quantification in the role of solute on grain refinement was also established. To quantify the growth restriction and its effect on grain refinement, back in the 1970s, Tarshis *et al* in the first instance proposed a *Supercooling Parameter P* to rationalize the grain refinement led by the addition of solute in binary Ni-X and Al-X alloys [50], and P was defined as

$$P = \frac{mc_0(k-1)}{k} \quad \text{Eq. 2-30}$$

Where c_0 is the alloy composition, m is the gradient of the liquidus and k is the partition coefficient. As depicted in **Fig. 2.7(a)**, P equals to the freezing range for alloy with a solute concentration of c_0 . There comes a later comprehensive work on the effect of Cr, Cu, Fe, Mg, Mn, Si, Zn and Zr on the solidified grain size of high purity Al inoculated with and without 0.2 wt.% Al-5Ti-1B master alloy [51], the results show a relatively good correlation between the grain size and P .

Another parameter Q is found to better quantify the degree of growth restriction than P since the re-plotting of grain size in a function of Q shows less deviation from the prediction curve than that of P [17]. Q was first defined by Maxwell and Hellawell as a parameter inversely proportional to the growth rate of spherical crystal growth restricted by partitioning of a single solute [52].

$$Q = mc_0(k - 1) \quad \text{Eq. 2-31}$$

Q is termed as *growth-restriction factor* and labelled in the phase diagram (**Fig. 2.7(a)**). Its effectiveness allows the application into the free growth model (see **section 2.2.1**) for numerical simulation of the growth of solid and the corresponding heat released. In an isothermal melt, the growth rate of a spherical crystal is given as [17]

$$V = \frac{\lambda_s^2 D}{2r} \quad \text{Eq. 2-32}$$

Where D is the diffusion coefficient of solute in the liquid, r is the radius of the spherical crystal and λ_s is a function of S and can be obtained with the invariant-size approximation [53]. S can be given by

$$S = \frac{2(c_l - c_o)}{c_s - c_l} = \frac{2[\Delta T - \Delta T_c]}{mc_0(k - 1) + (\Delta T - \Delta T_c)(k - 1)} \quad \text{Eq. 2-33}$$

Where c_l and c_s are the solute content in the liquid and solid at the S/L interface, respectively. ΔT is the overall undercooling and ΔT_c is the curvature undercooling. Therefore, the growth rate of a spherical solid depends on many factors including $Q = mc_0(k - 1)$.

Recently, Fan *et al* simulated the growth velocity in binary and ternary systems with various Q values [54]. The resultant data showed a considerably scatter as resulted from the variations in the k and/or ΔT for a given Q . They claimed that the growth velocity is not a unique function of Q . A new *growth restriction parameter* β was therefore developed to effectively quantify the growth restriction in multicomponent alloy systems [54].

$$\beta = \frac{f_L}{f_S} = \frac{Q}{\Delta T} - k \quad \text{Eq. 2-34}$$

Where f_L and f_S are respectively the phase fraction of the liquid and the solid. **Fig. 2.7(b)** shows that the growth restriction coefficient $\frac{\lambda_S^2}{2}$ increases monotonically with the increasing β for all solutes. Being independent of the nature of solute, β for multicomponent alloys can be expressed, without consideration of solute interactions, by the linear sum of the β_i from binary alloys [54].

$$\beta = \sum_{i=1}^n \beta_i \quad \text{Eq. 2-35}$$

Fig. 2.7(c) shows the comparison between the overall β from **Eq. 2-34** through thermodynamic approach and the simple addition by **Eq. 2-35**, where the agreement demonstrates a great convince of simple addition of each β_i for a multicomponent system. In addition, as shown in **Fig. 2.7(d)**, the simulated growth velocities by phase field simulations as a function of for binary and ternary system are consistently aligned to one curve. All suggest that β is a unique function to evaluate growth restriction, regardless of the nature of solutes, concentration and solidification conditions.

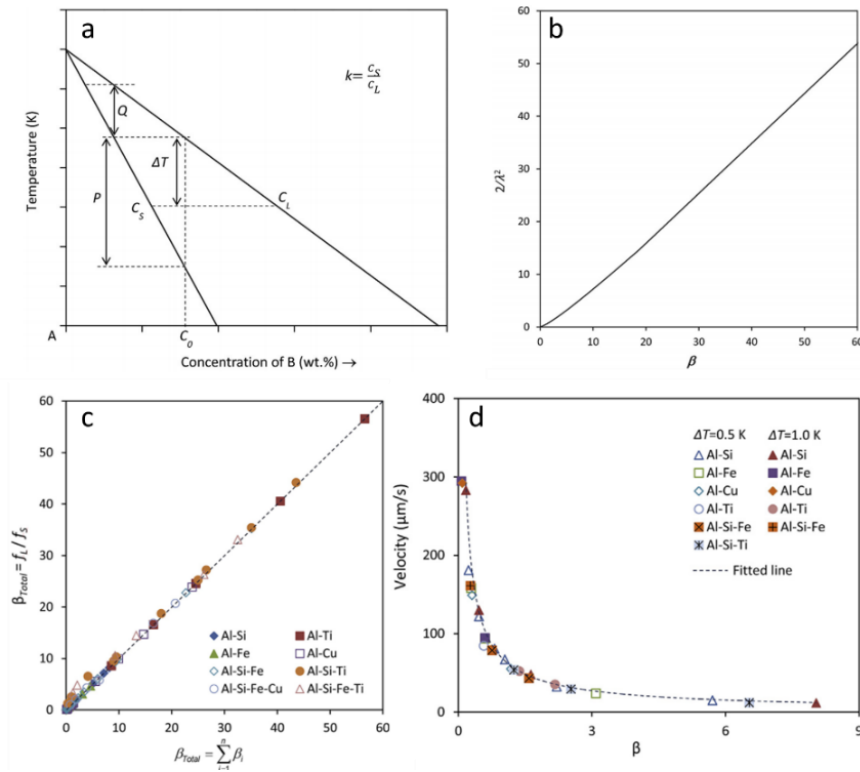


Fig. 2.7 (a) A schematic showing a linear phase diagram of a binary A-B system; (b) Plot of growth restriction coefficient for spherical growth in a binary alloy against β ; (c) Comparison between the true β given by Eq. 2-35 and that by linear addition (Eq. 2-34) of β_i of the constituent solutes; and (d) Plot of growth velocity calculated by phase field simulations against β under different levels of undercooling. Redrawn based on Reference [54].

Although it is generally understood that growth restriction is the direct result of solute segregation/depletion at the S/L interface, the physical origin of growth restriction was discussed under atomic level as the blockage of the supply of critical elements for solid growth. For instance, for the eutectic alloys ($k < 1$) solutes enrich at the S/L interface to block the supply of solvent atoms. While for peritectic alloys ($k > 1$) solutes deplete at the S/L interface (equivalent to solvent enrichment) to block the supply of solute atoms. Both ways of the blocking atoms result in a decreased growth velocity.

2.1.5.3 Columnar to Equiaxed Transition (CET)

Typically, the solidified grain structure of metallic materials can be equiaxed, columnar or mixture of the both in the transition area. The equiaxed grain structure is usually desirable due to its positive impact on the integrity, mechanical property and chemical homogeneity of the final castings. In a system of controlled directional solidification, the origin of the columnar to equiaxed transition (CET) is more likely the blocking grains that heterogeneously nucleate and grow ahead of the columnar front [55–57]. Besides, the dispersed grains may either originate ahead of the columnar front or formed elsewhere earlier being transported there. At which position, the aforementioned CS zone, also, is critical for their nucleation, growth and survival in the supercooled liquid. Therefore, the achievement of homogeneous microstructure requires both sufficient amounts of solute and nucleating particles under a certain solidification condition. Based on the understanding of growth kinetics of solid grains that in correlation with the resultant growth restriction from solute partitioning during solidification, Hunt introduced a front blocking mechanism for the CET during a steady state solidification [56]. As shown in **Fig. 2.8(a)**, there is a geometric argument that the columnar front can only be blocked by the equiaxed grains ahead with a critical volume fraction over 0.49. The original columnar grains then transit into equiaxed grain structures. The criterion for a fully equiaxed grain structure was derived as [56]:

$$G < 0.617(N^o)^{1/3} \left\{ 1 - \frac{(\Delta T_N)^3}{(\Delta T_{tip})^3} \right\} \Delta T_{tip} \quad \text{Eq. 2-36}$$

Where G is the thermal gradient, N^o is the number density of nucleation site, ΔT_N is the undercooling for heterogeneous nucleation, ΔT_{tip} is the tip undercooling. However, the blocking grains should be in free growth stage already so that N_o should be more

reasonable the number density of nucleation sites with successful grain initiation. And correspondingly, the ΔT_N should be replaced by undercooling for free growth ΔT_{fg} .

It is found from the criterion that the equiaxed grain structure is favoured in an alloy melt with a high number density of effective nucleation particles (*i.e.*, low nucleation/free growth undercooling), high concentration of solute, high cooling rate (high front velocity v) and low thermal gradient (see **Fig. 2.8(b)**).

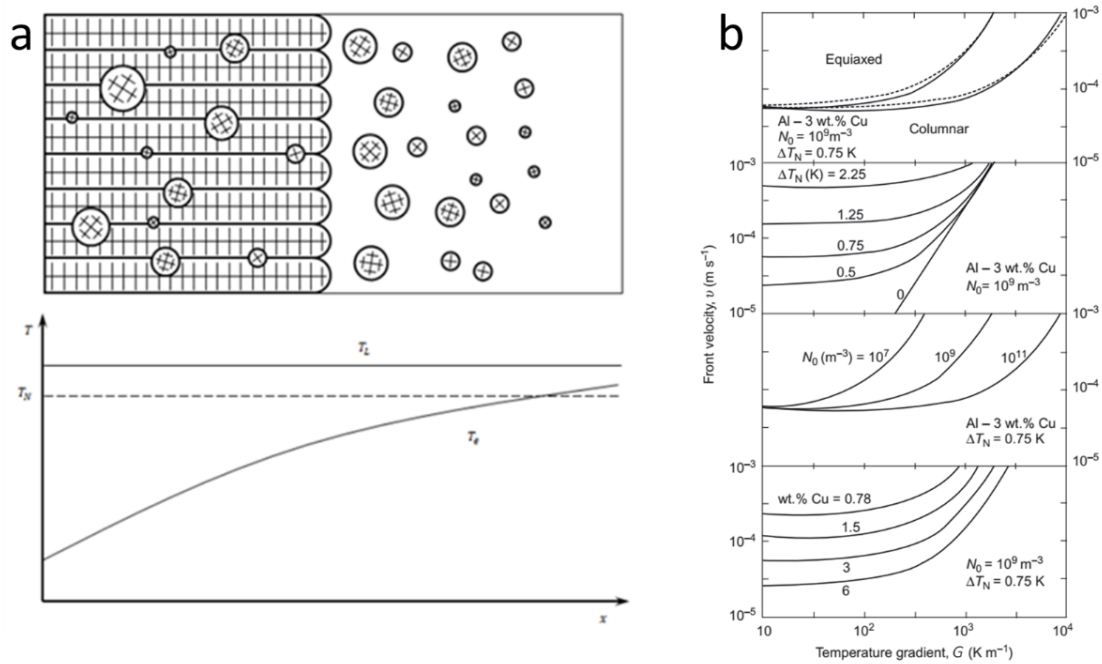


Fig. 2.8 (a) Schematic diagram showing the columnar front with grains nucleating and growing ahead of the columnar front (Top) and the corresponding actual temperature T_e in relation to the liquidus T_L (Bottom);(b) CET maps of growth velocity versus temperature gradient in Al-Cu alloys, showing how nucleation undercooling, N_0 and solute affects the gradual CET behaviour. Adapt from references [56,58,59].

2.2 Theoretical models to predict grain size

2.2.1 Free growth model

The spherical-cap model breaks down for the solid phase nucleates on a potent substrate, on which nucleation forms as a mono-atomic layer of a few layers of adsorbed atoms in solid phase. In the solidification process of a melt inoculated with potent particles, the role of nucleation becomes a hidden factor [17] as the continuous growth of the nucleated embryo in layer stage will be impeded by the Gibbs-Thomson effect resulting from the curved solid/liquid interface. As shown in **Fig. 2.9(a)**, the free growth criterion can be set up for a given substrate with a certain radius, undercooling beyond that critical value will

allow continuous growths of the hemisphere over the substrate radius without the need to surmount any energy barrier. Further growth is spontaneously free with decreasing interface curvature. Therefore, in such cases with potent inoculation, the grain initiation becomes a deterministic process depending on whether the critical temperature is satisfied or not. Similar phenomena have been experimentally observed by Turnbull who adopted the definition of ‘athermal nucleation’ from Fisher *et al* to explain the abnormal nucleation rate of mercury droplets [60,61]. The fraction of droplets solidified was found dependent on undercooling with no relationship with time, indicating a deterministic event rather than stochastic one for the thermal nucleation described in CNT. A relationship was built between the size of surface patches and a critical radius derived from undercooling, based on that he successfully derived the size distribution of patches from the distribution of undercooling values at which the droplet solidified. Quisted and Greer calculated the work of formation for the initiation of solid grains on a size-defined nucleating particle, confirming that athermal nucleation is dominant in a solidifying system with potent inoculations [62].

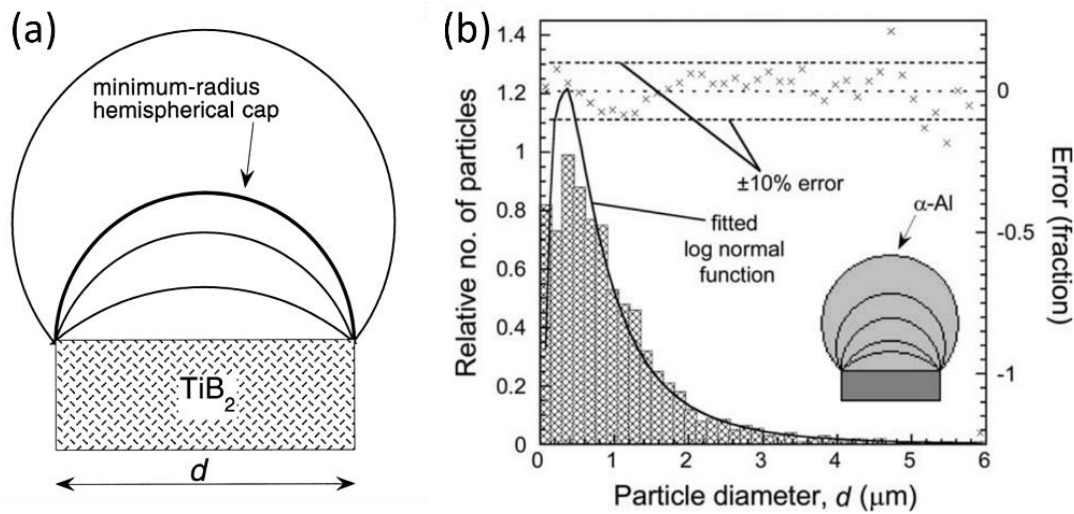


Fig. 2.9 (a) Crystal growth following nucleation on one {0001} face of a boride particle. Thickening of the crystal reduces the radius of curvature of its interface with the liquid. (b) log-normal distribution of the nucleant TiB_2 particles in a commercial Al–5Ti–1B refiner, the inset shows the growth of $\alpha\text{-Al}$ from the (0001) face of a hexagonal particle in the melt [17,63].

As shown in **Fig. 2.9(a)**, growth of newly formed solid can only continue by reducing the radius of curvature. A critical radius of r_{fg}^* is set below which the growth can't proceed, then if the particle size $d < 2r_{fg}^*$, a barrier prevent further growth occurs then this particle can't nucleate a grain. While when greater undercooling is obtained, r_{fg}^* decrease until

$d < 2r_{fg}^*$, the diameter of the grown crystal can surpass r_{fg}^* and grows freely beyond that. The undercooling required for free growth can be given by [17]:

$$\Delta T_{fg} = \frac{4\gamma_{LS}}{\Delta S_v d} \quad \text{Eq. 2-37}$$

Where γ_{LS} is the solid-liquid interfacial energy, ΔS_v is the entropy of fusion per unit volume, and d is the diameter of the nucleating substrate. The grain initiation process during solidification then will happen on the largest particles first followed progressively by the smaller ones until the on-set of recalescence.

Being an adaptation of the work of Maxwell and Hellawell [52], free growth criterion was then introduced into the previous numerical model to simulate the thermal history of a specific volume of isothermal melt with certain inoculations [17]. Some modifications were made, including the application the detected log-normal size distribution of TiB₂ particles in the Al melt (**Fig. 2.9(b)**), and the application of athermal nucleation rather than classical heterogeneous nucleation. The numerical model simulates the competition between the latent heat released from grain growth (combined with growth restriction effect reviewed in **section 2.1.5**) and the imposed heat extraction. Grain initiation will be stifled when recalescence occurs and then the predicted grain size can be determined. Therefore, numerical modelling can be established as [17]:

$$(q(d)\delta d)_n = N(d)\delta d 4\pi r_{n-1}^2 (r_n - r_{n-1}) \Delta H_v \quad \text{Eq. 2-38}$$

Where $(q(d)\delta d)_n$ is the heat input when particle grows from d to $d + \delta d$, ΔH_v is the latent heat of solidification per unit volume [17].

$$r_{n+1} = r_n + Vdt \quad \text{Eq. 2-39}$$

r_n can be calculated from the last r_{n-1} with the V in the last $(n-1)^{th}$ interval.

So, in every time increment, the melt temperature in the next interval can be calculated as [17]:

$$T_{n+1} = T_n - Rdt + \frac{q_{total}}{C_{pv}} \quad \text{Eq. 2-40}$$

Where C_{pv} is the heat capacity of the melt per unit volume.

Free growth model turned out to have a good agreement with the measured grain sizes of Al and Al alloys inoculated with Al-Ti-B refiner by different casting methods [17,51].

This model was also successfully adopted in the SiC-inoculation Mg alloys [64,65]. Additionally, free growth model itself is also a tool to optimize the grain refiners by taking into considerations of factors like casting conditions, alloy compositions, addition level, size distribution, *etc.* [63].

2.2.2 Explosive grain initiation (EGI) model

In **section 2.1.3**, the mechanism of initiation of solid phase on a substrate at the atomic scale has been described in the epitaxial model, where the energy barrier has derived to be zero for the layer-by-layer formation of PS structure [34]. However, a certain critical undercooling (ΔT_c) is necessary to allow the PS layer growing beyond the critical thickness, over which the further growth is constrained by the free growth criterion (ΔT_{fg}). As a result, heterogeneous nucleation is a deterministic process as that of grain initiation, occurring at the point when ΔT surpasses ΔT_c . And ΔT_c herein equals to nucleation undercooling (ΔT_n). The following growth is also deterministic that a new grain proceeds when $\Delta T > \Delta T_{fg}$. Therefore, the solidification process can be either nucleation controlled (or dominant) or grain initiation controlled (or dominant) with dependence on the comparison between ΔT_c and ΔT_{fg} .

If $\Delta T_n < \Delta T_{fg}^{1st}$, nucleation proceeds easily before any grain initiation events. As the temperature keeps dropping down, it follows the manner depicted in the free growth model that grain initiation proceeds firstly on the largest particle, continues with the progressively smaller ones, finishes at recalescence point. Progressive grain initiation (PGI) mode is generally observed in practice for the vast majority of engineering alloys inoculated with potent inoculant particles [29]. Such as Mg alloys with Zr inoculation, and Al alloys with TiB₂ based grain refiners. A drawback is that the nature of size distribution of particles, under a certain solidifying condition in a melt, decides already the efficiency of grain refiner, which is usually low.

On the other way, as shown in **Fig. 2.10(a)**, when thermal undercooling satisfies: $\Delta T = \Delta T_n \approx \Delta T_{fg}^{last}$, *i.e.*, $T_n \approx T_{fg}^{1st} \approx T_{fg}^{last}$, no grain initiation occurs at the temperature with $T = T_{fg}^{1st}$ due to the absence of nucleation ($\Delta T = \Delta T_{fg}^{last} < \Delta T_n$). While nucleation and grain initiation take place simultaneously when $T = T_n$ on all satisfied substrates ($\Delta T = \Delta T_n = \Delta T_{fg}^{last}$), then a fast growth and the corresponding latent heat result in an immediate recalescence (**Fig. 2.10(b)**). As shown in **Fig. 2.10(c)**, a significant grain

initiation rate is achieved as well. this process is named as explosive grain initiation (EGI) [29].

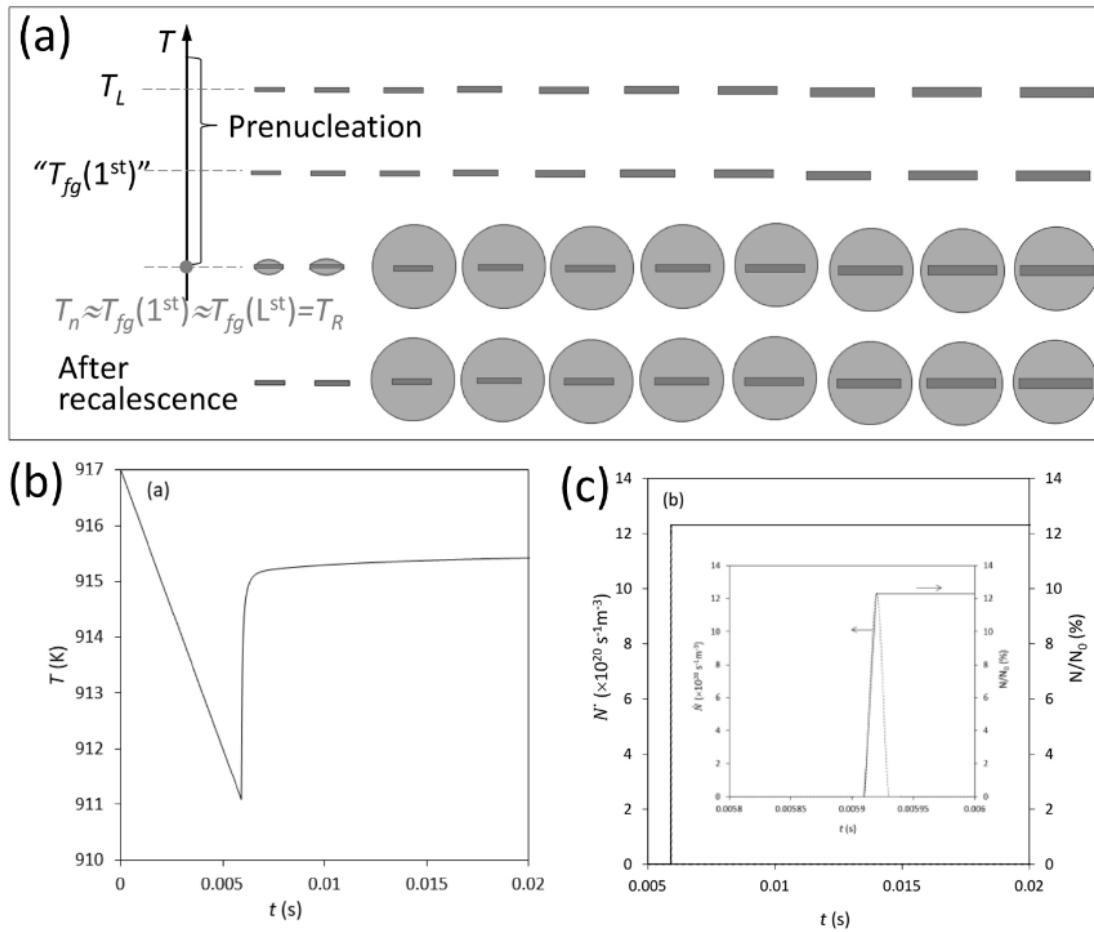


Fig. 2.10 (a) Schematic illustration of explosive grain initiating process during solidification of alloys containing native MgO particles. (a) Calculated cooling curve and (b) the instantaneous grain initiation rate and accumulative grain initiation events per unit volume normalised by the total number density of MgO particles, showing the explosive grain initiation behaviour during solidification of Mg-1Al alloy containing native MgO particles ($N_0 = 1 \times 10^{17} \text{m}^{-3}$) under a cooling rate of 10^3K s^{-1} . The insert in (b) shows the detailed grain initiation rate in a finer time scale [28,29].

Recent studies show that the native MgO particle (poor potency to nucleate Mg grains) in Mg alloy melts provides a good example to study the solidification behaviour in such manner. For an Mg-0.3Al alloy melt containing native MgO particles in a number density of $10^{17}/\text{m}^3$, a numerical model was applied to simulate its thermal history when solidified by high pressure die casting (HPDC, the cooling rate is around 1000 K/s) [28]. The results showed a vertical rise in temperature shortly after grain initiation, along with an enhanced grain initiation rate of 13.4%. The predicted average grain size was $3.4 \mu\text{m}$, close to that of $3 \mu\text{m}$ quantified by experiment. The comparison of grain sizes between CP-Mg and Mg-1Ca-1Zr alloys cast by HPDC suggests EGI is more powerful in gran refinement

compared with PGI [29]. The potential of EGI shows a superior potential than PGI on grain refinement. More significantly, the application of native and impotent MgO particles as grain refiner in an EGI manner has the potential to promote Mg alloys in more industrial application. It is not only a cost-efficient method but also a contribution to the circular economy by repeatedly applying the native MgO particles as grain refiners, eliminating the worry about accumulation of external grain refiners far from consideration. Being found as a potential candidate to achieve grain refinement in Mg alloys, the native MgO particles in Mg alloy melts are going to be extensively studied in this work.

2.2.3 Interdependence model

With the understanding of the contribution of solutes (constitutional undercooling ahead of the liquid/solid interface) [66] and nucleating particles (heterogeneous nucleation) [67] to grain refinement, StJohn and co-workers developed the interdependence theory to address the interconnections between growth and nucleation during the solidification cycles starting from the cold end to the hot end [18].

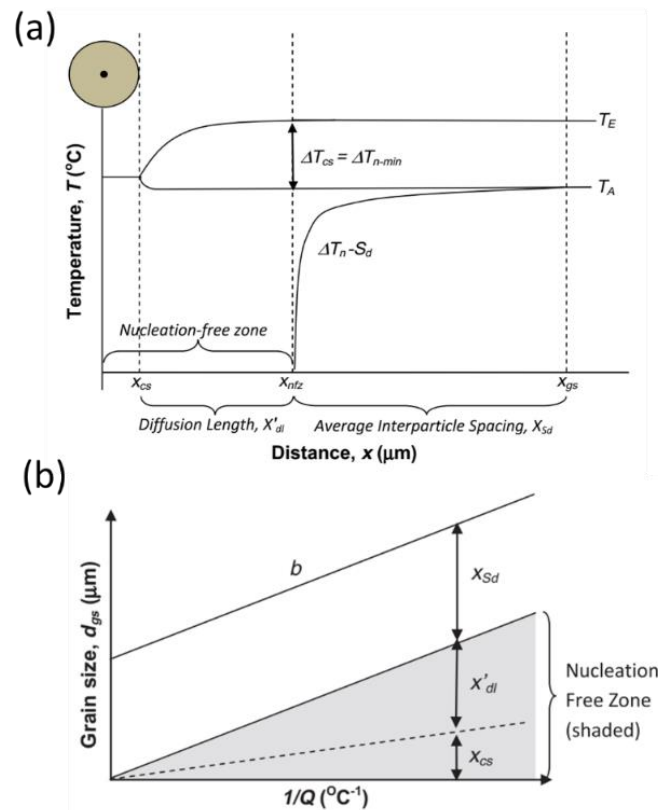


Fig. 2.11 (a) Schematic showing the three regions that together establish the grain size of the microstructure: x_{cs} , x'_{dl} and x_{sd} . The first two regions x_{cs} and x'_{dl} together represent a nucleation-free zone, where nucleation is not possible for the particle distribution described by

$\Delta T_n - S_d$; (b) a simple representation showing how each of the three terms contributes to the d_{gs} to $1/Q$ curve.

As shown in **Fig. 2.11(a)**, in one cycle, the nucleated grain is required to grow into a certain distance (x_{cs}), which builds up a sufficient CS (solute rejection and pile-up) ahead of the S/L interface. Due to the distribution of pile-up solute ahead of the S/L front (correlates to the temperature profiles), an extra distance (x'_{dl}) is necessary to obtain a critical CS that equals to the subtraction of equilibrium liquid temperature (T_E) and actual liquid temperature (T_A), *i.e.*, $\Delta T_{cs} = \Delta T_E - \Delta T_A = \Delta T_{n-min}$, to generate next event of nucleation. Lastly, nucleation happens on the most potent particle with an additional distance (x_{sd}) above $x_{cs} + x'_{dl}$, and next round the cycle begins again. With further consideration of the solidification as repetitive cycles of growth and nucleation towards the thermal centre of the casting, in the next round, the growth of grain only requires to re-establish part of critical ΔT_{n-min} by a shorten distance, which corresponds to $z\Delta T_{n-min}$, $0 < z < 1$. Therefore, the established grain size in this theory can be derived as

$$d_{gs} = b + \frac{a}{Q} = x_{cs} + x'_{dl} + x_{sd} \quad \text{Eq. 2-41}$$

$$= \frac{Dz\Delta T_n}{vQ} + \frac{4.6D}{v} * \left(\frac{C_l^* - C_o}{C_l^* * (1 - k)} \right) + x_{sd}$$

Where D is the diffusion coefficient, v is the growth velocity of S/L interface, k is partition coefficient, ΔT_n is the critical undercooling for nucleation (here the criterion applies that in free growth model), C_o is the alloy composition, C_l^* represents the composition of the liquid in front of the S/L interface, Q equals to $mC_o(1 - k)$ and represents the growth restriction factor, and x_{sd} represents the probability of a particle with potency of $1/\Delta T_{n-min}$ being enveloped by the CS zone, which is a function of the particle density and particle size distribution.

Fig. 2.11(b) illustrates how the three terms formulated above contributes to the simple $d_{gs} = b + \frac{a}{Q}$ relationship. StJohn *et al* demonstrated that some experimental data can be plotted as grain size against $1/Q$ in different systems [18,23,25], *e.g.* aluminium system added with TiB₂ [68], commercial purity and high purity Mg-Al alloys [69] addition of Zr and other solute elements as grain refiner in various Mg alloys [25,70]. All of them obey the linear relationship as shown in **Fig. 2.11(b)**. From interdependence theory and

some interpretation of experiment data, it also guides the practical ways for grain refinement. That is to minimise the size of nucleation-free zone, for example, by adding proper elements with high Q factor and also with low ΔT_n . Additionally, from **Eq. 2-41**, we also know that increasing growth rate is another efficient way to minimise the nucleation-free zone, for instance, casting in a high cooling rate. Further, different size distributions lead to difference in possibility of nucleation and growth event, for a given number density of nucleating particles the narrow distribution in active size range is desirable for achieving grain refinement.

2.3 Evaluation of substrate potency for heterogeneous nucleation

Potency of a substrate usually refers to the effectiveness or ability of the substrate to nucleate heterogeneously a solid from liquid phase. As aforementioned in the historical development of theories about heterogeneous nucleation, it has been known that the interfacial energy (γ_{SN}) between the solid and the substrate acts as the controlling factor in nucleation behaviour. This means that with a lower γ_{SN} , a smaller contacting angle, a lower energy barrier to overcome, an easier set-up of heterogeneous nucleation would result. A great number of studies have been undertaken to determine the factors that dominantly affect the interfacial energy between the substrate and solid. As realised from their research, γ_{SN} can be affected by many factors including the crystallographic matching, electronegativity difference, chemical nature of the substrate, size of the nucleating particle and topographic of the substance, *etc.*

2.3.1 Turnbull's model

Turnbull and Vonnegut [14] summarised plenty of previous work on nucleation, including ice formation; crystallization of mercury; aluminium and other metals; as well as the oriented epitaxial growth. With a critical review, they found the qualitative evidence that a potent substrate has a low-index plane where the atomic configuration is similar, in terms of symmetry and interatomic spacing, to that in a certain low-index plane of the nucleating solid crystal. A simple crystallographic theory to evaluate the catalysis of a substrate was proposed, which predicts that the potency of a substrate will be identical with the reciprocal of their disregistry with the low-index planes of the forming solid phase. The linear disregistry, δ_l , can be derived as:

$$\delta_l = |\Delta a/a_o| \quad \text{Eq. 2-42}$$

Where Δa is the difference between the lattice parameters for low-index comparison planes of the nucleation substrate and the solid, a_o is the lattice parameter for the low index comparison plane of the solid.

The minimisation of free energy is generally favoured by the condition that the nucleus is not coherent by with a certain strain amount of:

$$\epsilon = |(a_{act} - a_o)/a_o| \quad \text{Eq. 2-43}$$

Where a_{act} and a_o are the lattice parameters of the solid in the strained and strain-free condition, respectively. When δ_l is relatively small the nucleus forms coherently on the catalyst with $\epsilon = \delta_l$, in which condition, the nucleation undercooling will be proportional to δ_l^2 . While as δ_l is too larger, the interface will be incoherent or semi-coherent (ϵ is negligible at this condition), consisting of good-fitting areas separated by dislocation gridworks. The nucleation undercooling then becomes proportional to δ_l .

2.3.2 Bramfitt's model

Although successful applications of linear disregistry had been applied for a substantial amount of cases, its inapplicability was also found. When Bradshaw and his co-workers studied the nucleation behaviour of gold droplet on different substrates, the most potent oxides in terms of linear disregistry theory were found the least effective nucleation catalysts evinced by experiments [15]. Other than that, Bramfitt also found another discrepancy in his study that the calculated linear disregistry does not always in a good fitting with the measured characteristic undercooling [71]. In the case of iron nucleating on different substrates, comparable linear disregistries are expected for two compounds tungsten carbide (WC) and zirconium carbide (ZrC),

this equation so that the planar disregistry based on the real geometry on the matching crystal planes can be considered and calculated as [71]:

$$\delta_p = \frac{\delta_1 + \delta_2 + \delta_3}{3} \times 100\% \quad \text{Eq. 2-44}$$

Where δ_1 , δ_2 , δ_3 are the disregistries along three lowest-index directions which are selected from the match planes within a 90-degree quadrant. Each of the diregistry can be calculated by the following:

$$\delta_p = \sum_{i=1}^3 \frac{1}{3} * \frac{|(d_{[uvw]_s}^i \cos\theta) - d_{[uvw]_n}^i|}{d_{[uvw]_n}^i} \quad \text{Eq. 2-45}$$

As illustrated in **Fig. 2.11**, the $d_{[uvw]_s}$ and $d_{[uvw]_n}$ is the interatomic spacings along a low-index direction $[uvw]_s$ in $(hkl)_s$ and $[uvw]_n$ in $(hkl)_n$, respectively. And s represents the substrate, n refers to the nucleated solid, and θ is the angle between two crystal directions selected. The calculated planar disregistry for WC was 12.7% based on the OR as: $(0001)[\bar{1}2\bar{1}0]_{wc} // (110)[100]_{Fe}$, showing a general agreement with the predicted trend [71]. It is noted that linear disregistry and planar disregistry are the same when the atomic arrangement at the matching planes are in the same symmetry, *i.e.*, $\theta = 0^\circ$.

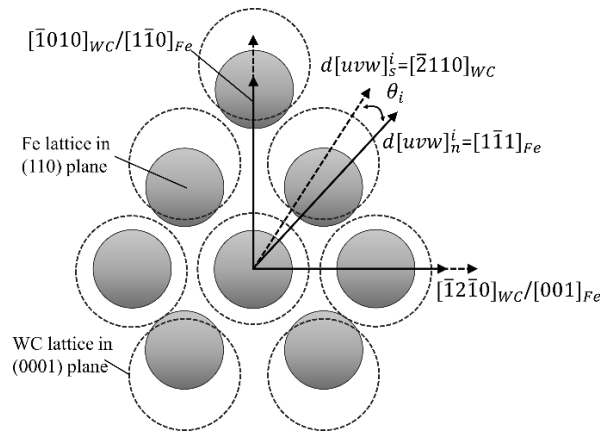


Fig. 2.12 Schematic showing the selection of the crystal directions for calculation of planar disregistry in a WC/Fe system. The planar matching follows the OR as: $(0001)[\bar{1}2\bar{1}0]_{wc} // (110)[100]_{Fe}$. Redrawn from reference [71].

2.3.3 Edge-to-edge matching model

Recently, a model named edge-to-edge matching (E2EM) was proposed by Zhang and Kelly to understand the crystallographic characteristics of phase transformation in solid materials: metals, ceramics and alloys [16]. The extensional application of E2EM into solidification also found itself a good tool to evaluate the grain refining effectiveness of systems of Al and Mg alloys [72–76]. Based on the assumption that the minimization of interfacial energy is promoted by the matching of atomic rows in two crystal phases, E2EM model is able to yield favourable interfacial crystallographic relationships between the substrate and the nucleating solid. The matching criterion is schematically shown in **Fig. 2.13**, where the good matching between two phases was fulfilled at the edge created by the intersection of a pair of crystallographic planes at the interface. To maximize the

atomic matching along the parallel rows, it is required that the matching rows parallel to the directions being the close-packed (C.P.) or near C.P. crystal directions for both phases. It is also required that the interatomic spacings along the matching rows are similar with each other. The matching atomic rows can be straight row or zigzag row, while they have to be identical for a pair of matching rows. In addition to the good matching along one pair of atomic rows, the extended matching expanding over the interface requires extra criterion, which is the similarity between the matching planes (also require to be C.P. or C.P. planes) that carrying the matching rows. As indicated from the huge amount of cases in bicrystal systems with diffusion-controlled phases transformation, empirical criterions for the matching rows (f_r) and planes (f_d). It is energetically to form favourable matchings at the interface in a certain OR when it meets the criterion as: $f_r < 10\%$, and $f_d < 6\%$. For such OR, most of the time the matching planes are needed to rotate a certain degree to yield the crystal plane of the interface (or named the habit plane in solid state) with an optimized atomic configuration. $\Delta\mathbf{g}$ criterion [77] then can be utilised to find this angular deviation. One more pair of planes from phases A and B are selected and identified in reciprocal space with satisfaction of defined rules [78]. Then rotation starts around the zone axis (matching rows) until $\Delta\mathbf{g}_1$ and $\Delta\mathbf{g}_2$ in reciprocal space are parallel to each other, determining a rotation angle ϕ . After that the OR can be defined by the matching atom rows and the two sets of planes in each of the two phases.

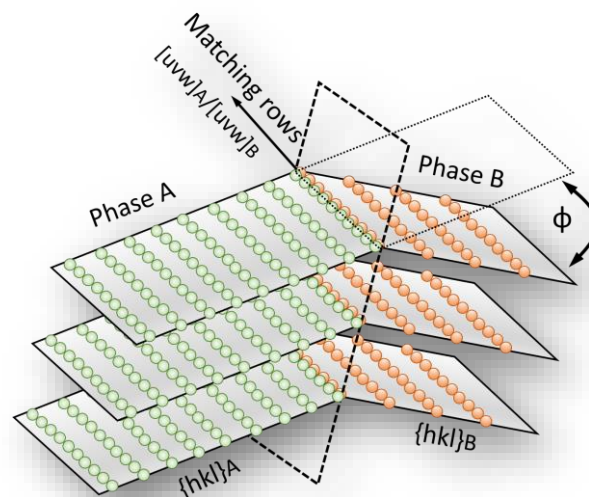


Fig. 2.13 Schematic diagram of an interface meeting the edge-to-edge matching conditions. Redraw based on reference [16].

2.4 Practical methods for grain refinement of Mg alloys

As with other metallic materials systems, grain refinement is essential for Mg alloys since a refined and uniform microstructure improves the material's performance in many aspects, such as mechanical properties, creep resistance, resistance to hot tearing and to any down-stream thermal processing of the as-cast alloys, *etc.* [9,10]. Tremendous work in both laboratory and industry, have been carried out in the last few decades to understand heterogeneous nucleation and to achieve grain refinement in Mg alloys. According to the aforementioned theories and models about grain refinement (heterogeneous nucleation and grain initiation), it is essential to have a proper combination of heterogeneity (external or internal) and solute to achieve a refined as-cast microstructure for metallic materials. Such ideas are either reflected in or instructive to the historical work on grain refinement of Mg alloys that are reviewed as follows.

2.4.1 Zr inoculation

Zirconium acts as an exceptionally potent grain refiner for Mg alloys without or containing little content of interfering elements like Al, Mn, Si and Fe (which are Zr stabilizer by forming stable compounds) [26]. Being the only grain refiner commercially available in Mg industry, Mg-Zr master alloys have been widely applied to grain refine ZK, EZ, ZE and WE series Mg alloys [79] that are cable to be used under high temperatures. The excellent performance of Zr on grain refinement is attributed to the combined effect of the great growth restriction provided by dissolved Zr as well as the nucleating substrate of undissolved Zr particles [52,80–84]. Both contributions have been qualitatively incorporated into numerical models, with successful explanations on the grain refining behaviour [25,70].

Historically, the understanding of the refining mechanism appears after the practical invention of Zr refiner. The fast dissolved Zr was considered as the only reason for grain refinement by Sauerwald and Von in the early work [81]. The Zr solute afterwards was thermodynamically understood having strong solute partitioning during solidification to generate growth restriction [52,82]. Lee observed the grain refinement of pure Mg with low concentrations of Zr, *i.e.*, 0.04 to 0.32 wt.% [80]. It started to be noticed that there is an additional contribution attributed from the undissolved Zr particles with high settling tendency, where the agitation after holding for certain periods was found to be able to reinvigorate the refining performance [83,84]. For the high value-added class of Mg-Re-Zr alloys, the agitation before casting is beneficial for not only re-flowing the settling Zr

particles, but also recovering of Zr solute level by re-melting the Zr precipitate from supersaturated Mg matrix during heating [85]. As revealed by back-scattered-diffraction (BSD) SEM, the nucleating Zr particles appear as Zr-rich core inside the Mg grain [83,84], with a size range from 1 to 5 μ m [86]. Fragmentation of the large Zr particles in Zirmax® alloy through rolling or extrusion was executed to redistribute the size distribution of Zr particles, rearranging the size distribution allowing more particles entering the optimal size range. In turn, this offered an enhanced Zr alloying efficiency together with better refining performance [87].

The long-existing preconceived crystallographic orientation relationship (OR) between Zr particle and Mg was finally confirmed by TEM characterisation [88–90], *i.e.*, HCP-on-HCP OR. Notwithstanding, Saha and Viswanathan believed that only the faceted Zr particle nucleates primary Mg [88], while Yang *et al* showed the contrary HRTEM results of the same OR between both round-shape and faceted Zr particles [89]. Also, some of the results in Saha's work contradict their own statement while indirectly support Yang's viewpoint, where the increased fraction of faceted particles by longer holding time at 815 °C yet posts invariant effect on grain size [88].

In general, Mg-Zr master alloy is a successful grain refiner for Al-free Mg alloys. Nonetheless, due to the high cost and limited application, increasing effort has been made to look for its alternatives.

2.4.2 Superheating

Traced back to 1931, a British patent reported that Mg-Al alloys can be grain refined by superheating the melt [19]. Specifically, the melt is heated above liquidus with a superheat in the range from 180°C to 300°C, and it is poured into a mould at a rapid cooling rate after a short holding time.

The essential element of Al is the characteristics of this technique, and superheating effect was limitedly found in Mg-Al alloys with a certain amount of Mn/Fe content [20,26,91]. The occurrence of other solutes consuming Al to form other particles (such as Mn, Zr and Be), leading to competition in nucleation or grain initiation, was found detrimental to superheating [20,91–93]. Other than this, an optimum overheating temperature exists for specific alloy systems, under which the maximum refining performance is achieved. For instance, 850°C to 900°C for Mg-9Al-2Zn [91]. Moreover, either longer holding time or repeated process cannot gain further grain refining effect once a fine grain size is attained

after sufficient treatment time [20]. Lastly, a fast cooling down to the pouring temperature is also crucial to yield fine grain size [25].

The mechanism underlying superheating has been studied over decades, with different groups of explanation being raised. One of them is the ‘temperature-solubility’ theory [94,95], in which the size and the number density of inoculant particles can be modified by dissolution (overheating) and re-precipitation (fast cooling). Refined grain size is attributed to the large number density of small-sized particles. However, the theory fails to clarify the nature of the possible particles; although the primitive identification showed that one type of intermetallic particles contains Al, C, O and Fe [95]. One other mechanism is the formation of Al_4C_3 as the result of Al solute reacting with carbon (C) that is released from steel crucible at high temperature [26]. Based on that, a model was proposed by Cao *et al* [69] that the poisoning coating containing Fe and/or Mn on Al_4C_3 is dissolved at superheat temperature, while their reprecipitation is prevented by fast cooling so that the potent Al_4C_3 give rise to grain refinement. But other particles rather than Al_4C_3 may work since certain grain refinement was achieved in AZ31 and AZ91 alloys melted in carbon-free crucibles [96]. Another explanation is the formation of intermetallic particles including as Al-Fe, Fe-Mn and/or Al-Fe-Mn [97]. Further supports were provided by Tiner [91] who observed that the addition of iron promotes grain refining effect. A similar compound of $\text{Al}_8(\text{Fe}, \text{Mn})_5$ particle was observed in the centre of grains by Byun *et al*, suggesting a highly possible nucleating site [98]. Contradictorily, this compound was found as a poor substrate for nucleating Mg due to the inferior crystallographic matching with Mg [72]. This has been experimentally evidenced by Cao *et al* that the transformation of stable Al_8Mn_5 particles from metastable $\varepsilon\text{-AlMn}$ leads to a coarser grain size [99]. The crystallographic matching between possible Al-Mn(Fe) phases and Mg was systematically studied by Qiu *et al* [100], showing that $\tau\text{-AlMn(Fe)}$ is the most-likely nucleating substrate. It was proposed that $\tau\text{-AlMn(Fe)}$ can form via the massive transformation of the $\varepsilon\text{-AlMn(Fe)}$ phase.

It has been shown above that the as-cast microstructure of Al-bearing Mg alloys can be refined by superheating, with many proposed mechanisms functioning in this phenomenon. Many factors likely contribute to the outcome and each of the changing parameters in the design experiments affects more or less the solidified structure, bringing out different explanations. Nevertheless, it is still useful to see that all the explanation stems from the speculation and investigation of the potential nucleating particles, such as phase type, size, number density, *etc.*

2.4.3 Native grain refinement

It was reported that high purity Mg-Al alloys have a fine grain structure after solidification as the result of native grain refiner [20]. Similar to the superheating, this phenomenon is limited in Mg-Al alloys. It does not appear in Mg-Zn or Mg-Ca alloys [101]. High purity is essential and several impurities like Fe, Mn, Be, Zr degrade the refining effect [92,93,101]. With the carbon extraction from the steel crucible, the primary reason for the native grain refinement points to the formation of Al_4C_3 and Al_2CO particles, both of which show good crystallographic matching with Mg [72]. Following the previous viewpoint [93], Cao *et al* suggested that Al_4C_3 is the nucleating site, and the Al_2CO identified through EDS should be the result of contamination by reaction with H_2O during sample preparation [101]. Interestingly, Al_4C_3 and/or Al_2CO are considered to be the nucleating particles in the explanations shared among native grain refinement, superheating and carbon inoculation. For instance, the interconnection was illustrated by Cao *et al*, where Al_4C_3 particle is poisoned by the formation of Fe, Mn-containing coating in the commercial purity Mg-9Al alloy. However, the potency of Al_4C_3 is recovered by dissolving the coating through superheating and preventing the reprecipitation through fast cooling, which in turn leads to grain refinement in Mg-9Al alloy with commercial purity level [95].

2.4.4 Carbon-based inoculation

Being employed for decades in industry, carbon inoculation is another effective and major way to refine Mg-Al-based alloys through either direct addition of carbon or indirect introduction of carbon carriers. The element of Al plays a key role in the refining mechanism since carbon inoculation seems only work in Al-bearing alloys (usually up to 2wt.%) [21,102,103]. Moreover, the elements of Be, Zr, Ti and RE that consumes Al solute in the melt by the formation of Al_2X compounds pose a negative effect on the grain refining effect. Since both C and Al are of critical importance for grain refinement, a consensus about the nucleating particle is realised as Al_4C_3 [26,102]. Lu *et al* reported that the addition of Al_4C_3 particles (25 vol.% of them have a diameter less than $3\mu m$) reduces the as-cast grain size of high purity Mg-3Al alloy [104]. A similar result was also found in AZ91D reported by Liu *et al*. [105]. A relatively small planar disregistry of 4.05% supposes that Al_4C_3 is a potent particle for nucleating primary Mg, which is corroborated by the finding of Al_4C_3 in the grain centre.

Although the indication of a phase of Al-C-O from the affiliated detection of O is believed to be the results the reaction between Al_4C_3 and water during sample preparation, it is possible, from the viewpoint of crystallography, Al_2CO is potentially a better nucleating substrate than Al_4C_3 [72]. Another possible change in nucleating particles happens in the case of carbon inoculation through SiC addition, which is, from one group of understanding, unstable and possibly transforms into Al_4C_3 [106] or Al_2MgC_2 [107], the latter shows a smaller planar disregistry than the former one. While the other group of understanding is that SiC itself is a potent particle in terms of crystallographic matching [74,108] with a proper size distribution [64].

2.4.5 Elfinal process-addition of FeCl_3

As firstly reported in a Belgian patent, the addition of FeCl_3 ranging from 0.4 to 1.0 wt.% at temperatures between 740°C to 780°C dramatically refined the grain size of Mg-Al-Zn alloys [22]. Being identical to one of the nucleating particles for superheating, native grain refinement and carbon inoculation, Al_4C_3 was proposed by Emley [26], being the reaction product between Al solute and C that is liberated of from steel crucible as the result of erosion. Contradictorily, this process even worked when carbon-free Al_2TiO_5 crucible was applied, indicating that Al_4C_3 has little to do with the gran refinement [96]. In that circumstance, they convincingly demonstrated the finding of Al- and Fe- rich intermetallic compounds in the primary Mg grains, suggesting they are highly possible nucleating particles. This argument gained support from Emley who found that ion removal agents like Zr and Be inhibit the refining performance [26]. With little concentration of Mn in the melt, intermetallic particles containing Mn (AlMn type, Al_8Mn_5 or $\text{Al}_8(\text{Fe}, \text{Mn})_5$) are less likely to occur.

2.4.6 Theory-guided exploration of grain refiners

In general, the development of the above practical methods for grain refinement follows the basic idea of enhancing heterogeneous nucleation, together with countless trial and error experiments. It is admitted that foundation of the theoretical framework has made a significant contribution to understanding the underlying mechanism and the optimization of the existing methods (see **section 2.1**). Due to the accompanying drawbacks (environmental contamination, high cost, instability, difficulty in practical operation, *etc.*) for each practical method aforementioned, work is still being carried out on searching reliable, efficient, economical and practical grain refiners for Mg alloys. Thankfully, material scientists nowadays can predict a potential grain refiner easier with the existing

theories and models. The following section summarises some of the practical cases in the literature.

2.4.6.1 Al₂Y with extension to Al_aX_b compounds

Rather than evaluating and understanding the pre-existed phenomena of grain refinement, the edge-to-edge model (E2EM) was applied to predict potentially effective grain refiners for Mg alloys. For instance, prediction of Al₂Y, a Laves phase (Cu₂Mg type), was derived from E2EM model [109], with two possible ORs along and small lattice misfits of 0.1%. After modification by applying $\Delta\mathbf{g}$ criterion, they become:

OR1, $[2\bar{1}\bar{1}0]_{\text{Mg}} \parallel [121]_{\text{Al}_2\text{Y}}, (0\bar{1}10)_{\text{Mg}} 0.2^\circ \text{ from } (40\bar{4})_{\text{Al}_2\text{Y}}, (0\bar{1}11)_{\text{Mg}} 3.2^\circ \text{ from } (3\bar{1}\bar{1})_{\text{Al}_2\text{Y}}$;

OR2, $[1\bar{1}00]_{\text{Mg}} \parallel [1\bar{1}0]_{\text{Al}_2\text{Y}}, (0002)_{\text{Mg}} 0.3^\circ \text{ from } (440)_{\text{Al}_2\text{Y}}, (\bar{1}\bar{1}20)_{\text{Mg}} 0.3^\circ \text{ from } (004)_{\text{Al}_2\text{Y}}$.

This prediction was approved by design experiments in the Mg-10Y-xAl system, whereby grain refinement was achieved by extra addition of Al [109–112]. The Al₂Y phase appearing in the grain's centre as expected was believed contributing to the grain refinement [109]. Systematic identification of the ORs between a few tens of Al₂Y particles and Mg matrix by EBSD technology showed that the experimentally reproducible ORs agree well with the predictions from E2EM [109,110]. The convincing identification of such nucleating particle and its OR with Mg matrix was completed with the aid of focus-ion-beam (FIB) technique to lift out and thin the nucleating Al₂Y particle for TEM characterisation [111]. The OR1 was repetitively confirmed [111]. Further work focused on the study of grain refinement efficiency of the *in-situ* Al₂Y particles from aspects of the number density, size and size distribution. Al concentration brought changes and interplays between them under a certain casting condition, with an optimum Al addition being 2 wt.%, over which grain coarsening appeared [112]. The successful prediction, confirmation and application of Al₂Y were further extended into other isomorphic Al₂X (X refers to rare earth elements, Gd, Sm, Dy, Nd and Ce) compounds with the assistance of the E2EM model and the introduction of interfacial energy calculation [111]. As evidenced by later researches, Al₂Gd [113], Al₂Sm [114], Al₂Ce [115] and Al₂Nd [116] compounds were found competent of nucleating substrates for Mg grain and effective on grain refinement.

2.4.6.2 ZnO, AlN and CaO

With consideration and evaluation from the crystallographic point of view, other potential grain refiner candidates: zinc oxide (ZnO) [117], aluminium nitride (AlN) [118] and calcium oxide (CaO) [119] were proposed. All of them were proved as feasible and effective grain refiners by experimental confirmation.

The misfit between ZnO and Mg was measured to be 0.59% under an HCP-on-HCP OR, indicating that ZnO could be a potent nucleating substrate. However, the grain refinement was believed to be the result of many factors other than potency: *i*) growth restriction from Zn solute by the reduction of ZnO [117]; and *ii*) formation of MgO [117,120,121]. The reduction of ZnO was evidenced by the occurrence of eutectic Mg₂Zn phase, dendritic grains in pure Mg with inoculation of ZnO (adding temperature is 720 °C) and the EDS detection of MgO particle [120]. Fu *et al* realised that the thermodynamically favoured ZnO reduction is low in kinetics at temperature even above Mg liquidus, so that both the remaining ZnO particles and Zn solute contribute to the refined grain size. This is advocated by the grain size comparison between AZ31 alloys: one group with different level ZnO additions and the other group with correspondingly equivalent Zn additions. The latter alloys have a larger grain size than the former [122]. However, no further work was carried out to understand how other factors, such as the competition between new-born MgO and ZnO, or the number density, size distribution and morphology affect the grain refinement. And these might be the reasons behind the abnormal coarsening when ZnO content was up to 4 wt.%.

It has been reported that AlN particle is an effective nucleating particle for Mg-based alloys [20] as the lattice discrepancy between two crystals is only 2.81 % [80]. Same conclusion was derived by E2EM model, with a prediction of possible OR between AlN and Mg [118] having a misfit of 2.6% (misfit deviation appears as results of different crystal data and temperature consideration). Indeed, moderate grain refinement was achieved by AlN addition at 720 °C in Mg-1Al [80] and Mg-3Al [118]. The evolution of grain size as a function of adding temperature showed that the optimum efficiency is achieved at 765 °C in Mg-3Al [118]. Even though the experimental OR between AlN and Mg has not yet been detected, it is quite convincing that AlN addition is beneficial for grain refinement of Mg alloys. Other than grain refinement, AlN also served as reinforced particles that own a good wetting ability with Mg matrix to produce Mg-based composites [123–125].

Calcium (Ca) and calcium oxide (CaO) have been well known as ignition-resistant agents for Mg-based alloys [126,127]. Along with the promotion in ignition resistance, CaO was also found beneficial to grain refinement in pure Mg as an identical finding, with better performance than that inoculated with equivalent Ca addition [127]. Ali *et al* derived the possible ORs between FCC-CaO and Mg with favourably low misfits by E2EM application [119]. Although without solid confirmation of ORs by electron microscopy, CaO was shown to be capable of refining pure Mg and Mg-Zn alloys by casting experiments. Similar to ZnO [128], CaO reduction appears in the Mg melt through reaction with Mg, which was experimentally observed and thermodynamically favoured [129–131]. But this observation contradicts with the Ellingham diagram [132]. Partitioning effect of Ca solute during solidification provides certain levels of growth restriction, with which the remaining CaO particles can effectively nucleate Mg grains and result in grain refinement. Nevertheless, the reduction process also makes it possible that all CaO particles are reduced and converted into MgO particles, in which case the solidification behaviour might be totally different from that with remaining CaO particles. Other than that, the application of CaO is limited as one demerit along with Ca solute is the elemental reaction in Al-bearing Mg alloys, such as Al₂Ca formation. Al₂Ca is also a potent substrate for Mg nucleation, but it can be detrimental to the grain refinement due to competition between different type of particles and the shortage in Ca solute [119].

2.4.7 Grain refinement by MgO

As described by the existing theories and models, plus the practical exploration of grain refiners reviewed above, it is accepted that both the solute and the nucleating particles are of importance for grain refinement of metallic materials. With respect to inoculation, the deep-rooted mind of enhancing heterogeneous nucleation make engineers and scientists eager to search potent substrates based on the instruction of crystallographic matching. Few researches have paid attention to the particles which have a poor lattice matching with Mg. This hinders the development in aspects of both theories and experiments of grain refinement.

MgO, a ceramic crystal with rock-salt structure, has relatively poor potency for nucleating Mg in terms of crystallographic matching. The lattice misfit was reported as 7.1% by Lee [80], while this value varied under different ORs [133] or different Mg alloys in which the lattice constant of Mg varies duo to compositional changes [134,135]. Although with relatively large misfits with Mg, either external MgO addition [80,135] or *in-situ* MgO particles [134,136] was demonstrated to contribute to grain refinement of Mg alloys.

Besides, the understanding of MgO as potential grain refiner should rationalize some conjectures that the mechanisms underlying some of the practical methods such as superheating [137], CaO inoculation [119,127] and ZnO inoculation [117] supposedly shared common mechanism that MgO particles actually act the heterogeneous nucleation site.

Decades ago, MgO had been proposed to be a potential nucleating substrate for the heterogeneous nucleation of Mg in Mg alloys [137]. Lee demonstrated that the addition of external MgO showed some degree of grain refinement in binary Mg-Al alloys [80]. By introducing externally the cubic MgO particles in form as a master alloy into AZ91D, Jiang showed that the grain size kept decreasing with the MgO addition [135]. Recently, significant grain refinement in AZ91D alloy and pure Mg was achieved through manipulating the native MgO particles by a novel approach of intensive melt shearing [138], which is capable of dispersing the native MgO particles into separated and wetted particles with homogeneous distribution and a high number density [134,135]. Such opinion was corroborated by the experimentally observed orientation relationships (ORs) between the faceted MgO particles and α -Mg grains in both AZ91D and CP Mg refined by native MgO particles [134,139,140], *i.e.*, OR1 for {111} facet: (0002)[11-20]Mg//{(111)[01-1]MgO}; OR2 for {100} facet: (0-112)[01-11]Mg//{(100)[0-11]MgO}. This is direct experimental evidence indicating that α -Mg grains heterogeneously nucleate on the substrates of MgO particles during solidification. Interestingly, the native MgO particles showed extraordinary performance in pure Mg cast by HPDC technique, by which an ultra-fine grain size of 3 μ m was achieved [28]. It was proposed that the native MgO particles/films and newly formed ones during handling are spatially dispersed and distributed by the severe shearing force at the narrow gate. Moreover, as enlightened from the application of impotent MgO for grain refinement, theoretical development leads to the concept of explosive grain initiation by Fan *et al*, stating that impotent MgO particles have a larger potential than any other more potent particles in refining Mg alloys [28,29]. When the nucleation undercooling is larger than the grain initiation undercooling for a huge number of MgO particles, nucleation and grain initiation of the primary Mg phase occur at the same time when thermal undercooling reaches the value of nucleation undercooling. Hence, recalescence occurs immediately and significant grain refinement was obtained.

2.5 The native MgO in Mg and its alloys

2.5.1 Oxidation in Mg and its alloys

Mg and its alloys are prone to oxidation when exposed to the oxygen-containing environment, as it is well known that Mg is so active that it can easily react with oxygen:



MgO has a NaCl crystal structure with a lattice parameter of 4.211 Å [141], a formation enthalpy is -143.81 kcal/mol, a density of 3.58 g/cm³ and a melting temperature of 2852 °C [79]. The huge amount of heat released from this exothermal reaction make the burning of Mg a self-sustainable process. Which is also one of the major issues hindering the application of Mg and its alloys in the aerospace industry [142].

Oxidation of Mg and its alloys has been an important topic for decades since their widespread applications have been hindered by many drawbacks originated from oxidation issues, such as corrosion [143,144], ignition tendency at high temperature [142] and oxide impurity during casting [145,146], *etc.* However, it is unavoidable since oxidation is ubiquitous throughout the life span of Mg and its alloy products. At high temperature such as during the smelting process or casting of alloy products, the molten Mg experiences oxidation when it is in contact with the oxygen-containing atmosphere, forming MgO films/particles that can be easily entrapped into the melt by turbulent flow [147–152]. Specifically, practices like metal transfer, excessive splashing and turbulence may entrap the oxide products or air bubbles into the melt. While at medium and low temperature, oxidation also happens at the surface of solid magnesium and the resultant oxide skin may become inclusions in the melt during re-melting [147,149,153,154]. With the moisture existed in the atmosphere, the reaction product is Mg(OH)₂ that can be reduced into MgO at elevated temperatures. Such phenomena continue in the recovery of Mg from scrap, where the surface oxides together with other impurities are easily introduced into the melt. Also, it can be seen as an accumulative process when the circulate economy is taken into consideration, where the recycling process generates and accumulates oxides from one generation to the next.

A practical method to study the oxidation behaviour is to monitor the weight gain of the sample as a function of time or temperatures. From the result of thermogravimetric analysis (TGA) reported by Czerwinski, there are two characteristic stages: 1, a parabolic stage at the initial period. 2, an acceleration stage after a platform stage (incubation) [143].

For AZ91D alloy at a relatively low temperature (197°C), there only exists the parabolic stage and the weight gain levels over a critical time. While when the temperature goes up to 437°C and higher, an acceleration stage occurs followed by the platform which becomes shorter when the temperature goes higher. During solid state oxidation, the MgO film form at the early stage is generally accepted as a thin and compact layer offering protection for further oxidation [143,155]. The kinetics of oxidation of Mg at low temperatures has been generally accepted that the growth of the oxide layer is based on a solid-solid transportation process, including the bulk diffusion of metal atoms to the oxide-gas interface or the diffusion of oxygen to the metal-oxide subsurface interface [143]. Without any easy-paths for Mg and O transportation, the oxidation is controlled by the diffusivity of Mg within the MO lattice, which is expressed as [156]:

$$D_{mg} = 1.0 * 10^{-6} \exp\left(-\frac{15000}{RT}\right) m^2/s \quad \text{Eq. 2-47}$$

The diffusivity D_{mg} is very low and corresponding to the negligible gain of weight at the incubation stage. The oxidation procedure before cracks happen above also agree with the view of Cabrera-Mott theory [157], where the oxidation mechanism is a solid-gas interaction that includes the following reaction steps:

1. Adsorption of oxygen on the metal surface;
2. Tunnelling of electrons across the initial oxide layer from the metal;
3. Oxygen atoms on surface ionize and create a potential difference across the oxide layer that facilitates further oxidation;
4. Growth of the oxide layer until a certain critical thickness is reached, after which the growth of the oxide layer is practically negligible.

At high temperature, however, the accelerated transportation of Mg^{2+} cations and O^{2-} anions leads to the voids forming at the interface between oxide layer and metal, which then introduce local stress causing the later cracks [143]. As supported by the $P-B$ ratio of MgO is 0.81 suggesting that MgO film is porous and non-protected to inhibit oxidation of Mg [158]. Rupture of the film happens when the oxide thickness grows beyond the critical value [143]. The onset of porous oxide film makes the evaporation of Mg, rather than diffusion, dominates the oxidation process. As a consequence, a boosted rate of oxidation in a linear law at a higher temperature (even above liquidus) was observed for

the tested weight grain-time curve [143,159,160]. The evaporation rate of Mg can be described by the Arrhenius equation [161]:

$$K_{evap} = 0.6 \exp\left(-\frac{25000}{RT}\right) g/cm^2s \quad \text{Eq. 2-48}$$

2.5.2 The morphology of oxidation products

2.5.2.1 Characteristic at the micron scale

Owing to the development of the recycling industry in parallel with the growing market of Mg products, the cleanliness of recycled metal has attracted great consciousness [162]. Being one type of major inclusions, MgO in the form of films had been well studied. Either oxide films and oxide clusters in size of micron scale was revealed in molten Mg [148]. The former appears as strings with a thin thickness but a long length, having the ability to be crumpled and appearing as curved strings. The latter appears as a thick scale that has a few tens of microns in thickness, associated with oxide cluster distributed on one side. The results are in consistence with the following work [133,134,163]. Progress on the classification of oxide films and their origins were made by the extensive study by Fan *et al.* Specifically, three types of MgO films differed in morphologies were identified. The first one is young oxide film with a typical width of 1 to 2 μ m, rather than a compact film, it is composed of discrete nano MgO particles in size about 100 to 200nm. The second type is named old oxide film, which has a similar morphology as the young film except for the coarser particles size by one order. Thirdly the old skin refers to the type that appears as a straight segment consisting of MgO particles as well. It has a thickness of 10-15 μ m and is harder to be crumpled.

2.5.2.2 Characteristic at nano-scale

The finding of particulate MgO film sets up the important precondition for their possible application as a heterogeneity for nucleation of primary Mg [133,134,163]. More knowledge about the native MgO film/particle is required to be clarified before its successful application. One consideration originates from the nucleation theories that the lattice configuration and chemical state of the termination facet contacting with Mg melt are of crucial importance for their ability for nucleation [32,34]. From the grain initiation point of view, the size distribution of the MgO particles is one of the parameters determining the grain size [17].

Men *et al* [164] did the statistic measurement of native MgO particles in the melt AZ91D concentrated by pressurised filtration technology, a log normal size distribution was identified with a geometric mean diameter $d_o = 70 \text{ nm}$ and a geometric standard deviation $\sigma = 0.45$. By applying numerical modelling, the size distribution was employed yielding predictions of grain size and cooling curve with good agreements with the experimental results. While a different size distribution was found for the external cubic MgO added into AZ91D alloy, where the particles have a log normal size distribution with different parameters: $d_o = 130 \text{ nm}$ and $\sigma = 0.45$.

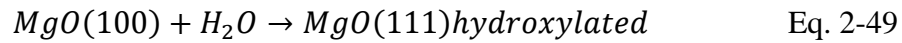
2.5.2.3 The shape of MgO crystal

The equilibrium shape of a crystal, in thermodynamics, is determined by the minimization of surface free energy [165]. A geometrical interpretation provided by Wulff illustrates how the orientation of crystal depends on the surface free energy [166]. The criterion is referred to as Wulff rule stating that the distances of a crystal facet from the Wulff's point within the crystal are proportional to the corresponding specific surface energy. Additionally, the growth kinetics of a crystal, *i.e.*, growth paths and rate on different sites on a crystal surface, is also crucially correlated to the resultant crystal shape [165,167].

In the case of the faceted behaviour, MgO crystal should be of cubic morphology in terms of the thermodynamic stability of {100} terminations, which is evinced by extensive theoretical and experimental results [168–172]. It has been well known in terms of experiment that the burning of Mg strip is a simple way of producing cuboidal MgO nano particles [168,173], whose simple crystal structure makes it a prototype for the study of epitaxial growth, surface structure and chemical reactions of oxide. Henrich observed the faceting behaviour of (110) and (111) facets of MgO in ultrahigh vacuum, where both facets turned into (100) at different conditions (ambient Ar ions bombardment and annealing at 900 to 1400K.) [174]. Such findings were in agreement with Mark's conclusion, in which the Madelung potential for various crystal facets of alkali halides indicates the most stable crystal facet is (100) [169]. Huang reported the similar phenomenon, whereby the growth orientation of MgO turns into (100) from (111) as the temperature of Si(111) substrate changes from 600 to 900 °C [175].

Surface energy for the crystal facets can be modifiable by many variables in the surrounding environment. Zhang *et al* in his review work classified such surface-regulating agents into three kinds: *i*) surfactants, *ii*) adsorbates and *iii*) foreign metal ions, through which the alternation of the morphology of nanocrystal is achievable [167]. The

morphology of cubic MgO crystal was found dissolvable under wet condition, where the original edges were firstly cut by (110) truncations, and then the growth of (111) cuts proceeded until the crystallites become octahedra with limited by (111) sides [172]. Such experimental result was in agreement with the previous energy calculation by Refson *et al* who predicted that the low-energy hydrated orientation is the OH-stabilized polar (111) facet [171]. As a consequence, the following chemical reaction is exothermal with heat release of 90.2 kJmol⁻¹.



Unlike the most stable cubic MgO in a dry environment, the product of internal oxidation MgO in solid bulk of FCC metal systems, *i.e.*, Ag-MgO [176], Cu-MgO [176–178] and Pd-MgO [176,177], shows universal cube-on-cube orientation relationship with the metal matrix. The {111} faceting of MgO was found in all cases, with an exception for the Pd-MgO case where the MgO nanoparticles were found as tetradecahedral shape with additionally six {100} facets [177]. It was argued that the elastic strain energy is not the deterministic factor for the faceting characteristic as the matrix strain would be too small to alter the growth orientation at high temperature. Also, since the crystal structure of MgO and the metal matrix are all FCC in crystal structure, the same symmetry leads to the same misfits on different interfaces under the cube-on-cube orientation relationship. In other words, the strain generated would be the same and isotropic on any interface. A reasonable explanation was provided by Finnis *et al* [179] and supported by later researches [180] that the charged {111} termination of MgO crystal can be stabilised within a metal that has strong charge transferring ability.

The realization of the potentially positive role of MgO particles on grain refinement of Mg alloys raises the importance of their natural characteristics, including size distribution (**Section 2.5.2.2**), crystal morphology and even the precise atomic configuration at the surface [80,90,134,135,139,140,164,181–183]. It was observed in AZ91D alloy that the native oxide films consist of nanosized particles with faceted shape, such particulate liquid film can be dispersed for grain refinement with the application of intensive melt shearing [134]. Their morphology was further systematically characterised by Wang *et al* [139], who observed the faceting characteristic of native MgO particle as {111} bounded octahedral shape. A particularly different shape of MgO particle was detected in commercial purity Mg melt as cubic shape bounded by {100} facets only [140]. Both of the types were found in an AZ91 alloy prepared by Thixomolding in a reactive

atmosphere with Ar and CO₂ [183]. The different morphology of MgO particles observed in AZ91D and commercial purity Mg suggest one of the possible factors altering the crystal shape, *i.e.*, solute element. A proposed mechanism was the elemental adsorption (Al and/or Zn) on specific {111} facet in AZ91D melt can reduce the interfacial energy making such type of facet the most stable one in such environment [140]. However, more evidence is still in a requirement to elucidate the above mechanism or a rational explanation to the resultant morphology of the native MgO in Mg melts.

2.6 Manipulation of nucleation potency by elemental segregation

Solute segregation is a general phenomenon occurring at the interfaces including liquid/substrate, solid/precipitate, grain boundary and crystal surface [33,184–186]. With the physical and chemical changes at the interface, many properties were correspondingly changed, such as wetting, catalysis, welding, electronic property, embrittlement and heterogeneous nucleation. As governed by the minimization of the total free energy of the system [187], in general, the equilibrium segregation at the interface will find themselves an energy-favoured configuration. Elucidation of such segregation phenomenon can be ascribed by the Gibbs adsorption isotherm [33]:

$$d\gamma = - \sum_i \Gamma_i d\mu_i \quad \text{Eq. 2-50}$$

Where γ is the interfacial energy, μ_i is the chemical potential of i in the system, Γ_i represents the specific excess number of moles of the component. In a binary substitutional system with two bulk phases with the adoption of the monolayer model, the change of interfacial energy $\Delta\gamma$ can be derived as [33]:

$$\Delta\gamma = - \frac{RT}{\sigma_a} [\ln(1 + kx_2) - x_2] \quad \text{Eq. 2-51}$$

Where R is the gas constant, T is the absolute temperature, σ_a is the area per mole, k is an interface enrichment factor defined by $k \approx x_2^s / [(1 - x_2^s)x_2]$, x_2 and x_2^s are the bulk and surface atomic fractions of solutes, respectively. The above equation indicates the interfacial enrichment of a solute is driven by the decrease in interfacial energy. Kim *et al* proposed an adsorption model for A-B eutectic or monotectic alloy system during solidification [32]. In the model, the interfacial energy is calculated by summing the pairwise bonding energies under a monolayer assumption. After minimization of the

interfacial energy for an Ag-Pb system, the undercooling required for adsorption is found to be zero, suggesting an energy favour process.

An extended model was proposed by Men and Fan [188] to describe the solute segregation at the liquid/substrate interface that is more relevant to the solidification with existence of heterogeneity [188].

$$\frac{X^i}{1-X^i} = \frac{X^l}{1-X^l} \exp \left\{ - \left\{ a^i (\gamma_{BS}^i - \gamma_{AS}^i) - \frac{2\Omega}{Z} \left[Z_l (X^i - X^l) - Z_v \left(X^l - \frac{1}{2} \right) \right] - T(\Delta S_A - \Delta S_B) \right\} / RT \right\} \quad \text{Eq. 2-52}$$

Where X^i and X^l are the molar fraction of the solute atoms in the interfacial monolayer and the liquid, respectively. γ_{XS}^i are the interfacial energy between pure liquid (X=A or B) and the substrate, while a^i is the interface area per mole atoms. Z and Z_l are the atomic coordination number in the liquid and interfacial monolayer, respectively. Z_v is the atomic coordination number to one of the adjacent atomic layers. And ΔS_A and ΔS_B are the changes in the entropy of solvent and solute atoms, respectively. Application of this model into the liquid Al-Ti/TiB₂ system with 0.1 at.% Ti in the bulk liquid showed a good agreement with the experimental data. As shown in **Fig. 2.14**, the calculated Ti content at the liquid Al/TiB₂ interface is 17.5 % at 933K, while it drops gradually down to 11.6 % as the temperature goes to 1233K. This implies either the formation of Al₃Ti monolayer beyond liquidus of Al or the dissolution of it when exposed to a much higher temperature, being reasonably agreed with the experimental observations [189].

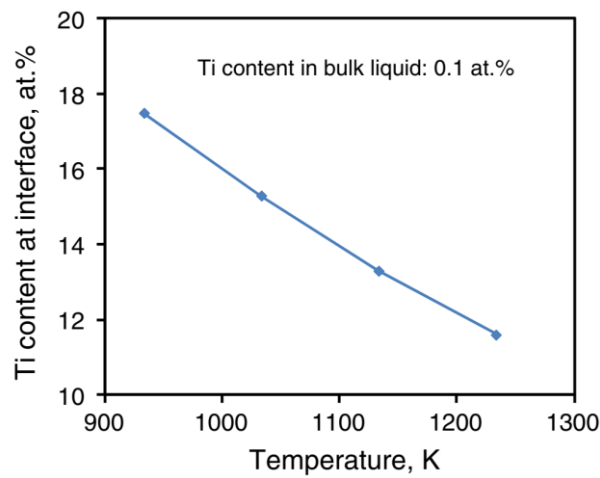


Fig. 2.14 Plot of the calculated Ti content at the interface in the liquid Al-Ti/TiB₂ system with 0.1 at.% Ti in the bulk liquid against the temperature [188].

It has been reviewed in **section 2.3** that the heterogeneous nucleation ability of a substrate is in the function of many variables, including lattice misfit, surface roughness and chemical interaction. Being an important role in nucleation, the atomic configuration at the termination facet contacting liquid metal becomes critical to the potency for nucleation. The application of grain refiner in various alloy systems may raise the interaction between substrate and the solute elements, causing solute adsorption or chemical reaction. Through such way the substrate surface might be modified in terms of nucleating potency, being possibly one of the reasons why there are no universal grain refiners for either Al or Mg alloys.

2.6.1 Elemental segregation on TiB₂ in Al alloys

Taking the Al alloys for example, the well-recognised Al-5Ti-1B master alloy has been widely applied in Al alloys in industry. However, the effectiveness of grain refinement is dramatically degraded for the Al alloys containing poisoning elements like Zr [51], Cr [190], Li [191] and Si [192], resulting in a coarse and/or even columnar grain structure. It has been a long-standing issue on the mechanism underlying the potency of TiB₂. While with the aid of advanced electron microscopy, recent works have made progress by providing strong evidence of the atomic modification at the substrate facet, which acts as a deterministic role on the behaviour of heterogeneous nucleation [47,189]. Specifically, TiB₂ particle itself, having a misfit of -4.2% with Al, is not a potent nucleating site for primary Al. However, with the access Ti solute in the Al-5Ti-1B master alloy during its production process, the Ti adsorption onto the TiB₂ surface is thermodynamically feasible above the liquidus [188]. An atomic monolayer of Al₃Ti 2DC forms on the {0001} facet of TiB₂ as explicitly characterised by Cs-corrected STEM in aspects of structure and chemistry, which renders TiB₂ particle a high potent adsorbed by changing the original misfit into only 0.09% [189]. In contrast to the enhanced potency through Ti segregation and formation of Al₃Ti 2DC monolayer, poisoning effect was found under the existence of Zr solute in the Al melt. Similarly, this had been argued for a long time until the application of advanced EM capable of probing the structural and chemical information at the TiB₂/Al interface. It was found that the original monolayer of Al₃Ti 2DC dissolves and the outmost {0001} Ti-layer is alternatively substituted by Zr atoms, a new monolayer of Ti₂Zr 2DC forms [47]. Such a new atomic layer not only brings back the misfit of -4.2%, but also has certain level of atomic roughness resulted from the Zr adsorption. As a result, TiB₂ was rendered impotent for heterogeneous nucleation of primary Al. As inspired from the aforementioned cases, it is foreseeable that the

mechanism underlying the poisoning effect of Li, Cr and Si might also fall on the atomic modification at the TiB₂ surface, although yet has the convinced experimental results been provided. However, a lot of experimental evidence verify the modifiable heterogeneous nucleation through atomic modification of the substrate surface.

2.6.1 Interaction between substrate and solute in Mg alloys

There are few studies in the literature that provided with explicit experimental or theoretical proof to reveal the mechanisms underlying the grain refinement of Mg alloys with various inoculations, let alone the connection to the modification of substrate at the atomic scale. One of the possible cases is the modification of Al₄C₃ during the superheating of commercial purity Mg-Al alloys. Under the assumption that Al₄C₃ is the nucleating particles, the impurity coating (Fe, Mn containing) on the Al₄C₃ particle dissolves at superheat temperature. A clean and potent surface of Al₄C₃ is obtained and can be retained by subsequent fast cooling. Nevertheless, a low cooling rate will lead to the re-precipitation of the poisoned coating, resulting in a poorly potent coated Al₄C₃. This model reasonably explains most of the experimental observations about superheating [69]. Another case is the SiC inoculated Al-bearing Mg alloys, where the SiC particles are believed to dissolve due to the reaction with Al solute in the melt [106,193,194]. Liu *et al* prepared the Al₄C₃-SiC/Al master alloy by adding SiC powder in molten Al with a holding time of 15 min at 950 °C, the authors proposed that Al₄C₃ forms at the surface of SiC particles, acting as a transitional layer contacting Al matrix and therefore, the real nucleating substrate [193]. The formation of Al₄C₃ can be indirectly supported by the formation of Mg₂Si (reduction of SiC occurs), as well as the decreasing grain size with increasing addition temperature (Al₄C₃ formation is favoured at a higher temperature). However, more accurate experimental evidence is still required, such as direct examination of the Al₄C₃ on SiC by the advanced electron microscopy. Although the above two cases are reluctantly classified as atomic modification due to the unknown modifying scales, which might be quite large (micron scale) in the Al₄C₃/SiC case, we should bear in mind that interaction between solutes and nucleating particles can't be overlooked for heterogeneous nucleation.

More experiments in MgO-inoculated Mg alloys indicated the possible interaction and its subsequent influence on heterogeneous nucleation and grain refinement [80,90,181,182,195]. There was a hint in Lee's PhD work [80] where the combination of 0.3wt.% Sr and 1 vol.% MgO addition shows better grain refining result than either the sole addition of 0.3wt.% Sr or 1 vol.% MgO. Even though there was no further

characterisation in his work suggesting any interaction between the MgO and Sr solute above liquidus, it might be the obscured but primary factor since the small growth restriction provided by 0.3wt.% Sr ($Q = 1.05 K$) should not lead to such a great grain reduction. It is well known that Sr and Ca have a similar chemical nature staying in the same group of the periodic table. The interaction between Sr and MgO should be re-considered when similar refining phenomenon was observed in Mg-Ca alloys with high shear melt conditioning treatment [90,195]. The adsorption layer containing Ca and N was identified in Mg-0.5Ca-HSMC by *Cs*-corrected atomic-resolution STEM and electron energy loss (EEL) spectroscopy, featuring as a few atomic layers in thickness identical in atomic structure as MgO matrix, while differentiating in chemistry [195]. It is also analogous to see only a tiny amount of Ca addition (0.01 wt.%) contributes to a significant reduction in grain size [90], the atomic modification would be more reasonable than the growth restriction to explain the grain refinement outcome. Another case is the great grain refinement achieved in Mg-0.1Zr with high shear melt conditioning (HSMC) treatment before casting, whereby Zr solute in the melt was promoted to adsorb onto the dispersed MgO particles [181,182]. With the identification of Zr adsorption on {111} facet of MgO particle in six atomic layers, the mechanism was proposed as the significantly reduced misfit due to the formation of a new interface MgO/Zr/Mg, heterogeneous nucleation was dramatically enhanced.

With the rapid development of characterisation techniques, the limitation in methods would not be an excuse at all to study the atomic modification on heterogeneous nucleation. However, the complexity of the segregation phenomena is not as simple as determined by only one factor, even with some factors being unknown. By now, a lot of experimental evidence has been obtained, however, the adsorption criterion is still unclear yet. There is not a general equation containing explicit parameters to judge whether segregation phenomena happen in a specific particle/alloy metal system. It seems expectable that the increasing experimental evidence obtained through the advanced characterisation technologies might set as the foundation to build up a relationship between heterogeneous nucleation and interfacial status.

2.7 Application of electron microscopy

With the invention of electron microscopy (EM) by Knoll and Ruska back in 1931, the resolution limitation imposed by visible light was eventually overcome by the introduction of new illumination source: electron. Since then, the on-going progress have

led to the advent of scanning electron microscope (SEM) and transmission electron microscope (TEM), making the experimental resolution able to routinely down to atomic scale [196]. Together with various detectors that are capable to interpret different types of signals from the interaction between electron and materials, electron microscopy has now been a powerful instrument to provide different aspects of information in a large range of length scale for researches in materials science, physics and chemistry, *etc.* [197].

In research of solidification of metallic materials, one of the major challenges is the experimental difficulties in detecting directly the nucleation process that occurs in a non-opaque medium at a high temperature within an extremely short time period. As a result, nucleation research, in general practice, is usually conducted by postmortem examination of the solidified materials combined with some speculations. The judgement of a nucleating particle is usually based on its relative position in the solidified microstructure, chemistry and its crystallographic orientation with respect to the metal matrix.

With the easy access to the characterisation of morphology and analysis of the composition, SEM plays an important role in grain refinement study of Mg alloys in the early days. For instance, the mechanism of grain refinement for Zr-inoculated Mg alloys was found attributed to the undissolved Zr particles, which were identified by BSD SEM images as bright cores [84]. Unfortunately, the limitation of SEM in special resolution and compositional precision fails to convincingly answer the long-term debates on the grain refining mechanism of superheating, native grain refinement, Elfinal process and carbon inoculation reviewed in **sections 2.4.1-2.4.4**.

The introduction of by electron backscatter diffraction (EBSD) to identify the nucleating particle by crystal structure and its relative crystal orientation with the matrix allow a more solid confirmation of nucleating particles. For example, the Al_4C_3 in Mg-Al alloys [198] had been identified by EBSD as the nucleating particles. Moreover, the identifiable crystallographic orientation with the primary Mg grains enables us to understand the mechanism underlying the heterogeneous nucleation, and therefore, the grain refinement. EBSD technique has been applied to identify the ORs in systems of SiC/Mg [108], Al_2Y/Mg [109] and Al_2X ($X = Gd, Sm, Dy, Nd$ and Ce)/Mg [113–116], the reproducible ORs and the corresponding lattice misfits indicate that these particles are potent substrates for heterogeneous nucleation attributing to the grain refinement.

Being able to identify structure and chemistry down to atomic scale, TEM offers a powerful technique to study grain refinement in light alloy materials. The well-defined ORs between Zr/Mg [89] and MgO/Mg [134] have been identified by SAED and HRTEM, showing that Zr and MgO can act as the nucleating substrate for primary Mg crystals. However, because of the extremely low number density and size of the nucleating particles, the preparation of TEM samples is generally difficult to make sure the interest particles are exactly contained in the electron transparent area of the thin foil specimen. The equipped Focus Ion Beam (FIB) in SEM and the appendant lifting-out technique allow us to target the nucleating particles for further TEM examination, providing trusted and direct-interpreted information. Typical examples in Al alloys can be found in AlP/Si [199], Al₃Ti/Al [200], Al₂O₃/Al₃Ti [76] and MgAl₂O₄/AlP/Si [201] in Al alloys. Other examples in Mg alloys reflect in Mg-10Y alloy [111] and Mg-CaO alloy [119], where Al₂Y and CaO in the centre of Mg grain were lifted out and identified to be the nucleating substrates.

When the catalysis of a substrate on heterogeneous nucleation is significantly controlled by the atomic configuration on the surface, the TEM then becomes a unique technique. The very dilute solute element is critical to determine the potency of a substrate in Al alloys. For example, the minor addition of phosphorus (P) reduced significantly to the nucleation undercooling for Si [202], in which the mono-layer AlP was found as the reason underlying the catalysis [203]. The other case goes to the grain refinement mechanism of TiB₂ in Al alloys. The application of TEM/HRTEM found the thin layer of Al₃Ti on the basal plane of TiB₂ [204], which was finally identified to be Al₃Ti 2DC by the *C_s*-corrected STEM and EELS [189]. In terms of MgO in Mg alloys, although there are some clues that the native MgO might be modified by the surrounding solute elements (**section 2.6.1**), the previous study on the MgO/Mg interface was very limited. In the current study, one of major duty is to find out the interaction product between MgO and the surrounding solutes and its effect of solidification behaviour and grain refinement. The application of TEM/STEM will play an important role in this study.

2.8 Summary

To understand the solidification behaviour and achieve grain refinement in Mg alloys, this chapter has reviewed the fundamental theories and models of solidification in metallic materials, including two intrinsic stages of nucleation and growth. It has been realised that the grain refinement can be achieved by a combination of enhanced

nucleation and inhibited growth, *i.e.*, nucleating particles and solutes are both important for grain refinement. This idea has led to the exploitation of potent grain refiners for Mg alloys, which normally classified as two categories: Al-free and Al-bearing Mg alloys. Unfortunately, the only commercial grain refiner Zr master alloys for Al-free Mg alloys suggests that the grain refinement in Mg alloys is more complex than expected by theories, and the interference from the solutes in the Mg melts may alter greatly the solidification behaviour, and therefore the grain refinement. There are not commercial grain refiners for Al-bearing Mg alloys yet.

In contrast, the other group of research has attempted recently in the opposite direction by applying impotent particles (*e.g.*, native MgO), which are also able to promote grain refinement following the explosive grain initiation scheme. Although with a bright perspective, the widespread application of native MgO particles for grain refinement in Mg alloys is inhibited by the limited study. There are several theoretical and technical issues required to be resolved.

- Firstly, the natural characteristics of native MgO particles in Mg melts were rarely studied before. It is crucial to reveal their crystallographic morphology, size and size distribution to understand their effects on the subsequent solidification behaviour.
- Secondly, the application of native MgO particles was confined in CP Mg and Mg-Al and AZ series in previous studies, their performance of grain refinement in other Mg alloys remains unknown, so does the related mechanism behind.
- Thirdly, in both aspects of theory and experiment, the modification of particle potency has been found applicable through elemental adsorption or segregation. This makes one more aspect needed to be considered: how the native MgO particles interact with alloying elements and what alteration in nucleating potency of the particles results.
- Lastly, it is essential to reveal the correlation between grain refinement behaviour and exact configuration of inclusions inside the melt, which is crucial to interpret the corresponding solidification behaviour based on the existed theories and models.

3 Experimental procedure

3.1 Raw materials

The raw material used in the present study is commercial purity magnesium (CP Mg) with purity of 99.9 wt.% as shown in **Table 3-1**. To prepare binary Mg-X alloys (where X=Al, Y, Ca or Sn), other pure materials or master alloys were also used, with their purity being given in **Table 3-2** and **Table 3-3**.

Table 3-1 Chemical composition of CP Mg (in wt.%).

| Al | Zn | Mn | Si | Fe | Cu | Ni | Be | Mg | Suppliers |
|-------|-------|-------|-------|-------|--------|--------|-------|-----------------|--------------|
| 0.019 | 0.002 | 0.032 | 0.013 | 0.002 | <0.001 | <0.001 | <1ppm | Balance (>99.9) | Magontec Ltd |

Table 3-2 Chemical composition of CP Al (in wt.%).

| Si | Fe | Ti | Cr | Cu | Ni | Zn | Al | Suppliers |
|------|------|------|-------|-------|-------|-------|---------|----------------------|
| 0.03 | 0.08 | 0.06 | 0.001 | 0.001 | 0.005 | 0.003 | Balance | Norton Aluminium Ltd |

Table 3-3 Chemical composition of Y, Ca and Sn (in wt.%).

| Materials | Purity (wt.%) | Suppliers |
|-----------|---------------|--------------------------|
| Y | 99.9 | Fisher Scientific UK Ltd |
| Ca | 99 | Fisher Scientific UK Ltd |
| Sn | 99.9 | William Rowland Ltd |

3.2 Facilities

3.2.1 Furnaces and handling tools

As shown in **Fig. 3.1(a)**, the melting unit is composed of an electric resistance furnace, a steel liner that can prevent the leaking of SF₆ from eroding the resistance heating elements of the furnace, a tube to deliver the mixture gas of 99.5 vol.% N₂ and 0.5 vol.% SF₆, and a K-type thermal couple. Intensive melt shearing (**Fig. 3.1(b)**) was applied with the shearing device (detailed description is provided in **section 3.2.2**) being inserted into the melt that was thermally isolated by fireproof blankets.

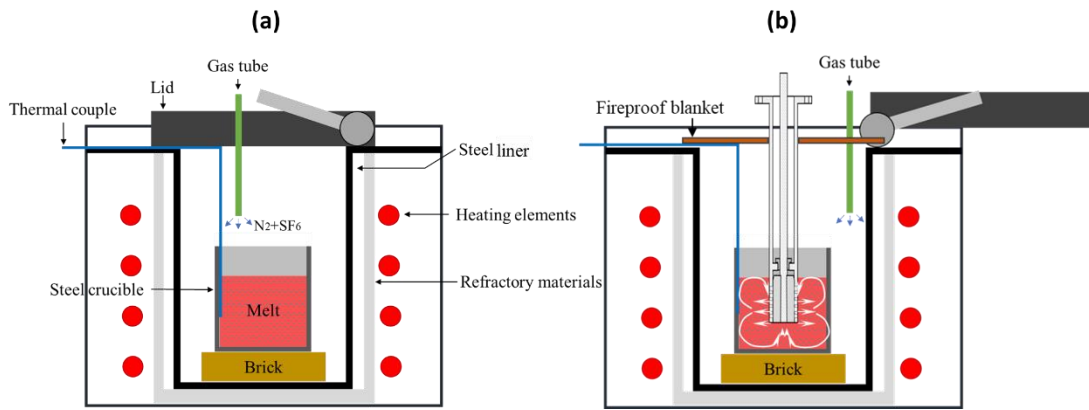


Fig. 3.1 Schematics of the casting units (a) without and (b) with high shearing device.

Other tools made of steel including stirring rod, skimmer and plunger were necessary to handle the Mg and Mg alloy melts. Before casting experiment, thorough cleaning of the steel liner, steel crucible and handling tools was carried out by preheating them to a temperature higher than 700 °C and held for a period of time to burn off the remaining Mg. After cooling down to the room temperature, machine hoover was used to remove all the burning products remained in the liner and crucibles. The remaining Mg on other tools was also burned off and then cleaned thoroughly by the rotating wire brush.

A MAM-1 model compact arc melter (Edmund Bühler GmbH) was applied to do casting at an ultra-high cooling rate ($\approx 200\text{K}\cdot\text{s}^{-1}$). Firstly, a graphite plate is placed on top of the Mg alloy ingot. Then the chamber is repetitively evacuated and purged to get an Ar atmosphere. After that, the Ar arc is triggered to heat up the ingot, once the ingot is melted the valve beneath is opened to allow the vacuum to suck the melt into the 3mm mould that is cooled rapidly by the flowing water.

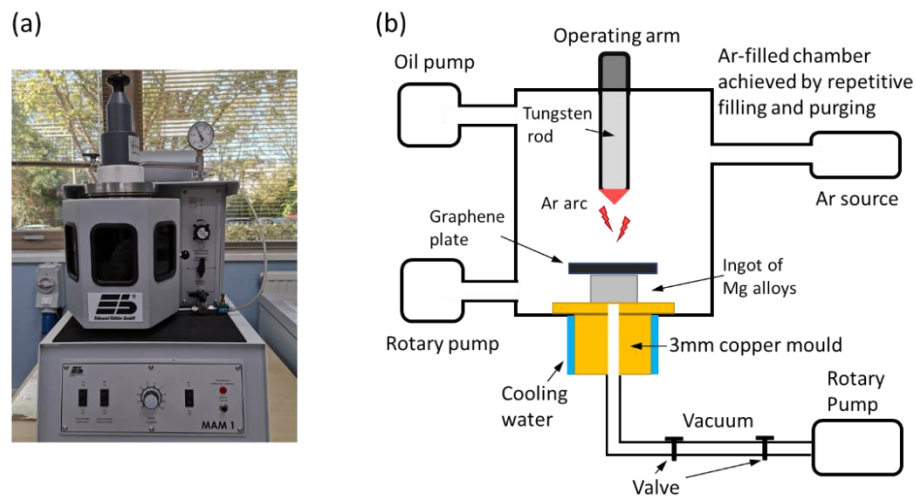


Fig. 3.2 (a) MAM-1 model compact arc melter and the corresponding (b) schematic showing the suction casting process.

3.2.2 Rotor-stator mixer

Invented by Fan and his co-worker [138], the rotor-stator mixer is a facility to impose high shear melt conditioning (HSMC) to the melt prior to casting. It consists of a stator with multi openings and a rotor connected to a motor, as shown schematically in **Fig. 3.3**. The rotation rate of the rotor was controllable (4000 rpm was applied in this work). Near the tip position of the device, the centrifugal force created by the rotating blades forces the liquid metal pushing out through the openings, while a negative pressure is created inside the shearing chamber to sucks the liquid metal for feeding. Such cycles produce not only the macro melt flows but also intensive melt shearing at the openings [205]. The main advantages of this shearing mechanism include: *i*) enhanced kinetics of any chemical reactions or phase transformations; *ii*) good dispersion and uniform distribution of solid particles; *iii*) size reduction of solid particles; *iv*) homogenization of chemical composition and temperature fields, and *v*) forced wetting [205]. The application of this technique in several Mg alloys prior to solidification has shown to result in significant grain refinement.

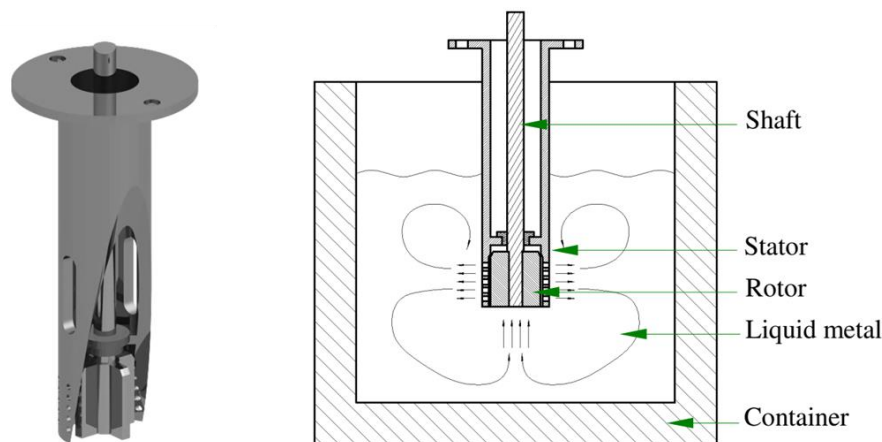


Fig. 3.3 Schematics of the rotor-stator mixer device for high shear melt conditioning treatment.

3.2.3 Pressurised filtration Device

In this study, Prefil[®]-Footprinter (*ABB Inc*) was used to collect oxide and other inclusion particles from the melt to facilitate the examination of the potential nucleation substrate. This device is originally designed for inclusion measurement of the molten metals, process control, optimization and collection of residues for metallographic analysis. It is an integrated system with a control system, filter system and monitoring system (**Fig. 3.4(a)**). As shown in **Figs. 3.4(b-d)**, firstly, the sample of liquid metal is poured into the preheated crucible which is installed in a pressure chamber. Secondly, when the melt temperature drops down to the target value for the test, a constant pressure (0.83 bar) is

applied by the introduction of argon gas forcing the melt to flow through the filter fixed at the bottom. an on-line data acquisition system, the process can be automatically stopped when the filtered melt hits a set value. Finally, the inclusions are concentrated and collected just above the porous filter.

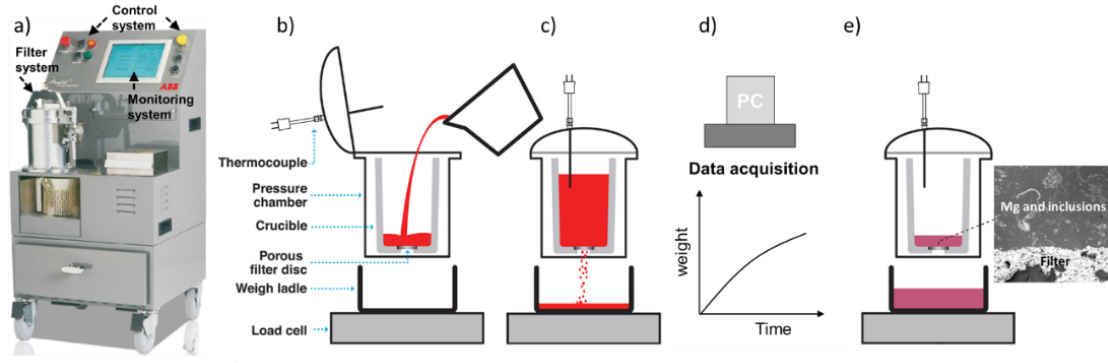


Fig. 3.4 (a) Picture of the Prefil®-Footprinter (ABB Inc); (b-e) schematics showing the filtration procedure.

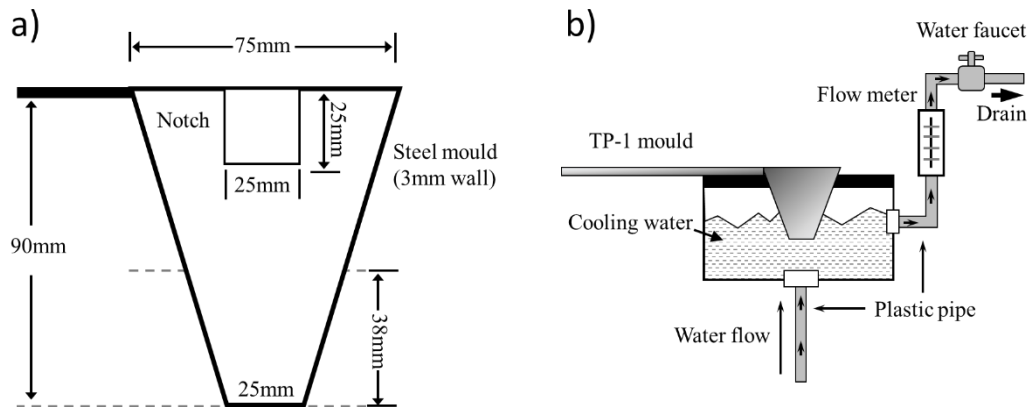


Fig. 3.5 Schematics showing the (a) geometric size of TP-1 mould and (b) cooling unit for casting.

3.2.4 TP-1 test unit

A standard casting method named Al Association TP-1 test was adopted to assess the grain size of various Mg alloys in this study. Originally the TP-1 test was developed for the aim of better comparison of the efficiency between different grain refiners for Al alloys [206]. The dimension of the TP-1 mould and the set-up of the relevant water-cooling unit in the TP-1 test are schematically shown in **Fig. 3.5**. Alloy melt was poured into the 350°C pre-heated TP-1 mould, which was immediately moved to the cooling unit (**Fig. 3.5(b)**). The constant water flow continuously removed the heat directionally from the bottom of the mould, providing an estimated cooling rate ($3.5\text{K}\cdot\text{s}^{-1}$) at the cross-

section 38mm from the bottom. The application of TP-1 test is a proper and reliable way to rule out the effects of cooling condition on as-solidified microstructure.

3.3 Casting Processes

3.3.1 Evaluation of grain refinement by TP-1 test

To evaluate the performance of grain refinement for binary Mg-X alloys (X=Y, Ca, Sn, Al), the TP-1 test, which is a standard procedure for assessment of grain refiner for Al alloys in industry, was applied to provide consistent solidification conditions in this study. The casting procedure is schematically portrayed in **Fig. 3.6**. With the protection of 99.5Vol.% SF₆ + 0.5Vol.% N₂ atmosphere, CP Mg ingot was melted in the steel crucible at 700 °C and followed by addition of certain amounts of alloying elements X. After homogenization by holding the melt for 30 minutes and manual stirrings, the melt temperature was lowered down to 680 °C. Then the melt was manually stirred and poured into the pre-heated TP-1 mould, which was then moved to the cooling unit where the bottom of the mould could be cooled by water spray at a flow rate of 3.8 L·min⁻¹.

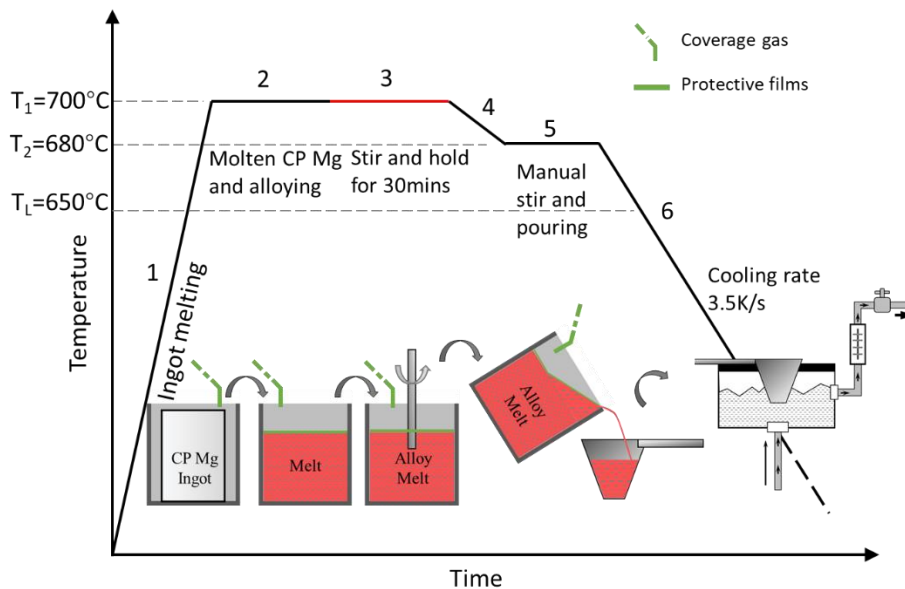


Fig. 3.6 A flow diagram showing the casting procedure of TP-1 test.

3.3.2 TP-1 test with intensive high shear melt conditioning (HSMC) treatment

Intensive high shear melt conditioning (HSMC) has been proved to be effective to refine the as-cast grain microstructure of Al and Mg alloys, and the refining mechanism was proposed as the enhanced wettability, dispersion and uniform distribution of native oxides due to the extensive local shearing rate (10^5 s^{-1}) [207]. To figure out the contribution of high shearing on the grain refinement in terms of both dispersion of native MgO and

promotion of elemental segregations, the melts of binary Mg-X (X=Y, Ca, Sn) alloys were treated by HSMC before casting into TP-1 mould. The casting experiment is shown in **Fig. 3.7**. After homogenization by holding the molten alloys for 30 minutes at 700°C, the alloy melts were sheared by a 40 mm rotor-stator device operating at 4000 rpm for 5 mins, with an inserting depth of 40 mm into the melts. Vibration of melt temperature and local sparks near the device/melt interface occasionally happened during HSMC. After HSMC treatment, the melt temperature was cooled down to 680 °C, under which the melt was manually stirred and poured TP-1 mould and transferred to the cooling unit.

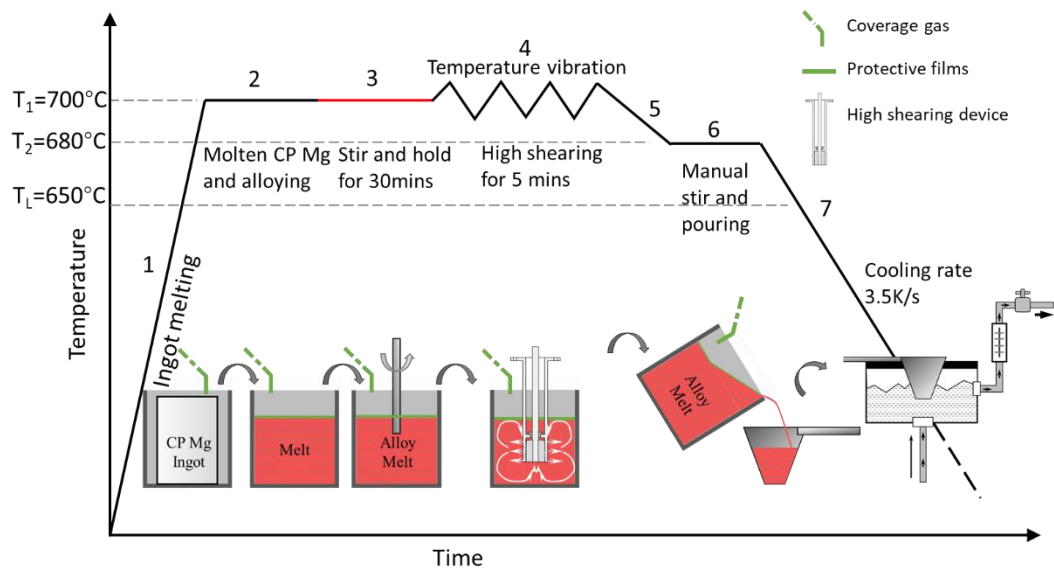


Fig. 3.7 A flow diagram showing the casting procedure of TP-1 test with HSMC treatment.

3.3.3 TP-1 test with HSMC and controlled extra oxidation

It is well known that Mg has a high affinity with oxygen; oxidation is a general phenomenon during casting of Mg and its alloys. This exothermal process can even lead to the self-sustaining oxidation in forms of burning without proper protection. Normally, flux or gas coverage is applied to prevent further oxidation. In this experiment, the strategy was trying to create more oxide by deliberately moving away the cover gas for a short time. The intensive high shear melt conditioning was applied (4000 rpm at 700°C) after cleaning away the surface slags, during when the gas coverage was removed. Surface oxidation soon appeared in forms of black films, local ignitions or burning. These oxidation products were then pushed down into the melt by a self-made tool. During this process (**Fig. 3.8**), the oxidation was manually controlled by putting the gas back on position to extinguish the possible heavy oxidations/burnings. The push-down process proceeded up to 5 minutes to create a significant number of oxides, which were dispersed by the high shearing device at the same time. Note that the melt temperature will increase

a few tens of degrees due to the exothermal oxidation reaction. The gas coverage was restored, and the speed of the rotor was lowered down to allow the addition of alloying elements into the melt. After a few tens of seconds to minutes (depend on the amount of added materials) to allow the dissolution of added solutes, the high shearing speed went up to 4000rpm again for 5 minutes with gas protection; this process not only brought further dispersion but also enhancement of kinetics of possible elemental segregation or interaction between solutes and oxides. After that, the melt temperature was lowered to 680°C, followed by casting of the melt in the TP-1 mould.

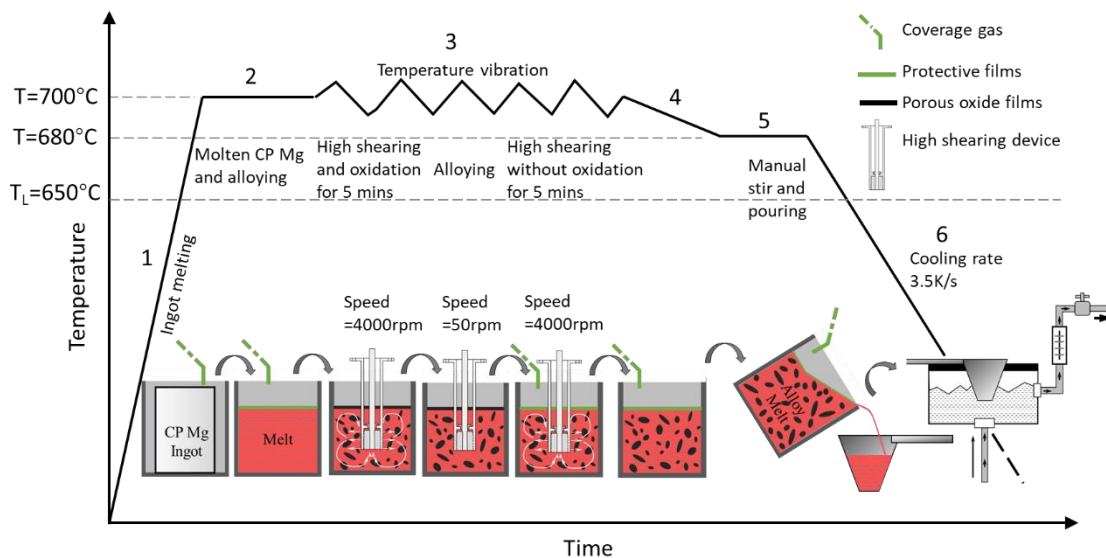


Fig. 3.8 A flow diagram showing the casting procedure of TP-1 test with controlled oxidation and HSMC treatment.

3.3.4 Collection of MgO by pressurised filtration

Direct examination of native MgO by OM, SEM and TEM was facilitated by the collection of the oxide particles from melts by a pressurised melt filtration technique. To guarantee a collection of a sufficient amount of oxides (and other impurities) in CP Mg, Mg-9Al, Mg-0.5/3Y, Mg-0.5Ca and Mg-2Sn alloy melts, the total weight of the melt for each filtration was around 1.2 kg. After melting of the CP Mg ingot at 700 °C under the protective atmosphere (mixture of 99.5 vol.% N₂ and 0.5 vol.% SF₆), the addition of certain levels of alloying elements was followed to achieve the nominal compositions. Manual stirring by a steel rod was occasionally applied to the melt during the isothermally holding for 1.5 hours to allow the homogeneity. The melt was then transferred into the pre-heated crucible in the chamber isolated from air in the filtration unit (**Fig. 3.4**). Introduction of argon into the isolated chamber provided sufficient pressure onto the melt, forcing the liquid melt to flow through a filter attached at the bottom of the crucible. The

remaining melt in the crucible solidified steadily afterwards and left concentrated oxides and other impurities above the filter.

3.3.5 Evaluation of the dispersity of native MgO

The native MgO particles were firstly concentrated by pressurised filtration method. There was round 2kg melt for each run, then the filtration follows the procedure in section 3.3.4 with around 500g melts left in the crucible and solidified in air. The 500g ingot, which was concentrated in native MgO particles, was re-melted and treated by the intensive high shear melt conditioning. The treated melt finally cast into TP-1 mould. The qualitative evaluation of dispersity of native MgO was conducted by comparing the SEM images of the solidified samples.

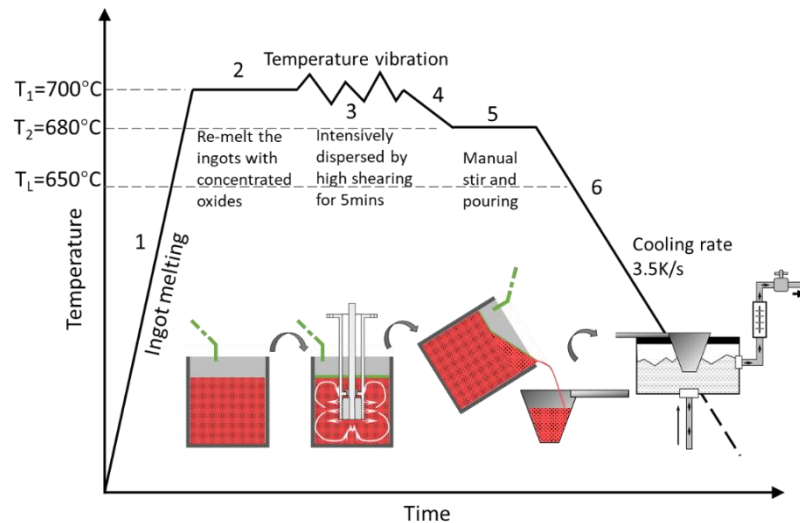


Fig. 3.9 A flow diagram showing the re-melting and casting procedure of filtered ingot by TP-1 test with HSMC treatment.

3.3.6 Collection of the oxides from melt surface

To study the original characteristics of MgO particles, the oxide films formed on the melt surface was collected in the following way. The CP Mg ingot was heated and melted into liquid at 700°C with protection by a gas mixture of SF_6+N_2 . The crucible with molten Mg was then moved out of the furnace, with the coverage gas being applied to prevent a catastrophic burning. Soon after that the residues on the melt surface was skimmed off and the protection gas was moved away, so that the melt was oxidised in the ambient atmosphere. This allowed the formation of fresh oxide films and products on the melt surface, together with some occasional ignitions appeared as nodules. The oxidation gradually vanished when the melt solidified and cooled to lower temperature.

3.4 Sample preparation

3.4.1 OM samples

The samples of optical micrography were made from different areas of the solidified TP-1 cone ingot for macro or micro grain structure measurement. As shown in **Fig. 3.10**, the solidified TP-1 cone is cut into two parts by an abrasive cut-off wheel at the position 38mm from the bottom; the head part with a circular section is the specimen for macro grain structure characterisation. The lower part then is cut longitudinally into two equal portions that have a trapezoidal section, which become the second specimen for measurement of macro grain structure. The grain size and columnar-to-equiaxed transition (CET) will be revealed on both the sections. After completion of macro measurement for the head part, another sample for precise grain structure measurement was sliced from the central area of it.

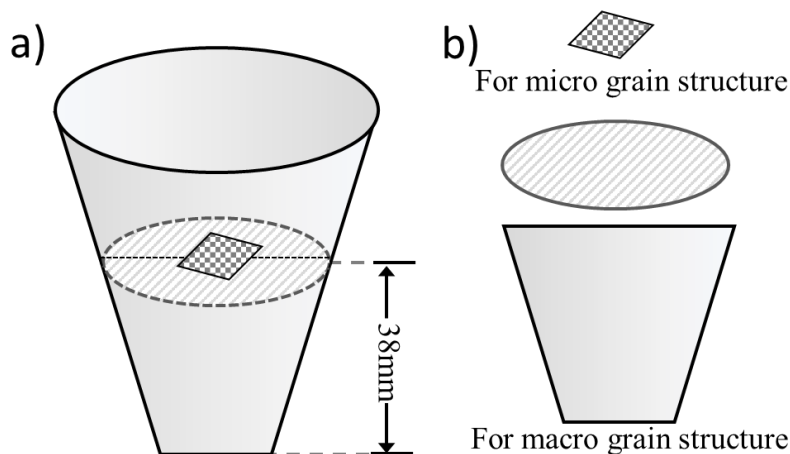


Fig. 3.10 Schematics showing the selection of samples from TP-1 cone for macro and micro grain structure measurement.

The samples for micro characterisation by optical microscopy were cold mounted to avoid the effect from temperature and pressure-induced deformation during hot mounting. The cold mounting consumables are provided by MetPrep Ltd.

For both macro and micro grain structure measurement, the sample preparations followed the same route listed in **Table 3-4**. The consumables either from Struer Ltd or MetPrep Ltd, as indicated in the table.

Table 3-4 Procedure of the metallographic sample preparation for OM samples.

| Step | Surface | Abrasive type | Lubricant | Force (N) | Speed (rpm) | Holder direction | Time |
|----------------|-----------------|------------------------------------|-------------|-----------|-------------|------------------|-----------------|
| Grinding 1 | 320#/Metprep | None | Water | 25 | 150 | × | 1min/until flat |
| Grinding 2 | 800#/Metprep | None | Water | 20-25 | 150 | × | 2mins |
| Grinding 3 | 1200#/Metprep | None | Water | 15-20 | 150 | × | 3mins |
| Grinding 4 | 2500#/Metprep | None | Water | 12-15 | 150 | × | 4mins |
| Grinding 5 | 4000#/Metprep | None | Water | 8-12 | 150 | × | 5mins |
| Primary polish | MD-Mol/Struers | DP Susp. 3µm. | DP-Yellow | 5-12 | 150 | × | 5mins |
| Fine polish | MD-Nap/Struers | DP Susp. 1µm. | DP-Yellow | 6-10 | 150 | × | 2mins |
| Optimal polish | MD-Chem/Struers | OP-S (0.04 µm, SiO ₂). | 50% ethanol | 6-10 | 150 | × | 8mins |

3.4.2 SEM samples

Samples for the measurement of the size distribution of the native MgO particles by SEM were made from the ingot obtained by melt pressurised filtration, which contained concentrated oxide particles above the filter. By cutting across the filter by an abrasive cutting-off wheel, the cross section contains both the filter and the solid above with concentrated oxides.

For evaluation of the dispersity of native MgO particles, the samples were sectioned from the central area that is 38 mm from the bottom of the TP-1 cone, which is solidified from the melt with concentrated MgO particles (**section 3.3.5**).

The above samples were mounted in $\Phi 30\text{mm} \times 15\text{mm}$ cylinder with conductive mounting resin (Conducto-Mount, MetPrep Ltd) using a hot mounting press (OPAL 410, ATM GmbH). Application of alcohol-based suspensions and lubricants shown in **Table 3-5** greatly reduced the risk of damage from the oxidation of Mg and reaction between MgO and water. The metallographic sample preparation then followed the routes listed in the table. Final cleaning was completed by ultrasonic cleaning in ethanol for 6 minutes.

Specimens for metallurgical characterisation of the fresh oxide film and products were obtained from the sample oxidised and solidified in crucible at three positions (**section 3.3.6**): *i*) cross-section showing the oxide film at the surface; *ii*) white-coloured product observed on the crucible wall; and *iii*) nodules on the surface of the solidified melt. The first sample was prepared by mechanical grinding and polished as aforementioned (**Table 3-5**). The latter two samples were firstly milled and followed by dispersion into ethanol solvent by ultrasonic stirring, obtaining a suspension with homogeneously dispersed particles. Certain doses of the suspension containing dispersed MgO particles were dropped onto a copper grid with carbon films (200-mesh grid, Agar Scientific Ltd) and dried in the oven at a temperature of 150 °C.

Table 3-5 Procedure of the metallographic sample preparation for SEM samples.

| Step | Surface | Abrasive type | Lubricant | Force (N) | Speed (rpm) | Holder direction | Time |
|------------------|--------------|---|-----------|-----------|-------------|------------------|------------------|
| Primary grinding | MD-Piano 500 | None | DP-Brown | 20 | 300 | >> | 1 min until flat |
| Fine grinding | MD-Largo | DP Suspension 9µm. | DP-Brown | 20-25 | 150 | >> | 4 mins |
| Polish 1 | MD-Mol | DP Suspension 3µm. | DP-Yellow | 15-20 | 150 | >> | 6 mins |
| Polish 2 | MD-Nap | DP Suspension 1µm. | DP-Yellow | 10-15 | 150 | >> | 3 mins |
| Optimal polish | MD-Chem | 50%/50%-mixed solution of ethanol and OP-S (0.04µm, SiO ₂). | None | 6-10 | 150 | << | 8 mins |

3.4.3 TEM samples

3.4.3.1 Sampling and grinding






After pressurised filtration, samples with a size of around 15mm×15mm×15mm were sliced from the solidified ingot at the position immediately above the filter. Fine cutting to about 1 mm thickness was then conducted using a diamond cutting machine (ACCUTOM-10, Struers Ltd). The thickness of the sample was further ground down to about 200µm by mechanical grinding with SiC abrasive papers (from 320# to 1200# provided by MetPrep Ltd). The 3mm diameter discs were cut from the slice by a disc puncher provided by Gatan Inc. To avoid oxidation of magnesium and the reaction of

MgO with water, we applied ethanol lubricant for further mechanical thinning by 2500# and 4000# abrasive papers. In this step, the primary work of 2500# paper is to reduce the thickness down to about 100µm for electropolishing or around 60µm for ion beam polishing. Final grinding was conducted by using 4000# SiC paper to achieve a smooth and flat surface by removing away the deep scratches.

3.4.3.2 Electropolishing

Electropolishing is performed using a TenuPol-5 device from Struers Ltd. The electrolyte applied was made of 5.3g LiCl, 11.16g Mg (ClO₄)₂, 500ml methanol and 100ml 2-butoxy-ethanol. The 3mm diameter disc was placed into the specimen holder as anode. The thinning process was conducted at a voltage of 90V and a temperature between -30°C and -40°C. Light sensor allowed the process to stop once perforation occurs. Then the sample holder was quickly removed from the unit and dipped in sequence into three containers with ethanol, and then the disc specimen was gently removed out from the holder and rinsed by ethanol again. For the pre-thinned samples that need further PIPS polishing, a thinning time was set as 80% of the time required for perforation.

Table 3-6 Details of the TEM foil thinning process using precision ion polishing system.

| Step | Voltage (kV) | Angle (°) | Polishing mode | Rotation (rpm) | Time | Illustration |
|------|--------------|-----------|----------------|----------------|---------------------------------|---|
| 1 | 5 | ±5 | Dual | 3 | Until perforate |  |
| 2 | 4 | ±4 | Dual | 3 | Until a proper size of the hole |  |
| 3 | 3 | ±3 | Dual | 3 | 35mins |  |
| 4 | 1 | ±5 | Dual | 3 | 15mins |  |
| 5 | 0.1 | ±5 | Dual | 3 | 5mins |  |

3.4.3.3 Ion beam polishing

Argon Ion beam polishing was conducted using a precision ion polishing system (PIPS, model 691, Gatan, Inc). Either the well-polished disc with thickness around 60µm or the pre-thinned ones by electropolishing was subjected to thinning in PIPS. They were transferred to the sample holder and placed properly into the airlock chamber which can

be lowered pneumatically to the position for Ar ion milling. Then the procedure listed in **Table 3-6** was followed to get a well-prepared final foil for TEM characterisation, with minimised damage and less amorphous area for better results.

3.5 Characterisation methods

3.5.1 Optical microscope (OM)

The optical microscopy was performed on a Carl Zeiss AxioScope A1 optical microscope equipped with objective lenses of different magnifications: 2.5x, 5x, 10x, 25x, 50x, 100x (**Fig. 3.11(a)**). The imaging mode was either polarization field or bright field. For measurement of grain size, polarization images were taken by the AxioCam Mrm digital camera on the top of the microscope and saved by the built-in operation software, AxioVision 4.9.

The picturing of the macro grain structures of the colour-etched TP-1 samples was carried on an Epson scanner (model V600 Photo, see **Fig. 3.11(b)**) with the built-in software. The Dots Per Inch (dpi) for each picture was kept for 1200 to make sure a good resolution.

3.5.2 Scanning electron microscopy (SEM)

3.5.2.1 Imaging and EDS analysis

A Carl Zeiss Crossbeam 340 SEM (**Fig. 3.11(c)**) was used for characterisation of the morphology, chemistry of the native MgO particles. This SEM is equipped with energy dispersive X-ray spectroscopy (EDS) detector (EDAX Inc), electron backscattered diffraction (EBSD) detector (EDAX Inc) and focused ion beam (FIB) system (Carl Zeiss Ltd). The In-lens secondary electron (SE) imaging mode offers an optimal resolution and sensitivity on the native MgO particles with a size around 100 nm. Therefore, most images were taken under this mode with the aperture size of 30 μ m, an accelerating voltage of 5 kV, and a working distance of 5 mm. Normally the working distance increases in a function of the accelerating voltage, the longer distance requires a larger voltage. Team suite software (EDAX Inc) was applied to collect and analysis the EDS data with a compromise among the beam/matrix interaction volume, imaging quality, signal strength. The suitable accelerating voltage for SEM was chosen based on the simulation data by Casino v3.3.0.4 to simulate the electron trajectory in the sample, as well as the Castaing formula [208]: $Z_m = 0.033(E_o^{1.7} - E_c^{1.7}) \frac{A}{\rho Z}$. To detect the desired elemental signals with small interference from Mg matrix, a voltage of 5 kV was applied

for MgO in CP Mg and Mg-Y alloys, while the voltage was 7 kV for Mg-Ca and Mg-Sn alloys.

3.5.2.2 Slice milling and 3D reconstruction

To reveal the 3D morphology of MgO particles, the sequential FIB slice milling and the simultaneous In-lens SE SEM imaging were conducted on a Carl Zeiss Crossbeam 340 SEM (Carl Zeiss Ltd). In the dual-beam mode, the Ga ion beam and imaging electron beam intersect at a 54° angle at the coincident point on the sample surface, allowing immediate, high resolution SEM imaging of the FIB-milling. Application of software Atlas 5 (Carl Zeiss Ltd) was used to set up the workflow including protective platinum deposition, special registration and slice milling. The cycles of milling, imaging and re-registration were automatically performed by the Atlas 5 with pre-set parameters. Specifically, Ga ion beam with a voltage of 10kV and a current of 100mA was applied to assure both efficiency and precision of the milling process. The function of registration in Atlas 5 allowed the milling thickness per slice down to 12 nm. Each image has a size of 10×10 μm², a pixel size of 2560×2560² (each pixel equals 3.9 nm). The collected images were cropped, contrast-improved by Fiji Image J and then reconstructed by Aviso 5.0 (Thermo Fisher Scientific Inc.).

3.5.3 Transmission electron microscopy (TEM)

3.5.3.1 JEM-2100F

A JEM-2100F field emission electron microscope (JEOL Ltd. **Fig. 3.11(d)**), equipped with a digital Gatan Orius CCD camera, EDS detector (Thermo Fisher Scientific Inc) and annular dark field (ADF) detector (Gatan Inc), was employed for characterisation at an accelerating voltage of 200 kV. A double-tilt sample holder (JEOL Ltd., Tokyo Japan) was utilised to feasibly tilt the MgO particles into desire zone axes. To identify the native MgO particles and characterise their morphology, crystallography, as well as the atomic and chemical configuration at the MgO/Mg interface, various imaging and diffraction modes were applied during the characterisation, which included bright field (BF) imaging, selected area electron diffraction (SAED), convergent beam diffraction (CBD), high-resolution transmission electron microscopy (HRTEM), ADF scanning transmission electron microscopy (ADF-STEM) and EDS mappings.

3.5.3.2 Nion UltraSTEM100

Characterisation of the MgO/Mg interface at the atomic scale was carried out in high angle annular dark field (HAADF) STEM mode using a Nion UltraSTEM100 dedicated STEM (**Fig. 3.11(e)**) located at the SuperSTEM Laboratory. The microscope was operated at an acceleration voltage of 100 kV, with the probe forming optics configured for a 33mrad convergence semi-angle. The microscope is equipped with a Gatan Enfina electron energy loss (EEL) spectrometer for chemical analysis. The collection semiangular range for HAADF, MAADF and ABF images were 89-195mrad, 52-100mrad and 15-32mrad. And the EELS collection semiangle was 36 mrad. The schematics of optics and signals acquisition in STEM mode is shown in **Fig. 3.12(a)**. To minimise the drifting of images, we utilised a home-made script to acquire 30 frames of image or more. The acquisition speed was 2.7 or 5 μ s per pixel (0.71s for each frame with 512 \times 512 pixel² or 256 \times 256 pixel²). EELS spectrum images (EELS SI) were acquired by recording EEL spectra at each pixel across a defined area of the specimen. The details image acquisition and processing are shown in **Figs. 3.12(b-d)**.

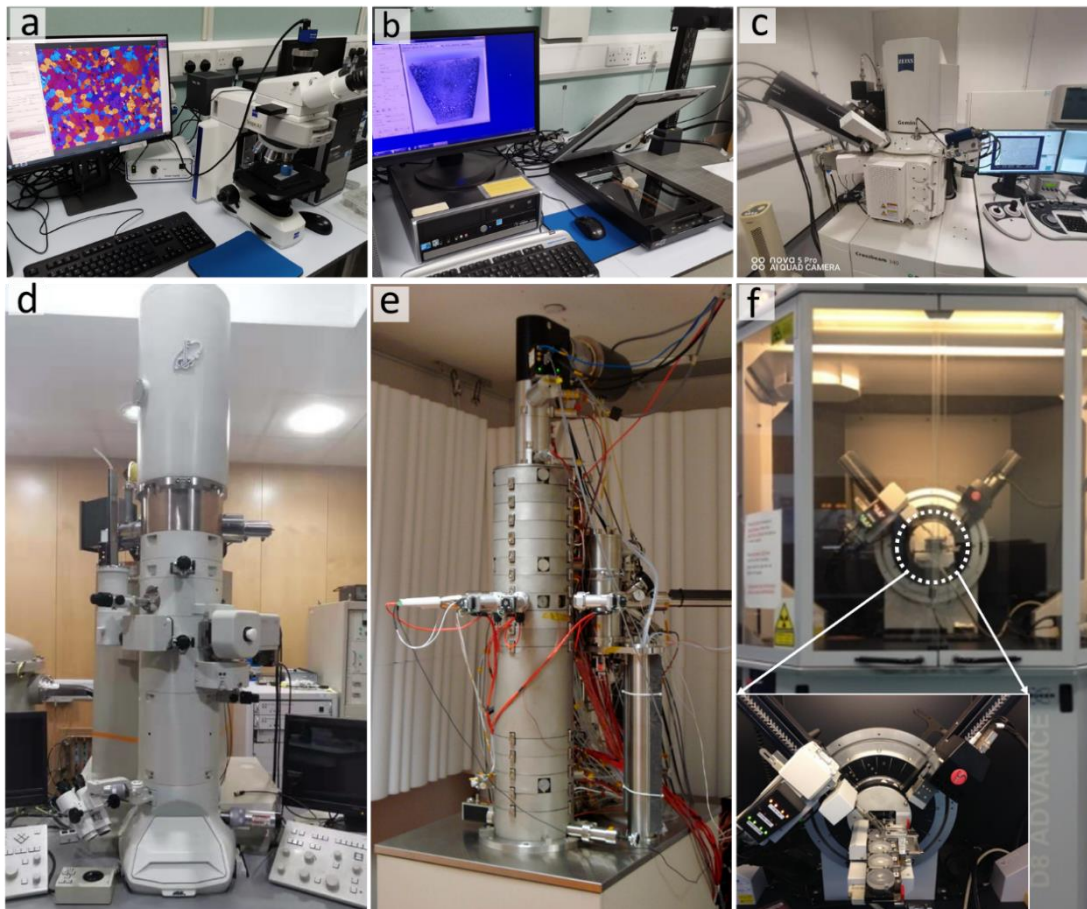


Fig. 3.11 Pictures of the facilities applied for characterisation. (a) Carl Zeiss AxioScope A1 optical microscope; (b) V600 Photo Epson scanner; (c) Carl Zeiss Crossbeam 340 SEM; (d) JEM-2100F; (e) Nion UltraSTEM100; and (f) Bruker D8 Advance X-ray diffractometer.

All the basic analyses of the TEM/STEM images including measurements of atomic spacing, interplanar angle were completed using Digital Micrograph Suite version 2.3.1. Necessary image processing was applied including rotation, crop, adjustment of brightness and contrast onto the images with conscious avoidance of artefact. The alignments of the HAADF/MAADF/ABF image stacks were performed using the built-in function of image alignment in the Digital Micrograph Suite. The chemical maps were created by integrating the signal above the relevant ionisation edges over a suitable window, after removal of the continuous decaying background using a standard power law model. Noise reduction was applied using Principal Component Analysis (PCA), as implemented in the HREM Research MSA plugin for Digital Micrograph [209]. The number of necessary components was evaluated after careful inspection of the residuals to avoid introducing artefacts or discarding meaningful information in the PCA-processed datasets.

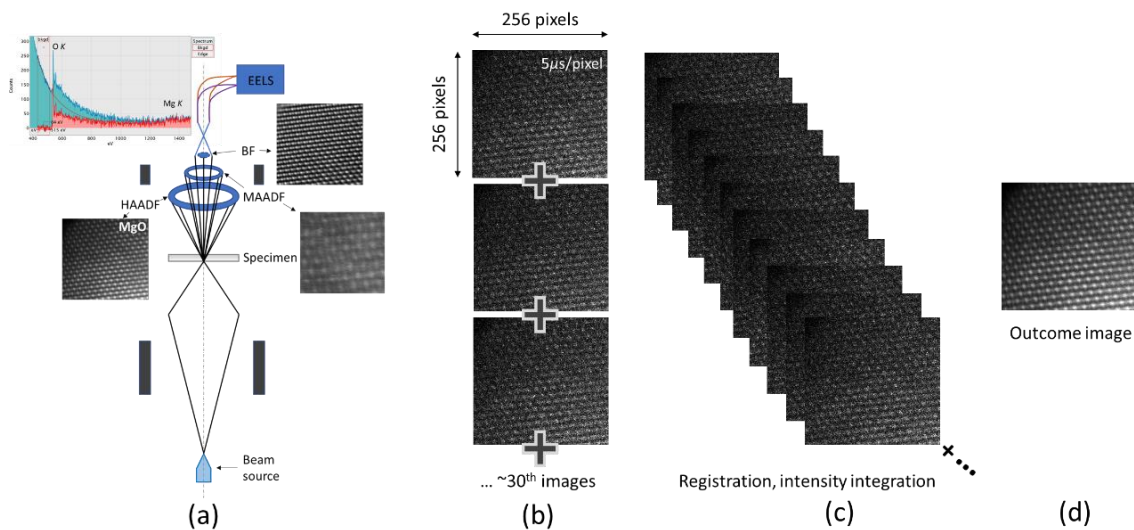


Fig. 3.12 (a) Schematics of optical configuration for STEM mode; (b-d) procedure of the acquisition and processing of image stacks to yield an outcome image with minimised distortion. Note that the illustrated STEM images are collected from MgO studied in this work.

3.5.4 X-ray diffraction

To identify the phases of inclusions in the filtered sample, X-ray diffraction (XRD) analysis was conducted on a Bruker D8 Advance X-ray diffractometer (Fig. 3.11f) that was equipped with LYNXEYE high resolution energy-dispersive 1-D detector and DIFFRAC.SUITE software package for operation (Bruker, Coventry, UK). Cu- α radiation at 40 kV (wavelength $\lambda_{K\alpha}=1.54056 \text{ \AA}$) with a Ni filter and a current of 40 mA was applied for the 2 \times Theta angle of XRD analysis ranging from 30° to 70° with the step size of 0.01°/s.

3.5.5 Quantitative measurement

3.5.5.1 Grain size assessment

In this study, the size of equiaxed grains is measured using linear intercept method, whilst the quantitative assessment of the columnar grains is performed by the measurement of their width. The linear intercept method is based on Standard ASTM E112-10. All the measurements were done on the polarized micrographs taken on the central area 38 mm away from the bottom of TP-1 sample (sections 3.4.1 and 3.5.1). As a result, the measured value can be either the average columnar width or the average equiaxed grain size. As shown in Fig. 3.13(a), during the measurement from an OM image, six lines (L_i) with known distance were drawn in random directions intersecting the grain boundaries. Followed the equations in Fig. 3.13(b), an average columnar width or average equiaxed grain valued by lineal intercept length (\bar{l}) can be calculated by dividing the total length of the lines by the total number of intersections. To have a reliable measurement of the grain size, at least 500 grains were measured to yield an average grain size and a standard deviation (s) (Fig. 3.13(b)).

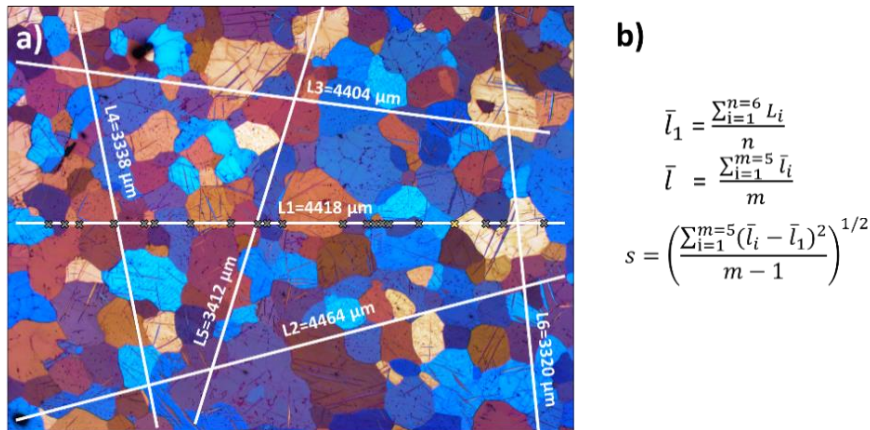


Fig. 3.13 The process to measure the average grain size based on the linear intersection method. (a) random lines with known distance intersecting the grain boundaries on an OM picture, the counts at an intersection is marked as dark 'x', the intersection at triple grain boundary is marked as yellow 'x'; (b) the equations for calculating mean lineal intercept length and corresponding standard deviation.

3.5.5.2 Size distribution of MgO particles

The dimensions of the native MgO particles were measured from the In-lens SEM images using a Fiji Image J software. The pixel size of the image was firstly defined by the original scale bar. Then the image was processed by the bandpass filter function to improve the contrast of MgO particles. Two types of MgO particles were found, octahedral and cubic shape. For the octahedral MgO (Figs. 3.14(a-d)), each resolved

particle was picked up by ‘Wand’ tool or manual polygonal selection, then the measured area can be transferred into diameter under the approximation of circular shape. For the cubic MgO (**Figs. 3.14(e-h)**), after the same procedure of improving contrast the particle size was directly measured as the longest length perpendicular to the facet. About 1500 particles were measured for each type of MgO particle and the statistics data was plotted and analysed using Origin 9.0 (© OriginLab Corporation). It was found that the log-normal function fits statistic data satisfactorily.

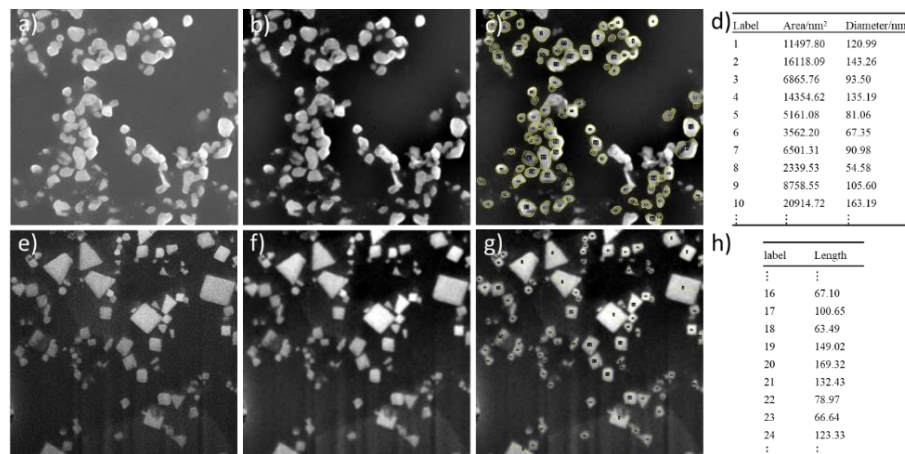


Fig. 3.14 Imaging data processing and measurement for (a-d) octahedral MgO particles and (e-h) cubic MgO particles.

3.5.5.3 Crystallographic measurement from the TEM/STEM images

Measurements of the interatomic spacings, interplanar spacings, interplanar angles from experimental images were done by the specific built-in tools in Digital Micrograph Suite version 2.3.1. Multiple measurements were undertaken to produce reliable averages and standard deviations. Specifically, for SAED ring patterns, multiple measurements were applied along different directions, for example, along lines with 45° from each other. While for SAED spot patterns, multiple measurements of the distances between $\{-xh, -xk, -xl\}$ and $\{-yh, -yk, -yl\}$ reflections (where $x, y = 1, 2, \dots$) were carried out for the reflection of $\{hkl\}$. For HRTEM images, multiple measurements of the interatomic and interplanar spacings were carried on the identical directions, with the interplanar angles correspondingly being measured for a given pair of planes.

While for the atomic characteristics formed on the MgO facets revealed by HAADF STEM or HRTEM images, the MgO matrix was applied as an internal reference in terms of atomic spacings and angles to re-calibrate the pixel size and image distortions. The measurement of the crystallographic values was performed afterwards.

4 The nature of native MgO in pure Mg and Mg-9Al

4.1 Chapter overview

In this chapter, the nature of native MgO formed in CP-Mg and Mg-9Al alloy melts is extensively investigated by the advanced electron microscopy (SEM and TEM/STEM). Firstly, the macro characteristic of MgO films was categorized into three types. Secondly, rather than compact films, the MgO films were found to be composed of discrete nano-sized particles. Thirdly, the discrete MgO particles have two types of morphologies, octahedron and cube, which were independent of the Al addition. The mechanism behind their formation was investigated and discussed. In addition, the potency of MgO for nucleating α -Mg was discussed as based on the theoretical framework of lattice misfit evaluation. Finally, the native MgO particles could be also harnessed for grain refinement based on the explosive grain initiation model, which was verified by the evaluation of grain size in CP Mg with and without dispersed native MgO.

4.2 Results

4.2.1 Native MgO films/particles

Figs. 4.1(a-b) shows the macro morphology of the oxide films and other inclusions in CP Mg and Mg-9Al concentrated above the filters, with the corresponding XRD spectra in **Fig. 4.1(c)** confirming that magnesium oxide (MgO) exists in both melts. As presented in 2D section, the oxide films were of either curved strips, patches or tangled strips, with size ranging from tens of microns to hundreds of microns. There are no distinct differences in terms of morphology between the MgO particles in CP-Mg and Mg-9Al specimens. In other words, the Al addition has little effect on the macro morphology of the oxide films. The oxide films can be divided into three types of oxide films: young film, old film and old skin as marked by the arrows in the SEM images.

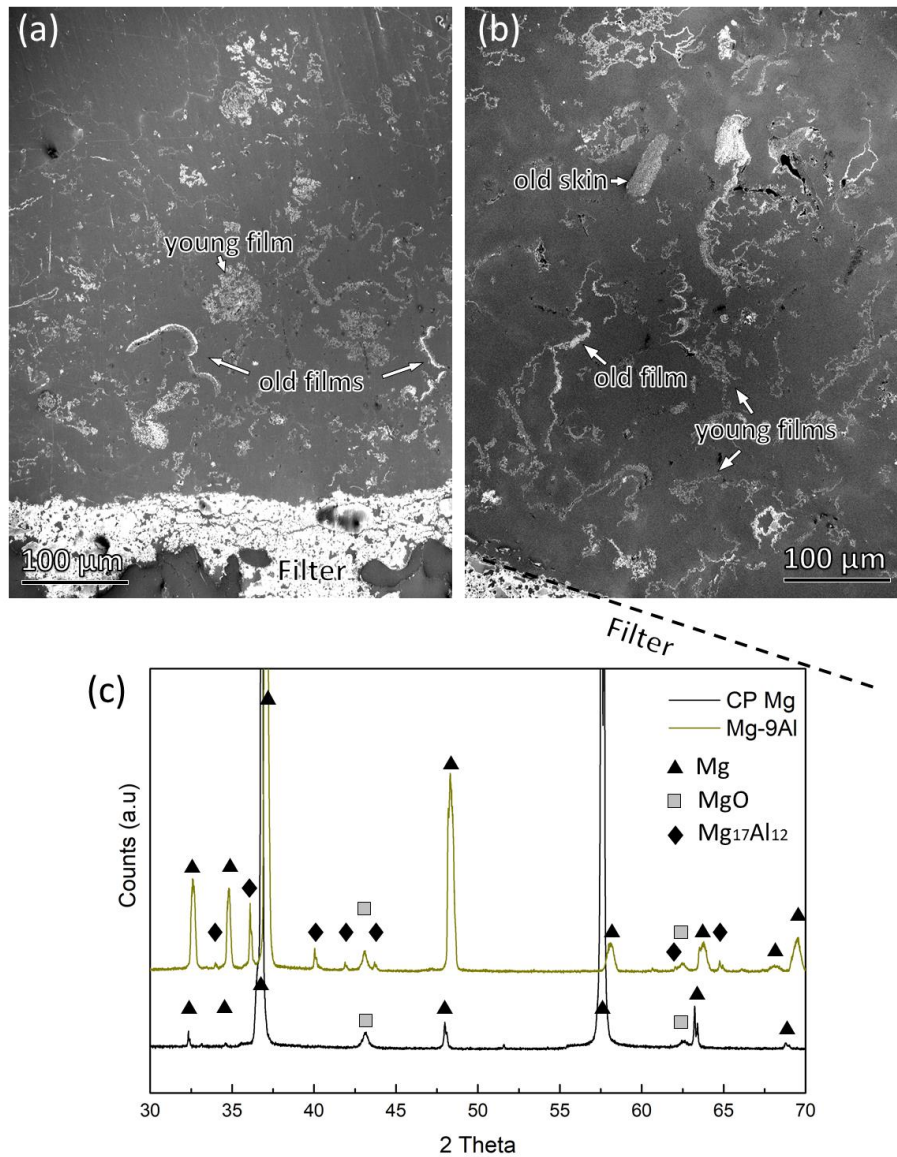


Fig. 4.1 (a, b) SE SEM images showing the oxide films collected by pressurised filtration technique from (a) CP Mg and (b) Mg-9Al alloy, respectively, and (c) the corresponding XRD spectra confirming the existence of MgO phase.

Fig. 4.2 shows the morphology of oxide films in both CP Mg and Mg-9Al at higher magnifications. The young oxide film is not a solid film, but effectively a flexible liquid film, which consists of nano-sized oxide particles in a liquid matrix and has an average thickness of 0.5 μ m. The incorporation and crumpling of such oxide films in the alloy melt lead to the aggregation of the young oxide films, as shown in **Figs. 4.2(a, d)**. There are no cracks between the young oxide films, suggesting that the oxide films formed on the melt surface are easily wetted by the melt once they are incorporated into the melt, and therefore both sides of the young oxide film are wet. This is different from the bifilms observed in Al-alloy melts, which are formed by folding the oxide films with a dry side and a wet side [145,146].

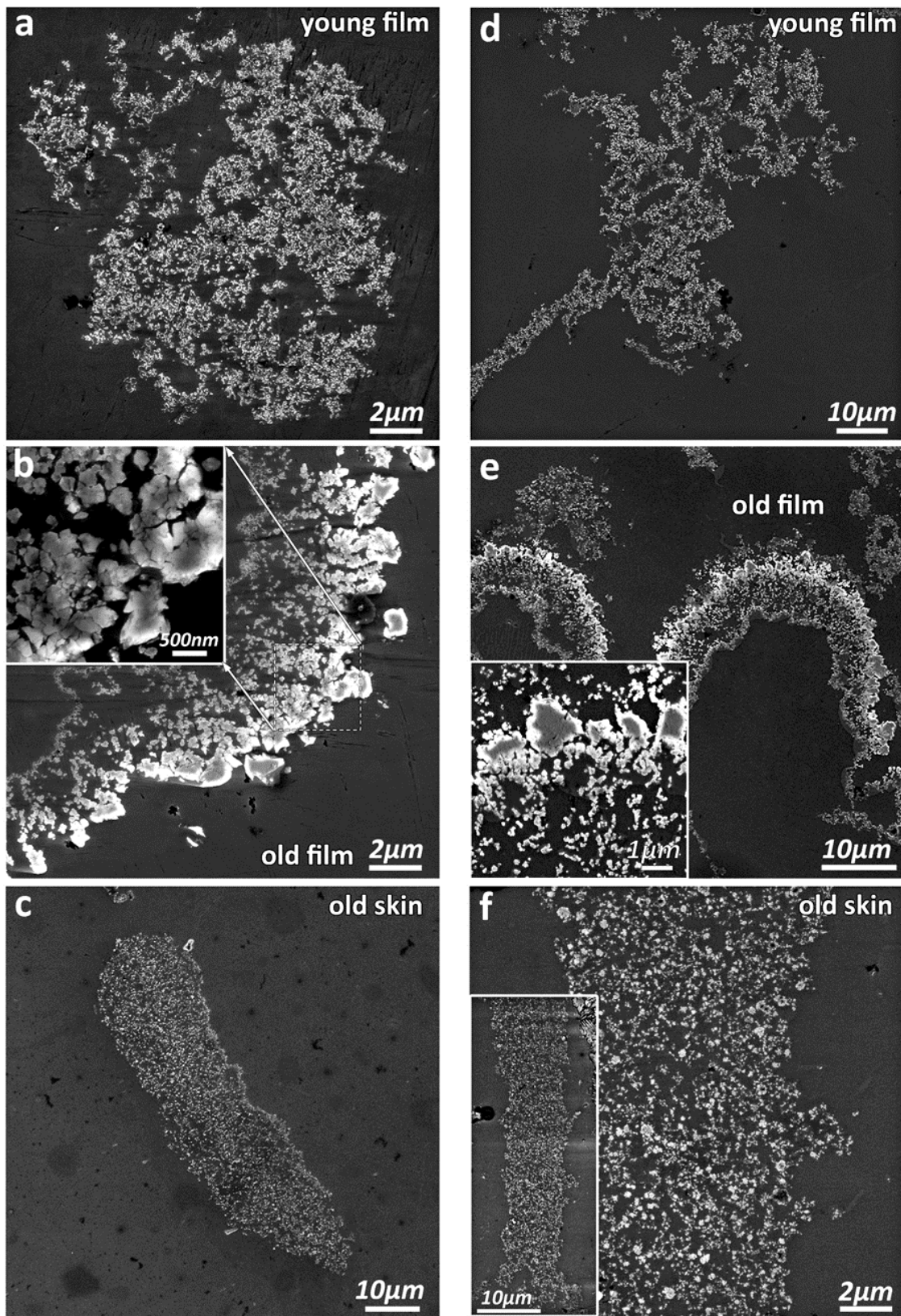


Fig. 4.2 SE SEM images showing the morphology of MgO film/particles at micron scale in (a, b, c) CP-Mg and (d, e, f) Mg-9Al alloy including (a, d) young film, (b, e) old film and (c, f) old skin. Note that the oxide films were collected by the pressurised filtration technique.

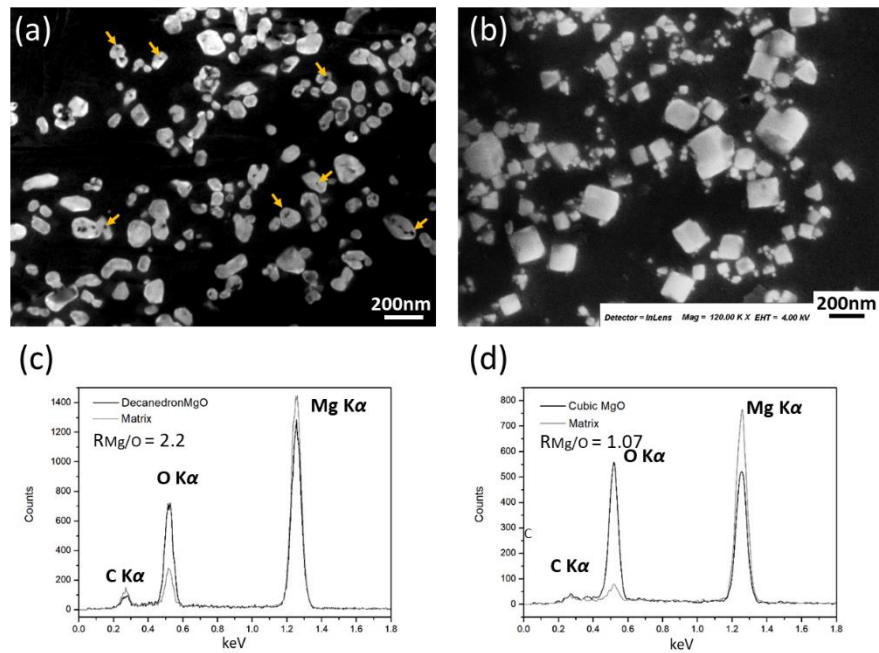


Fig. 4.3 (a, b) SE SEM images and (c, d) the related EDS spectra of the (a, c) polyhedral and (b, d) cubic MgO particles in CP Mg.

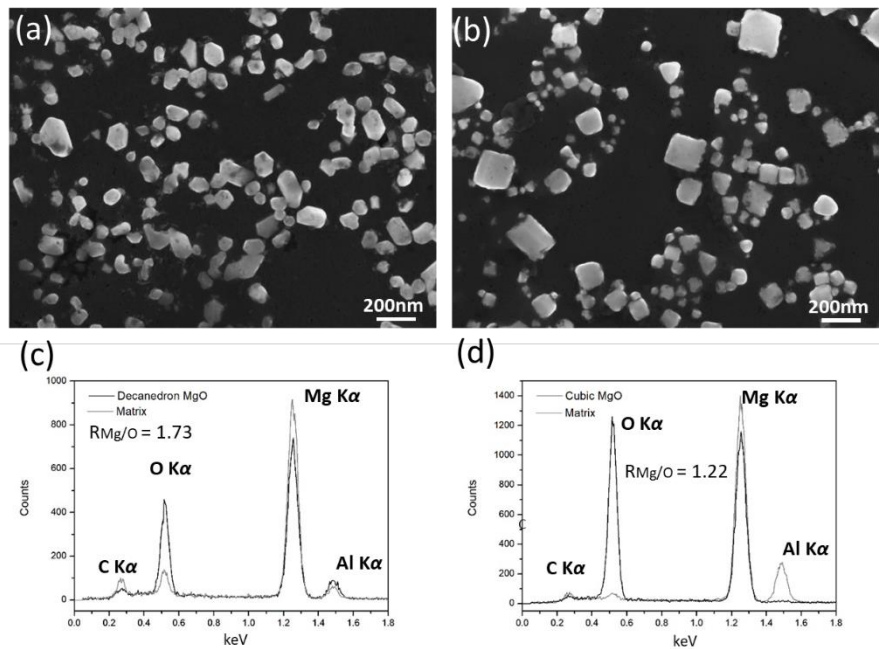


Fig. 4.4 (a, b) SE SEM images and (c, d) the related EDS spectra of the (a, c) polyhedral and (b, d) cubic MgO particles in Mg-9Al.

In contrast, the old oxide film is assumed to be the result of long-term oxidation of the melt surface despite the protective atmosphere. As shown in **Figs. 4.2(b, e)**, the old oxide films consist of coarse particles (about $1\mu\text{m}$ in average size) on one side that contains fluorine (F) and nitrogen (N), the elements from the protective gas (EDS evidence is presented later). The coarse particles form a relatively dense scale on the local melt surface, and further oxidation of the melt underneath takes place through the supply of

oxygen via the cracks in the scale, forming finer oxide particles beneath the old oxide film. Compared with the young films, the old films are relatively stiff and do not easily form tangled aggregates.

The third type of oxide agglomerates found in this work is the ingot skin, which appears in the alloy melt as straight segments (**Figs. 4.2(c, f)**). As inferred by its name, the ingot skin originates from the oxidation at the surface of the Mg ingot in solid state and is brought into the alloy melt. The ingot skins consist of densely populated nano-scale oxide particles, being similar to the young oxide films. In contrast to the young oxide films, the ingot skins are relatively stiff and can keep their straight shape in the melt.

As revealed at higher magnifications by the SE SEM images in **Fig. 4.3**, the young film in CP Mg is made of separated particles with size ranging from 50 to 100 nm. There exist two types of particles differing in morphology: polyhedral (**Fig. 4.3(a)**) and cubic shapes (**Fig. 4.3(b)**), both of which are identified as MgO in terms of the chemical composition (**Figs. 4.3(c-d)**). It is noted that cavities are found in some of the particles (labelled by the arrows in **Fig. 4.3(a)**). Similarly, **Fig. 4.4** illustrates that both types of MgO particles are also observed in Mg-9Al. The similarity in macro and micro characteristics of the oxide films and particles in CP Mg and Mg-9Al suggests that the solute Al has a negligible effect on their morphology.

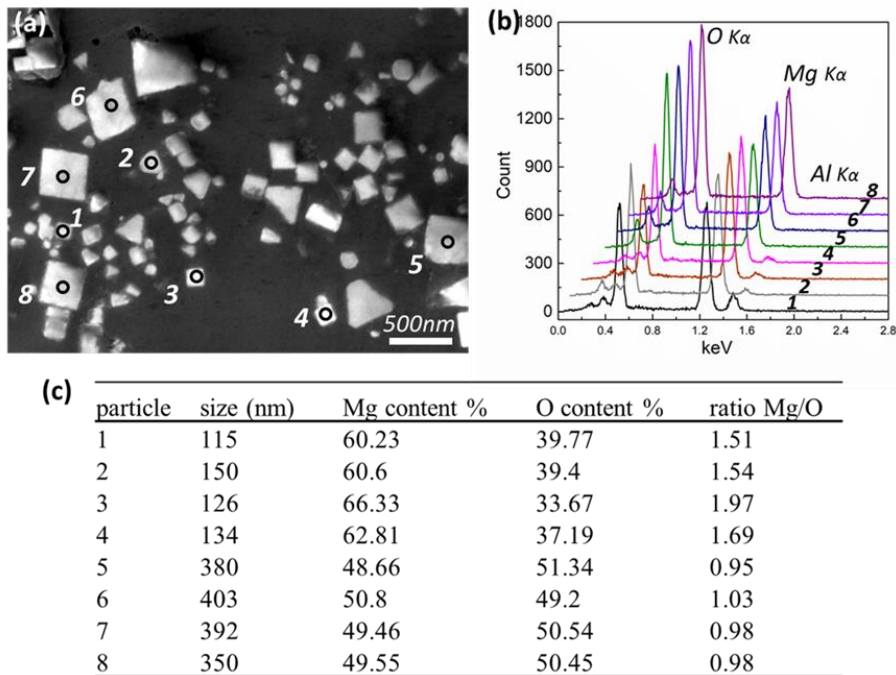


Fig. 4.5 a) SE SEM image of cubic MgO particles; (b) the corresponding EDS spectra; and (c) quantified EDS result of MgO in Mg-9Al.

From the EDS result, deviation of the Mg/O ratio from unity (*i.e.*, ideal for MgO) was noticed, with Mg content being more than 50 at.% for the small MgO particles. As illustrated in **Fig. 4.5**, the Mg/O ratio approaches '1' as the size increases. The deviation is attributed to the interaction volume between the electron beam and the sample. An interaction volume larger than the MgO particles leads to a contribution of the EDS from Mg matrix. Extra detection of Mg signal results. Therefore, the detected particles can be identified as MgO when the primary composition components are Mg and O only.

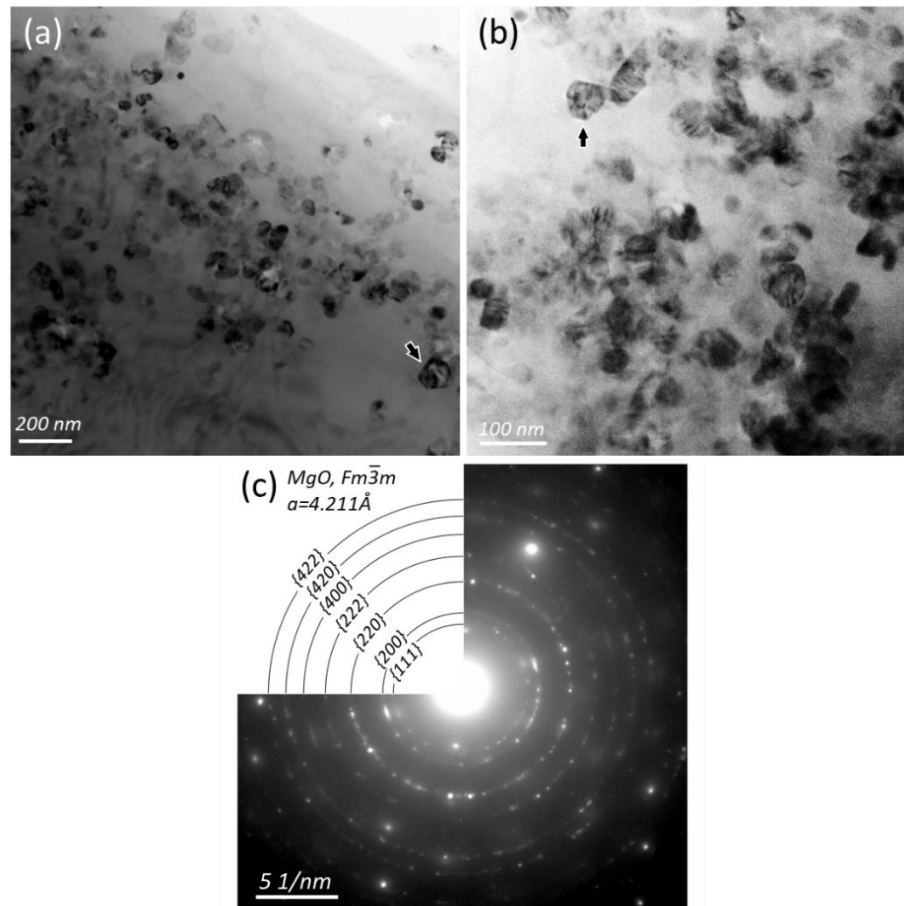


Fig. 4.6 TEM characterisations of the MgO films in CP-Mg. (a, b) BF images showing the MgO film composed of densely populated particles; and (c) SAED pattern from the MgO film in (a).

4.2.2 Crystallography of MgO particles

Fig. 4.6 shows the bright field (BF) TEM images and the corresponding selected area electron diffraction (SAED) of the native MgO films in CP Mg. The oxide film is composed of discrete particles in size, ranging from a few tens of nanometres to 100 nm (**Figs. 4.6(a-b)**). As marked by the arrows, some particles exhibit a faceted morphology. The SAED ring patterns in **Fig. 4.6(c)** suggests that the particles are MgO crystals randomly orientated in the oxide film. Detailed indexing of the diffraction rings is shown in **Table 4-1**, where the experimentally measured *d*-spacings (internal calibration using

the known lattice parameter of Mg matrix was applied) match well with the calculated values based on the reported crystal structure of MgO ($Fm\bar{3}m$, $a=4.211\text{\AA}$) [35]. As shown in **Fig. 4.7**, the oxide films in Mg-9Al also consists of separated MgO oxides. The randomly orientated MgO particles again lead to the diffraction rings shown in **Fig. 4.7(c)**. The corresponding indexing is also presented in **Table 4-1**, confirming they are MgO.

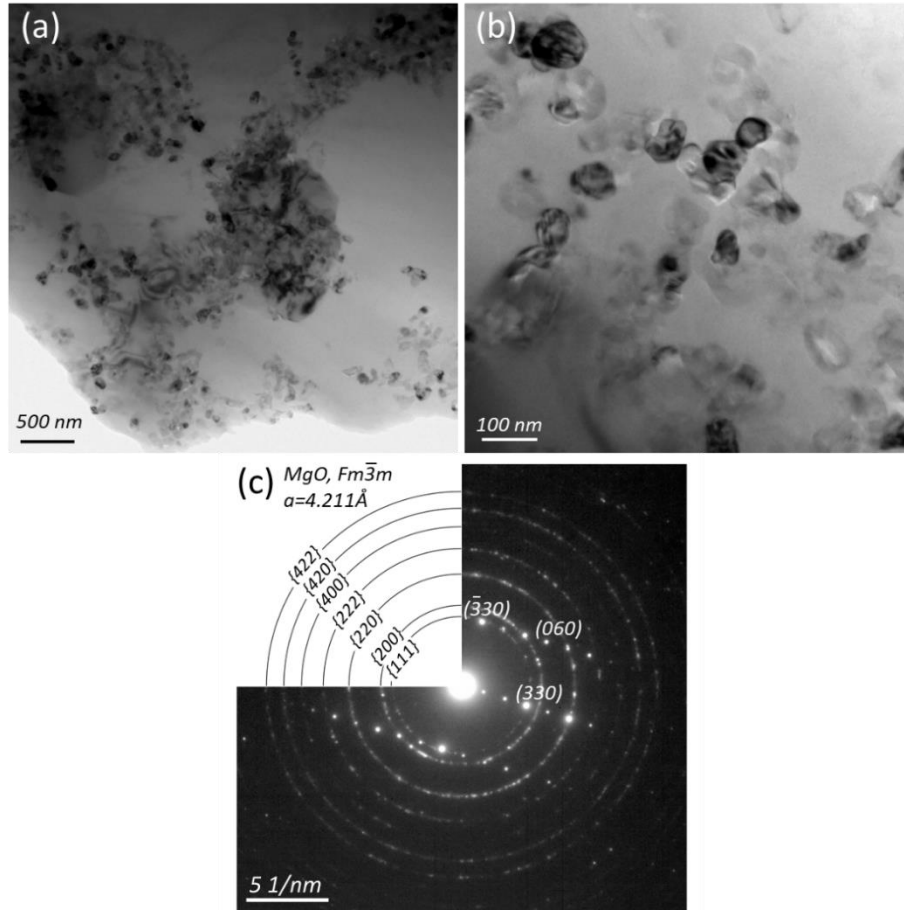


Fig. 4.7 TEM characterisations of the MgO films in Mg-9Al-prefil. (a, b) BF images showing the MgO film composed of densely populated particles; (c) SAED pattern from the MgO film in (a). Note that the large particles in (a) is identified as $Mg_{17}Al_{12}$ phase by the reflection spots in (c).

Table 4-1 Comparison between the measured d-spacings from the SAED patterns and the calculated d-spacings of MgO.

| Measured d-spacings in Fig. 4.6c (\AA) | Measured d-spacings in Fig. 4.7c (\AA) | Calculated d-spacings (\AA) * | Crystal plane {hkl} |
|---|---|--|---------------------|
| 2.443 ± 0.004 | 2.460 ± 0.019 | 2.431 | {111} |
| 2.110 ± 0.011 | 2.117 ± 0.008 | 2.106 | {200} |
| 1.497 ± 0.007 | 1.501 ± 0.012 | 1.489 | {220} |
| 1.223 ± 0.008 | 1.228 ± 0.009 | 1.216 | {222} |
| 1.058 ± 0.008 | 1.021 ± 0.044 | 1.053 | {400} |
| 0.947 ± 0.007 | 0.924 ± 0.035 | 0.942 | (420) |

| | | | |
|-------------------|-------------------|-------|-------|
| 0.865 ± 0.006 | 0.863 ± 0.005 | 0.860 | {422} |
|-------------------|-------------------|-------|-------|

*Calculated according to the lattice parameter of MgO $a = 4.211 \text{ \AA}$ reported in the literature [35]. The d-spacings were measured from the SAED ring patterns in Fig. 4.6(c) and Fig. 4.7(c) along three directions (0, 45 and 90 degrees from horizontal), yielding the average values and standard deviations.

4.2.3 Morphology of MgO particles

4.2.3.1 Octahedral MgO

Deep etching by electropolishing was carried out to remove the Mg matrix and reveal the 3-dimensional (3D) morphology of the MgO particles. **Fig. 4.8(a)** shows two MgO particles with a distinct octahedral shape. Specific symmetries can be noticed: the configuration of the four side facets (i to iv or 1 to 4) shows a 4-fold symmetry along the normal axis of the small ‘top’ facet (v or 5 in **Fig. 4.8(a1)**), while each side facet (i to iv or 1 to 4) itself shows a 3-fold symmetry with the axis along its own normal (**Fig. 4.8(a2)**). Being shown in **Fig. 4.8(b)**, the morphology of the MgO particle re-constructed from FIB milling slices confirms further its octahedral shape.

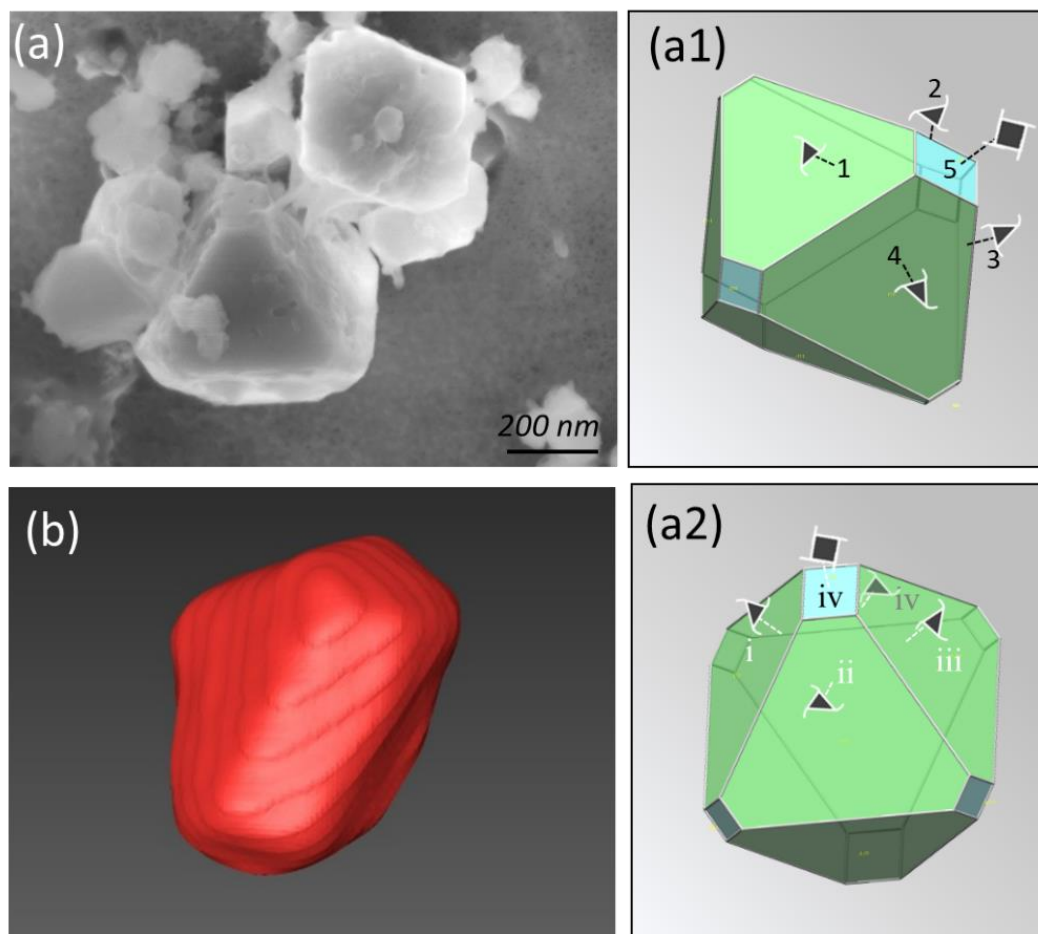


Fig. 4.8 (a) SE SEM image showing two distinct MgO particles with octahedral shape in Mg-9Al-prefil, (a1, a2) schematics of $\{111\}_{MgO}$ faceted octahedron shape with additional $\{001\}_{MgO}$ facets

at the corners showing good agreement with that found in (a). (b) Re-constructed morphology of an octahedral MgO particle from FIB slice-milling images.

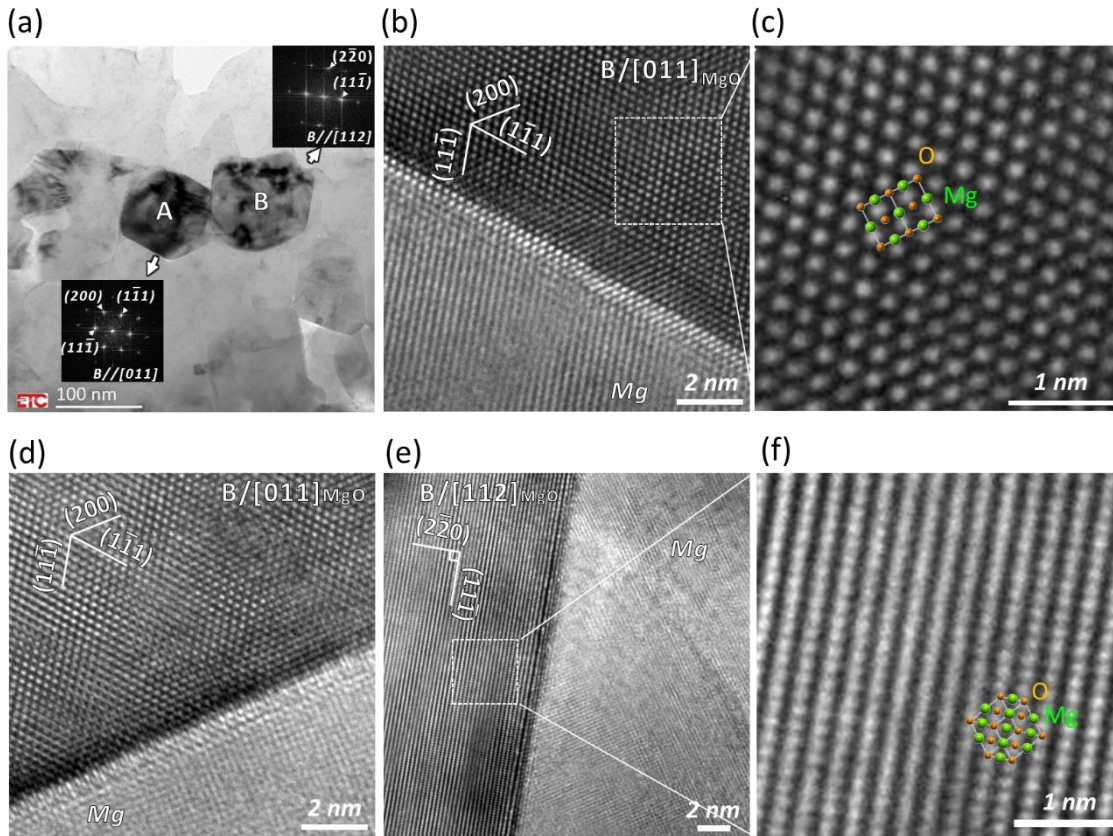


Fig. 4.9 Identification of octahedral MgO in Mg-9Al by TEM characterisation. (a) BF TEM image of the octahedral MgO particles truncated mainly by $\{111\}_{\text{MgO}}$ faceted planes, insets are the related FFT patterns from HRTEM images in (b and e); (b-d) HRTEM images showing the (b, c) $(11\bar{1})_{\text{MgO}}$ facet and (d) $(\bar{2}00)_{\text{MgO}}$ facet, respectively, with a beam direction parallel to $[011]_{\text{MgO}}$ of MgO particle 'A' in (a). (e, f) HRTEM image taken from the $(11\bar{1})_{\text{MgO}}$ facet of particle 'B' in (a), with the zone axis of $[112]_{\text{MgO}}$.

The exact crystallography of the MgO facets was further determined by combining the projection images with crystallographic information obtained by TEM characterisation.

Fig. 4.9(a) shows the BF TEM image of two MgO particles 'A' and 'B', with the fast Fourier transformation (FFT) insets belonging to the $[011]_{\text{MgO}}$ reflection for particle 'A' and the $[112]_{\text{MgO}}$ reflection for particle 'B'. As shown in **Figs. 4.9(b-f)**, their sharp facets are further characterised by HRTEM images, whose indexing of interplanar spacings and angles shows a good agreement to the values calculated from the reported crystal structure of MgO (**Table 4-2**). It confirms that MgO particle 'A' is either faceted by $\{111\}_{\text{MgO}}$ or $\{100\}_{\text{MgO}}$ planes when being viewed along the zone axis of $\langle 011 \rangle_{\text{MgO}}$, while particle 'B', viewed along $\langle 112 \rangle_{\text{MgO}}$, only shows $\{111\}_{\text{MgO}}$ terminations.

Combining information on both the morphology and crystallography of the truncated facets of this type of MgO particle, its morphology is concluded to be in the range from

a cuboctahedron (eight $\{111\}_{\text{MgO}}$ facets plus six $\{001\}_{\text{MgO}}$ facets, a truncated octahedron) to an octahedron (eight $\{111\}$ facets), with dependence on how many $\{100\}$ facets remain. Given the identified crystal terminations for this type of MgO crystal, the normal of $\{111\}$ facet shows a 3-fold symmetry, another normal of $\{100\}$ facet has a 4-fold symmetry. It is consistent with the symmetries derived from the morphology shown in **Fig. 4.8**. Moreover, it is found that the areas of $\{100\}$ facets reduce as the particle size increases, as shown in **Fig. 4.10**. This type of MgO is named as octahedral MgO or $\{111\}$ MgO in the following content.

Table 4-2 Comparison between the values of measured and calculated d -spacings of MgO, as well as the angles between specific crystal planes.

| Zone axis [uvw] | Crystal plane {hkl} | Measured d-spacing (Å) | Calculated d-spacing (Å)* | Measured angle (°) between crystal planes | Remarks |
|--------------------|------------------------|---------------------------|------------------------------|--|------------|
| [011] | {111} | 2.430±0.014 | 2.431 | 70.5, $\langle(1\bar{1}1), (\bar{1}\bar{1}1)\rangle$ | Fig. 4.9b |
| | {200} | 2.082±0.018 | 2.106 | 54.7, $\langle(200), (1\bar{1}1)\rangle$ | |
| [112] | {220} | 1.502±0.014 | 1.489 | 90, $\langle(2\bar{2}0), (1\bar{1}1)\rangle$ | Fig. 4.9e |
| [001] | {020} | 2.111±0.022 | 2.106 | 90, $\langle(200), (020)\rangle$ | Fig. 4.11c |

*Calculated according to the lattice parameter of MgO $a = 4.211 \text{ \AA}$ reported in the reference [141].

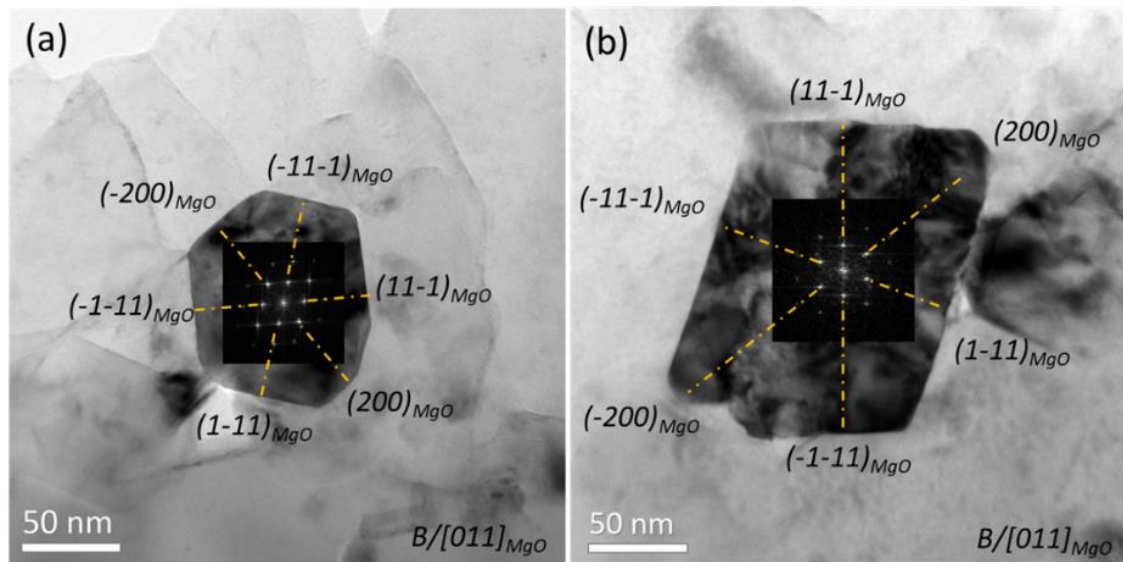


Fig. 4.10 BF TEM images of octahedral MgO particles (a) with relatively large proportion of remained $\{100\}_{\text{MgO}}$ facets and (b) with nearly absent $\{100\}_{\text{MgO}}$ facets in Mg-9Al. Both particles are viewed from its $[011]_{\text{MgO}}$ zone axis.

4.2.3.2 Cubic MgO

By reconstructing the FIB-milling slice images, a cubic particle is shown in **Fig. 4.11(a)**. Its morphology is in consistence with the TEM observation in **Fig. 4.11(b)**, where the

sample is deliberately tilted a few degrees away from zone axis to show the stereogram of the particles. The inset of SAED pattern taken on the exact zone axis of $\langle 001 \rangle_{\text{MgO}}$ reveals that they are cubic MgO particles truncated by $\{100\}$ planes, which can be further confirmed by the HRTEM images (**Figs. 4.11(c-d)**) acquired from the particle edge.

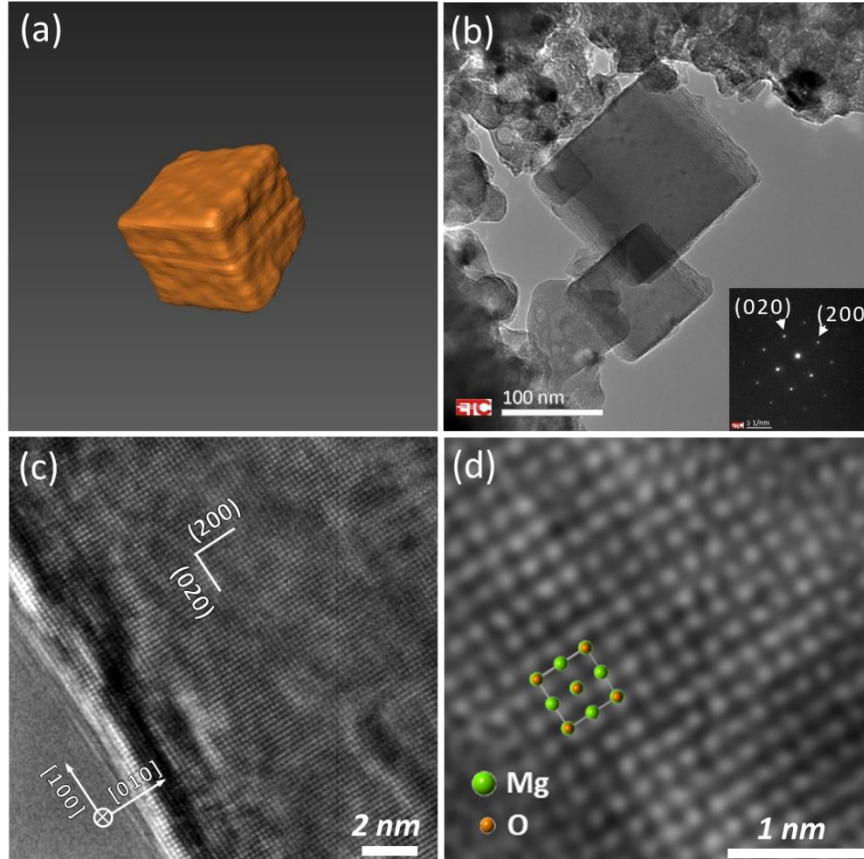


Fig. 4.11 Identification of cubic MgO by FIB and TEM characterisation in Mg-9Al. (a) reconstructed morphology of MgO by FIB serial sectioning images; (b) BF TEM image of octahedral MgO particles truncated by $\{001\}_{\text{MgO}}$ planes, with the inset showing the corresponding diffraction pattern; and (c, d) HRTEM image of the MgO in (b) in a beam direction parallel to $[001]_{\text{MgO}}$.

4.2.4 Size distribution of MgO particles

To quantify the size distribution of the MgO particles, about 1500 MgO particles from CP-Mg and Mg-9Al, either $\{111\}$ or $\{100\}$ faceted particles, were measured, respectively. The statistical results in **Fig. 4.12** show that the size distributions follow a log-normal function [63]:

$$N(d) = \frac{N_o}{\delta d \sqrt{2\pi}} \exp - \left(\frac{[\ln(d) - \ln(d_o)]^2}{2\delta^2} \right) \quad \text{Eq. 4-1}$$

where $N(d)$ is the number of particles in diameter between d and $d + \Delta d$, N_o is the total number of particles, d_o is the geometric mean diameter and δ is the geometric standard

deviation. Overall, both types of MgO particles in CP Mg and Mg-9Al show similar size distributions, with similar values of d_o and δ . Although the differences are small, it is still seen that the d_o for both $\{111\}$ (84 nm) and $\{100\}$ MgO (93 nm) in Mg-9Al is a little larger than the values of 68 nm for $\{111\}$ and 85 nm for $\{100\}$ MgO in CP Mg. Besides, the $\{100\}$ MgO particles obviously have a larger d_o than $\{111\}$ MgO particles in both alloys.

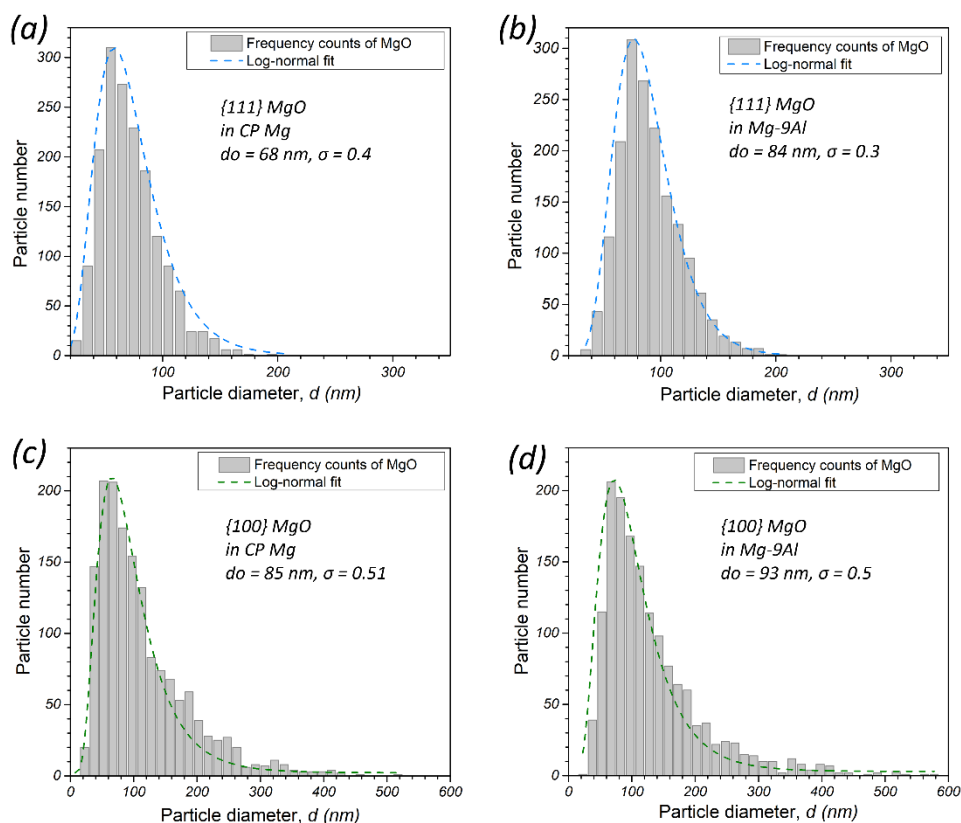


Fig. 4.12 Statistics of the size distribution for (a, b) octahedral and (c, d) cubic MgO particles in (a, c) CP-Mg and (b, d) Mg-9Al alloy.

4.2.5 Chemical and structural configuration of MgO surface

Fig. 4.13 presents the HAADF STEM images of a $\{100\}$ MgO particle in CP Mg viewed along its $[001]_{\text{MgO}}$ direction, under which the edge-on $\{100\}_{\text{MgO}}$ facets are revealed clearly. The uniform contrast at the atomically flat interface between $\{100\}_{\text{MgO}}$ and Mg also suggests that there is no elemental segregation. Similarly, **Fig. 4.14(a)** shows a $\{111\}$ MgO particle in CP Mg by BF TEM image and the corresponding SAED pattern viewed along its $[011]_{\text{MgO}}$ direction. On the $\{111\}_{\text{MgO}}$ facet that is examined by HAADF imaging (**Fig. 4.14(b)**), the atomic columns on the atomically flat $\{111\}$ facet are identical in intensity along the MgO/Mg interface, suggesting a clean facet without segregation of heavier impurity elements. Besides, the intensity is lower than that inside the MgO bulk, due to the thickness difference (mass contrast).

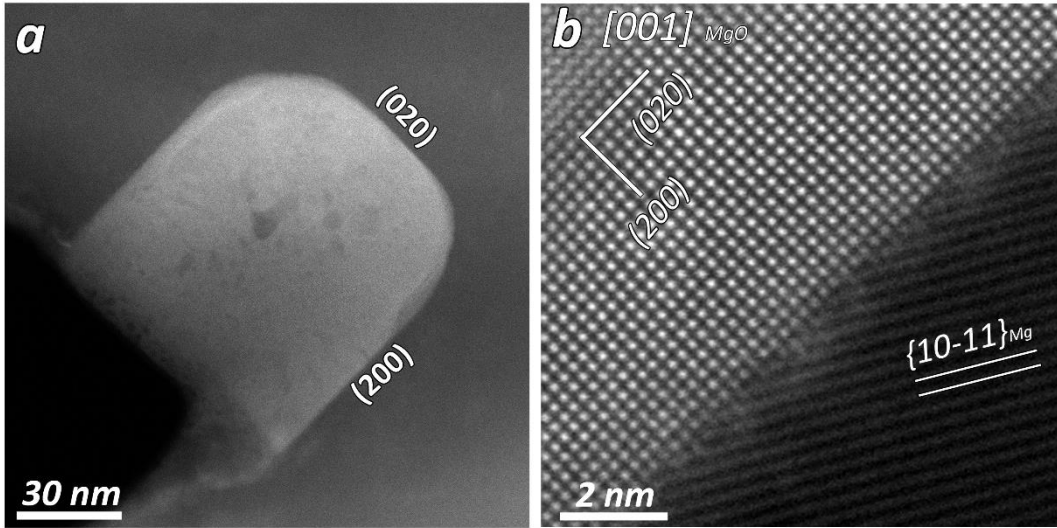


Fig. 4.13 HAADF STEM images showing the $\{100\}$ MgO particle in CP Mg. The incident beam is parallel to $[001]_{\text{MgO}}$ direction.

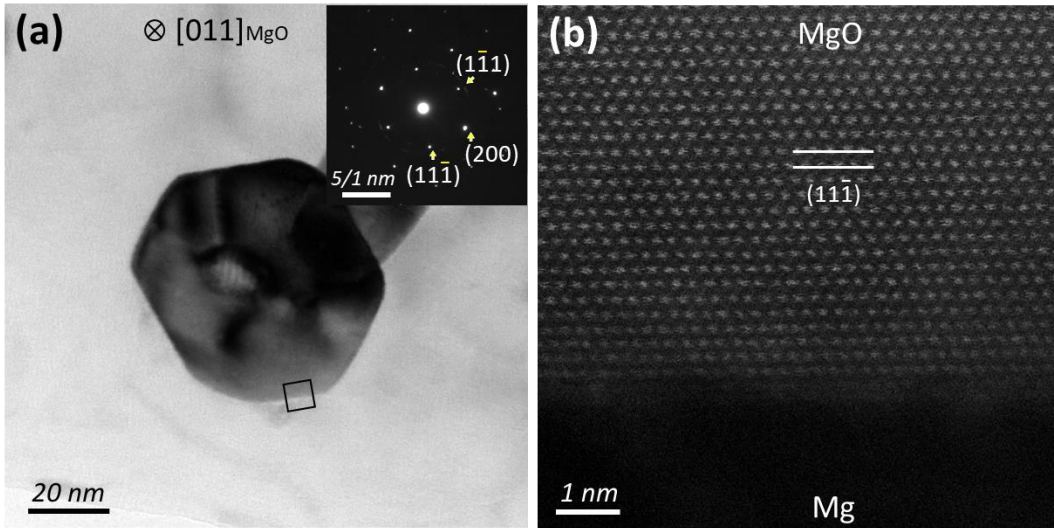


Fig. 4.14 (a) BF TEM of a $\{111\}$ MgO particle in CP Mg and (b) the corresponding HAADF STEM image acquired across of MgO/Mg interface that is marked by black cube in (a). The inset in (a) is the corresponding SAED patterns. The incident beam is parallel to $[011]_{\text{MgO}}$ direction.

Fig. 4.15 exhibits the EDS mappings acquired from the $(010)_{\text{MgO}}$ facet of a MgO particle in Mg-9Al, where no preferential segregation of Al is found at the MgO/Mg interface. For another $\{111\}$ MgO particle in Mg-9Al alloys (**Figs. 4.16(a-b)**), the corresponding HRTEM image shows monotonous lattice structures from the MgO matrix to the MgO/Mg interface (**Fig. 4.16(c)**). Delocalization effect exists as a general phenomenon caused by spherical aberration for TEM without C_s -corrector, whose feature can be distinguished by the faded contrast at the MgO edge. Without consideration of the delocalization effect, it is reasonable to suggest that there is no difference in the lattice structure on the $\{111\}_{\text{MgO}}$ facet from the MgO matrix. For another $\{111\}$ MgO particle (**Fig. 4.17(a)**), the corresponding C_s -corrected HAADF STEM image in **Fig. 4.17(b)**

shows the uniform contrast of an atomically flat facet. Segregation of trace impurities such as Fe, Mn and Si are less likely to occur at the interface, as these elements with an atomic number higher than that of Mg would be expected to produce brighter contrast in these chemically sensitive HAADF images. Furthermore, the atomic structure of MgO is seen to be unchanged from MgO to the interface when Al is present in the melt. The comparison between the arrangement of atomic columns at the MgO/Mg interface in both CP Mg and Mg-9Al suggest there is no interfacial segregation of solutes in both cases. Combining the chemical and structural information, we can conclude that there is no segregation of Al on the MgO surface in Mg-9Al. Therefore, no interfacial segregation layers can be detected.

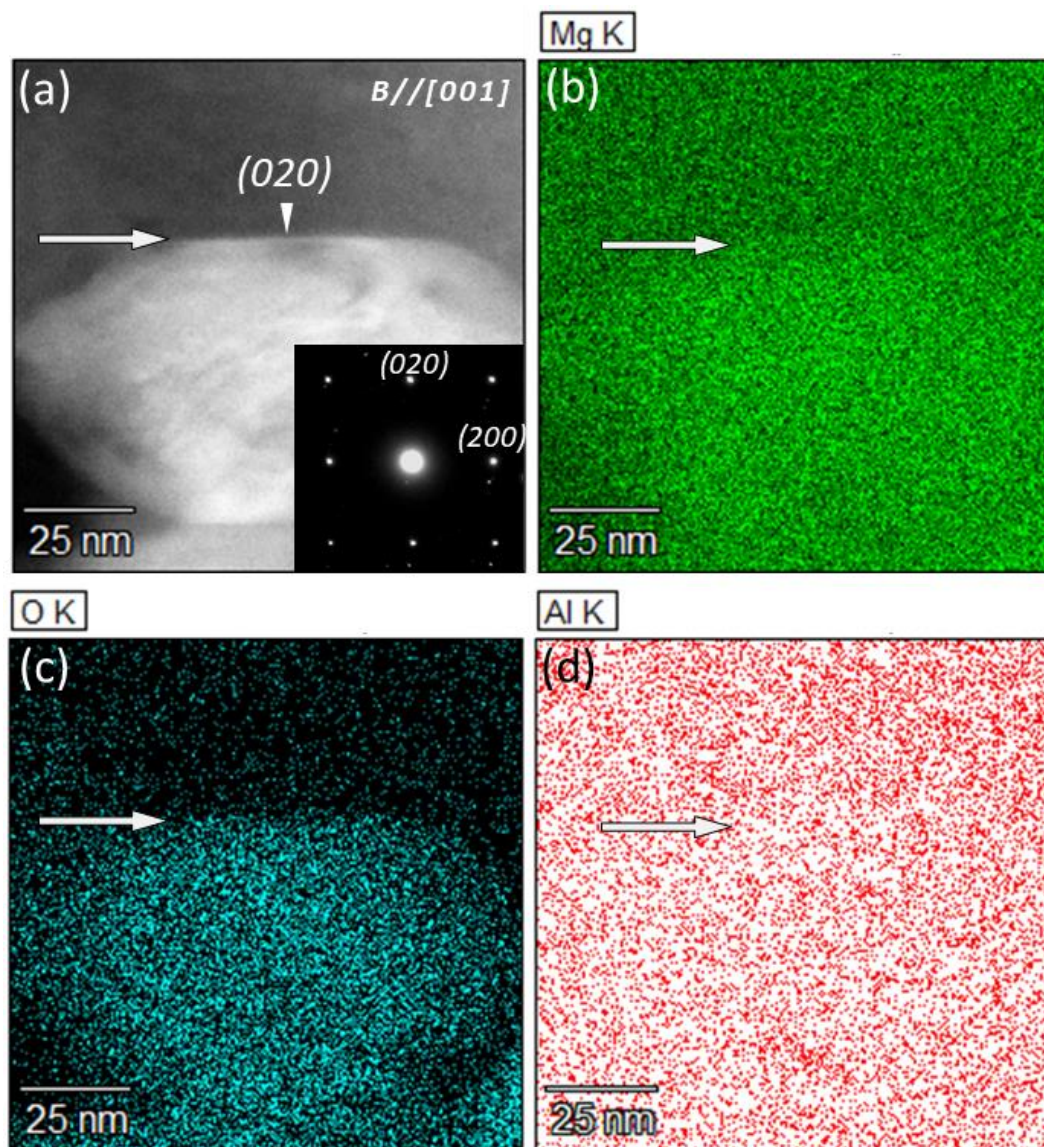


Fig. 4.15 Elemental distribution across the MgO/Mg interface in Mg-9Al alloy. (a) ADF STEM image and the inset of SAED pattern of a MgO particle viewed from its $[001]_{\text{MgO}}$ direction, (b-d) EDS maps of Mg K, O K and Al K. Note that Al adsorption on the interface was not detected.

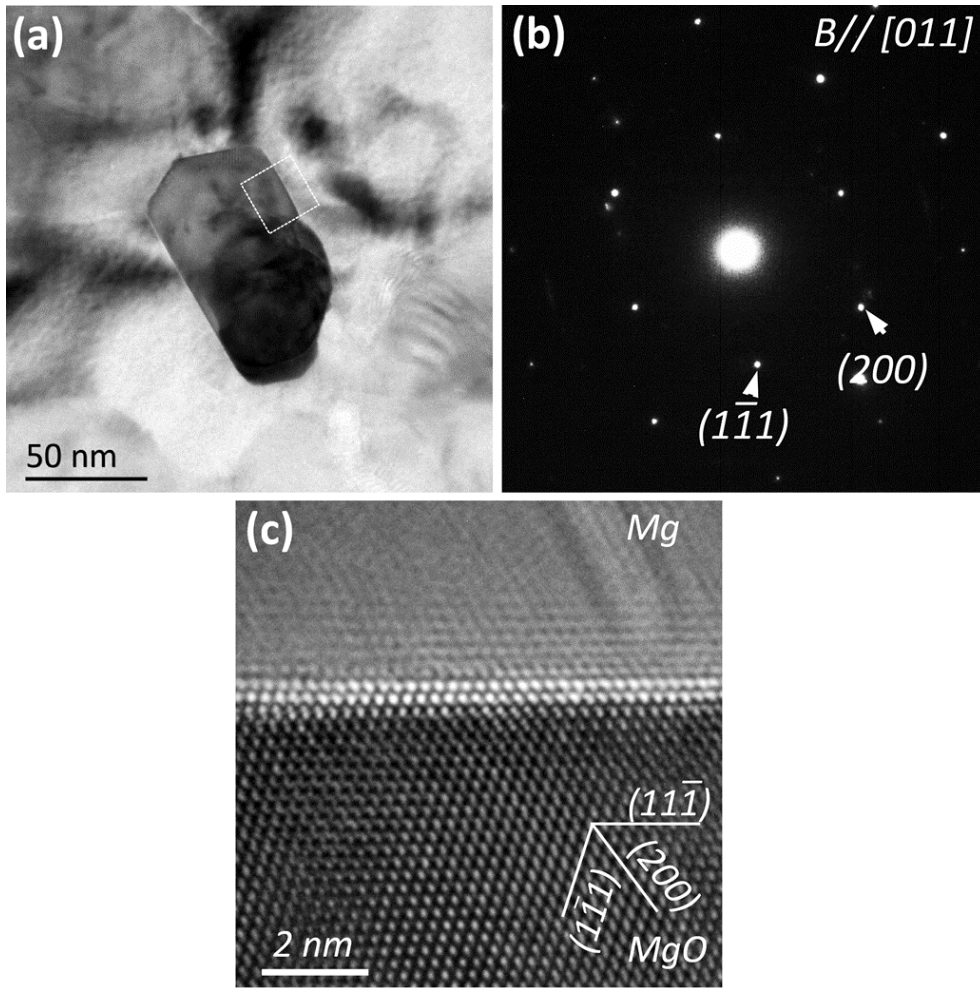


Fig. 4.16 (a) BF TEM image showing an octahedral shaped MgO particle in Mg-9Al with (b) the related diffraction pattern, and (c) the corresponding HRTEM image shows the $\{111\}_{\text{MgO}}$ truncated surface of MgO. The incident beam is parallel to $[011]_{\text{MgO}}$ direction.

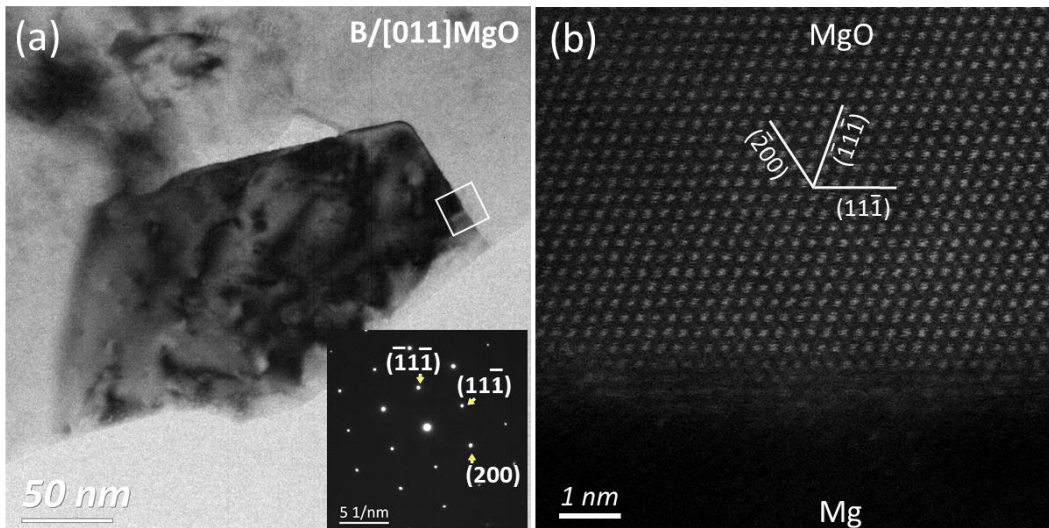


Fig. 4.17 (a) BF TEM of a $\{111\}$ MgO particle in Mg-9Al and (b) the corresponding HAADF STEM image acquired across the MgO/Mg interface marked by white cube in (a). The insets in (a) is the corresponding SAED patterns. The incident beam is parallel to $[011]_{\text{MgO}}$ direction.

4.2.6 Origin of {111} MgO and {100} MgO

CP Mg melt was steadily solidified in a steel crucible to make a minimal disturbance to the melt, allowing the preservation of the natural characteristics of oxides on the melt surface. **Fig. 4.18** compares the morphology of samples collected from two positions: one from the crucible wall and the other from the nodules (a typical feature of local ignition) on the melt surface. It is found that both the collected samples are composed of cubic particles, with the EDS result in **Figs. 4.18(c-d)** suggesting they are MgO crystals. Besides, it is worth noting that no {111} MgO being detected together with {100} MgO in the two samples. In addition, aluminium nitride (AlN) was frequently found to be associated with the {100} MgO particles in Mg-9Al sample. As shown in **Figs. 4.19(a-b)**, lath-like particles are seen among the cubic MgO particles. The composition analyses in **Fig. 4.19(c)** indicate that these phases are rich in Al and N. **Fig. 4.20** shows the preparation of TEM lamella prepared by FIB and the further TEM characterisation of the AlN particles in the area. **Figs. 4.20(c-d)** show the BF TEM image of an AlN particle, along with the SAED pattern acquired from its $[10\bar{1}0]$ zone axis. The phase identification is consolidated by the EDS mapping over the AlN particles (**Fig. 4.20(e)**). Besides, the spatial association of AlN and cubic MgO (**Figs. 4.19(b)** and **4.20(b)**) indicates that AlN probably nucleates on MgO.

After solidification, most area of the ingot surface is relatively smooth without the nodules. The vertical cross section perpendicular to the surface of the ingot was characterised by SEM/EDS. As presented in **Fig. 4.21(a)**, at some positions, there exist compact oxide films which prevent oxidation from penetrating into the Mg bulk. The composition analysis in **Fig. 4.21(b)** shows that the surface oxide film contains mainly Mg and O, plus a certain amount of F, while the content of O and F decreases quickly towards the Mg matrix. In contrast, some regions on the surface experienced severer oxidation than the other areas. **Fig. 4.21(c)** shows the curved oxide films on the surface containing some cracks, which provide fast diffusion paths for mass transport of both oxygen and Mg. The oxidation was therefore promoted as evidenced by the appearance of numbers of MgO particles underneath the non-protective oxide film. According to the results in **section 4.2.3.1**, their polyhedral profile of the particles is the projection of their octahedral shape in 2D. Also, it is found that all these MgO particles are in the shape of octahedron, and no cubic MgO particles were observed.

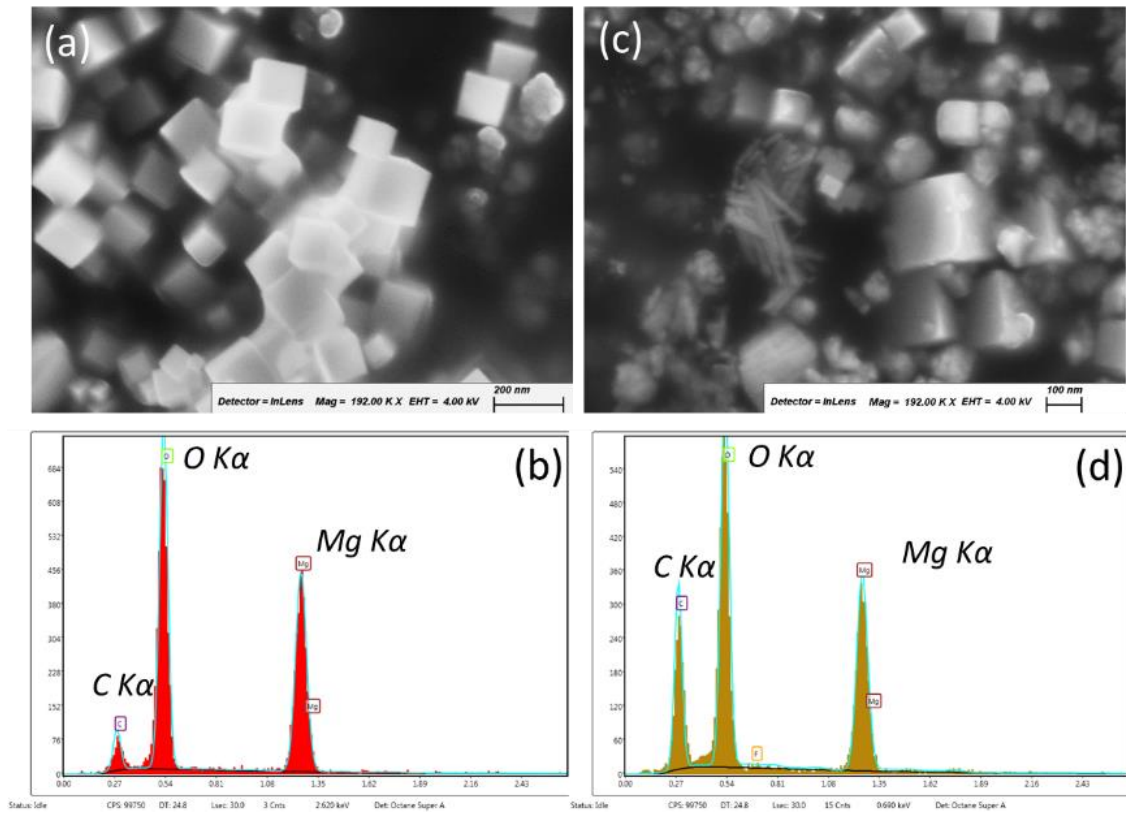


Fig. 4.18 (a, c) SEM images and (b, d) the related EDS spectra showing the cubic MgO particles of burning products collected from (a, b) the crucible wall and (c, d) the nodule positions at the solidified melt surface.

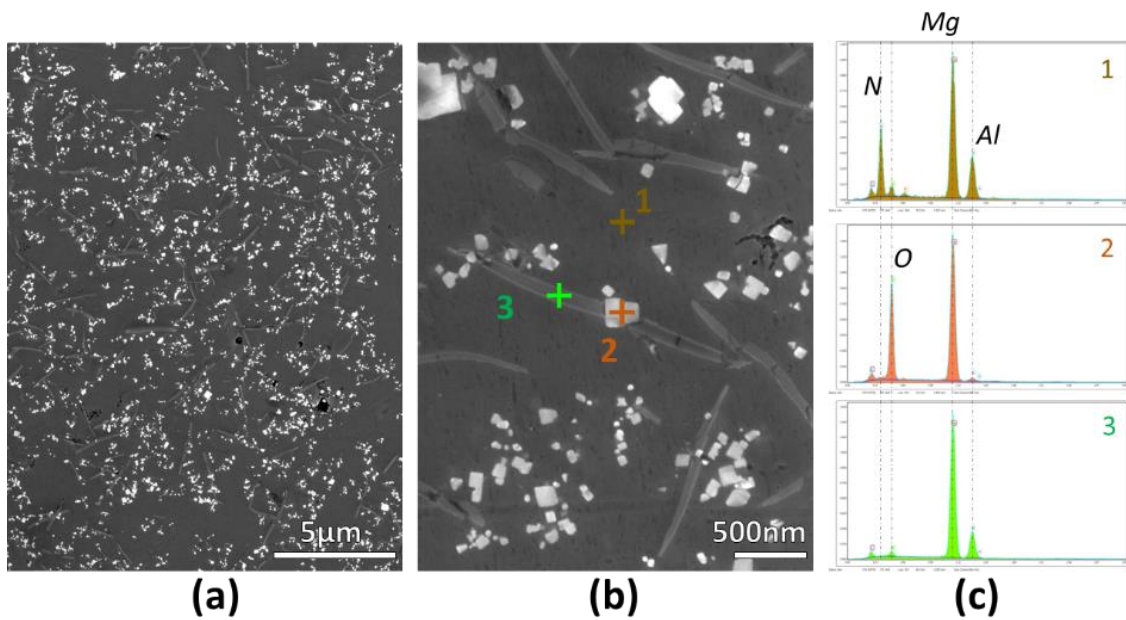


Fig. 4.19 SE SEM images and the corresponding EDS results showing the appearance of AlN phases associated with {100} MgO particles in Mg-9Al.

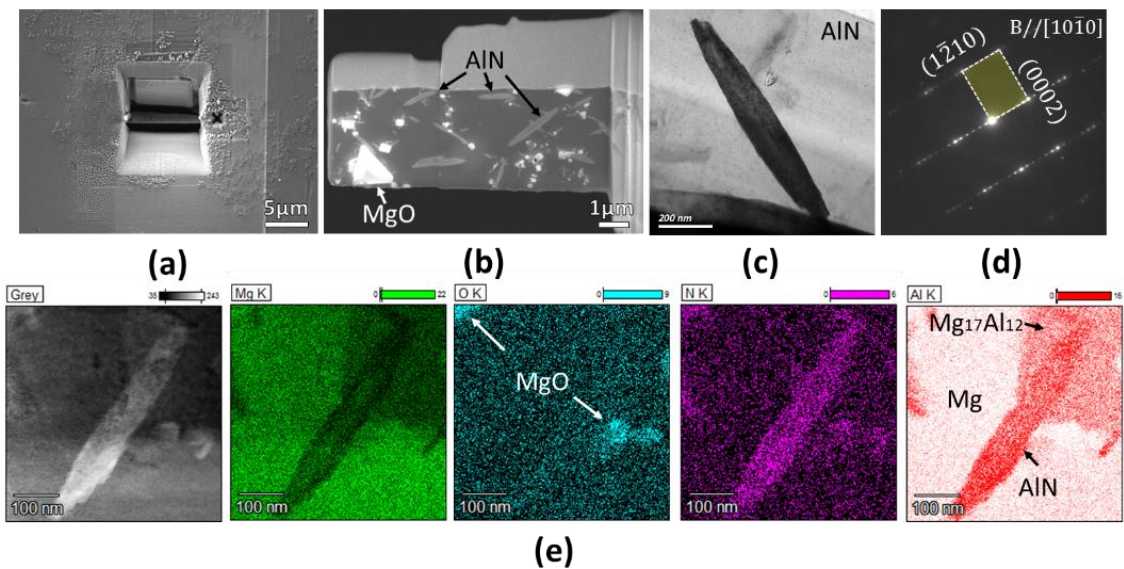


Fig. 4.20 The identification of AlN in Mg-9Al-prefil by application of FIB and TEM. (a, b) SE SEM images showing the (a) cutting position and (b) lift-out lamella; (c) BF TEM image and (d) the corresponding SAED pattern; and (e) the EDS maps showing the elemental distribution of Mg (green), O (cyan), N (purple) and Al (red).

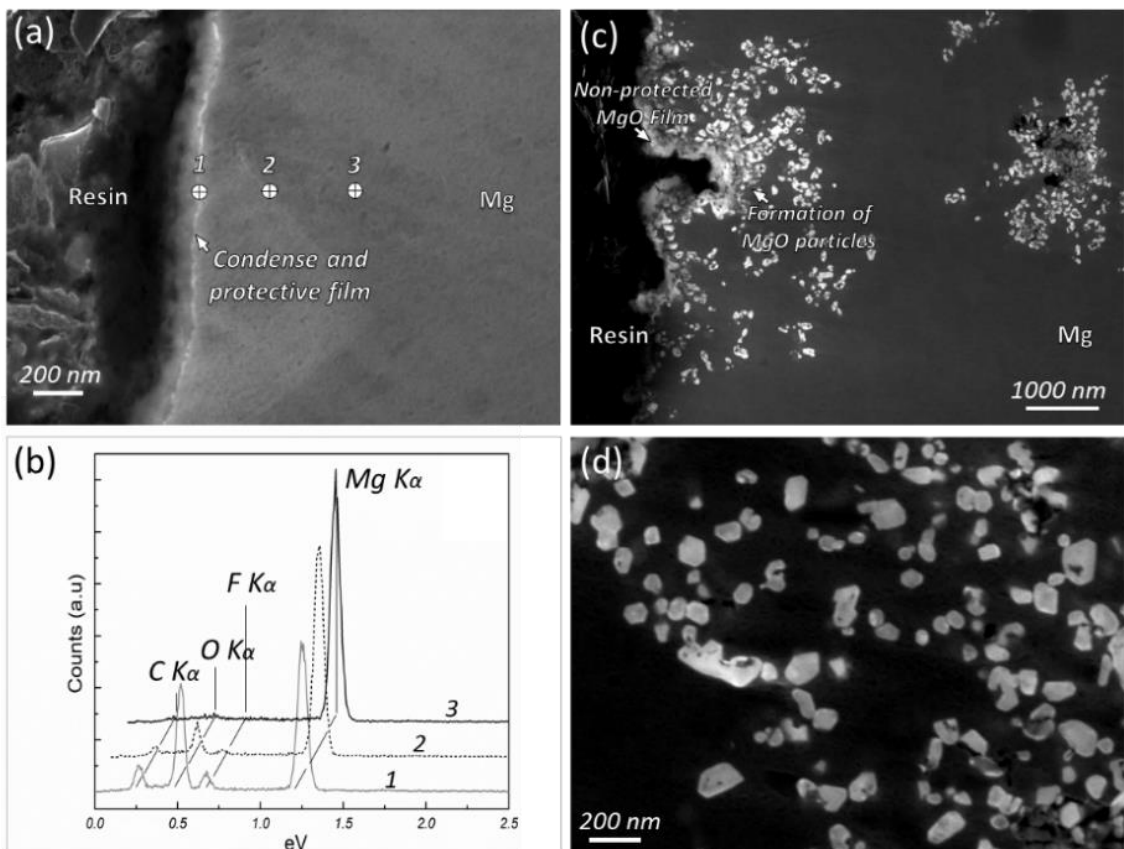


Fig. 4.21 SE SEM images and EDS spectra showing the morphology of MgO film/particles formed on the surface of CP Mg ingot. (a) a compact MgO film on the surface, (b) the EDS signals taken at point 1, 2, 3 in (a); (c) a cracked MgO film and the MgO particles formed beneath; and (d) exaggerated SEM image illustrates that the oxides are in octahedral shape only.

4.3 Discussion

The wide application of Mg alloys has been impeded by the issue of oxide films, from the foundry to practice serving, among which the bifilm has been identified as defects leading to the deterioration of the material's mechanical properties [145,146,150]. Effort has been made to uncover the mechanism underlying Mg oxidation and to develop techniques to purify the alloy melt. From a different angle, the research in this thesis focuses on the utilisation of native oxides in Mg alloys for grain refinement. This makes the revelation of the microstructures of MgO at hierarchical scales (*i.e.*, from micron scale to nanoscale) very important.

4.3.1 Formation of oxide films/particles in Mg alloys

The collected oxide films by melt filtration include both original oxides in the ingot and newly formed oxide films during melt handling and casting. All the three types of oxide: young film, old film and ingot skin, consist of densely populated MgO particle (**Figs. 4.1** and **4.2**). Since the solubility of O in the Mg melt is negligibly small, the MgO particles inside the melt can hardly grow. The chemical reactions to form MgO is likely to occur at the melt/air interface or in the air (react in vapour phases). These can be verified by the investigation of MgO origins shown in **Figs. 4.18** and **4.21**. If not being entrapped into the melt, the oxide film on the surface will proceed into an old film with coarser particle size on the side contacting the air as the oxidation time increases. As shown in **Fig. 4.21**, the thickness of the oxide film on the surface stays in a transition stage; it would grow with oxidation time and finally turn into the old film which has coarser particle sizes in one side (in **Fig. 4.2**). The mechanism behind the formation of oxide films is proposed as schematically portrayed in **Fig. 4.22**. Oxidation of Mg melt instantly happens when it is exposed to the air, which forms a thin liquid oxide film containing discrete MgO solid particles (**Figs. 4.22(a-b)**). This film can be easily folded and entrapped into the melt by any external or internal forces, after which the fresh melt exposes to air again (**Fig. 4.22(c)**). The folding of young film and tangling between films are continued, leading to the agglomeration of oxide films in micron scales. Finally, new fresh oxide film forms again on the melt surface, and the circulation starts again (**Fig. 4.22(d)**). When the fresh film on the melt surface is allowed to grow for a long period of time, it eventually becomes an old film, appearing as a curved feature since folding becomes difficult.

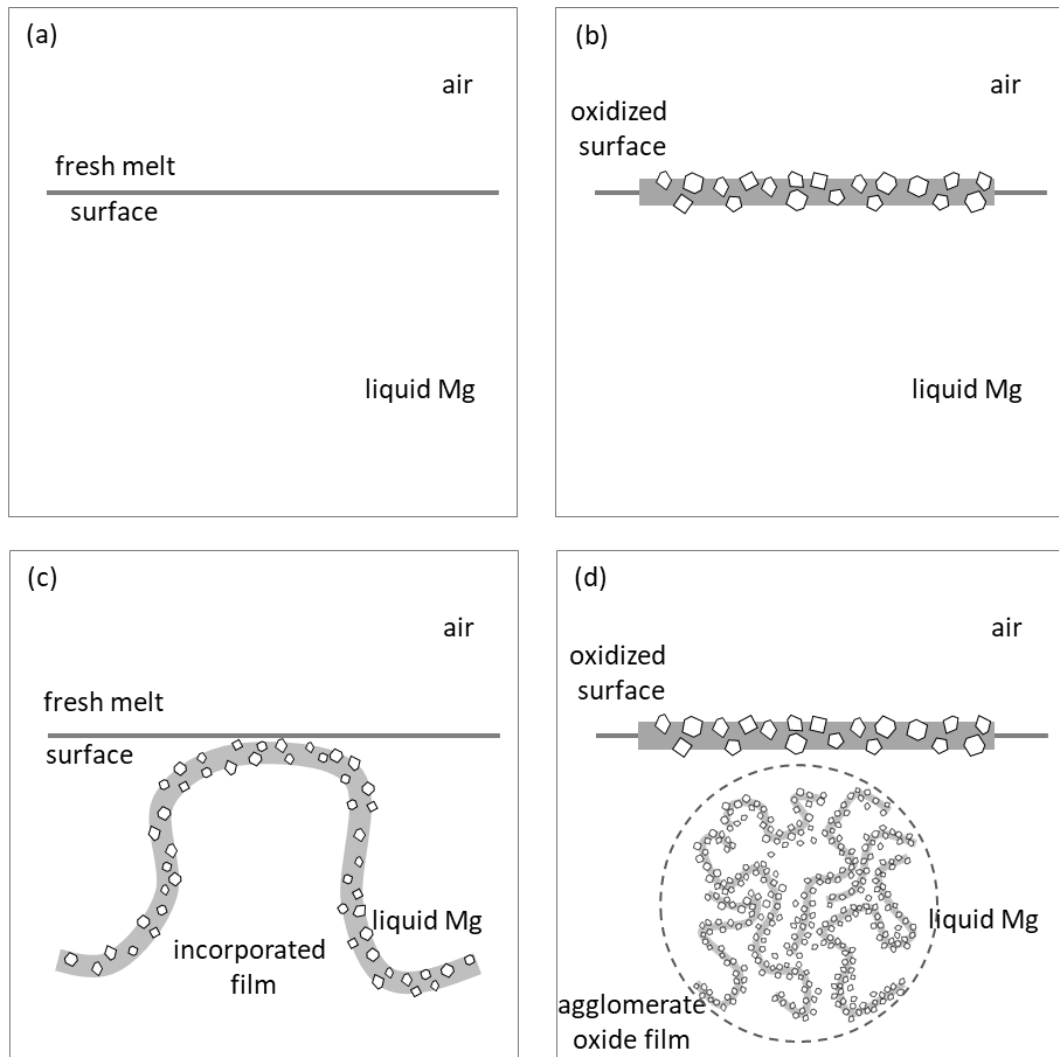


Fig. 4.22 Schematics showing the oxidation and formation of the oxide agglomerates in the melt of Mg alloys during the casting process.

The ingot skin is usually of a straight segment (Figs. 4.1 and 4.2(c, f)), indicating that this type of film is difficult to be folded during casting, in other words, it has enough thickness to overcome the folding forces. Besides, the number density of this film type is relatively small since they are rarely detected during SEM/TEM experiments. It is believed that this type of film comes from long-term solid-state oxidation at the surface of the original Mg ingot, at ambient temperature or during heating in the furnace before melting.

4.3.2 Formation mechanism of {100} MgO

In this study, {100} MgO particles have been observed both in CP Mg and Mg-9Al. This observation shows a difference from the previous studies in which the cubic MgO particles were not found in AZ91D. It was claimed that the {111}_{MgO} terminations of MgO (facets of octahedral MgO) are probably more stable than the {100}_{MgO} due to the

Al and/or Zn segregation on MgO surface [140]. Decrease of interfacial energy induced by elemental segregation was proposed probably behind the mechanism of morphology variation.

In the literature, there is extensive experimental evidence supporting the thermodynamic stability of cubic MgO particles with {100} terminations [168–170]. Experimentally, combustion is one of the easiest ways to prepare MgO nanocubes. The burning product of Mg strip was characterised to be cubic in the 1940s [168]. It was consistent with the theoretical calculation of the Madelung potential and density functional theory (DFT) results, whereby the surface state for the {100} plane of MgO was found to be the most stable amongst all lattice planes [169,170]. Given the calculated surface energies, Wulff's reconstruction theory [166] indicates a thermodynamic equilibrium shape of MgO terminated by its {100} planes. It was verified by the experimental results where the relatively unstable {011} and {111} facets turned into the most stable {001} facets when annealed by electron bombardment [174]. In addition, MgO crystal favours to be cubic shape in terms of crystallography, since the rock salt structure of MgO has the close packed plane of {100} which should be the preferential termination plane.

Besides thermodynamics, kinetics factor should be considered as a factor determining the crystal shape. During combustion of Mg, the self-sustaining severe oxidation can proceed to be a thermodynamics-controlled process, where the high temperature and the reservoir of Mg and O vapours ensure that the rate of atomic/molecule attachment will not be a limiting factor at all. It explains why the chemical vapour synthesis produces cubic MgO crystals. Such a mechanism seems to be followed by the formation of cubic MgO in this study as well. During the casting of Mg and Mg-9Al alloy in this work, local burning occasionally occurs, similar to the combustion of Mg. The molten Mg above the liquidus has the following characteristics: *i*) a high affinity with oxygen, *ii*) a high vapour pressure; and *iii*) the absence of protective oxide film. At the positions with these features: the crucible wall and ignition nodules [143], the MgO particles were detected having a perfect cubic shape (**Fig. 4.18**). Their similar size to those MgO inside the melt (**Figs. 4.3** and **4.4**) indicates the same origin for all the {100} MgO particles.

In addition, the powder product from the oxidation of Mg vapour above the melt can involve some unreacted N₂ into the melt, making the formation of AlN possible by the reaction between Al solute and N₂ inside the melt. The frequent observation of AlN

particles associated with {100} MgO (**Figs. 4.19** and **4.20**) indirectly support the formation origin of {100} MgO above the melt.

One interesting phenomenon is that there is no {111} MgO ever being observed among the {100} MgO particles collected from the nodules and the crucible wall, which strongly suggests the different formation mechanisms from each other.

The formation mechanism for cubic MgO described above is also valid in the case of Mg-9Al alloy, where local ignition and burning are inevitable during casting. However, due to the enhanced resistance of Mg against evaporation after Al addition, the tendency to burning is significantly decreased. As a result, the number density of the cubic MgO particles in Mg-9Al alloy would be lower compared with those in CP-Mg. This mechanism explains why the cubic MgO particles have not been reported previously in AZ91D, and why no octahedral MgO particles have been reported in CP Mg.

4.3.3 Formation mechanism of {111} MgO

MgO in the shape of octahedron has been validated by 3D morphology (**Fig. 4.8**) and high resolution TEM lattice images (**Fig. 4.9**), with the particles showing their main facets truncated by {111} crystal planes. This type of MgO was observed by Wang *et al* in AZ91D alloy [139]. It was realised that the {111} faceting of MgO in AZ91D alloy, instead of {100} faceting, is due to the reduction of interfacial energy through adsorption of Al and /or Zn onto their {111} surfaces [140]. The interfacial energy of a crystal is modifiable in terms of thermodynamics, such as surface facet tailoring through a surface-regulating agent, as reviewed in detail recently by Zhang *et al* [167]. However, the EDS result in the present work rules out the possibility of Al segregation at the MgO/Mg interface (**Fig. 4.15**). Besides, the HRTEM imaging shows a sole lattice structure across the MgO/Mg interface (**Figs. 4.16** and **4.17**), indicating no other segregation phases formed at the interface. Thus the formation of {111} MgO is apparently independent upon the presence of Al alloying element, which is also indirectly evidenced by the appearance of octahedral {111} MgO in CP-Mg (see **Figs. 4.3** and **4.21**).

The formation mechanism for {111} MgO is different from that for {100} MgO since the two types of MgO were not observed at the same position (see **Figs. 4.18** and **4.21**). The sole appearance of {111} MgO on the melt surface (**Fig. 4.21**) indicates that it is more energetically favourable than that of {100} MgO. However, this contradicts with the fact that {111} facet is less stable than {100} facet due to the charging polarity in a dry

environment [210]. There should exist some factors modifying the surface energy. It has been reported that the alteration of the surface energy of a crystal is achievable through various methods [167,171,172,211]. For instance, hydroxylation has been proposed as one of the means to stabilise the polar {111} facet into a non-polar state, which achieves the lowering of surface energy [171,211]. In this case, since {111} MgO is also found in CP Mg and in Mg-9Al given the absence of Al segregation on any facets, and the adsorption or segregation of alloying elements should be excluded as the reason for the depolarization of {111} facet. It is speculated that the Mg melt, which has a good wetting behaviour on the octahedral MgO particles, might play a role in switching MgO into an octahedral morphology in a nonpolar manner. This conjecture agrees with the theory of metal screening, which is an effective way of polarity compensation for 2D MgO nanoribbons [180]. In a recent work Fang *et al* applied *ab initio* MD to study the atomic configuration of MgO substrate attaching liquid Mg, they showed that both the O-terminated {111} plane and the Mg-terminated {111} plane eventually evolve into a similar equilibrium state: a terminating surface layer that has a hexagonal atomic arrangement as {111} MgO plane containing a certain amount of vacancies for charge balance [31].

It is obvious that the temperature at the place of {111} MgO formation is lower than at the position with ignition, leading to smaller diffusion coefficients of O²⁻ ions. Also, the obstacle of oxide film on the melt surface also contributes to a shortage of oxygen. In consideration of the crystallographic structure of MgO crystal, the growth kinetics is likely to affect the morphology of MgO. Specifically, the stacking sequence for either {111} 'Mg' planes 'O' planes is '...ABCABC...', with 'Mg' planes and 'O' planes stack alternatively onto each other. In contrast, each {100} facet is uniformly composed of Mg cations and O anions in the ratio of 1:1. As treated one {100} plane as 'A', then the next one stacks above it shifting $\frac{1}{2}[001]$ displacement can be treated as 'B'. The next plane goes back to 'A' again, giving a stacking sequence of '...ABAB...'. If the shortage in oxygen acts as a limiting factor, the growth of {100} planes of MgO crystal should be preferential because {100} planes require fewer oxygen atoms than {111} planes. As a result, the growth along the <100> direction becomes faster than along the <111> direction. With growth continues, there appears the gradual disappearance of {100} facets and the predominance of {111} facets. Inversely, for the {100} MgO, a higher diffusion rate and abundant oxygen source make the growth rate independent of crystal direction, so that the shape of MgO is fully determined by equilibrium thermodynamics.

The overall relatively low growth kinetics for {111} MgO may account for the smaller size compared to {100} MgO, as verified by the statistics results in **Fig. 4.12**. It is also possible that some {100} terminations are retained if the growth is insufficient. As evidenced by the results in **Figs. 4.9** and **4.10**, the {100} terminations are observed while they gradually shrink as the particle size increases. If the growth of a MgO crystal is allowed to proceed long enough, ultimately the {100} facet will disappear. However, the reality is that most of the native MgO particles found in the melt experience insufficient growth beforehand, so that {100} facets are generally observed. Ripening of MgO particles may also be possible as there is a limited solubility O in the liquid Mg suggested by a recent thermodynamic study of Mg-O binary phase diagram [131]. Nevertheless, the dynamic process would be sluggish due to the diffusivity of O in Mg melts.

4.3.4 Effect of MgO on heterogeneous nucleation and grain refinement

4.3.4.1 Potency for nucleation

Nucleation potency of a substrate is affected by many factors, including lattice misfit [34], substrate surface roughness [46] and chemical interaction between the substrate and the melt [45], *etc.* In the absence of information of the latter two factors, lattice misfit is usually used as an indicator to assess the potency. The smaller the lattice misfit at the interface, the more potent the substrate for heterogeneous nucleation usually is. Chemical inoculation is the most practical method to refine the as-cast microstructure of metallic materials. The criterion of lattice matching has led to some successes in searching for grain refiners for Mg alloys. For instance, Zr-containing master alloy for the Al-free Mg alloys [26,88,89], and some carbides, oxides and nitrides for Al-bearing Mg alloys [72,74,117–119]. In the current case of MgO particles, it is essential to analysis their capacity on heterogeneous nucleation of Mg in terms of lattice misfit.

The terminating facets of octahedral and cube MgO available for heterogeneous nucleation are {111} and {100} planes. Experimental observation has confirmed the following orientation relationships (ORs) between MgO and Mg:

OR1: $(111)[01\bar{1}]_{\text{MgO}} // (0002)[1\bar{1}\bar{2}]_{\text{Mg}}$ (**Fig. 4.23**);

OR2: $(200)[0\bar{1}\bar{1}]_{\text{MgO}} // (1\bar{1}02)[1\bar{1}0\bar{1}]_{\text{Mg}}$ (**Fig. 4.24**).

According to these ORs, the lattice misfit (f) between the solid (S) and the nucleating substrate (N) and can be calculated using the equation below [34]:

$$f = \frac{d_S - d_N}{d_S} \times 100\% \quad \text{Eq. 4-2}$$

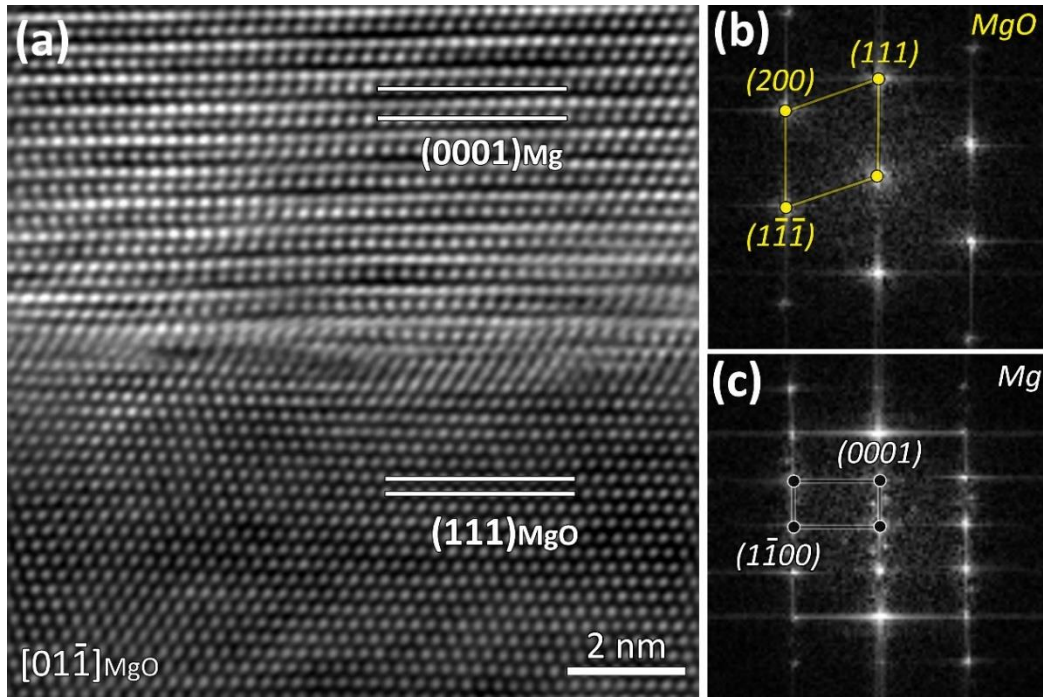


Fig. 4.23 HRTEM images showing the orientation relationship between $\{100\}$ MgO and α -Mg, which is $(111)[01\bar{1}]_{\text{MgO}} // (0002)[11\bar{2}0]_{\text{Mg}}$.

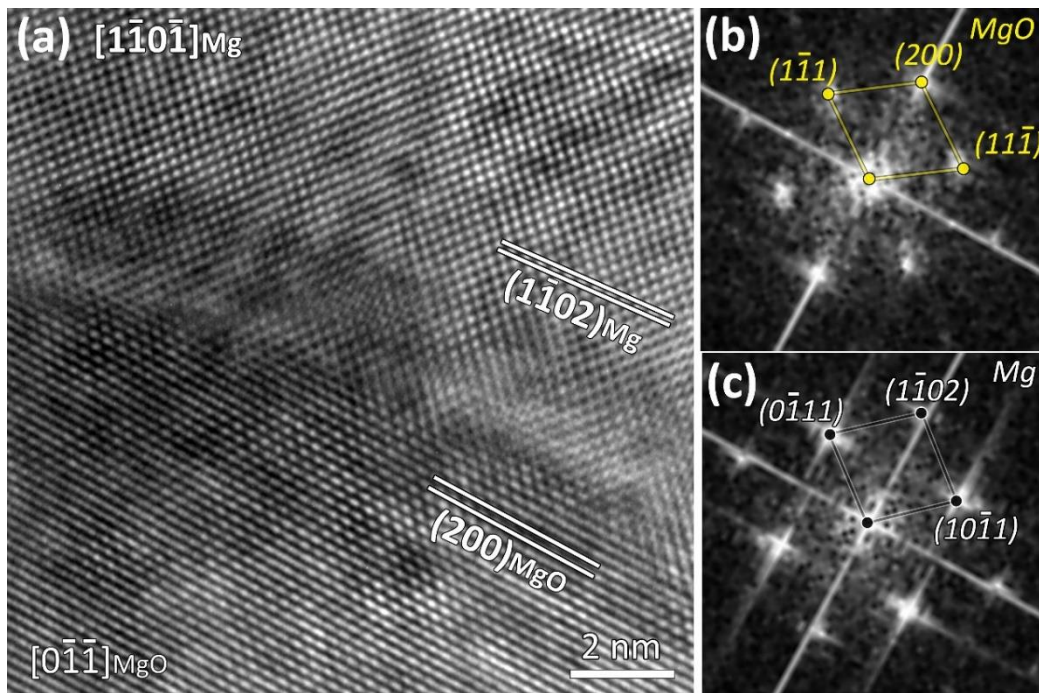


Fig. 4.24 HRTEM images showing the orientation relationship between $\{100\}$ MgO and α -Mg, which is : $(200)[0\bar{1}\bar{1}]_{\text{MgO}} // (\bar{1}102)[1\bar{1}0\bar{1}]_{\text{Mg}}$.

Table 4-3 Crystallographic data of Mg [212], MgO [141] and Zr [213] and the calculated lattice misfit based on the observed and reported ORs at 650°C. S = solid (Mg), N = nucleating substrate.

| Interface, N/S | Lattice parameter (Å) at 650°C | ORs: (h'k'l')[u'v'w'] _N // (hkl)[uvw] _S | d _[u'v'w'] (Å) | d _[uvw] (Å) | f (%) |
|----------------|--|--|----------------------------|----------------------------|-------|
| MgO/Mg | N: FCC, a=4.2476 S: HCP, a=3.2599, c=5.3001 | (111)[011] _{MgO} // (0002)[11 $\bar{2}$ 0] _{Mg} | <011> 3.0036 | <11 $\bar{2}$ 0> 3.2599 | 7.86 |
| | | (100)[01 $\bar{1}$] _{MgO} // ($\bar{1}$ 102)[1 $\bar{1}$ 0 $\bar{1}$] _{Mg} , as equivalent to (100)[011] _{MgO} // ($\bar{1}$ 102)[11 $\bar{2}$ 0] _{Mg} | <011> 3.0036 | <11 $\bar{2}$ 0> 3.2599 | 7.86 |
| Zr/Mg | N: HCP, a=3.2435, c=5.1838 S: HCP, a=3.2599, c=5.3001 | (0002)[11 $\bar{2}$ 0] _{Zr} // (0002)[11 $\bar{2}$ 0] _{Mg} [182] | <11 $\bar{2}$ 0> 3.2435 | <11 $\bar{2}$ 0> 3.2599 | 0.50 |

Note that the lattice parameter for each phase at room temperature (20°C) is: Mg, a=3.2092, c=5.2121; MgO, a=4.2113; Zr, a=3.233, c=5.148. while the coefficient of thermal expansion (1/K) is: Mg: //a 25.1×10⁻⁶, //c 26.8×10⁻⁶ [214], MgO: 13.68×10⁻⁶ [215], Zr: //a 5.15×10⁻⁶, //c 11.03×10⁻⁶ [213].

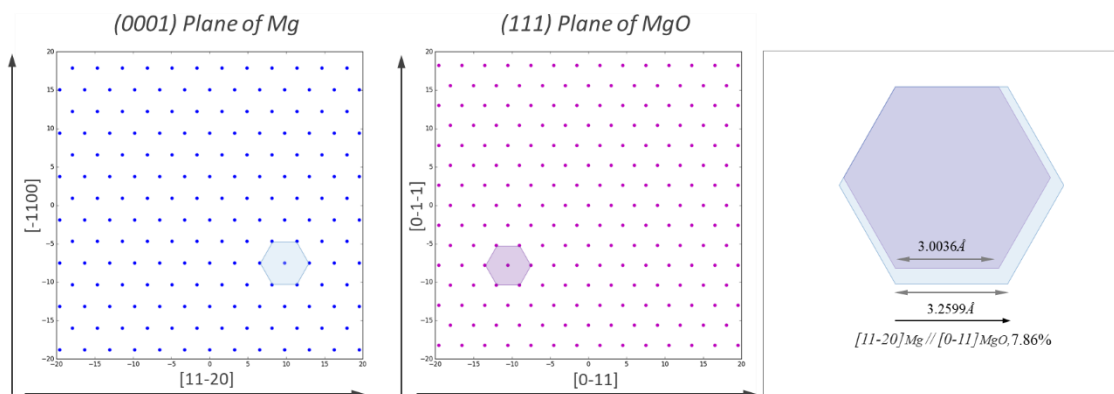


Fig. 4.25 Atomic configurations of the (a) (0001)Mg plane and (b) (111)MgO plane constructed following the orientation relationship as: (111)[01 $\bar{1}$]_{MgO} // (0002)[11 $\bar{2}$ 0]_{Mg}. (c) schematic showing the calculation of misfits.

Where d_S and d_N are the interatomic spacings along the matching directions for the solid and the nucleating substrate, respectively. Based on the crystallographic data and according to the experimentally observed ORs, the lattice misfits were calculated as given in **Table 4-3**, and compared to that for Zr substrate. The schematics in **Figs. 4.25** and **4.26** show the atomic matching of the involved crystal planes, crystal directions and the calculation of the lattice misfit according to the identified OR1 and OR2, respectively. The calculated lattice misfits are 7.86% for {111} MgO and {100} MgO termination along the matching crystal directions. This value is much larger than the misfit (0.5%)

between Zr and α -Mg, apparently indicating that MgO is less potent than Zr to nucleate α -Mg and thus requires larger nucleation undercooling. Besides, recent DFT work by Fang and Fan [31] revealed that the interaction between the O-terminated {111} MgO and liquid Mg gives rise to an ordered Mg layer on the MgO surface, and this ordered Mg layer is atomically rough due to the existence of about 8% of vacancies. The atomically rough surface makes {111} MgO even more impotent for nucleation of Mg [46], leading to a larger nucleation undercooling (ΔT_n). MgO is a relatively impotent substrate with a poor performance on grain refinement according to the lattice matching criterion. Nevertheless, further consideration about the grain initiation process in the Mg melt with dispersed native MgO particles is required to rationalize the experimental observation of grain refinement in AZ91D with HSMC.

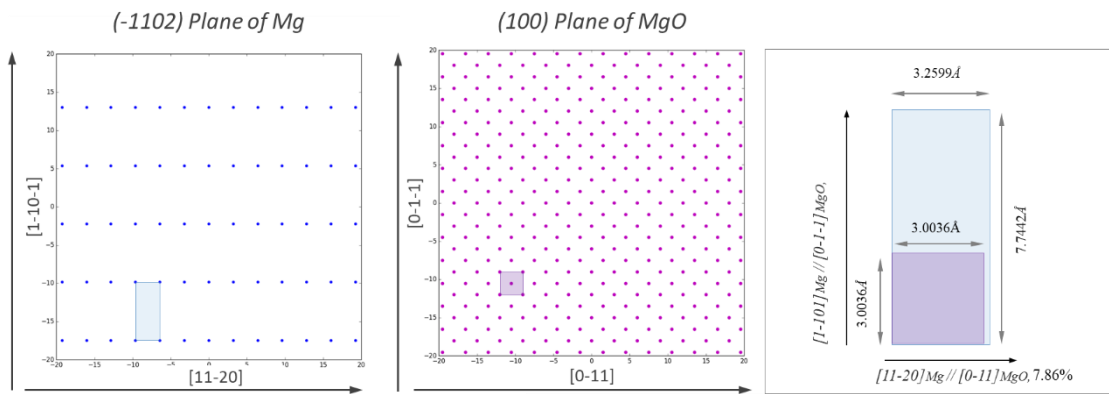


Fig. 4.26 Atomic configurations of (a) $(1-102)$ Mg plane and (b) (100) MgO plane constructed following the orientation relationship as: $(200)[0\bar{1}\bar{1}]_{\text{MgO}} // (1\bar{1}02)[1\bar{1}0\bar{1}]_{\text{Mg}}$. (c) schematic showing the calculation of misfits.

4.3.4.2 Grain refinement by explosive grain initiation (EGI)

Closely related to grain refinement, grain initiation is determined by the free growth undercooling ΔT_{fg} that is a function of substrate size [17]. As exemplified by the potent Zr particles ($(\Delta T_n < T_{fg})$) in Mg melts, initiation of free growth of Mg grain occurs on the largest Zr particle first, then progressively happens on the smaller ones. This behaviour is termed as progressive grain initiation (PGI) [29]. In contrast to the above situation, for impotent substrates ($\Delta T_n > \Delta T_{fg}$ for the largest particle(s)), such as MgO particles, grain initiation may occur in an explosive manner, which is referred to as explosive grain initiation (EGI) [54]. In Mg-alloy melts, MgO particles were found to have a small size (d_0), a narrow size distribution (σ) (**Fig. 4.12**) and a large number density ($\sim 10^{17} \text{cm}^3$) in the melt [164]. In this case ΔT_n is larger than the ΔT_{fg} required by quite a large amount of MgO particles, once the nucleation undercooling is satisfied these MgO particles can

initiate the Mg grains immediately after nucleation. This will lead to a significant proportion of grains being initiated in an "explosive" manner and results in a reduced grain size [28,29]. In practice, it has been confirmed that the well-dispersed native MgO particles can lead to significant grain refinement in Mg alloys [29,134,136,140,182]. The theoretically and practically achievable grain refinement through the explosive grain initiation (EGI) scheme raises the importance of understanding the nature of native MgO in Mg alloys. As validated by CP Mg cast by high pressure die casting, in which native MgO particle is the sole substrate with an estimated number density of $10^{17}/\text{m}^3$, the as-cast microstructure with a grain size of $6\mu\text{m}$ was achieved [29]. This grain size is much smaller than that of Mg-1Ca-1Zr, where the solidification was following the pattern of progressive grain initiation [29]. EGI has higher potential in grain refinement than PGI.

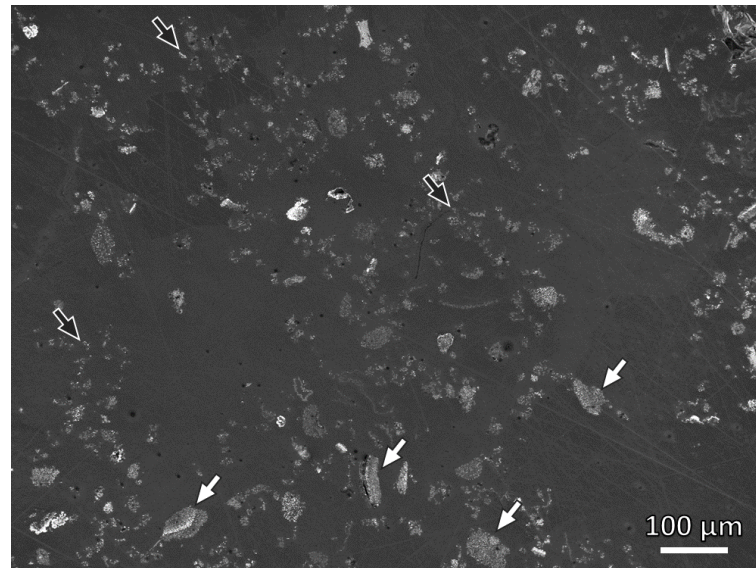


Fig. 4.27 SE SEM micrograph showing the dispersion of the native MgO films/particles after applying high shearing onto the CP Mg ingot concentrated with native MgO films, which is solidified by the left melt inside the crucible after pressurised filtration,

4.3.4.3 Enhanced grain refinement by dispersion of MgO

Usually, the native MgO particles present as oxide film in the Mg alloys melt, typically three types of oxide films as shown in **Fig. 4.2**. The agglomeration of grain refiners has been found as one of the reasons why their efficiency drops to cause a larger grain size after solidification. This has been known as the result of the reduction in the number density of substrates due to agglomeration. The MgO particles that naturally occur as agglomerates of films have an insufficient number density (estimated as $10^{14}/\text{m}^3$ [164]). In the current case, the dispersion of MgO particles by HSMC offers a high number density together with a relatively homogeneous distribution of the particles in the melt. **Fig. 4.27** shows that the original MgO films in the concentrated melt above the filter have

been dispersed by HSMC. Despite some of the oxide films experiencing little changes (marked by white arrows), the MgO films in most areas marked by black arrows have been well dispersed with a diameter much smaller than the oxide films. In comparison to that in **Fig. 4.1**, this result qualitatively shows the dispersion of oxide particles. Though a quantitative assessment cannot be provided, it is clear that both the number density and spatial distribution of the MgO particles can be modified by HSMC. Such dispersion of MgO particles is beneficial for a refined microstructure after solidification, as a high number density of particles will be involved in nucleation and grain initiation in EGI manner.

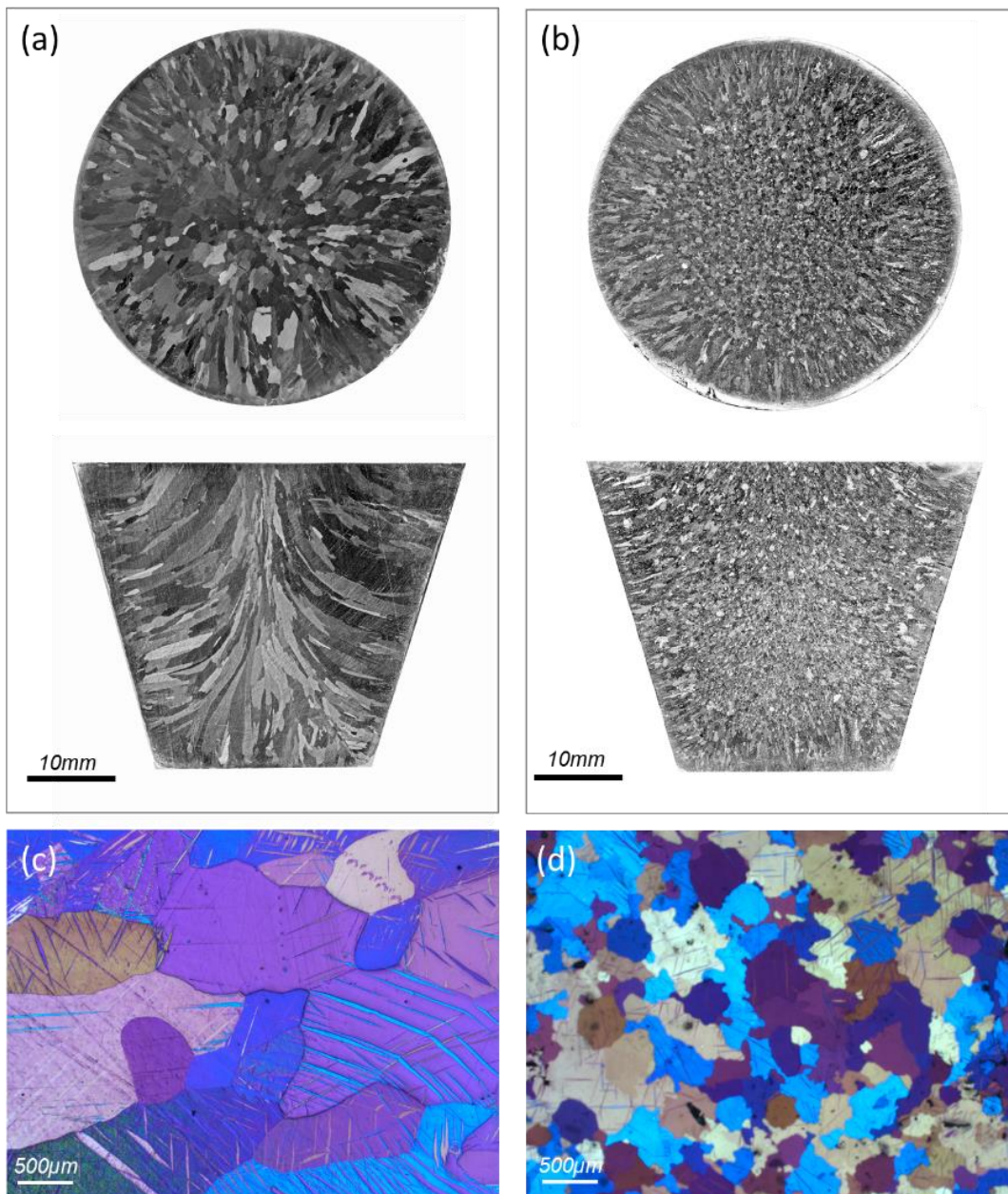


Fig. 4.28 Macro and micro OM micrographs showing the as-cast grain structures of CP Mg (a. d) without, (b. e) with HSMC.

By now, the effect of the native MgO particles on grain refinement has been discussed in two aspects: crystallographic lattice misfit and grain initiation scheme. With small sizes, a narrow distribution spread and a high number density after HSMC, the native MgO particles are beneficial to grain refinement via EGI scheme. As shown in **Fig. 4.28(a)**, a columnar grain structure appears in CP Mg when HSMC is not imposed, having a columnar width of $816.4 \pm 95.9 \mu\text{m}$ (**Fig. 4.28(c)**). With the application of HSMC, the grain structure of CP Mg becomes equiaxed in the central area of the TP-1 sample ($235.4 \pm 18.1 \mu\text{m}$, see **Figs. 4.28(c-d)**). The number density of MgO particles is dramatically increased due to HSMC, and more MgO particles are involved in the EGI process. The absence of solute allows the growth of columnar grains near the wall where columnar to equiaxed transition (CET) is not achieved. At a certain distance from the crucible wall towards the central area, the critical accumulation of impurity solute accounts for the CET.

4.4 Conclusions

1. The oxide films found in both CP Mg and Mg-9Al alloys have distinct characteristics in the macro scale, which can classify them into three types: young film, old film and old skin.
2. The oxide film is initially formed at the surface of the melt, and the oxidation time before they are entrapped into the melt determines whether it is young film or old film. The entrapped young film can be easily tangled with each other forming agglomerates. The old skin was proposed as oxidised at ambient temperature or during the melting procedure. All of the oxide films are made of discrete nanosized MgO particles.
3. Two types of MgO particles can be defined as $\{111\}$ MgO and $\{100\}$ MgO according to their morphology and faceting behaviour. The formation mechanism was proposed as: *i*) $\{100\}$ MgO was formed due to burning or reaction in vapour phases (kinetics is too fast to be controlling factor), leading to the truncation with the most stable $\{100\}$ crystal plane in the thermodynamics point of view; and *ii*) $\{111\}$ MgO was originated on the melt surface, where kinetically $\{111\}$ is more favoured at a relatively lower temperature than burning spot as the $\{111\}$ plane requires fewer oxygen ions than the $\{100\}$ plane, the Mg melt can provide a metal screening effect to stabilise the polar $\{111\}$ plane by reducing the interfacial energy.

4. Lastly, the grain refinement performance of native MgO particles was discussed in different theoretical frameworks, from heterogeneous nucleation to grain initiation. It was found that native MgO with a poor potency can be harnessed for grain refinement following an EGI scheme, which was confirmed by the experimental grain size results of CP Mg with and without HSMC treatment.

5 Interaction between Y and MgO and its effect on solidification of Mg-Y alloys

5.1 Chapter overview

In the last chapter, native MgO in Cp-Mg and Mg-9Al alloy has been verified as a potential substrate for heterogeneous nucleation of α -Mg, being able to offer grain refinement through explosive grain initiation (EGI) scheme during solidification. The nucleating potency of a substrate is a function of many factors, including lattice misfit [34], surface roughness [46] and chemical interaction at the substrate/melt interface [45]. Interaction between substrate and solute in a melt can modify the atomic configuration on the substrate surface, varying its potency and therefore affecting the consequent grain initiation behaviour and ultimately the grain size. To exploit native MgO particles as a possible universal grain refiner for various Mg alloys, it is essential to study the interaction between MgO and solutes. From an industrial perspective, Mg-Y system is the basis for the development of many Mg-Re alloys, which exhibit favourable mechanical properties like strength and creep resistance at elevated temperatures [216–218]. Commercial Mg-Re alloys, such as WE 43 and WE 54, have found widespread applications in the automotive industry. To achieve a refined grain size, 0.4 to 1 wt.% Zr is commonly added as grain refiners to the WE alloy series [23,218,219]. A sizeable reduction in cost will be achieved if the Zr addition is substituted by cheaper alternatives, such as the native MgO particles. From a scientific point of view, the interaction between native MgO particle and Y solute would be possible when there is a stronger affinity between Y-O and Mg-O. Yttria (Y_2O_3) is thermodynamically more stable than MgO when the Y content is higher than a critical value in the Mg-Y-O system [220]. A study of the possible interaction between Y and MgO and its effect on heterogeneous nucleation and grain refinement is therefore essential.

In this chapter, the experimental results of Y segregation at the MgO/Mg interfaces are presented, with the Y segregation giving rise to the formation of Y_2O_3 2D compound (2DC) on the $\{111\}_{MgO}$ facet, and the presence of substitutional Y atoms for partial Mg atoms in the $\{100\}_{MgO}$ terminated plane. Owing to a smaller lattice misfit (1.71%) between the Y_2O_3 2DC and Mg than that (7.86%) between MgO and Mg, as well as the attractive chemical interaction (negative heat of mixing) between Y and Mg atoms, this 2D segregation layer is suggested to enhance the potency of the $\{111\}_{MgO}$ substrate for

heterogeneous nucleation of α -Mg. In addition, Y segregation is shown to promote the dispersal of the native MgO particles during HSMC, so that more particles are available for the grain initiation process to refine the as-cast grain size of Mg-0.1/0.5Y-HSMC alloys. As the Y content or HSMC time increases, however, the interaction between MgO and Y solute leads to the formation of large bulk Y_2O_3 particles, resulting in a competition in grain initiation between the Y_2O_3 particles and the MgO particles with Y_2O_3 2DC modification. The small proportion of the large Y_2O_3 particles dominate the grain initiation process, resulting in a coarse and columnar grain structure. This work emphasizes the importance of changes in the nucleation particles, which can essentially affect subsequent solidification behaviour.

5.2 Results

5.2.1 Effect of Y addition on grain size

Fig. 5.1 illustrates the as-cast macrostructures of CP Mg, Mg-0.1Y, and Mg-0.5Y solidified in a TP-1 mould. Although equiaxed grain structures are observed on the transverse sections after Y addition (**Figs. 5.1 (a, c, e)**), columnar grains are clearly seen in the longitudinal sections of the TP-1 ingots. As the Y content increases, the grain structure is refined, and the area of columnar grains reduces. The grain structure significantly changed after HSMC was applied prior to casting. As shown in **Figs. 5.2(a-b)**, the grain size of CP Mg-HSMC is greatly refined, with fine columnar grains presenting near the mould wall and columnar-to-equiaxed transition (CET) occurring in the central position. Addition of 0.1Y offered further positive effects on the CET and grain refinement, where small equiaxed grains distributed throughout the section of the sample (**Figs. 5.2(c-d)**). The grain structure is almost invariant with a higher Y addition (Mg-0.5Y-HSMC), as shown in **Figs. 5.2(e, f)**.

Quantitative measurement of the grain size was carried out by optical micrography in polarized mode (**Fig. 5.3**). Without HSMC, the addition of Y slightly reduces the average columnar width (ACW) compared to CP Mg ($816.4 \pm 95.9 \mu\text{m}$), being $792.5 \pm 179.4 \mu\text{m}$ in Mg-0.1Y and $718.6 \pm 225.9 \mu\text{m}$ in Mg-0.5Y, respectively. With HSMC imposed, the average grain size (AGS) in CP Mg-HSMC was measured as $235.4 \pm 18.1 \mu\text{m}$, and it decreases to $105.5 \pm 4.3 \mu\text{m}$ when 0.1Y was added. More Y addition up to 0.5% has little effect on the grain size of the HSMC treated samples.

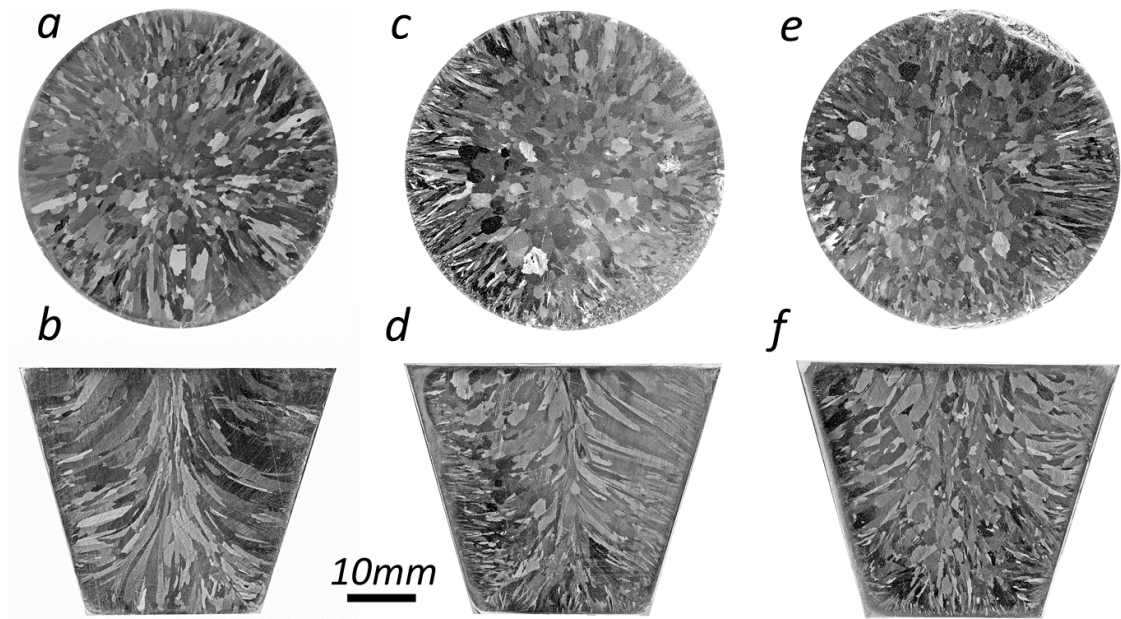


Fig. 5.1 Optical macrographs showing the grain structures on transverse and longitudinal sections of (a, b) CP Mg, (c, d) Mg-0.1Y and (e, f) Mg-0.5Y samples cast by TP-1 process without HSMC.

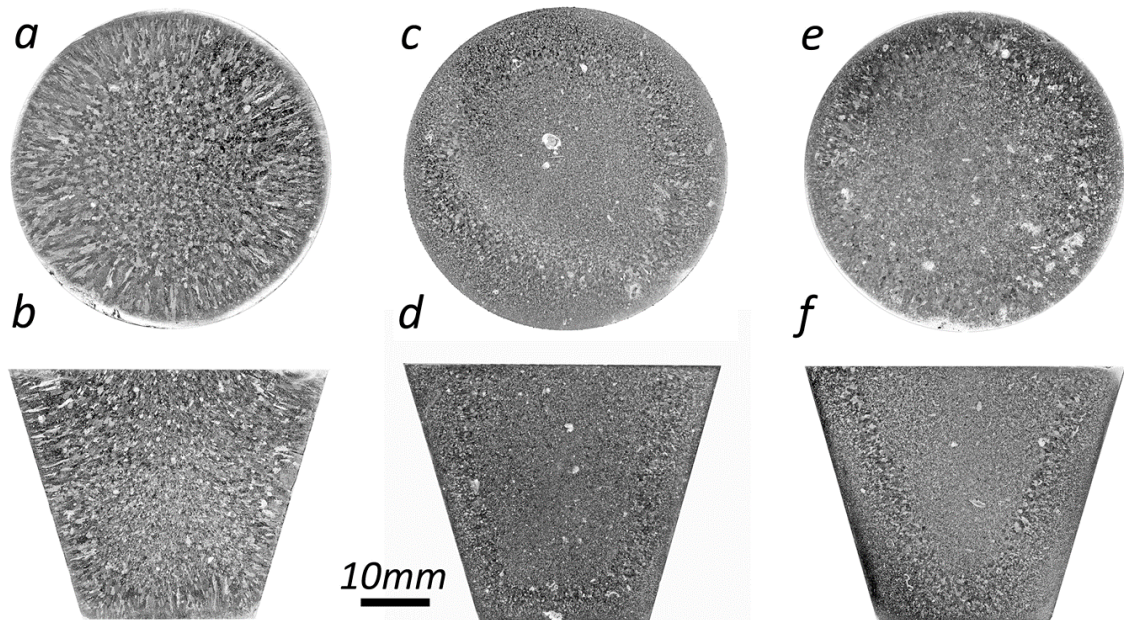


Fig. 5.2 Optical macrographs showing the grain structures on transverse and longitudinal sections of (a, b) CP Mg, (c, d) Mg-0.1Y and (e, f) Mg-0.5Y samples cast by TP-1 process with HSMC.

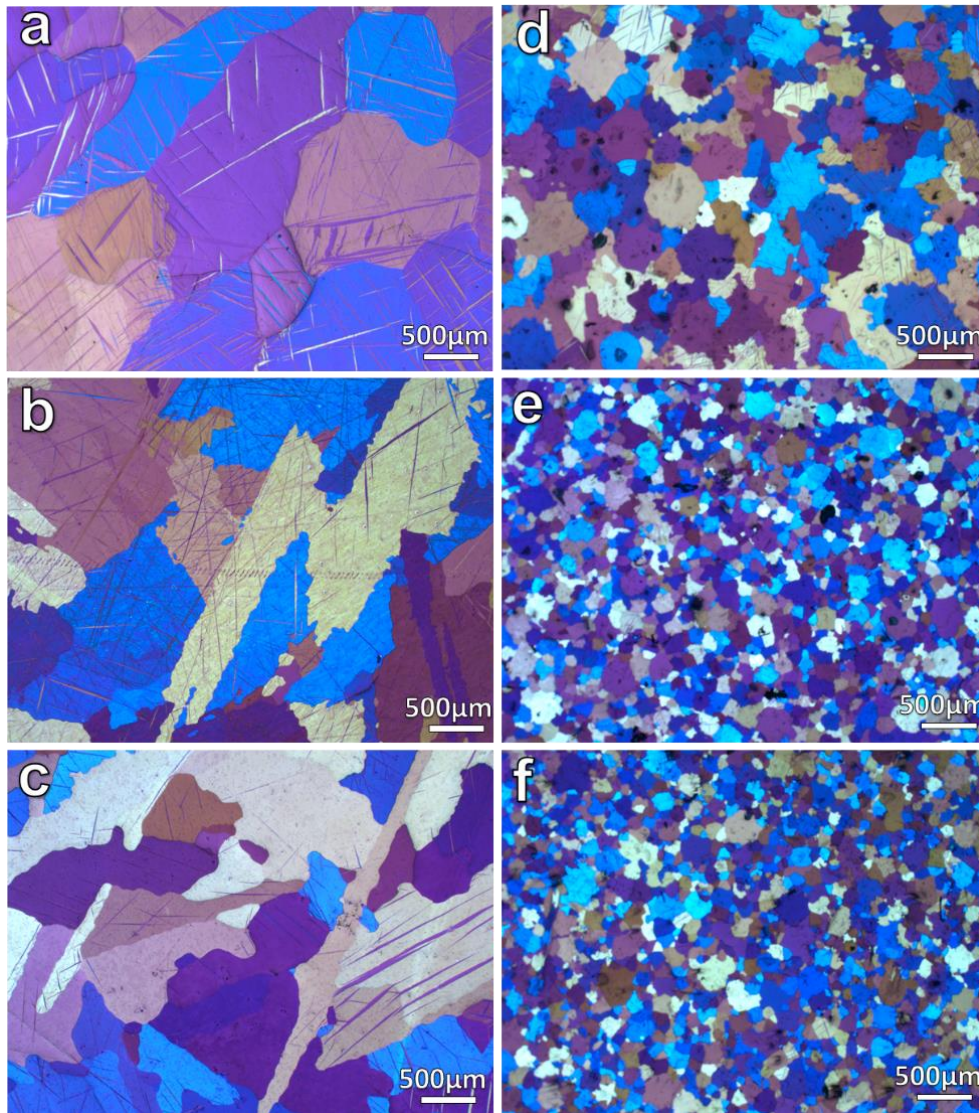


Fig. 5.3 Optical micrographs showing the grain structures on the centre of the transverse sections of (a, d) CP Mg, (b, e) Mg-0.1Y and (c, f) Mg-0.5Y samples cast in TP-1 mould.

5.2.2 Native MgO particles in Mg-0.5Y

SEM/EDS characterisation was carried out on the particles collected from Mg-0.5Y by the melt filtration method (Figs. 5.4 and 5.5). As compared to the native MgO particles found in CP Mg and Mg-9Al (Figs. 4.3 and 4.4) in terms of size, morphology and composition, the particles in Mg-0.5Y are suggested to be $\{111\}$ MgO and $\{100\}$ MgO particles. It is seen that the morphology of native MgO particles was not affected by the Y addition, either the $\{111\}$ MgO (Fig. 5.4(a)) or $\{100\}$ MgO particles (Fig. 5.5(a)) having size similar to that observed in the CP Mg (Figs. 4.3 and 4.4). Composition analyses were taken on a few tens of the MgO particles, with some of the EDS spectra being shown in Figs. 5.4(b-c) and 5.5(b-c). It is noticed that no signal of Y is seen in the EDS spectra from Mg matrix, while Y $L\alpha$ peaks with relatively weak strengths are found

at the perimeter of MgO particles, indicating that both types of the MgO particle contain Y that concentrated at the MgO/Mg interface.

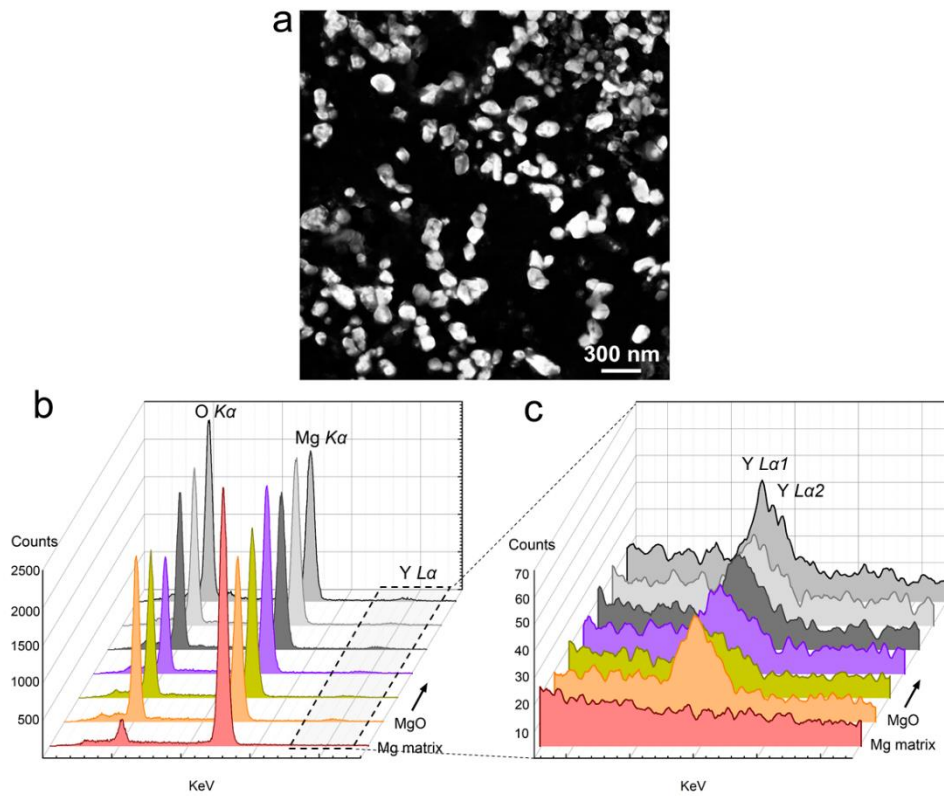


Fig. 5.4 (a) SE SEM image of the octahedral MgO particles in Mg-0.5Y-prefil collected by the pressurised melt filtration technique; and (b, c) the corresponding EDS spectra with Y L α signals. Note that the selection of MgO particles for the EDS point analyses on MgO particles is random.

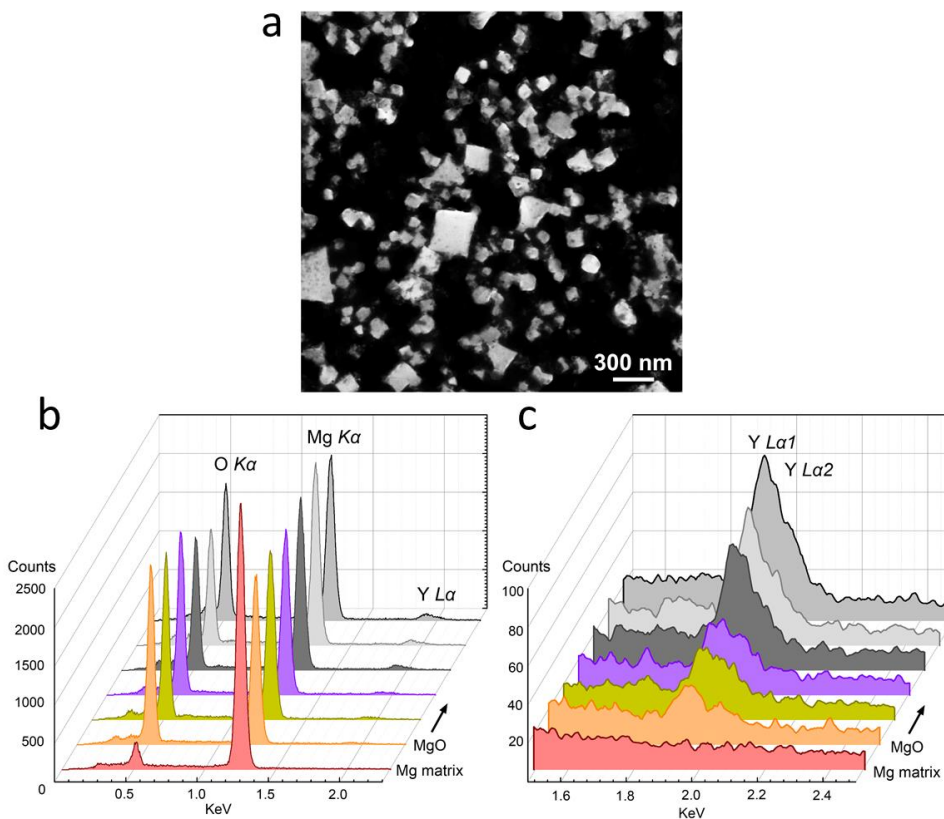


Fig. 5.5 (a) SE SEM image of the cubic MgO particles in Mg-0.5Y-prefil collected by the pressurised melt filtration technique; and (b, c) the corresponding EDS spectra with Y La signals. Note that the selection of MgO particles for the EDS point analyses on MgO particles is random/

The precise position where Y locates on the MgO particles was further examined by S/TEM examinations. **Figs. 5.6(a-b)** display the annular dark field (ADF) STEM images of a {111} MgO particles in Mg-0.5Y and the corresponding SEAD pattern, with the incident beam being parallel to $[011]_{\text{MgO}}$ zone axis. Obviously, on the $(200)_{\text{MgO}}$ and $(\bar{1}\bar{1}\bar{1})_{\text{MgO}}$ facets shown by the HAADF images in **Figs. 5.6(c-d)**, there exists a layer having a brighter contrast than the MgO matrix, indicating segregation of the heavy element Y ($Z_Y=40$). The Y segregation is verified by the identification of Y core-loss edges in the EELS spectrum acquired from the brighter layer at the MgO/Mg interface (**Fig. 5.7**). In contrast, Y edges are not seen in the spectra acquired from MgO and Mg matrix.

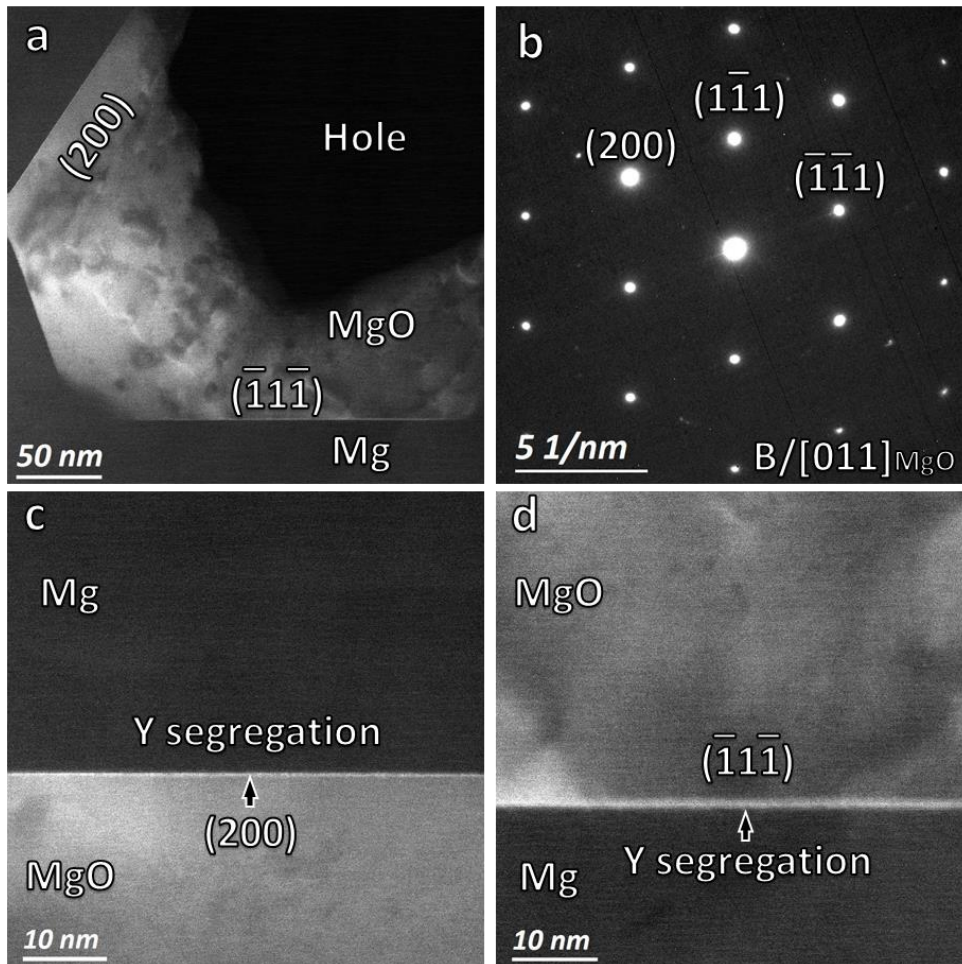


Fig. 5.6 (a, c, d) HAADF STEM micrographs and (b) SEAD presenting the segregation of Y onto both (c) {200} and (d) {111} facets of a {111} MgO particles in Mg-0.5Y-prefil specimen. Note that the incident beam is parallel to the $\langle 011 \rangle_{\text{MgO}}$ direction.

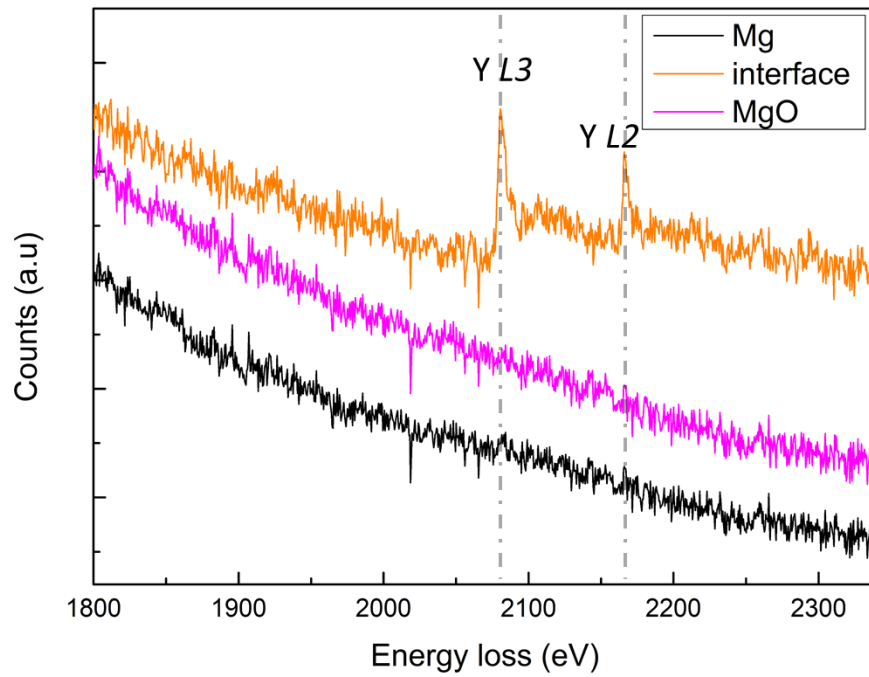


Fig. 5.7 Confirmation of Y segregation by EELS spectra acquired from Mg, MgO/Mg interface and MgO, respectively.

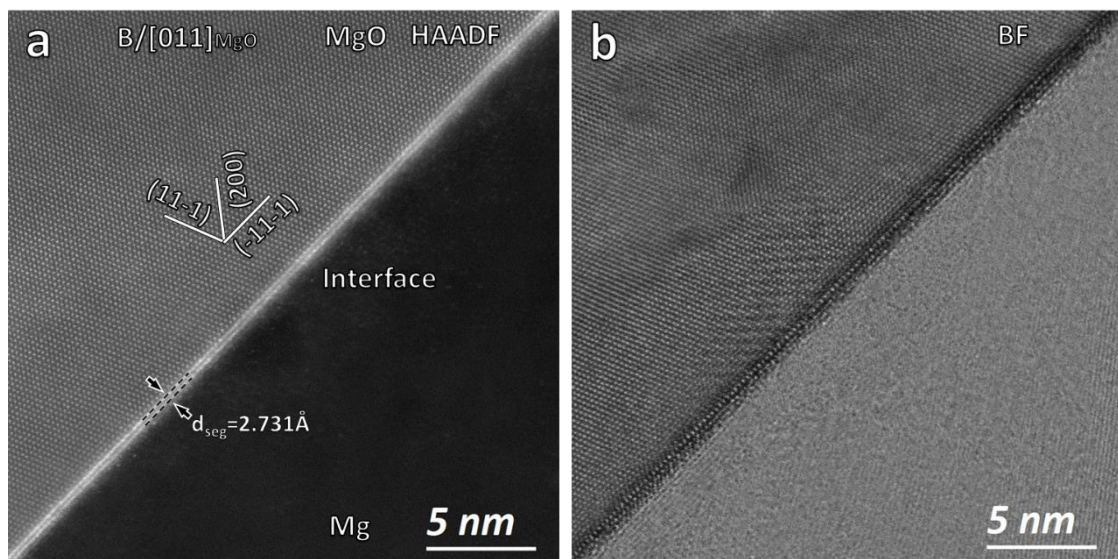


Fig. 5.8 Atomic-resolution (a) HAADF and (b) ABF STEM micrographs illustrating the segregation of Y on the $\{111\}$ facet of a $\{111\}$ MgO particles in Mg-0.5Y-prefil specimen. Note that the Y-rich feature exists as two atomic layers with brighter contrast in (a). The incident beam is parallel to the $[011]_{\text{MgO}}$ direction.

At higher magnifications, the atomically resolved HAADF and ABF STEM images in **Fig. 5.8** under zone axis of $[011]_{\text{MgO}}$ illustrate that the brighter layers on the $\{111\}_{\text{MgO}}$ facet consist of two atomic planes containing elements with a higher atomic number than Mg. With internal calibration by the known crystal structure of MgO, the spacing between

the two Y-rich atomic planes is measured as 2.731 Å, larger than (2.431Å) the d -spacing of $\{111\}_{\text{MgO}}$ plane. As shown by the HAADF image in **Fig. 5.8(a)** and the BF image in **Fig. 5.8(b)**, the Y segregation layers exhibit a different crystal structure from that of MgO. Unlike the resolved atomic columns in MgO, it is too fuzzy to distinguish periodic dots in the Y segregation layers.

Y segregation on another $\{111\}$ MgO particle was revealed by the HAADF and MAADF STEM images in **Fig. 5.9** along the zone axis of $\langle 112 \rangle_{\text{MgO}}$. Because of the collection of both diffraction intensity and high angle incoherent Rutherford' scattering of electrons by MAADF detector with an angular collection range from 52 to 100mrad, a MAADF image simultaneous contains interpretability of heavy atoms, as well as localised strains that diffract electron beam strongly. As easily recognised in the results, a distinct layer is noticed on the $\{111\}_{\text{MgO}}$ facet. Taken the contrast intensity of MgO matrix as a reference, it is noticed that the intensity ratio (inset in **Fig. 5.9(d)**, Y segregation layer vs. MgO matrix) is higher in the MAADF images (**Figs. 5.9(b, d)**) than that in the HAADF images (**Figs. 5.9(a, c)**). The contrast variations suggest that, other than Z -dependent contrast, there is extra brightness contrast resulted from the local strains inside the Y segregation layer. As recognised from both the HAADF and ABF STEM images (**Fig. 5.9(e)**), the brighter Y segregation layer consists of two atomic layers with a measured interplanar spacing of 2.731Å (see **Fig. 5.9(e)**, The spacing of 2.431Å for $\{111\}$ of MgO was applied as reference). In such a viewing direction, a square unit of 4 neighbouring atomic columns (length = 2.731Å) can be recognised in the Y-rich layers, as marked by the black cube in the inset **e1** in **Fig. 5.9(e)**. The atomic columns own a different repetitive rectangle (as marked by the white rectangle) unit from the atomic arrangement of the MgO matrix. Besides, some blurry features (see yellow arrows, and the inset **e2** in **Fig. 5.9(e)**) are observed periodically in the Y-rich layers, in a spacing of around 6nm.

Y segregation was also detected on the $\{100\}$ MgO particle in Mg-0.5Y. **Figs. 5.10(a-b)** show the BF TEM image of a $\{100\}$ MgO particle about 500nm in size, and the corresponding SAED pattern along the $[001]_{\text{MgO}}$ direction. The $\{100\}_{\text{MgO}}$ terminations are recognised. The HRTEM images of the $\{100\}_{\text{MgO}}/\text{Mg}$ interface in **Figs. 5.10(c, d)** show that the segregation layer has a periodic lattice structure, despite the artefacts induced by spherical aberration that makes it difficult to determine the exact structure. **Figs. 5.10(e, f)** are the ADF STEM images of the same particle, showing the brighter contrast of the segregation layer in a periodic pattern on $\{100\}_{\text{MgO}}$ facet.

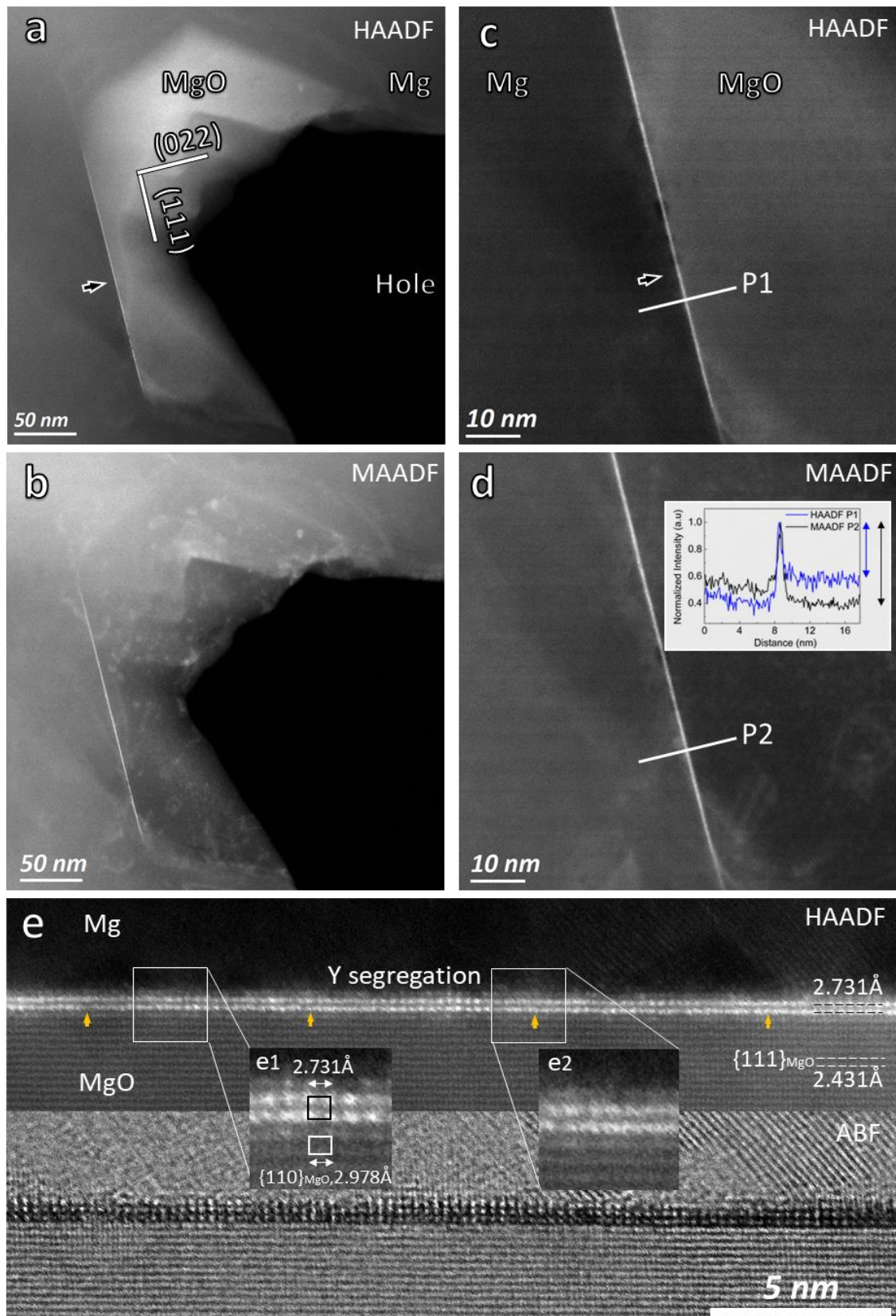


Fig. 5.9 STEM characterisation showing a $\{111\}$ MgO particle with Y segregation in Mg-0.5Y-prefil specimen, with an incident beam along the $\langle 112 \rangle_{\text{MgO}}$ direction. (a, c) HAADF, (b, d) MAADF and (e) HAADF + ABF STEM images. Inset in (d) is the plots of normalized contrast intensity along P1 and P2. Insets (e1) and (e2) show the local areas in the Y segregation layer, where a square unit is found in (e1), while blurry layers are found in (e2).

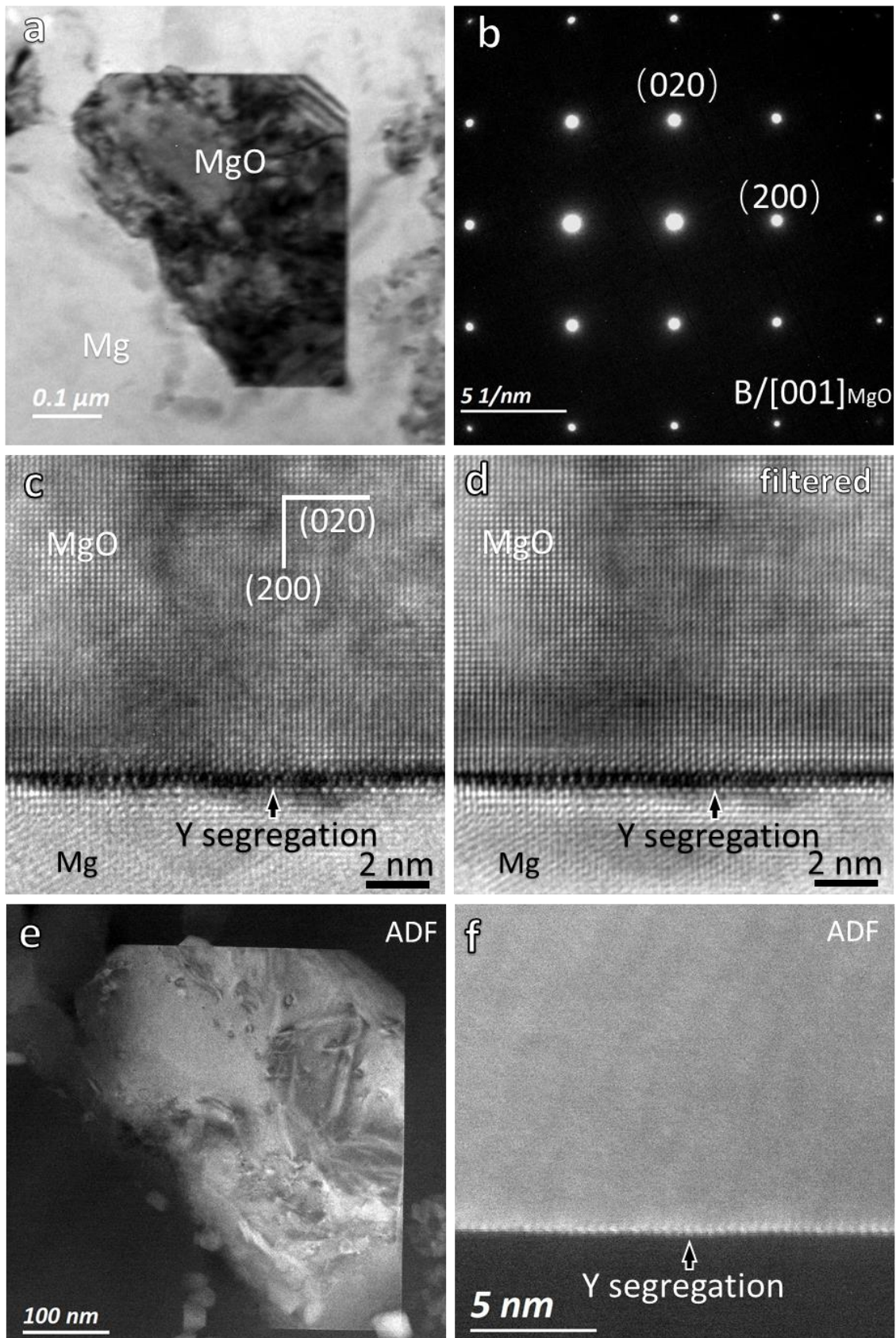


Fig. 5.10 Y-rich layer found on the facets of a {100} MgO particle in Mg-0.5Y-prefil specimen. (a) BF TEM image of the {100} MgO particle along with the (b) associated SEAD; (c, d) the corresponding raw and (d) filtered HRTEM images acquired on the {100} facet; and (e, f) the corresponding ADF STEM images, the Y segregation shows similar periodic feature as in (c, d). Note that the incident beam is parallel to the $\langle 001 \rangle_{\text{MgO}}$ direction.

Figs. 5.11(a-b) provides the HAADF/MAADF STEM results of the Y segregation on another $\{100\}$ MgO particle along the $[001]_{\text{MgO}}$ zone axis that is identified by the corresponding SAED pattern in **Fig. 5.11(c)**. The bright layer on the $\{100\}_{\text{MgO}}$ surface in the HAADF STEM image (**Fig. 5.11(a)**) is identical in position to the strain-induced contrast layer appearing in the strain sensitive MAADF image in **Fig. 5.11(b)**. Local strain seems to be introduced to the position where Y segregates. **Fig. 5.11(d)** shows the feature of the Y segregation layer at the atomic scale, where Y atoms are found enriched in alternate atomic columns in the terminated $\{100\}_{\text{MgO}}$ plane, producing continuous bright dots with an interval of 4.211\AA (same as $d_{\{100\}_{\text{MgO}}}$). The brighter columns are confined in one atomic layer, despite some steps occurring near the particle corner. The distinct bright dots disappear at the MgO corner that contains more such steps, with a fuzzy and bright contrast being resulted.

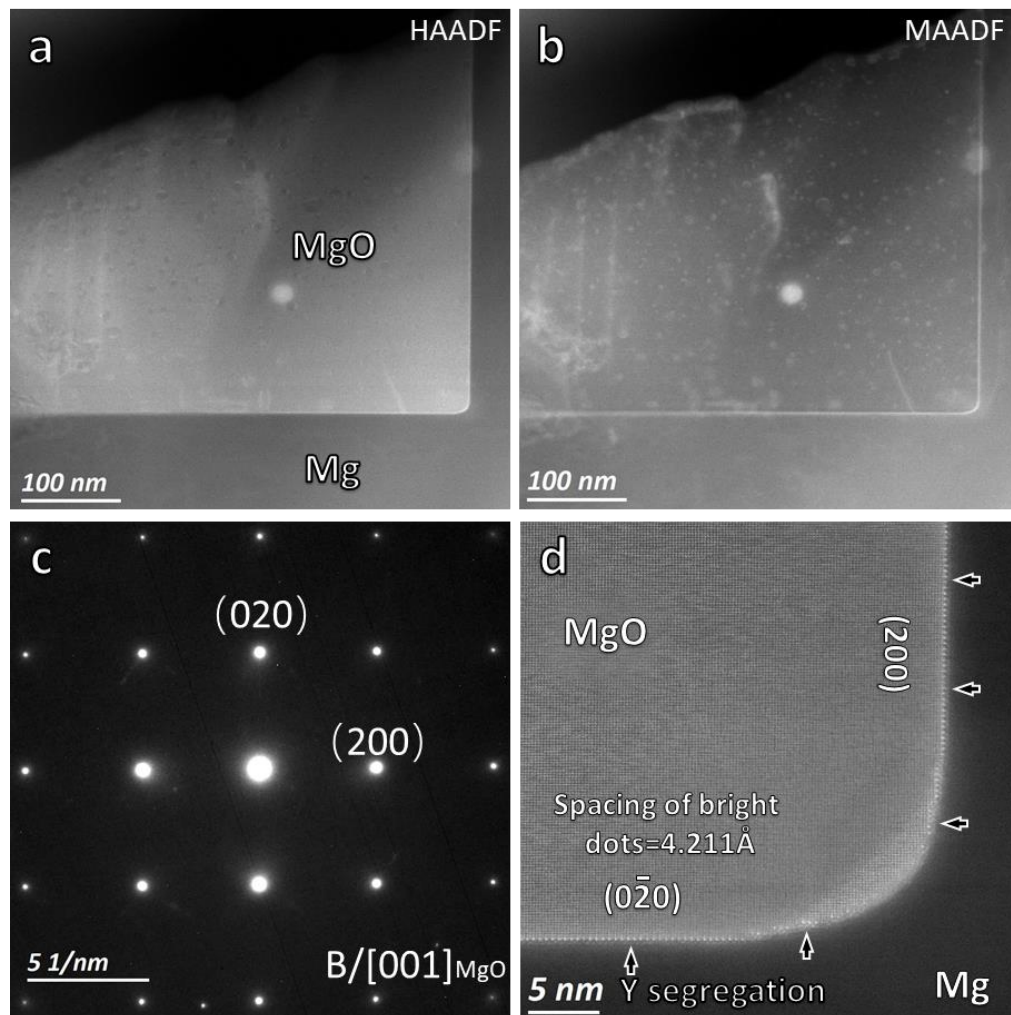


Fig. 5.11 Atomically-resolved Y-rich layer found on the facets of a $\{100\}$ MgO particle in Mg-0.5Y-prefil specimen along the $\langle 001 \rangle_{\text{MgO}}$ direction. (a) HAADF and (b) MAADF STEM images of the $\{100\}$ MgO particle associated with (c) the SAED; (d) HAADF STEM image acquired at the right bottom corner of MgO particle shows atomically that Y substitute alternate atomic columns.

The segregation of Y on the facets of native MgO particles has been widely observed in Mg-Y alloys, with 23 cases in Mg-0.5Y and 41 cases in Mg-3Y alloys being detected (Figs. A-1 to A-3, see appendix).

5.2.3 Structure and chemistry of Y segregation layer

5.2.3.1 Y segregation on $\{111\}_{\text{MgO}}$ facet

The atomic-resolution HAADF and ABF STEM images in **Fig. 5.12** show the Y segregation on the $\{11\bar{1}\}_{\text{MgO}}$ facet at different magnifications taken along the $\langle 2\bar{1}1 \rangle_{\text{MgO}}$ direction. The Y segregation on the $(11\bar{1})_{\text{MgO}}$ facet consists of two atomic planes with a periodicity represented by the repetitive square units. The square unit is different from that of the rectangle unit for the MgO matrix under $\langle 112 \rangle_{\text{MgO}}$ zone axis. Based on the known lattice parameters of MgO, a relationship in interplanar spacing between the Y segregation layer and the bulk MgO is highlighted in **Fig. 5.12(a)**: $6 \times d_{\{\text{Y-rich}\}} = 11 \times d_{\{220\}_{\text{MgO}}}$, $R = d_{\{\text{Y-rich}\}} / d_{\{220\}_{\text{MgO}}} = 0.917$, and $d_{\{\text{Y-rich}\}} = 2.731 \text{ \AA}$. This value 2.731 \AA is close (a 3.76% difference) to $d_{\{200\}_{\text{Y}_2\text{O}_3}} = 2.632 \text{ \AA}$ for the bulk FCC Y_2O_3 that has a lattice constant of $a = 5.264 \text{ \AA}$ and a space group of $\text{Fm}\bar{3}\text{m}$ [221]. Given the measured difference along the $[011]_{\text{MgO}}$ direction in atomic spacing between MgO and the Y segregation layer (2.978 \AA vs. 2.731 \AA , misfit = -9.04%, **Eq. 4-2**), misfit dislocations are generated at the interface as marked in **Fig. 5.12(b)**. Some atomic columns in the Y segregation layer aside the dislocation core lose their contrast sharpness, as marked by the arrow in **Fig. 5.12(b)**. The spacing of the misfit dislocations for the lattice mismatch of -9.04% was calculated as around 3.3 nm, which is about two times of the interval of the observed 'layer blurring' in **Fig. 5.9(e)**.

Fig. 5.13 shows the corresponding STEM/EELS analysis undertaken across the MgO/Mg interface. The comparison in **Fig. 5.13(b)** between spectra extracted from different coloured areas as labelled in **Fig. 5.13(a)** shows that Y only exists in the bright layers. The EELS maps generated over the area marked by the big green rectangle in **Fig. 5.13(c)** indicate again that Y is spatially confined within the two segregation atomic planes, where Mg is deficient compared to that in the Mg matrix and MgO.

Fig. 5.14 shows the HAADF and ABF STEM images at different magnifications of the Y segregation on the $\{111\}_{\text{MgO}}$ facet, where the viewing direction is parallel to the $[101]_{\text{MgO}}$ direction that is 30 or 90 degrees away from the $\langle 2\bar{1}1 \rangle_{\text{MgO}}$ in **Fig. 5.12**. The Y

segregation is recognised on the $\{111\}_{\text{MgO}}$ facet as two atomic planes in brighter intensity than that of the MgO matrix in the HAADF STEM images (Figs. 5.14(a, c, e)). Together with the ABF STEM images in Figs. 5.14(b, d, f), the structure of Y segregation layer is apparently different from that of the MgO matrix. Moreover, other than the distinct periodicity of the atomic columns for the Y segregation layers as shown in Fig. 5.12, the atomic columns of the Y-rich layers here exhibit as a blurry and linear feature in which the atomic columns are not resolved. Although being parallel to the $[101]_{\text{MgO}}$ direction for the MgO matrix, the viewing direction at this moment may be not parallel to a certain low-index zone axis for the Y-rich layers.

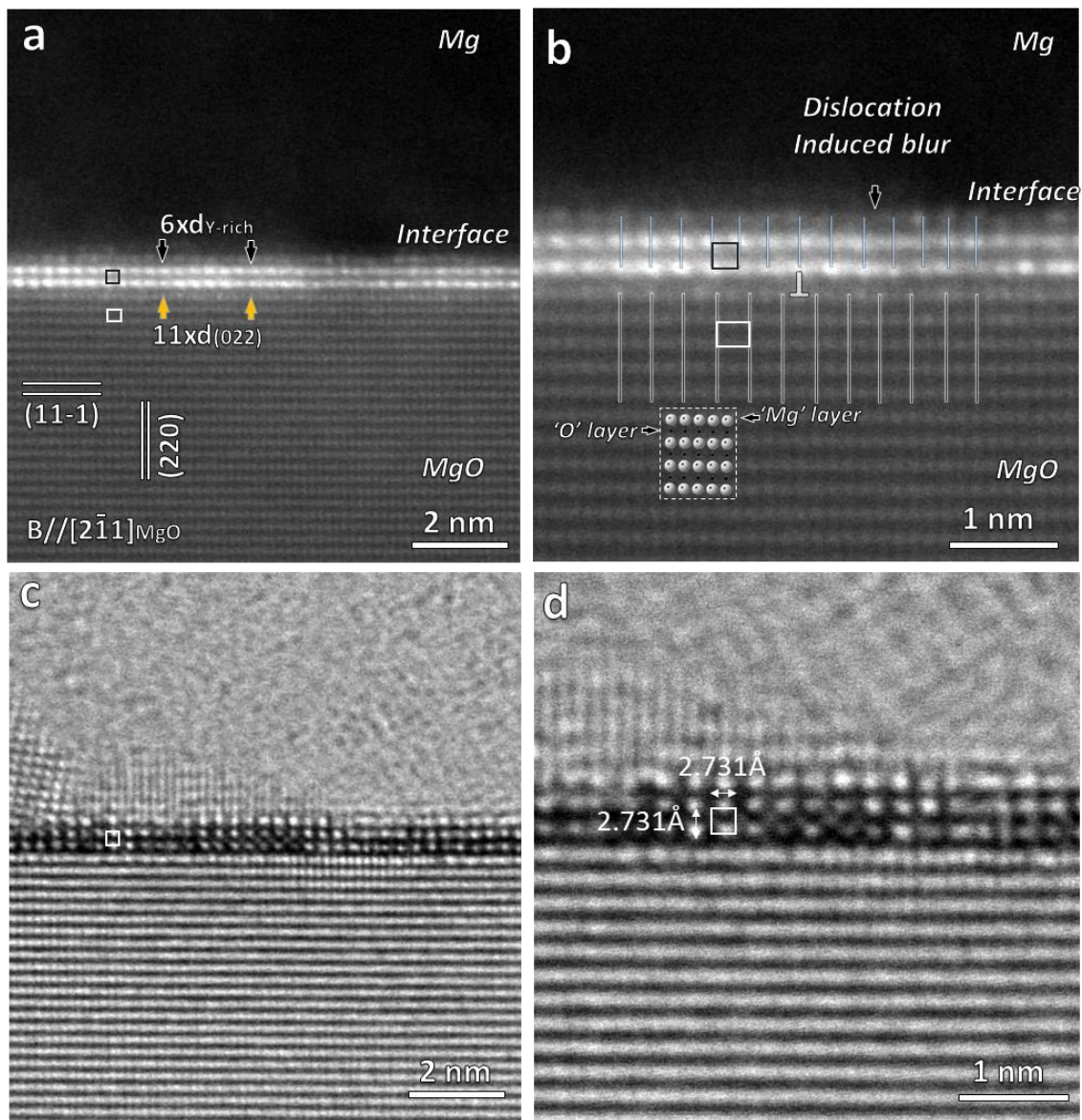


Fig. 5.12 (a, c) HAADF and (b, d) ABF STEM micrographs showing the decoration of Y on the $\{111\}$ facet of MgO in Mg-0.5Y-prefil specimen, with the viewing direction being parallel to $[2\bar{1}1]_{\text{MgO}}$. Inset in (b) is the corresponding atomic model of MgO. The brighter columns of the Y segregation layer can be repeated by a square unit, which is different from the repetitive unit for the MgO matrix. A relationship in interplanar spacings is found as: $6 \times d_{\text{Y-rich}} = 11 \times d(022)$.

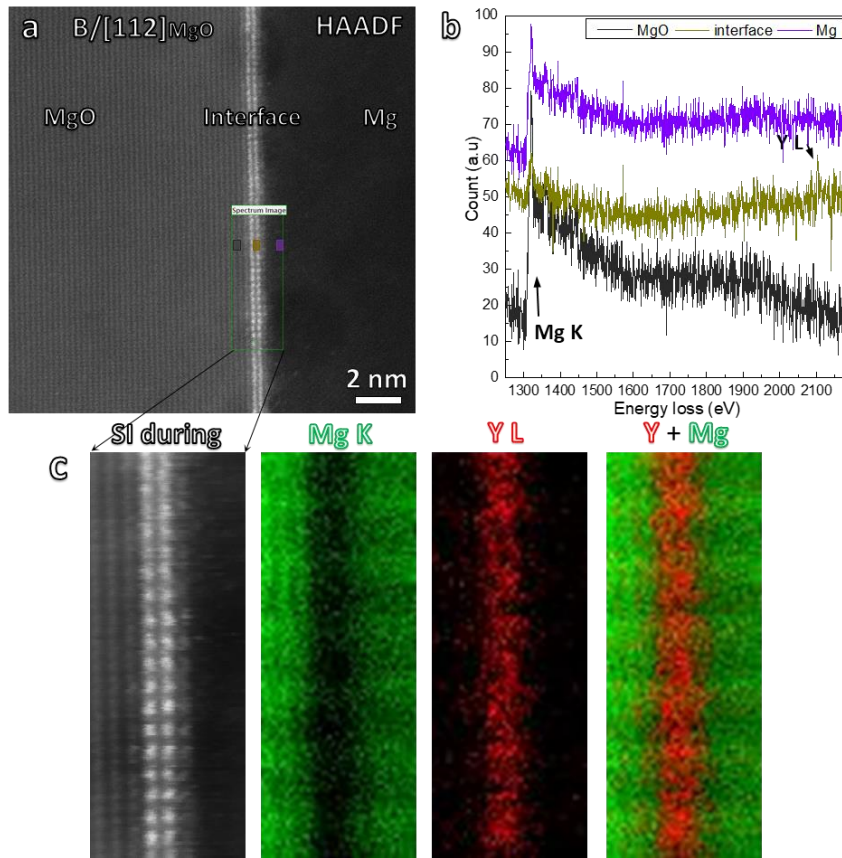


Fig. 5.13 (a) HAADF STEM image displaying the square feature of Y segregation at the interface between $\{111\}$ -faceted MgO and Mg in Mg-0.5Y-prefil, with incident beam parallel to $[112]_{\text{MgO}}$; (b) EELS spectra extracted from the labelled areas in (a) showing the presence of Y at the bright squares; (c) HAADF STEM image showing the exaggerated acquisition area marked by the green rectangle in (a), and the corresponding EELS elemental maps of Mg and Y by integrating Mg K and Y L edges with proper windows, respectively.

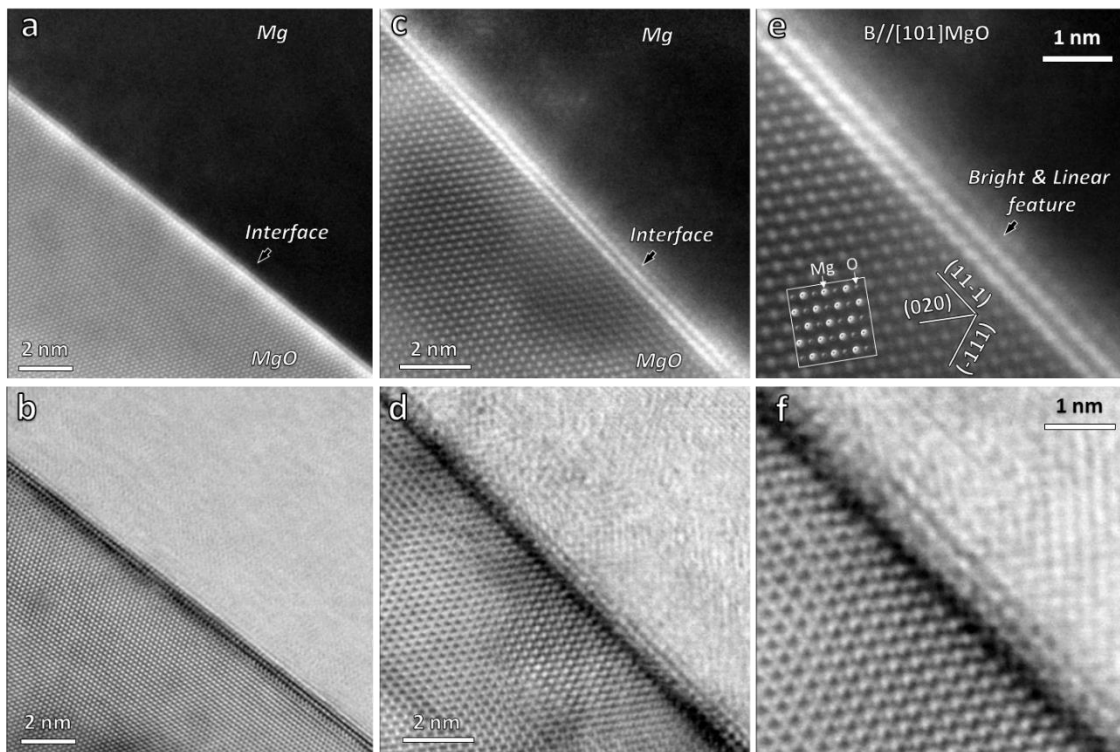


Fig. 5.14 (a, c, e) HAADF and (b, d, f) the corresponding ABF STEM micrographs showing the decoration of Y on {111} facet of MgO in Mg-0.5Y-prefil, with the viewing direction being parallel to [101]MgO. Inset in (e) is the corresponding atomic model of MgO.

The corresponding STEM/EELS analysis undertaken across the MgO/Mg interface is shown in Fig. 5.15. Two atomic planes in brighter contrast are resolved in Fig. 5.15(b), throughout which the elemental distribution of Y was created and shown in Fig. 5.15(c). Y is spatially localised within the two atomic planes of the bright interfacial layer (Figs. 5.15(b-c)). Fig. 5.15(d) shows the extracted EELS spectrum from the bright layers (orange rectangle in Fig. 5.15(b)), and the energy loss near edge structure (ELNES) can be identified as Y L₃, Y L₂ and Y L₁, respectively. In addition, it is seen in Fig. 5.15(e) that the strength of the O K signal acquired at the position between the brighter layers (highlighted by cyan rectangle ‘2’) is higher than the O K edge from the Mg matrix (cyan rectangle ‘1’). The difference in the strength of O K edges indicates that the segregation layers contain oxygen rather than the result of surface oxidation or oxygen adsorption at the surface of the thin TEM sample.

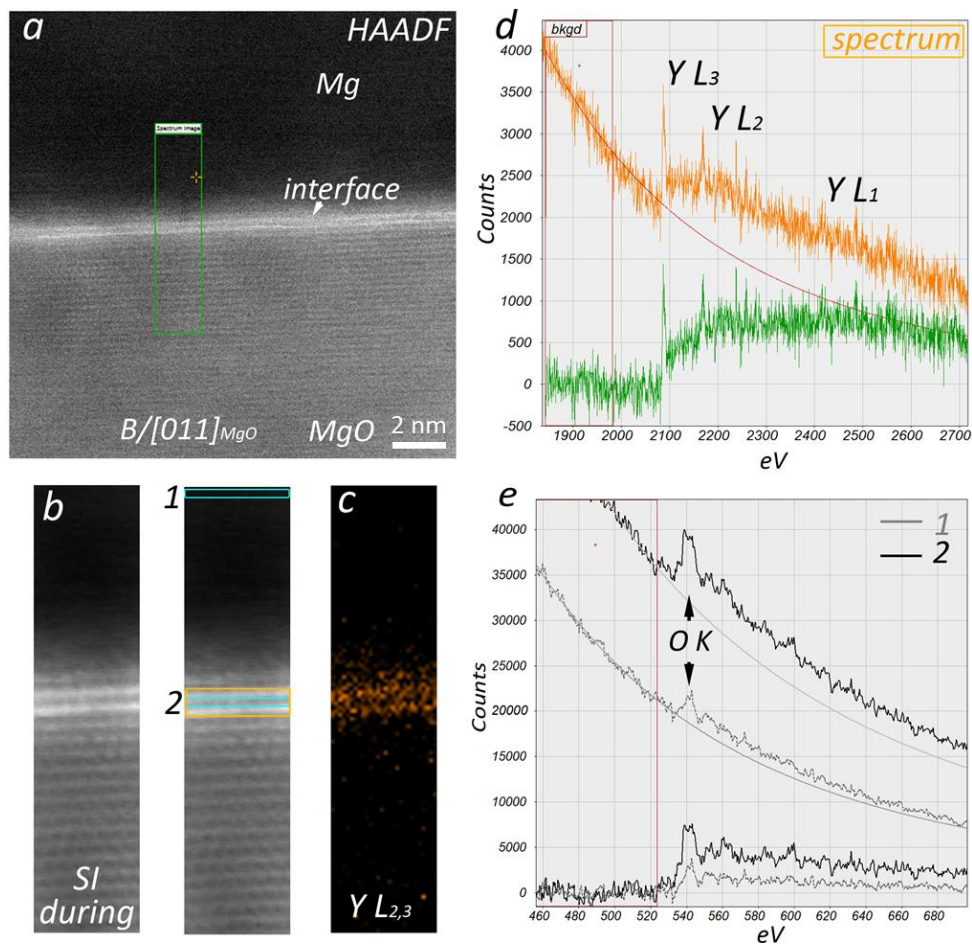


Fig. 5.15 HAADF STEM and EELS analysis presenting the segregation of Y on the {111} facet of MgO in Mg-0.5Y-prefil, with the incident beam parallel to [011]_{MgO}. (a) HAADF survey image with a green tangle marking the EELS acquisition area, which is exaggerated in (b); (c) the Y

distribution map; (d) EELS spectra extracted from the Y-rich layers; and (d) EELS spectra extracted from position 1 and 2 marked in (b). Note that the background subtraction had been applied for the spectra in (c, d).

To reveal the Y segregation layer from another viewing direction, we did further characterisation from another different zone axis directions of $[011]_{\text{MgO}}$ lying on the $\{11\bar{1}\}$ plane of MgO. **Figs. 5.16(a-b)** show the HRTEM image of Y segregation layers on the $(11\bar{1})_{\text{MgO}}$ facet, where the repetitive square unit is again recognised. The repetitive square unit is also verified by the HAADF and ABF STEM images shown in **Figs. 5.16(c-d)**. Although the zone axes of $[011]_{\text{MgO}}$ and $[101]_{\text{MgO}}$ (**Fig. 5.14**) belong to a family of crystal directions, the Y-rich layers here exhibit the repetitive square unit instead of blurry features in **Fig. 5.14**. Moreover, the Y segregation layers with the square unit feature are identical to that observed in **Fig. 5.12** when the $\{11\bar{1}\}$ facet is viewed along $[2\bar{1}1]_{\text{MgO}}$.

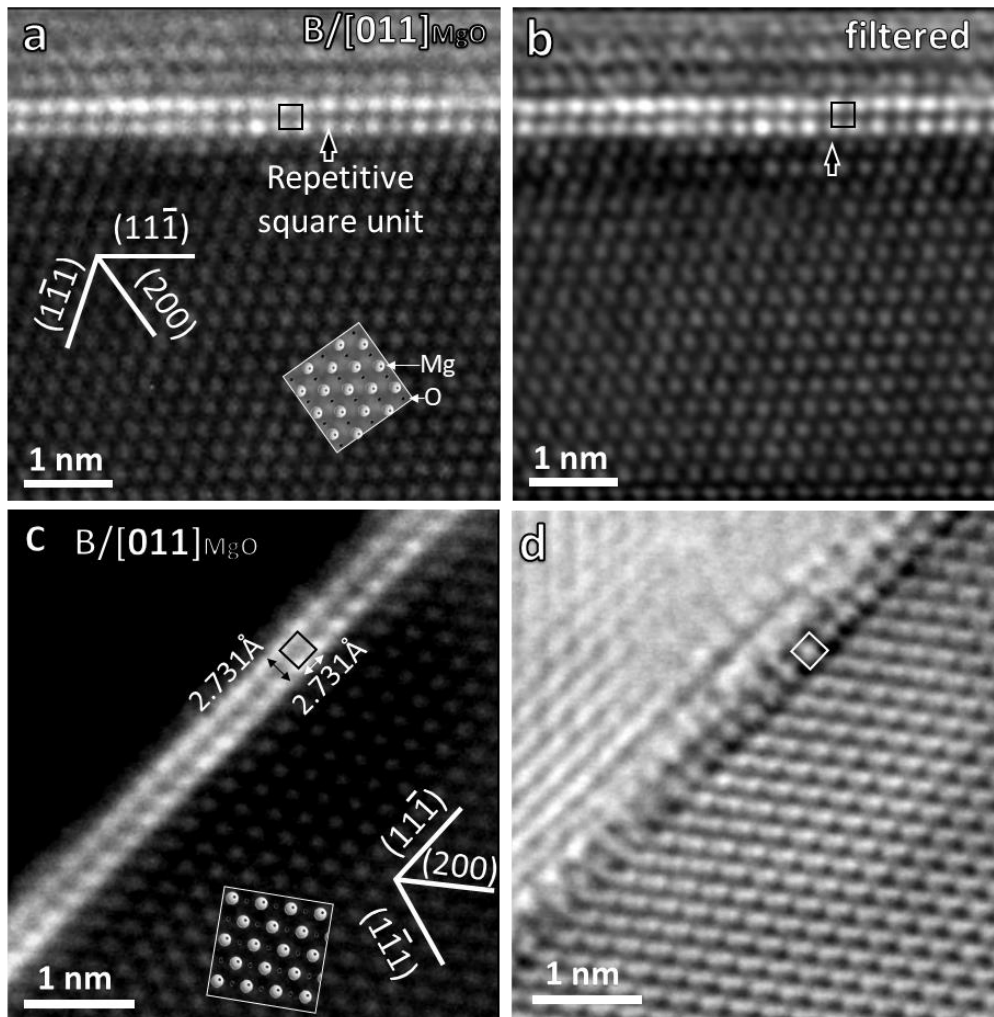


Fig. 5.16 (a) Raw and (b) filtered HRTEM images and (c) HAADF and (d) the corresponding ABF STEM showing the square feature of Y-rich segregation on a $\{111\}$ facet of a MgO particle in Mg-0.5Y-prefil, the beam direction is parallel to the $[011]_{\text{MgO}}$ direction. Insets in (a) and (c) are the corresponding atomic model of MgO.

5.2.3.2 Y segregation layer on $\{100\}_{\text{MgO}}$ facet

Fig. 5.17 presents the HAADF, ABF and MAADF images of the Y segregation on the $\{100\}_{\text{MgO}}$ facets with an incident beam parallel to the $[001]_{\text{MgO}}$ direction. It is seen that the Y segregation layer exhibits as brighter dots occurring in every two atomic columns along the $[010]_{\text{MgO}}$ direction. This feature is observed in the terminated $\{100\}_{\text{MgO}}$ atomic plane only. The Y atoms selectively dope the alternate atomic columns which originally contain 50% O and 50% Mg along the $[001]_{\text{MgO}}$ direction pointing into the page. Such Y substitution creates a local strain field, as shown in the strain sensitive MAADF image in **Fig. 5.17(d)**. This is evinced by the contrast profiles along ‘P1’ (**Fig. 5.17(d)**) and ‘P2’ (**Fig. 5.17(c)**) in the inset, the higher contrast ratio of the Y segregation to the MgO matrix indicates an extra contribution of contrast intensity from the local strains. More details can be seen in the HAADF STEM image in **Fig. 5.17(e)**. Due to the relatively larger atomic radius of Y (212 pm) than Mg (145 pm) [222], Y segregation generates protrusion in the direction normal to the $\{100\}_{\text{MgO}}$ faceted plane, shifting towards the Mg side. Besides, some bright dots on the right side in **Fig. 5.17(e)** are seen to protrude into the Mg side a relatively larger distance than the deviation, making two bright dots resolvable.

To figure out how the Y atoms substitute the Mg or O atoms in the terminated $\{100\}_{\text{MgO}}$ plane, we carried out STEM imaging along the zone axis of $[011]_{\text{MgO}}$. The atoms in each atomic column observed in this zone axis are either Mg or O only, making it easier to reveal Y segregation by the brightness contrast of atomic columns in a HAADF image. The HAADF, ABF and MAADF images in **Fig. 5.18** show the Y segregation layer on the $\{100\}_{\text{MgO}}$ facet in a projection parallel to the $[011]_{\text{MgO}}$ direction, which is 45 degrees away from $[001]_{\text{MgO}}$. Unlike the alternative bright dots of the Y segregation layer viewed from $[001]_{\text{MgO}}$ direction in **Fig. 5.17**, the bright dots appear continuously in **Figs. 5.18 (a, c, e)**, being identical in positions to the Mg columns of MgO. It is therefore believed that Y segregates onto the terminated $\{100\}_{\text{MgO}}$ plane and places in the Mg sites of MgO. The Y-substitution monolayer on $\{100\}_{\text{MgO}}$ facet also contains elastic strains. As shown by the inset that compares the contrast profiles along ‘P1’ and ‘P2’, the Y segregation layer introduces extra brightness contrast to the MAADF image in **Fig. 5.18(d)**, producing a higher contrast ratio to the MgO matrix than that in the HAADF image in **Fig. 5.18(c)**. Besides, when a critical electron dose is created by the scanning electron beam on the atomic columns, Y atoms are able to be kicked out from the Y-rich columns in the segregation layer, as shown in the marked area in **Fig. 5.18(c)**. In the HAADF image at

higher magnification in **Fig. 5.18(e)**, the brightness contrast of the atomic columns in the Y-substitution layer is quite uniform and elongated vertically. But there still exist some faint variations in brightness for each Y-rich column, which could be related to the extent of Y substitution and/or the position of the Y atoms in each atomic column. Also, the deviation of Y atoms from their original lattice positions can be seen, as schematically shown in **Fig. 5.18(f)**.

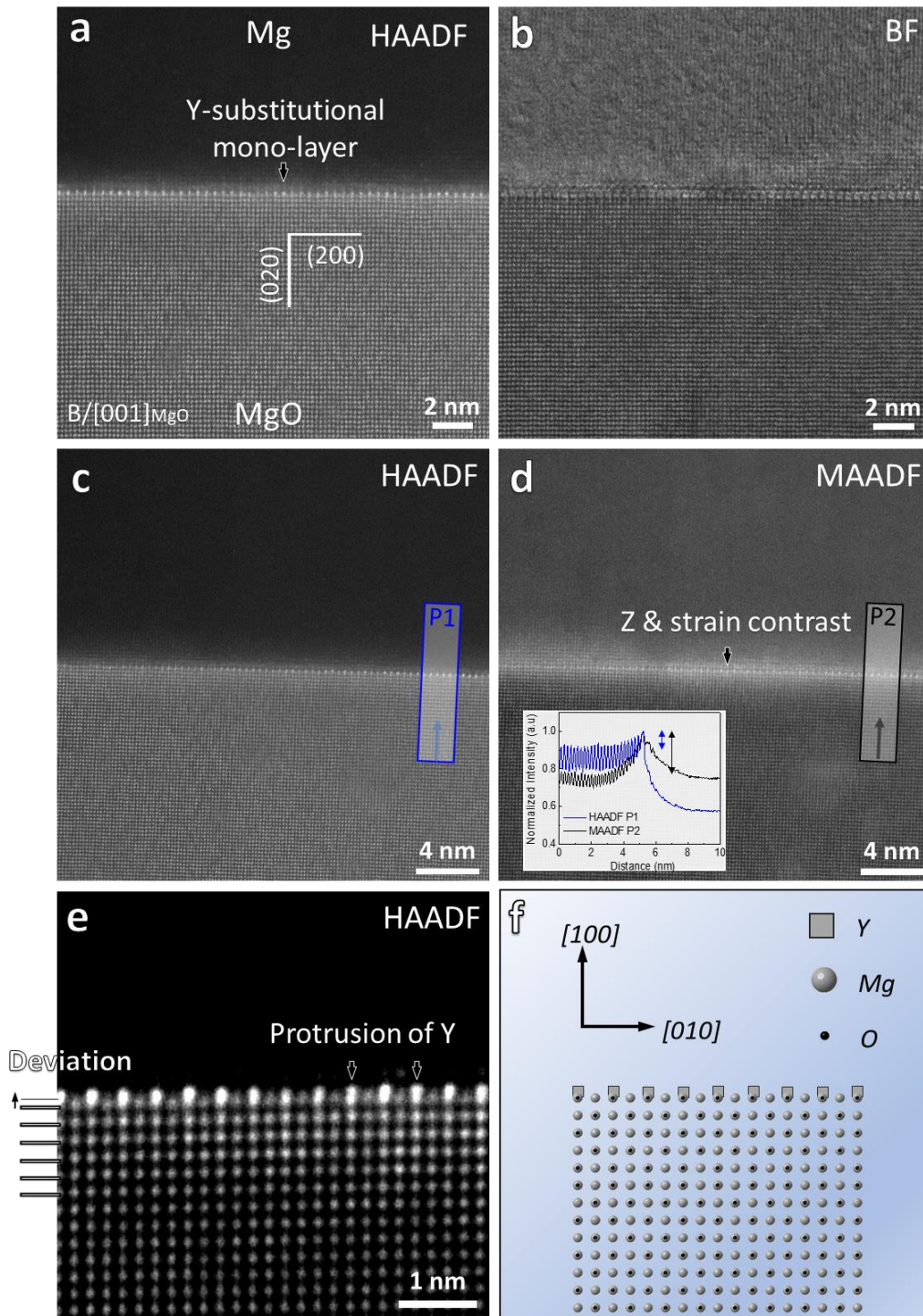


Fig. 5.17 Identification of Y-rich layer on the $\{100\}$ facet of MgO in Mg-0.5Y-prefil along the zone axis of $[001]_{MgO}$. (a, c, e) HAADF and the corresponding (b) BF, (d) MAADF STEM

micrographs showing a mono-atomic layer with brighter contrast. (f) The schematic insets illustrate how the position of Y atoms on the {100} faceted plane alters the contrasts in HAADF images such zone axis. Inset in (d) shows the contrast profiles along P1 in (c) and P2 in (d), P2 has a higher contrast ratio of the Y-rich layer to the MgO matrix than P1 has.

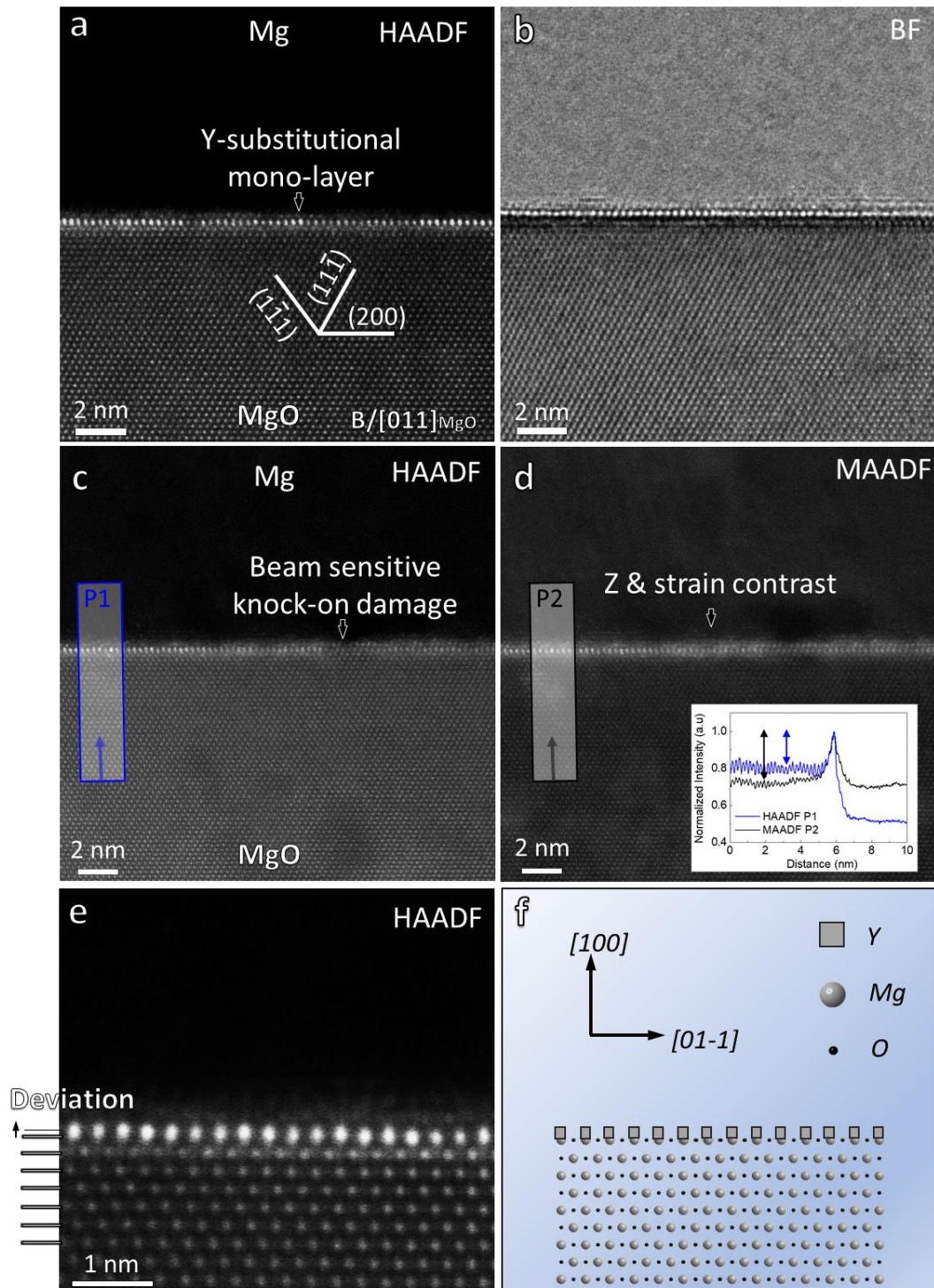


Fig. 5.18 (a, c, e) HAADF and the corresponding (b) BF, (d) MAADF STEM micrographs showing the decoration of Y on {100} facet of MgO in Mg-0.5Y-prefil along the zone axis of $[011]_{\text{MgO}}$, a mono-atomic layer with brighter contrast can be resolved. (f) The schematic insets illustrate how the position of Y atoms on the {100} faceted plane alters the contrasts in HAADF images along such zone axis.

5.2.3.3 Electron beam sensitivity of the Y segregation layer

Electron beam illumination during EELS acquisition was applied to evaluate the beam sensitivity of Y segregation layer. This test is critical since it could help us to correctly interpret which structure is the inherent nature of the Y segregation and to avoid the over interpretation of damaged features due to the electron beam illumination. **Fig. 5.19** shows the HAADF images of Y segregation on the $\{111\}_{\text{MgO}}$ facet before and after EELS acquisition. It suggests that such square-unit feature was damaged slightly by electron beam illumination after EELS acquisition following the parameters: beam time per pixel=0.12s, pixel size=44×115, accumulative time on each atomic column (5×5 pixel²) is 3s. The MgO part near to the Y segregation was somewhat damaged as well.

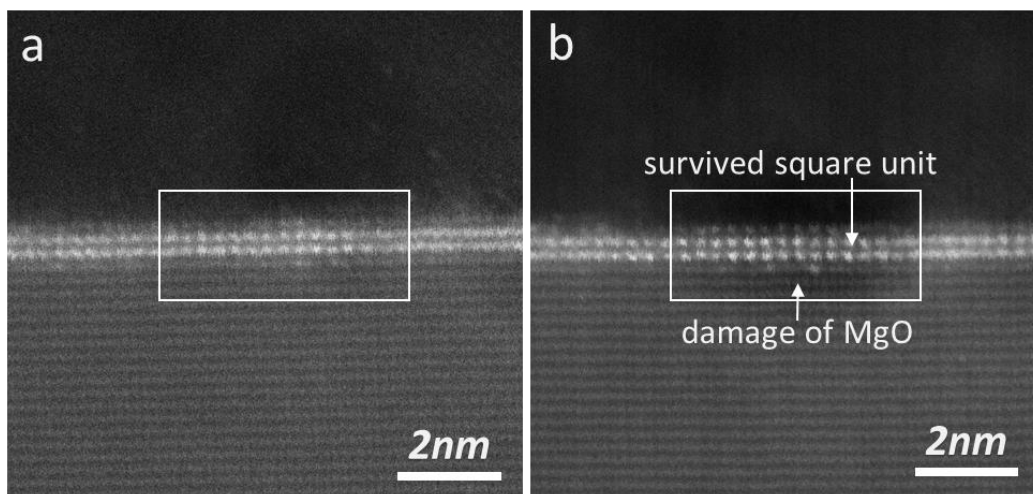


Fig. 5.19 HAADF STEM images (a) before and (b) after EELS acquisition showing the resistance of segregated Y₂O₃ 2DC to the electron beam illumination, where the square feature survives after EELS acquisition.

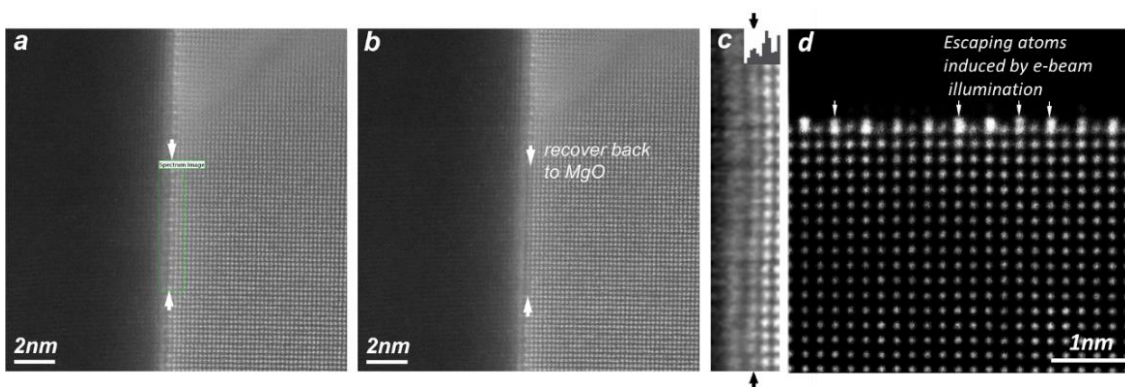


Fig. 5.20 HAADF STEM images (a) before and (b) after EELS acquisition showing the disappearance of the mono Y-rich layer on the $\{100\}$ plane of MgO, instead, being replaced by (c) a Mg-O mixed mono-layer with lower contrast than MgO matrix; and (d) A HAADF image shows that the bright dots have a trend of escaping after a long time of illumination as the result of the acquisition of stacking images.

However, the Y segregation layer on the $\{100\}_{\text{MgO}}$ facet is highly sensitive to the electron beam illumination. As illustrated in **Figs. 5.20(a-b)**, it was easily damaged by the electron beam illumination over time. The alternative bright dots disappeared after the EELS acquisition following the parameters: pixel time=0.05s, pixel size= 25×124 , and accumulative time on each column (5×5 pixel²) is 1.25s. The inset of contrast profile shows that after kicking out the Y atoms, Mg-O mixed atomic columns remain and have contrasts lower than the Mg-O mixed columns in MgO (**Fig. 5.20(c)**). The atom-resolved HAADF STEM image (512×512 pixel²) in **Fig. 5.20(d)** shows that the positional protrusion of brighter dots appears in almost every Y-doped column after 21s of acquisition time, with around 0.035s on an atomic column (21×21 pixel²). The beam sensitivity is closely related to the intrinsic chemistry and structure of the Y segregation layer on $\{111\}$ and $\{100\}$ facets.

5.2.4 Coarse and columnar grain due to Y₂O₃ particles

A coarse and columnar grain structure is observed in the as-cast Mg-1Y and Mg-3Y TP-1 samples without and with HSMC treatment, as shown in **Fig. 5.21**. In comparison to the Mg-Y (Y \leq 0.5%) samples in **Figs. 5.1** and **5.3(a-c)**, the addition of 3% Y slightly refines the as-cast grain structure and leads to CET in the central area (**Fig. 5.21(b)**), with an AGS of $611.6 \pm 106.8\mu\text{m}$. However, in comparison to the Mg-Y-HSMC (Y \leq 0.5%) samples in **Figs. 5.2** and **5.3(d-f)**, more Y addition fails to offer grain refinement. As shown in **Figs. 5.21(c-d)**, both Mg-1Y-HSMC and Mg-3Y-HSMC show columnar grain structures. And 3% Y contributes to the smaller columnar width in Mg-3Y-HSMC than that in Mg-1Y-HSMC.

The coarsening of grain size and failure of CET in Mg-Y alloy was also observed even when Y content was 0.5%. As shown in **Fig. 5.22**, a coarse and columnar grain structure occurs in Mg-0.5Y alloy when HSMC treatment was imposed for a long time up to 15 mins, with an average columnar width is $640.6 \pm 111.5\mu\text{m}$.

The coarsening of grain size and failure in CET with further increasing Y contents to 1% and 3% are unexpected, detailed study of Y addition on nucleation and grain initiation have to be carried out. It has been shown from the previous results (**section 5.2.3**) that Y segregation on MgO particles in Mg-0.5Y is confined in one or two atomic layers on the surface. In contrast, large bulk Y₂O₃ particles are observed when Y content is increased. For instance, Y₂O₃ and MgO particles are found to co-exist in Mg-3Y alloy, as shown in **Fig. 5.23**. In **Fig. 5.23(a)**, the large particles about 1 to 2 μm in size are present together

with nano-sized MgO particles. The corresponding EDS spectra in **Fig. 5.23(b)** show that these particles contain mainly Y and O. There are also smaller Y_2O_3 particles being adjacent to the nano-sized MgO particles, as shown in **Figs. 5.23(c-e)**. These two types of particle are further confirmed by the indexing of Kikuchi patterns in **Fig. 5.23(f)**; they are MgO and Y_2O_3 , respectively. Whilst, the index satisfies both the Y_2O_3 phases with $Fm\bar{3}m$ [221] and $Ia\bar{3}$ space groups [223], whose crystal structures are similar to each other, and their Kikuchi patterns can hardly be distinguished. The coexistence of MgO and Y_2O_3 particles are further confirmed by HAADF STEM image and EDS maps in **Fig. 5.23(g)**. The Y_2O_3 particles seem to form and grow by consuming the MgO particle which get shrinkage and lose its original cubic shape.

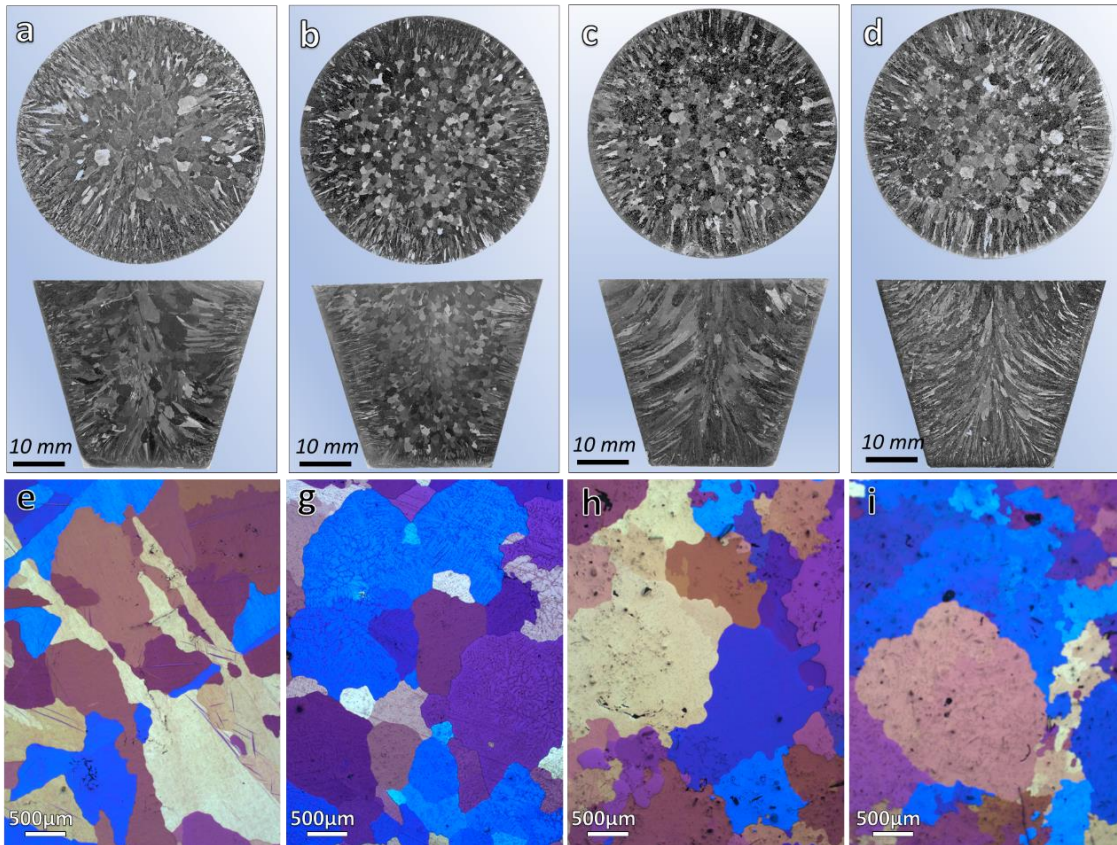


Fig. 5.21 (a-d) Optical macrographs showing the grain structures on transverse and longitudinal sections of (a) Mg-1Y, (b) Mg-3Y, (c) Mg-1Y-HSMC and (d) Mg-3Y-HSMC samples cast by TP-1 process. (e-f) The corresponding optical micrographs showing the grain structures at the centre of the transverse sections.

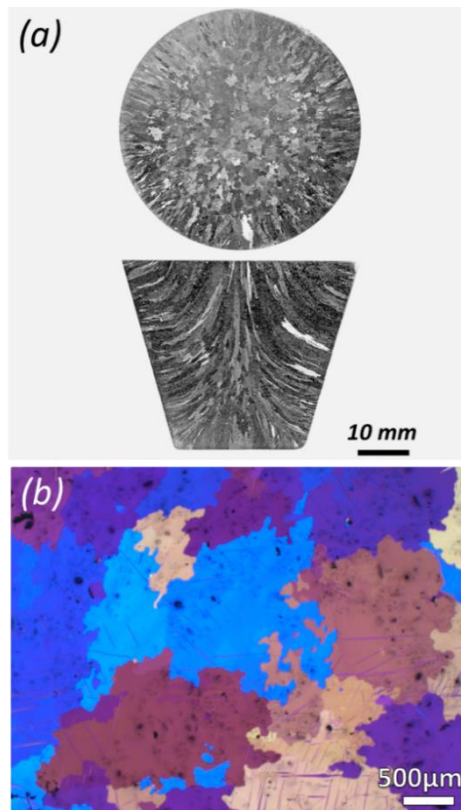


Fig. 5.22 Optical (a) macro and (b) micro graphs of the as-cast Mg-0.5Y-HSMC15mins.

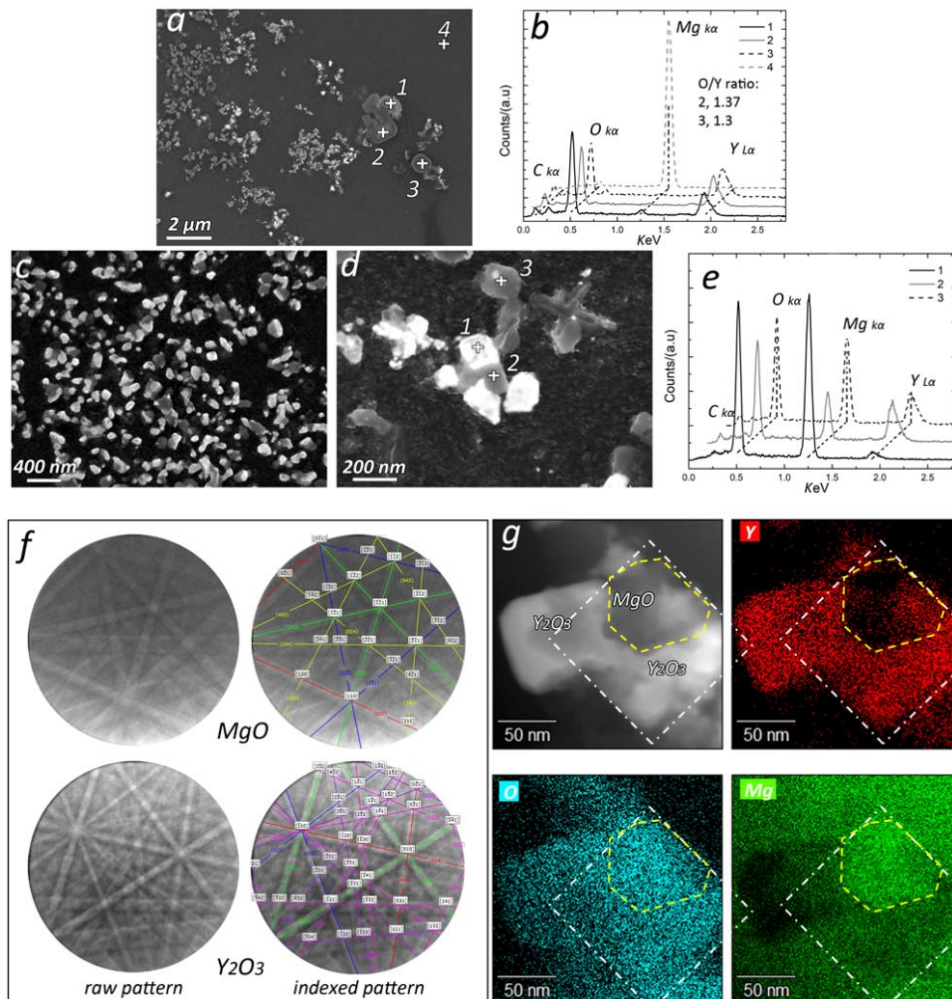


Fig. 5.23 (a) SE SEM image presenting nano-sized and micron-sized particles in Mg-3Y-prefil, the corresponding EDS spectra suggest that the larger particles are Y_2O_3 in chemistry. (c-e) Y_2O_3 are also found inside the MgO film where nano-sized MgO and Y_2O_3 coexist. The phases are confirmed either by (f) Kikuchi patterns and (g) STEM EDS mappings.

Fig. 5.24 shows two bulk Y_2O_3 particles characterised by BF TEM image, SEAD and HRTEM imaging. The indexing of the corresponding SAED pattern and HRTEM images identify them as Y_2O_3 , which has a space group of $Ia\bar{3}$ and a lattice constant $a = 1.06\text{nm}$ [223]. It is referred to as C- Y_2O_3 . Specifically, **Figs. 5.24(a-c)** shows a C- Y_2O_3 particle 200nm in size under the zone axis of $[001]_{C-Y_2O_3}$, which is bounded by $\{100\}_{C-Y_2O_3}$ facets plus minor $\{110\}_{C-Y_2O_3}$ facets. **Figs. 5.24(d-f)** demonstrate another C- Y_2O_3 particle around 400nm in size under the zone axis of $[111]_{C-Y_2O_3}$, with $\{112\}_{C-Y_2O_3}$ and $\{110\}_{C-Y_2O_3}$ terminated facets. Both the atomic models of C- Y_2O_3 along the zone axes of $[001]_{C-Y_2O_3}$ in **Fig. 5.24(c)** and $[111]_{C-Y_2O_3}$ in **Fig. 5.24(f)** show a good matching with the corresponding HRTEM lattice images.

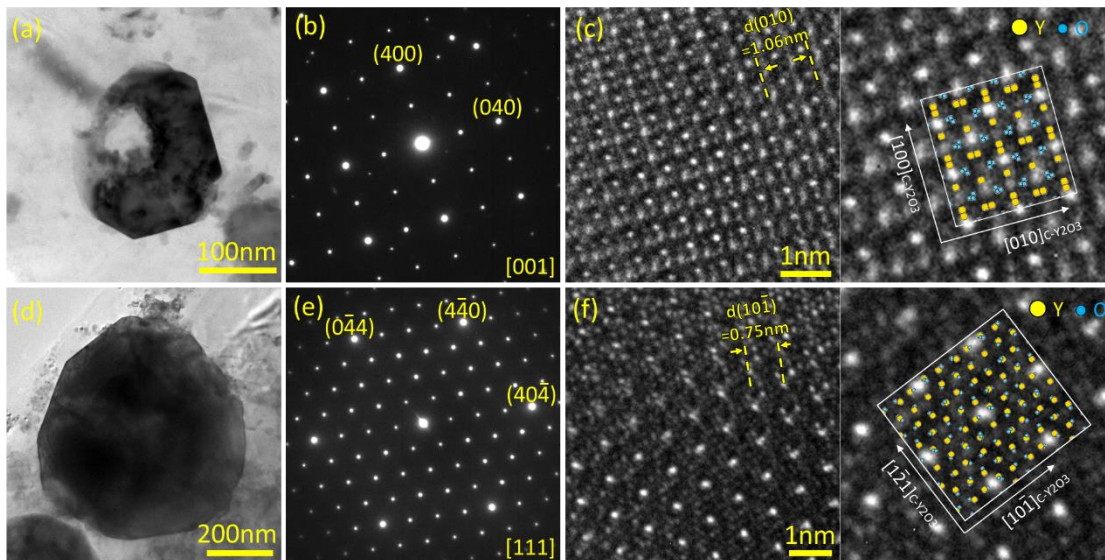


Fig. 5.24 Identification of C- Y_2O_3 by TEM characterisation in Mg-3Y-prefil through (a, d) BF imaging; (b, d) SAED; and (c, f) HRTEM imaging. (a-c) a C- Y_2O_3 particle viewed along $[001]$ zone axis; and (b-d) another one viewed along $[111]$ zone axis. The overlapped insets (c, d) are the atomic model of Y_2O_3 from the $[001]$ and $[111]$ axes, respectively. Note that the yellow circles represent Y atoms and the cyan circles represent oxygen atoms.

5.3 Discussion

5.3.1 Columnar to equiaxed transition

Columnar grain growth can be blocked by equiaxed grains initiated ahead of the solid/liquid front, and equiaxed grain microstructure is favoured by solute addition and enhanced grain initiation [56,224]. With the relatively low growth restriction factor in CP

Mg, Mg-0.1Y ($Q_{0.1Y}=0.17K$) and Mg-0.5Y ($Q_{0.5Y}=0.85K$) and the low number density of native MgO particles in the melt, columnar to equiaxed transition (CET) was absent without HSMC treatment (**Fig. 5.1**). Finer columnar width was achieved in the central area of CP Mg-HSMC when a high number density of native MgO (potential nucleating sites) was introduced by particle dispersion through HSMC (**Figs. 5.2(a-b)**). This trend was improved by further 0.1Y addition, reaching complete CET throughout the structure (**Figs. 5.2(c-d)**).

5.3.2 Grain refinement due to Y segregation

The number of grain initiation events determines the final as-cast grain size. **Table 5-1** lists the experimentally measured AGS and their conversions into the number of grains per unit volume (N_v), which is equal to the number of effective particles per unit volume (N_e) under the assumption that one grain initiation event corresponds to one free-grown grain. A great reduction in grain size is found after HSMC is applied to CP Mg (**Figs. 5.3(a-b)**), where the N_e is 41.7 times higher than that with no HSMC. This is consistent with previous studies that grain refining can be achieved by providing sufficient potential nucleating sites using HSMC to disperse the native MgO particles [134,182]. Grain refinement requires not only a nucleating substrate but also growth restriction that is able to delay the thermal recalescence, allowing more particles effective for nucleation and grain initiation. The grain size is thus closely related to the solute concentration [18,25]. An addition of 0.1Y (Mg-0.1Y-HSMC) results in a significant refining effect (**Figs. 5.3(b, c)**), with the increase of N_e by 463.4 times as compared to CP-Mg without HSMC, and 11.1 times compared to CP Mg-HSMC. However, the grain size is nearly unchanged when more Y is added (Mg-0.5Y-HSMC, see **Figs. 5.3(e, f)**). Therefore, there should be other factors outweighing the small growth restriction and contributing to the grain refinement. As revealed by the STEM analyses (**Figs. 5.6 to 5.13**), Y segregation on the native MgO particles could be one of the factors. As reported in previous work [189], atomic segregation in a few atomic layers on a substrate surface only requires a small amount of solute (56ppm Ti in Al/TiB₂ system for instance), so that the addition of 0.1Y (1000ppm) should be sufficient to modify the majority of the native MgO particles in the melt. Further addition of Y, therefore, does not deliver additional benefits from the segregation point of view. More Y addition simply increases the Q value and contribute little change in grain size (**Figs. 5.3(e, f)**). It has been reported that surface modification of a substrate in atomic level to influence heterogeneous nucleation and the subsequent solidification behaviour is possible through solute segregation. Studies have

demonstrated that Al₃Ti 2DC [189] and Ti₂Zr 2DC [47] enhances and impedes the potency of TiB₂ for heterogeneous nucleation, respectively.

Table 5-1 Calculated number of effective particles per unit volume (N_e) involved in grain initiation procedure, which also equals to the number of grains per unit volume (N_v) calculated by: $N_e = N_v = \frac{0.5}{\bar{l}^3}$, where \bar{l} is the average grain size evaluated by the mean linear intercept.

| Samples | CP Mg | Mg-0.1Y | Mg-0.5Y | CP Mg-HSMC | Mg-0.1Y-HSMC | Mg-0.5Y-HSMC |
|--------------------------|----------|----------|----------|------------|--------------|--------------|
| Average grain size (μm) | 816.4(c) | 792.5(c) | 718.6(c) | 235.4(e) | 105.50(e) | 115.5(e) |
| N_e (/m ³) | 9.19E+08 | 1.0E+09 | 1.35E+09 | 3.83E+10 | 4.26E+11 | 3.25E+11 |

Note that 'c' refers to columnar grain structure and 'e' for equiaxed grain structure, also the calculated N_e here for 'c' specimen was overestimated due to the columnar structure. The measured average grain size for samples with a columnar structure is overestimated.

5.3.3 Y segregation on MgO particles

5.3.3.1 Y₂O₃ 2DC on {111} facets of native MgO

Comprehensive HAADF STEM analyses (Figs. 5.6, 5.8, and 5.9 to 5.16) and EELS characterisations (Figs. 5.13 and 5.15) in this work have evidenced the formation of the Y segregation layers on the {111}_{MgO} facet. The rotation symmetry of the Y segregation layer is different from the 3-fold rotation symmetry of {111}_{MgO} facet plane around the facet normal. This is because either blurry feature (Fig. 5.14) or square unit (Figs. 5.12 and 5.16) was detected from the <011>_{MgO} family directions. It is speculated that the Y-rich layers have a 4-fold rotation symmetry around the normal direction of {111}_{MgO} facet since the square unit feature is repeated in the zone axes of [2 $\bar{1}$ 1]_{MgO} (Fig. 5.12) and [011]_{MgO} (Fig. 5.14). The angle between these two zone axes is 90 degrees around the normal to the {111}_{MgO} facet, fulfilling the 4-fold rotation symmetry and the same square features are detected.

In addition, O was confirmed existing in the Y segregation layer by the EELS spectroscopy analysis (Fig. 5.15). Further comparison between the spectra extracted from different areas crossing the interface is shown in Fig. 5.25, where the O K edge splits gradually into two peaks when approaching the interface, at which the edge structure is similar to the O edge from the reference Y₂O₃ spectrum. Therefore, the segregation layers

contain O atoms and they should stay in a similar surrounding environment to the O atoms in Y_2O_3 .

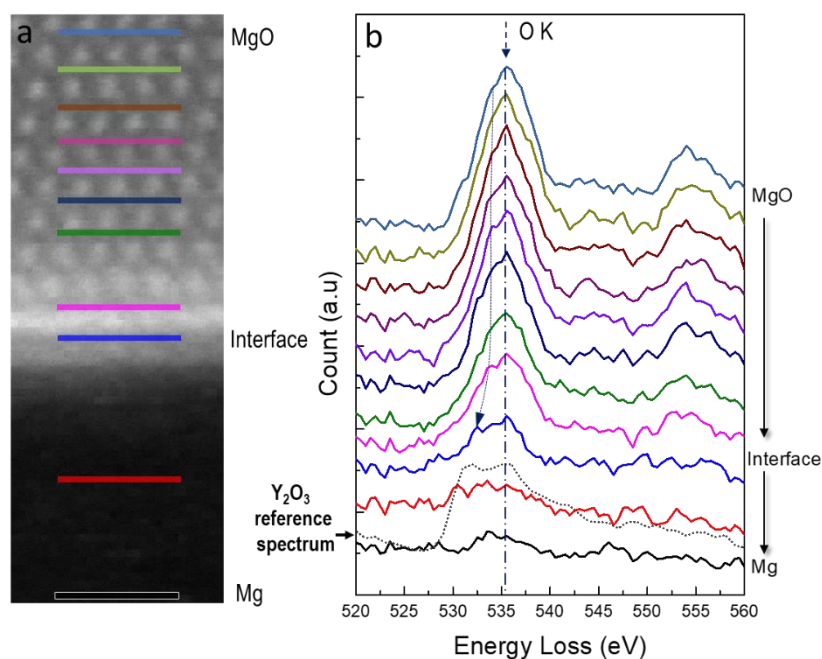


Fig. 5.25 EELS spectra showing the evolution of ‘O’ edges across the MgO/Mg interface with Y_2O_3 2DC in Mg-0.5Y-prefil. Note that the incident beam is parallel to $\langle 011 \rangle_{MgO}$ direction.

One of the reported bulk Y_2O_3 has a lattice structure of FCC (space group: $Fm\bar{3}m$, $a_{Y_2O_3-fcc}=5.264\text{\AA}$, atomic coordinates: ‘O’=(0.25,0.25,0.25); ‘Y’=(0,0,0)) [221]; and the other one has a BCC lattice structure (space group: $Ia\bar{3}$, $a_{Y_2O_3-Ia-3}=10.6\text{\AA}$, atomic coordinates: ‘O’=(0.25,0.25,0.25); ‘Y1’=(-0.032,0,0.25); Y2’=(0.391,0.152,0.38)). They both have a 4-fold symmetry around the normal direction of $\{001\}_{Y_2O_3}$. From the results of this work, the Y segregation layer on the $\{111\}_{MgO}$ facet owns the same symmetry as the bulk Y_2O_3 and a close lattice parameter ($2.731\text{\AA} \approx \frac{1}{2}a_{Y_2O_3-fcc} \approx \frac{1}{4}a_{Y_2O_3-Ia-3}$). Moreover, the similar contrast of the Y-rich columns suggests that Y atoms occupy only in one equivalent lattice site. Therefore, the Y segregation layer can be considered as Y_2O_3 two-dimensional compound (2DC) in a crystal structure similar to that of the FCC Y_2O_3 [223]. The “lattice parameters” of the Y_2O_3 2DC (2.731\AA) is 3.76% larger than that of the bulk FCC Y_2O_3 ($\frac{1}{2}a_{Y_2O_3-fcc}=2.632\text{\AA}$), which is probably the result of surface relaxation.

Applying the determined atomic configuration (Y_2O_3 2DC) on the $\{111\}$ facet of MgO, a well-defined orientation relationship between them is established according to the HAADF STEM images from different directions. As demonstrated by stereographic projection in Fig. 5.26, the OR is:

$$(11\bar{1})[2\bar{1}1]_{\text{MgO}} // (100)[001]_{\text{Y}_2\text{O}_3\text{-2DC}}$$

This OR explains the observed square unit and blurry feature for the Y_2O_3 2DC in HAADF STEM images (Figs. 5.12 to 5.16). As shown in Fig. 5.26, the square unit occurs under the projection parallel to $[2\bar{1}1]_{\text{MgO}}$ and $[0\bar{1}0]_{\text{Y}_2\text{O}_3\text{ 2DC}}$ (Fig. 5.12). In contrast, Y_2O_3 2DC get blurred when the zone axis becomes $[101]_{\text{MgO}}$ and $[0\ -0.866\ 0.5]_{\text{Y}_2\text{O}_3\text{ 2DC}}$, a rotation around $[11\bar{1}]_{\text{MgO}}$ by 30 degrees (Fig. 5.14). But the square unit reappears when the rotation is 90 degrees (Fig. 5.16), the new zone axis becomes $[011]_{\text{MgO}}$ or $[001]_{\text{Y}_2\text{O}_3\text{ 2DC}}$ at the moment. Therefore, for either zone axis of $\langle 011 \rangle_{\text{MgO}}$ or $\langle 112 \rangle_{\text{MgO}}$, the segregation layer can exhibit as a square or blurry feature. With the input of the proposed atomic model, STEM image simulations were carried out using the QSTEM [225]. The results in Fig. 5.27 exhibit an excellent qualitative agreement to the experimental results in Figs. 5.12 to 5.16.

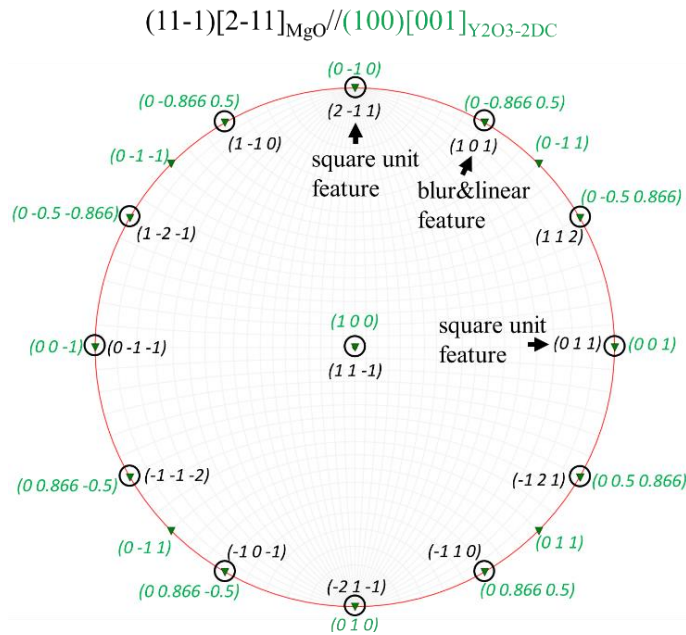


Fig. 5.26 Stereographic projection showing the OR between segregated Y_2O_3 2DC and MgO: $(11-1)[2-11]_{\text{MgO}} // (100)[001]_{\text{Y}_2\text{O}_3\text{-2DC}}$.

It was reported that Y_2O_3 is more stable than MgO in the Ellingham diagram [226,227], and recent thermodynamics calculations show that Y_2O_3 can form and coexist with MgO at 500°C when the Y concentration is sufficiently high [228]. Due to the locally atomic segregation of Y onto the $\{111\}$ faces of MgO driven by the reduction of interfacial energy, the chemical activity of Y atoms increases with local concentration, making the

replacement of Mg atoms and the formation of Y_2O_3 2DC possible when it goes beyond a critical value. The segregation layers replace MgO as a new substrate for nucleating the Mg grain. Its potency will be evaluated from both geometrical and chemical points of view in what follows.

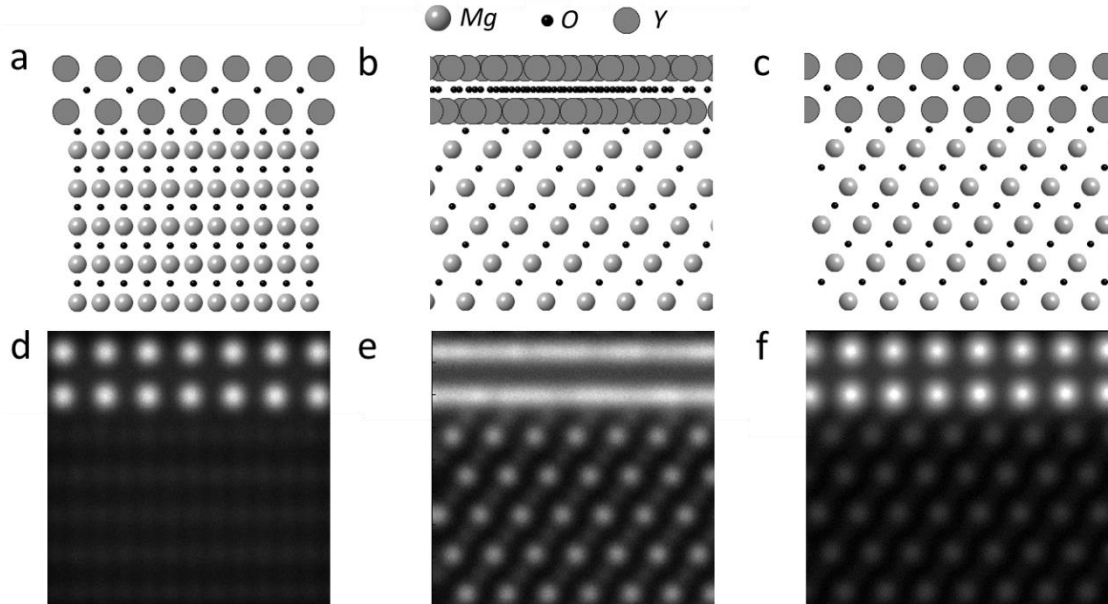


Fig. 5.27 (a-c) The constructed atomic model of segregated Y_2O_3 2DC onto $\{111\}$ plane of MgO being viewed along z zone axes of (a) $[2-11]_{MgO}$, (b) $[101]_{MgO}$ and (c) $[011]_{MgO}$, respectively; (d-f) The corresponding simulation of HAADF STEM images. As inputs for simulation, the proposed atomic model with a thickness of 10nm and relevant actual STEM parameters during the practical operation were applied for simulation.

5.3.3.2 The potency of Y_2O_3 2DC for nucleating α -Mg

The formation of an interface with a good crystallographic match between two phases is driven by lowering interfacial free energy. In terms of nucleation, the geometrical lattice match between a substrate and the nucleating solid thus becomes a criterion for evaluating nucleating potency, with many theoretical models being developed [14–16,34]. The epitaxial model [34] describes the mechanism of heterogeneous nucleation on a substrate as dynamic atomic adsorptions layer by layer, where the critical undercooling is related to the lattice misfit at the substrate/solid interface.

There will be a well-defined OR between the substrate (N) and the solid phase (S) as: $(hkl)[uvw]_S // (h'k'l')[u'v'w']_N$, from which the lattice misfit can be derived as: $f = \frac{d_S - d_N}{d_S} \times 100\%$, Where d_S and d_N are respectively the interatomic spacings along the matching directions for the solid and the nucleating substrate. And d_N lies on the terminating crystal plane of the substrate. If segregation occurs on the surface of a

substrate, the segregated layer will replace the original faceted plane and provides a new matching plane. In the case of Y segregation here, naturally exposed facet of $\{002\}_{Y_2O_3-2DC}$ is chosen for $(h'k'l')$ of the MgO with Y_2O_3-2DC . By comparing the mismatch between $\{002\}_{Y_2O_3-2DC}$ and the close or nearly close-packed planes in α -Mg (**Table 5-2**), two candidates ($\{0002\}_{Mg}$ and $\{10-10\}_{Mg}$) are found for (hkl) . In the next step, the lattice misfits for possible parallelism between direction pairs (close or near close-packed directions) on the above crystal planes are calculated. The minimum lattice misfit (1.71%) is achieved for $\langle 100 \rangle_{Y_2O_3-2DC} // \langle 10-10 \rangle_{Mg}$. Therefore, the most likely OR is: $\{002\} \langle 100 \rangle_{Y_2O_3-2DC} // \{0002\} \langle 10-10 \rangle_{Mg}$, under which the lattice misfit is minimised at the S/N interface, so as the interfacial energy in terms of lattice matching. The resulting atomic model is schematically shown in **Fig. 5.28(a)**, with atomic configurations on the matching crystal planes being shown in **Figs. 5.28 (b-c)**.

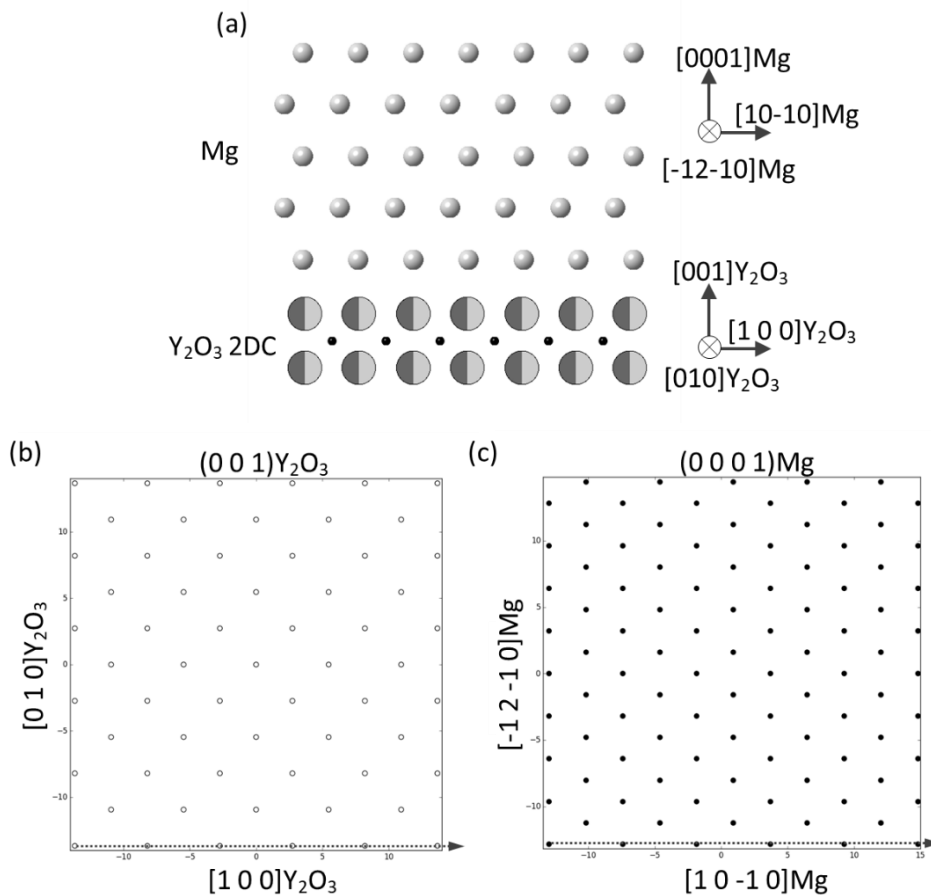


Fig. 5.28 (a) Atomic model of the predicted orientation relationship based on the epitaxial model; (b, c) the atomic configurations of the matching planes of $(001)_{Y_2O_3-2DC}$ and $(0001)_{Mg}$, respectively. The lattice misfit was calculated by applying the directions shown by dashed lines.

Such OR is yielded through the above procedure seeking a configuration with minimum misfit shows consistency with the experimental results found by Xu *et al* [229], although the substrate is C-Y₂O₃ that has the crystal structure of Ia $\bar{3}$ and a lattice parameter of $a=1.06\text{nm}$ [223], which can be considered as a distorted CaF₂ structure (Fm $\bar{3}m$) by removing a quarter of anions. The Y₂O₃ variants are identical to each other in terms of the lattice spacing with a certain tolerance of the lattice deviation. It is reasonable to see that such two types of Y₂O₃ should have the same OR with Mg when serving as the nucleating substrate. Moreover, we critically re-analyse the EDS and HRTEM results in their work [229]. The absence of misfit dislocation and local composition may conflict the author's argument that Cu formed on the edge of C-Y₂O₃ (space group: Ia-3). Instead, it is more likely to be Fm $\bar{3}m$ Y₂O₃. Additional proof comes from the thickness in HRTEM images (< 20 nm) being not identical as the indicated thickness of around 100 nm from the EDS profile across the Y₂O₃/Mg interface. Moreover, the bump of Cu intensity in the EDS profile is much smaller than the Mg intensity. It is more likely that Cu segregates at the Y₂O₃/Mg interface rather than forming nano-sized Cu layers. Therefore, the rational substrate contacting Mg becomes Fm $\bar{3}m$ Y₂O₃ rather than C-Y₂O₃ or Cu, which yields exactly the identical OR as we deduced above.

In addition to the influence of the crystalline structure on the potency of a substrate, previous work [45] has shown that chemistry at the interface also plays an essential role. The presence of an 'attractive' element on the termination surface can promote heterogeneous nucleation by enhancing pre-nucleation above liquidus. The concept of 'attractiveness' can be evaluated by the heat of mixing between two elements (ΔH^{mix}). In the case of MgO/Mg-Y system in this study, the surface layer of {200} Y₂O₃ 2DC contains Y only (**Figs. 5.12, 5.13, 5.15 and 5.16**), so that Y atoms directly contacts with the Mg atoms in the melt. The heat of mixing between Y and Mg was reported as: $\Delta H_{Y-Mg}^{mix} = -6 \text{ kJ/mol}$ [230], suggesting a strong and attractive force between Y and Mg atoms, which leads to a promotion of pre-nucleation resulting in an enhancement of both atomic layering and in-plane ordering. Since the end-state of prenucleation serves as the starting point for heterogeneous nucleation, the negative ΔH_{Y-Mg}^{mix} will facilitate the following heterogeneous nucleation as well.

As a result, the segregation of Y on {111} facets of MgO induces the formation of Y₂O₃ 2DC, which in turn will promote heterogeneous nucleation of α -Mg grains, both in terms

of its structure (by lowering the structural misfit between Mg and MgO) and in chemical terms (by enhancing the ‘attractiveness’ of the nucleating surface to Mg atoms in the melt).

Table 5-2 Planar mismatches (%) between $\{002\}_{Y_2O_3-2DC}$ and the close or nearly close-packed planes in Mg, and the lattice misfits (%) along the directions pairs on the matching planes.

| | $\{0002\}_{Mg}$ | $\{10-11\}_{Mg}$ | $\{11-20\}_{Mg}$ | $\{10-10\}_{Mg}$ |
|---|-----------------------------|------------------------------|------------------------------|------------------|
| | 0.2605 nm | 0.2452 nm | 0.1605 nm | 0.2779 nm |
| $\{002\}_{Y_2O_3-2DC}$ 0.2731 nm | -4.84 | -11.38 | -70.21 | 1.71 |
| | $\langle 0001 \rangle_{Mg}$ | $\langle 10-10 \rangle_{Mg}$ | $\langle 11-20 \rangle_{Mg}$ | |
| | 0.521 nm | 0.5557 nm | 0.3209 nm | |
| $\langle 110 \rangle_{Y_2O_3-2DC}$ 0.3862 nm | 25.87 | 30.5 | -20.35 | |
| $\langle 100 \rangle_{Y_2O_3-2DC}$ 0.5462 nm | -4.84 | 1.71 | -70.21 | |

Note that the lattice parameters of Mg (HCP, $a=0.3209\text{nm}$, $c=0.521\text{nm}$) at room temperature were applied for calculation, while the lattice parameters of segregated Y_2O_3 2DC ($a=0.5462\text{nm}$) were experimentally measured in this work.

5.3.3.3 Y-substitution mono layer on MgO {100} facets

Y segregation layer on the {100} facet of MgO exhibiting as a mono-layer on which Y atoms selectively substitute the Mg atoms (**Figs. 5.17** and **5.18**), which is different from the of Y_2O_3 2DC on the {111} facet. Although Y has a higher affinity with O, the large misfit in lattice parameters on this crystallographic facet impedes the formation of Y_2O_3 2DC on the $\{100\}_{MgO}$ facets ($a_{Y_2O_3-2DC} = 2.731\text{\AA}$ vs. $\frac{1}{2}a_{\langle 100 \rangle_{MgO}} = 2.105\text{\AA}$). According to the experimental results in **Figs. 5.10**, **5.11**, **5.17** and **5.18**, an atomic model is built as shown in **Fig. 5.29(a)**, some Mg atoms on the outmost {100} plane are substituted by Y atoms, in a configuration of square structural units with a lattice constant of 4.211\AA identical to the lattice constant of MgO (**Fig. 5.29(b)**). Such an atomic configuration leads to the bright contrast seen from different viewing directions (**Figs. 5.29(c-d)**). The Mg atoms on the {100} faceted are partially substituted by Y atoms. As illustrated in **Fig. 5.20**, after a critical electron dose the adsorbed Y substitution mono-layer was visibly damaged, leaving behind less occupied Mg/O mixed column than the adjacent MgO (in **Fig. 5.20(c)**). It is noted that the electron beam could have beam-assist healing [231] or beam drilling [232] when illuminating a sample, more careful study would be needed to

confirm our hypothesis. It may suggest that the damage proceeds by knocking out the substitutional Y atoms from the mixed columns, leaving only Mg and O originally present in these atomic columns. As applied proposed atomic model (Figs. 5.29(a-d)) as input for multi-slice image simulations with QSTEM software [225], qualitatively good matches with the experimental results are obtained, as shown in Figs. 5.29(e, f).

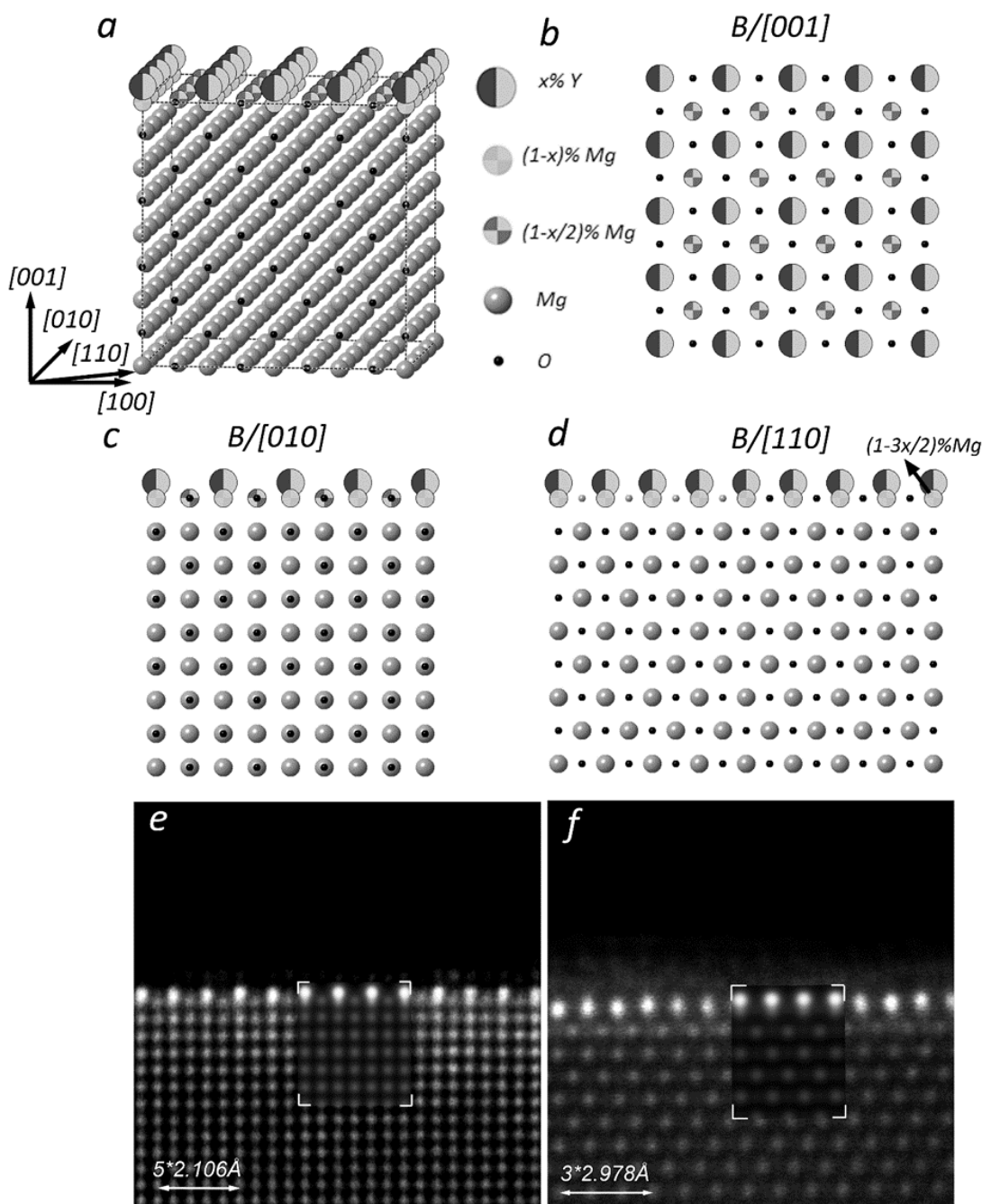


Fig. 5.29 (a) Atomic model of Y segregation onto {100} plane of MgO and (b-d) projections from zone axes of (b) [001], (c) [010] and (d) [110], respectively; and (e, f) simulation of HAADF STEM images showing good matches with the experimental HAADF images in Fig. 5.17 and Fig. 5.18. As inputs for simulation, the proposed atomic model with a thickness of 10nm and relevant actual STEM parameters during the practical operation were applied for simulation.

5.3.3.4 The potency of Y-substitution mono layer for nucleating α -Mg

Since the displacement is perpendicular to the interface, the spacings along a crystal direction lying on the terminated crystal plane will be invariant, the lattice misfit of {100} MgO before and after partial substitution of Y in the terminated {100} plane should be not changed. Nevertheless, the accurate atomic matching will be deteriorated to some extent as the result of the displacement of substituted Y^{3+} ions and the creation of Mg^{2+} vacancies due to the charge neutrality (as schematically shown in **(Fig. 5.29(d))**). Recent studies have shown that surface roughness of a substrate at the atomic scale can impede the prenucleation process above liquidus [46,233]. The Root mean square (RMS) relationship can evaluate the atomic roughness by [233]: $R_{RMS} = [\sum(\Delta z/d_p)^2/n]^{1/2} \times 100\%$, where Δz is the displacement of a substituted Y atom with respect to the original lattice plane with spacing of d_p , n is the number of atoms in the lattice plane. It shows that the substituted Y atoms will introduce atomic roughness as a function of the percentage of substituted Y atoms (**Fig. 5.30**). The maximum R_{RMS} value is 38.3% when 100% of indicated Mg atoms in the configuration are replaced by Y atoms, this value decays as the number of substituted Mg atoms decreases; the calculated roughness is 27.1% if only half of the Mg atoms are replaced. It is worth noting that the majority part of the roughness results from Mg-vacancies creation. The recent DFT work by Fang and Fan [31] has revealed that the interaction between the O-terminated {111} MgO and liquid Mg give rise to an ordered Mg layer on the MgO surface, and that this ordered Mg layer is atomically rough due to the existence of around 8% vacancies. The atomically rough surface makes {111} MgO even more impotent for nucleation of Mg [46], corresponding to the relatively high nucleation undercooling (ΔT_n) required. In this case of {100} facet with atomic roughness induced by Y substitution, its potency is suggested to be poisoned to a certain degree.

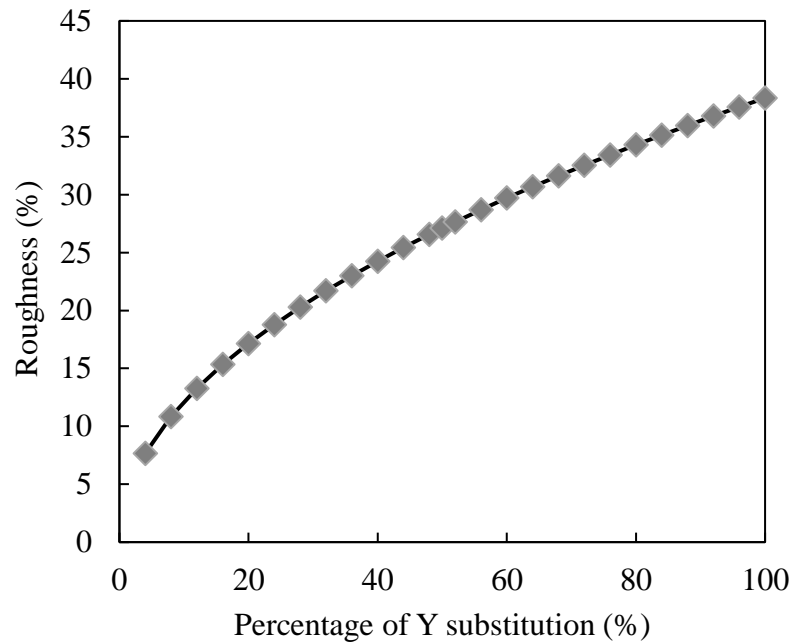


Fig. 5.30 The graph showing the surface roughness as a function of the percentage of Y substitution in terminated {100} plane of MgO.

5.3.4 Mechanism underlying grain refinement

The as-cast grain size is determined by the active number density of nuclei that can free grow before recalescence, which is the result of a competition between the latent heat released by grain growth and the heat extraction. The free growth model has been applied to describe grain initiation behaviour and to predict the as-cast grain size. For a specific system, the following variables are interdependent on each other to affect the grain size: *i*) potency, number density, size and size distribution for the nucleating particles; *ii*) solute concentration and other thermodynamic parameters for the melt; and *iii*) cooling rate for the casting condition [17,63,224]. It is necessary to verify any possible changes in these variables. Firstly, in the current case, the size distribution of the native MgO particles was invariant after Y addition, as shown in **Figs. 4.3, 4.4, 4.12** and **5.4** and **5.5**. Secondly, the growth restriction effect is necessary but not the predominant factor since: *a*) the effect of solute become minor over 0.1% Y addition, and 0.5% Y addition does not have any further positive effect on grain size (**Figs. 5.2(e,f)** and **5.3(e,f)**); *b*) the solute concentration in practice is less than the nominal 0.1Y due to the segregation of Y at the surface of MgO, diluting again the already marginal Q effect. Thirdly, the cooling rate was kept the same as 3.5K/s by casting into TP-1 mould. Lastly, significant changes happened in the samples after HSMC application: the native MgO particles are not only atomically decorated by Y segregation to modify the nucleation potency (**Figs. 5.6** to **5.17**), but also become more homogeneously distributed in the melt [134,164]. Among

them, those terminated by Y_2O_3 2DC on $\{111\}$ facets (**Fig. 5.27**) are made more potent for nucleating α -Mg owing to the tuned lattice misfit (1.71%) and the reduced chemical heat of mixing. Even though those $\{100\}$ terminated MgO may be poisoned due to the atomic surface roughness induced by the Y-rich monolayer at the interface, it has been verified in **Chapter 4** that $\{100\}$ MgO particles originated from vapour oxidation only represents a small proportion of the total population of MgO particles. The vast majority of MgO particles are the so-called ‘octahedral’ or $\{111\}$ MgO that is terminated mainly by $\{111\}$ facets. Therefore, it is reasonably concluded that the major proportion of the native $\{111\}$ MgO are enhanced for heterogeneous nucleation of α -Mg, in which case a lower undercooling is required. If all other parameters are constant or negligibly varied, it is thus highly possible that more particles of $\{111\}$ MgO with Y_2O_3 2DC will take part in and dominate the grain initiation process in both Mg-0.1Y-HSMC and Mg-0.5Y-HSMC, and hence achieving significant grain refinement.

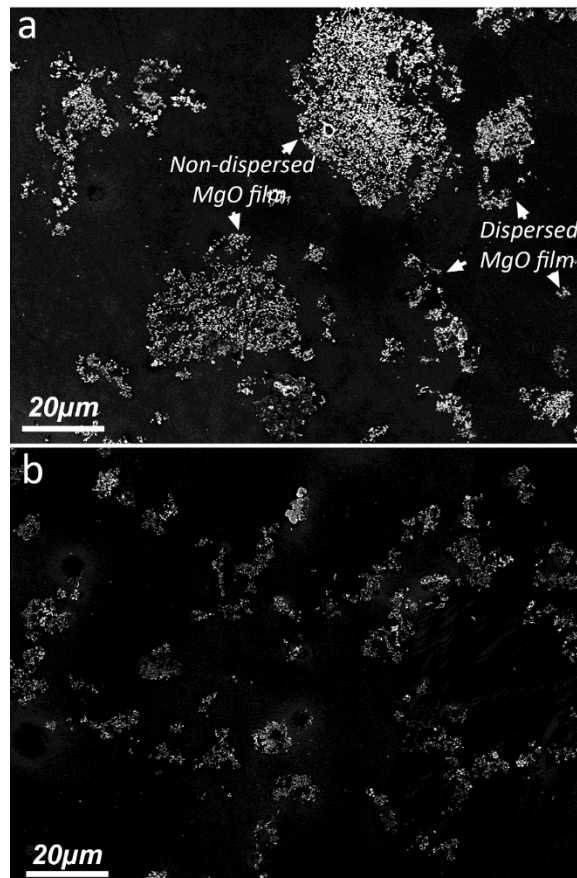


Fig. 5.31 SEM micrographs showing the dispersity of the native MgO in (a) filtered CP Mg and (b) filtered Mg-0.5Y after HS treatment.

The number density of nucleating particle is also of importance for grain refinement [63], an increasing number density decreases the grain size, and this effect will saturate beyond a critical value [17,63,67,234]. The enhanced grain refinement Mg alloys by native MgO particles has been studied before by Fan *et al.* who pointed out that the dispersion of MgO by HSMC plays a key role in providing sufficient particles for heterogeneous nucleation [134]. The driving force for the segregation of a solute is the minimization of the Gibbs free energy [33,184,187]; so that the segregation of Y at the MgO/Mg interface should lead to a reduction of interfacial energy. And the particle dispersion in a liquid can be promoted due to the reduction of the particle/liquid interfacial energy [235]. Thus, the native MgO particles in Mg-0.1Y-HSMC and Mg-0.5Y-HSMC with Y segregation would be less prone to agglomerate or easier to be dispersed, providing more potential substrates for nucleation and grain initiation.

To compare the dispersion in CP Mg-HSMC and Mg-0.5Y-HSMC, the filtered melt of CP Mg and Mg-0.5Y concentrated with native MgO were re-melted and subjected to HS to evaluate their dispersity. As shown by SEM images in **Fig. 5.31**, qualitatively, the native MgO particles are more dispersive in Mg-0.5Y than in CP Mg after HSMC. Large MgO films with tens of microns in size are still present in CP Mg, while all of them have been distributed into small MgO clusters in Mg-0.5Y. As a result, without changing the total amount of native MgO particles, the number density of the potential particles in Mg-0.5Y-HS shall increase as compared to that in CP Mg-HS, providing another positive contribution on grain refinement.

In summary, the enhanced grain refinement in Mg-0.1Y-HSMC and Mg-0.5Y-HSMC can be mainly attributed to the increased potency as well as the enhanced dispersion of native MgO, both resulting from the segregation of Y onto MgO.

5.3.5 Poisoning effect resulting from grain initiation competition

The average grain size (or average columnar width) against Y content (**Figs. 5.3, 5.21** and **5.22**) are summarised in **Fig. 5.32**. Without HSMC, the columnar width decreases with increasing Y addition, and the CET completion requires Y addition up to 3%. Nevertheless, HSMC significantly reduces the AGS when Y content is equal to or lower than 0.5Y. An exception was found when HSMC is running up to 15mins for Mg-0.5Y alloy, where a coarse and columnar grain structure results. When the Y content equals or over 1%, poisoning effects are also seen for the samples with HSMC treatment that coarse

and columnar grain structure occurs. The poisoning effect will be further discussed in the following content.

Due to the formation of bulk Y_2O_3 (Figs. 5.23 and 5.24), the configuration of inclusions, *i.e.* types (potency), size distribution, number density may be changed. With the same OR as well as minor changes in lattice spacing, the bulk C- Y_2O_3 and Y_2O_3 2DC have similar potency for nucleating α -Mg crystal. As listed in Table 5-3, the lattice misfit based on the OR of $\{004\}_{Y_2O_3-Ia-3} // \{10-10\}_{Mg}$ is -1.73%, whose absolute value is nearly the same as 1.71% for Y_2O_3 2DC (Table 5-2). While in the aspect of the size, the bulk C- Y_2O_3 particles are either comparable to or larger than the native MgO particles (see Fig. 5.23). Although without quantitative statistics, the bulk C- Y_2O_3 particles are believed to have a lower number density than that of the native MgO particles.

The lower number density of the larger C- Y_2O_3 particles, which require less undercooling for free growth, will affect the grain initiation behaviour. According to the free growth model [17], free growth undercooling (ΔT_{fg}) is a function of substrate size, which means grain initiation happens progressively from the largest particle to the smaller ones until recalescence. In Mg-Y-HSMC (Y=, >0.5, or HSMC=15mins), the large bulk C- Y_2O_3 particles nucleate and grain initiate first and gradually followed by the smaller ones. However, the number density of participating C- Y_2O_3 particles is very low until recalescence that stifles the participation of smaller native MgO with Y_2O_3 2DC modification. With a limited number of successful grain initiation events, the solidified grain structures are columnar and coarse.

Table 5-3 Planar mismatches (%) between $\{004\}_{Y_2O_3-Ia-3}$ and the close or nearly close-packed planes in Mg, and the calculated lattice misfits (%) along the directions pairs after selecting the matching planes.

| | $\{0002\}_{Mg}$ | $\{10-11\}_{Mg}$ | $\{11-20\}_{Mg}$ | $\{10-10\}_{Mg}$ |
|--|-----------------------------|------------------------------|------------------------------|------------------|
| | 0.2605nm | 0.2452nm | 0.16045nm | 0.27785nm |
| $\{004\}_{Y_2O_3-Ia-3}, 0.265nm$ | -1.73% | -8.08% | -65.16% | 4.62% |
| | $\langle 0001 \rangle_{Mg}$ | $\langle 10-10 \rangle_{Mg}$ | $\langle 11-20 \rangle_{Mg}$ | |
| | 0.521nm | 0.5557nm | 0.3209nm | |
| $\frac{1}{4}\langle 110 \rangle_{Y_2O_3-Ia-3}, 0.3748nm$ | 28.06% | 32.55% | -16.80% | |
| $\frac{1}{2}\langle 100 \rangle_{Y_2O_3-Ia-3}, 0.53nm$ | -1.73% | 4.62% | -65.16% | |

Note that the lattice parameters of Mg (HCP, a=0.3209nm, c=0.521nm) [35] and Y_2O_3 (Ia-3, a=1.06nm) [223] at room temperature were applied for calculation.

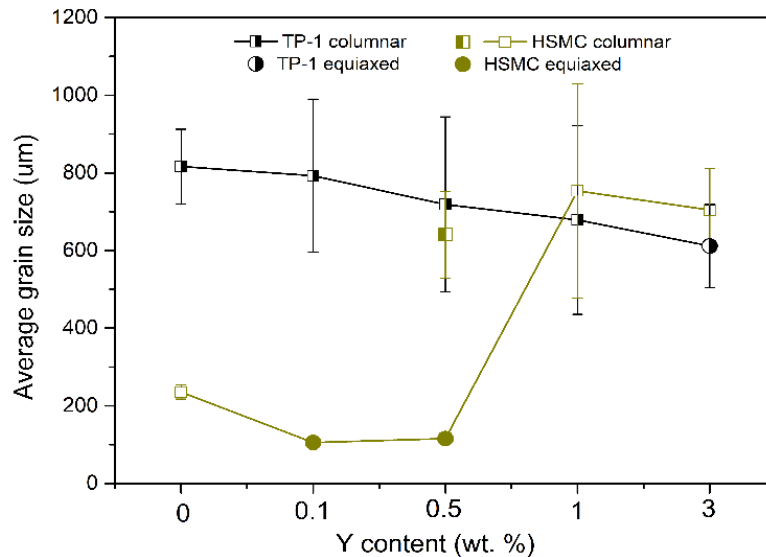


Fig. 5.32 Plot of grain size against Y content for Mg-Y alloys without and with HSMC treatment prior to TP-1 casting.

5.3.6 Effect of substrate on solidification behaviour

Nucleation and growth are two distinct stages for solidification. The changes of the nucleating substrates in terms of nucleation potency, number density, size and size distribution would affect the solidification behaviour [25,51,63,189,236]. It has been demonstrated in this chapter that the selected segregation of Y on native MgO and the formation of Y₂O₃ 2DC effectively promote the nucleation α-Mg grains. An enhanced progressive grain initiation (PGI) results in a refined grain size. The modification in the atomic configuration of the substrate surface is a general phenomenon as reported the previous studies [32,47,181,189,195,203,237,238]. Other than the surface modification, the interaction between Y and MgO particles can occur at the micron scale, resulting in the formation of bulk C-Y₂O₃ particles. The preferential nucleation and grain initiation of Mg on these large bulk C-Y₂O₃ particles result in a coarse columnar grain structure, *i.e.*, the poisoning effect.

It is noticed that the modification of the nucleating particles inevitably redistributes the original particles into two or more types of particles (differing in potency) and therefore the number density and size distribution will be reassigned to each type of particle as well. As a result, both nucleation and grain initiation in the solidification process will be affected, bringing differences in grain size after solidification. This can be illustrated by the cases where the kinetic processes of stripping of Al₃Ti 2DC on TiB₂ in Al alloys, where the remaining TiB₂ with Al₃Ti 2DC decides the final grain size [189]. Another case is the formation of Ti₂Zr 2DC [47] that causes the poisoning of grain refinement in a

function of holding time and/or Zr content, with the mechanism lying on the gradually decreasing number density of TiB_2 with Al_3Ti 2DC which governs the solidification process. Unfortunately, such a kinetic process was not detected in Mg-Y-HSMC ($Y \leq 0.5$), where the addition of 0.5Y brings almost no variation in grain size (**Fig. 5.3**). It is suggested that in Mg-0.1Y-HS the proportion of enhanced $\{111\}$ MgO has already reached a critical value beyond which it dominates both nucleation and grain initiation process. Although further study is required, it is possible that the accelerated kinetics results from the application of HSMC as well as the relatively higher content of Y addition (1000ppm) than 56ppm of free Ti in the case of Al with 0.2 wt.% addition of Al-5Ti-1B master alloy [189].

By either the surface modification of substrate or formation of new bulk phases, the configuration of nucleating particles (particle type, size distribution and number density) is essentially changed, which in turn affects the solidification behaviour. Such change can be originated from substrate/solute or solute/solute reactions ranging from micron to nano scale, or just simply the introduction of new particles. With this in mind, plenty of practically observed phenomena can be rationalised, such as the loss of Zr performance in Al-bearing Mg alloys results from the formation of impotent Al_3Zr that reduces the number density of undissolved Zr particles as well as the Zr solute concentration [26]. Similar cases include the formation of MgO in ZnO-inoculated Mg alloys [117] and of the AlCMn_3 phase in SiC-inoculated Mg alloys containing Mn [106], both of which lead to a poisoning effect. Changes on the number density and size distribution can be seen for Al_2Re intermetallics which coarsen with Al addition, the deviation away from the optimal configuration then results in grain coarsening [112,239].

Above all, the work in this chapter adds to the already wide body of work on grain refinement demonstrating that the interaction between substrate and solute or between solutes is a widely relevant phenomenon in understanding and controlling practical castings. The complexity of these interactions may be the reason why it has been proved so challenging to develop a universal grain refiner for either Al or Mg alloys. Our work emphasises the importance of characterising nucleating particle (crystal structure, number density, size and size distribution) inside an alloy melt, down to the atomic level, to ensure accurate input parameters for subsequent numerical models for simulating the solidification process to give a reliable prediction. This, in turn, should lead to a better understanding of the mechanisms underlying grain refinement at different length scales, ultimately providing valuable guidelines to tailor grain refiners for specific systems.

5.4 Conclusions

1. High shear melt conditioning and the addition of Y offer significant grain refinement accompanied by a fully columnar-to-equiaxed transition in Mg-Y alloys, with $Y \leq 0.5$ and HSMC time = 5mins.
2. Segregation of Y is experimentally confirmed on the both $\{111\}_{\text{MgO}}$ and $\{100\}_{\text{MgO}}$ facets of MgO particles.
3. Segregation of Y on the $\{111\}_{\text{MgO}}$ facet of MgO forms Y_2O_3 2DC that possesses chemical and structural characteristics close to $\text{Fm}\bar{3}\text{m}$ Y_2O_3 , except for a lattice expansion of 3.7%. Heterogeneous nucleation of Mg on the Y_2O_3 2DC modified MgO particle is promoted owing to: *i*) a small lattice misfit of 1.71%; and *ii*) the chemical affinity between Y and Mg.
3. Segregation of Y on the $\{100\}_{\text{MgO}}$ facet of MgO presents as a partial substitution of Mg atoms by Y atoms in the terminated $\{100\}_{\text{MgO}}$ plane. The nucleation potency of the $\{100\}_{\text{MgO}}$ substrate is impeded due to atomic surface roughness introduced by the deviation of Y atoms and the absence of Mg atoms.
4. The mechanism underlying the enhanced grain refinement is attributed to the Y segregation on $\{111\}$ MgO particles which provides: *i*) enhanced potency of $\{111\}$ MgO particles with Y_2O_3 2DC for heterogeneous nucleation of α -Mg; and *ii*) the promoted dispersal of the native MgO particles owing to the Y segregation. More MgO particles are involved in grain initiation activity.
5. The formation of large C- Y_2O_3 particles raises grain initiation competition against the $\{111\}$ MgO particles with Y_2O_3 2DC modification. The small proportion of large C- Y_2O_3 particles dominate the grain initiation, leading to the columnar grain structure with coarse grain widths.
6. The configuration of nucleating particles that includes particle type, size distribution and number density is closely related to the solidification behaviour. Modification in either atomic scale (segregation) or micron scale (new phase formation) alters the configuration of nucleating particles and therefore the resulting grain size.

6 Elemental segregation and its effect on solidification of Mg-Ca and Mg-Sn alloys

6.1 Chapter overview

Alloying is one of the most effective ways to improve the properties of Mg alloys. As two common alloy elements, Ca and Sn are widely used to enhance certain properties of various Mg alloys. For example, the addition of Ca brings about benefits to Mg alloys in many aspects, such as the creep resistance [240], corrosion resistance [126], grain refinement [82], mechanical strength [240] and biocompatibility [241]. As an alloy system developed initially in the early 1930s [242], Mg-Sn based alloys were believed to have the potential for high-temperature applications. The promising mechanical properties are mainly attributed to the intermetallic phase of Mg_2Sn that has a melting point of 770 °C. No matter serving as the major or subordinate alloy addition, both Ca and Sn play as important roles in the development of Mg alloys satisfying certain functions and being applied under certain environment.

In this chapter, the effect of solutes and native MgO particles on solidification of Mg-Ca and Mg-Sn binary alloys was investigated. Standard TP-1 casting was applied to evaluate the grain refinement behaviour in the alloys with different pre-treatments to the melt prior to casting: *i*) without HSMC; *ii*) with HSMC (dispersing oxides); and *iii*) with HSMC and intentional oxidation (introducing more oxides). With the advanced electron microscopy, characterisation was conducted focusing on the interaction between native MgO particles and solutes in the alloy melt. Discussions were made on the atomic modification on the surface of MgO particles that was correlated with their potency for heterogeneous nucleation of α -Mg. Numerical models were applied to rationalise the columnar-to-equiaxed transition (CET) and the grain initiation behaviour of Mg-Ca and Mg-Sn alloys.

6.2 Results

6.2.1 Grain size of Mg-Ca alloys without HSMC

Figs. 6.1 to 6.3 show the as-cast the grain structure and quantified grain size of Mg-Ca alloys (Ca = 0.05, 0.1, 0.3, 0.5, 0.7 and 1 wt.%) that were solidified in a TP-1 mould at a constant cooling rate of 3.5K/s. Obviously, the addition of Ca refines the as-cast grain

structure. Grain structures of the TP-1 samples from both the transverse and longitudinal sections are shown in **Fig. 6.1**, which not only reveal the grain size, but also clarify if the grain structure is columnar or equiaxed. The grain structure of Mg-0.05Ca and Mg-0.1Ca is columnar (**Fig. 6.1(a)**), whose width is narrower as compared to that of the CP Mg (**Fig. 5.1**). The length and width of the columnar grains decrease as the Ca addition increases up to 0.3% (Mg-0.3Ca, **Fig. 6.1(c)**), where equiaxed grains appear in most areas of the TP-1 ingot sample, except for some minor areas near the mould wall where columnar grains remain with a decreased width. Columnar to equiaxed transition (CET) is nearly completed at this stage. As indicated in **Fig. 6.1(d)**, the refining trend continues with increasing Ca addition, leading to the completion of CET in Mg-0.5Ca with fine grain size. More addition of Ca up to 0.7% and 1% reduces further the size of the equiaxed grains.

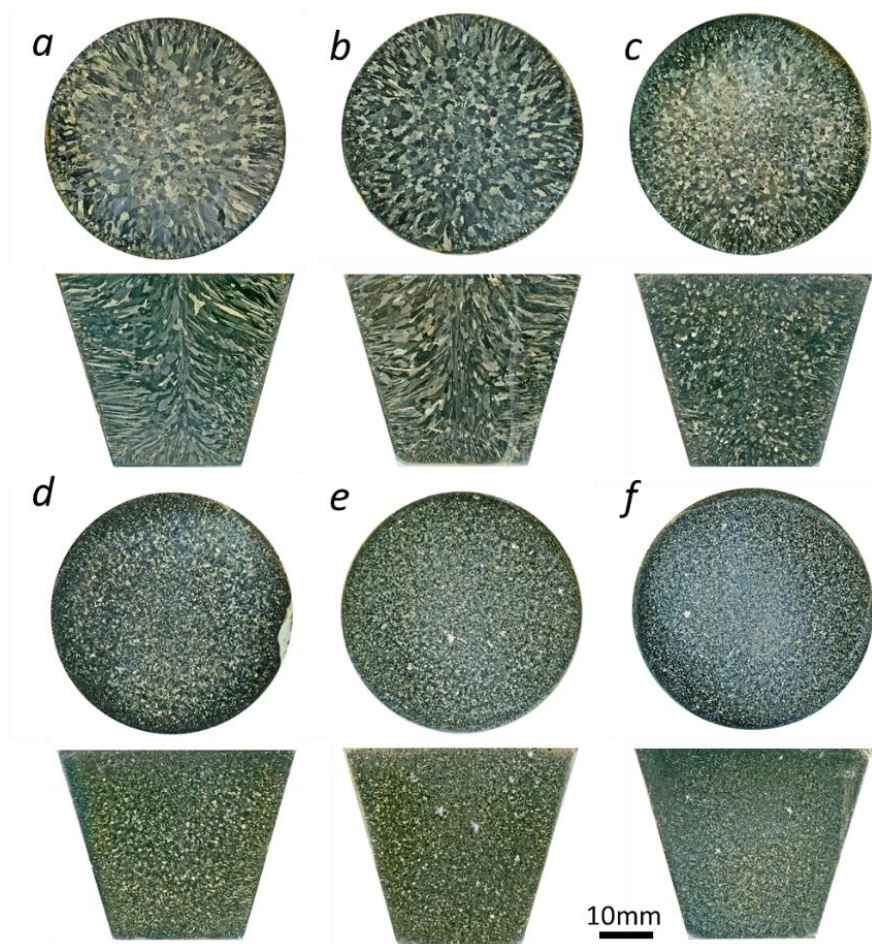


Fig. 6.1 Optical macrographs showing the grain structures on transverse and longitudinal sections of (a) Mg-0.05Ca, (b) Mg-0.1Ca, (c) Mg-0.3Ca, (d) Mg-0.5Ca, (e) Mg-0.7Ca and (f) Mg-1Ca samples without HSMC prior to casting in TP-1 mould.

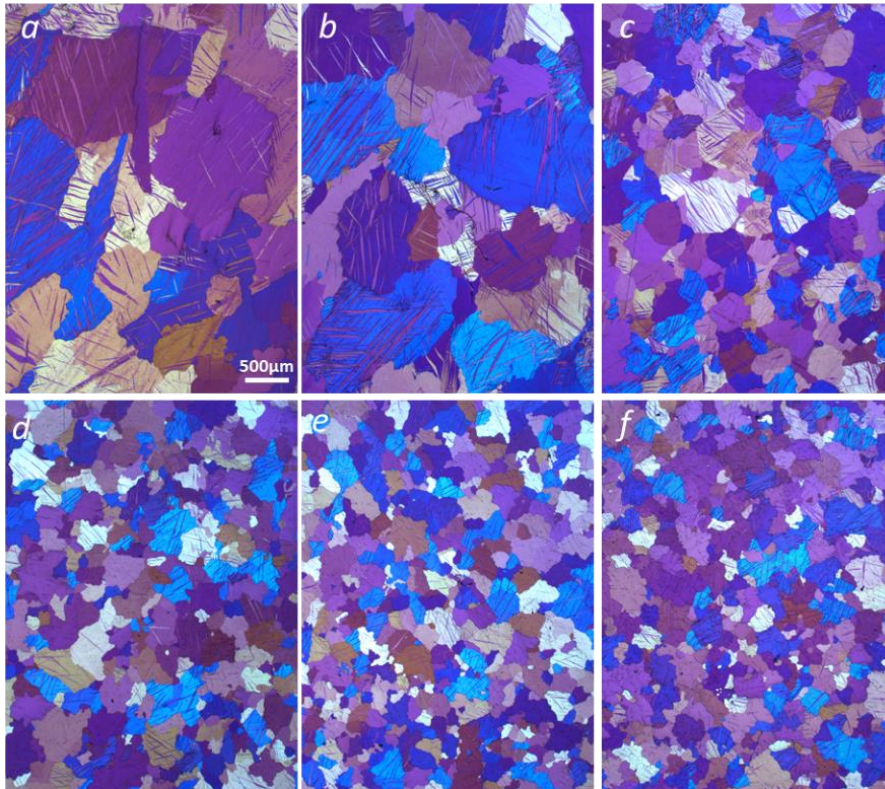


Fig. 6.2 Polarized optical micrographs showing the grain structure of (a) Mg-0.05Ca, (b) Mg-0.1Ca, (c) Mg-0.3Ca, (d) Mg-0.5Ca, (e) Mg-0.7Ca and (f) Mg-1Ca samples cast by TP-1 process without HSMC prior to casting in TP-1 mould. Specimens were sampled from the central area of the transverse section.

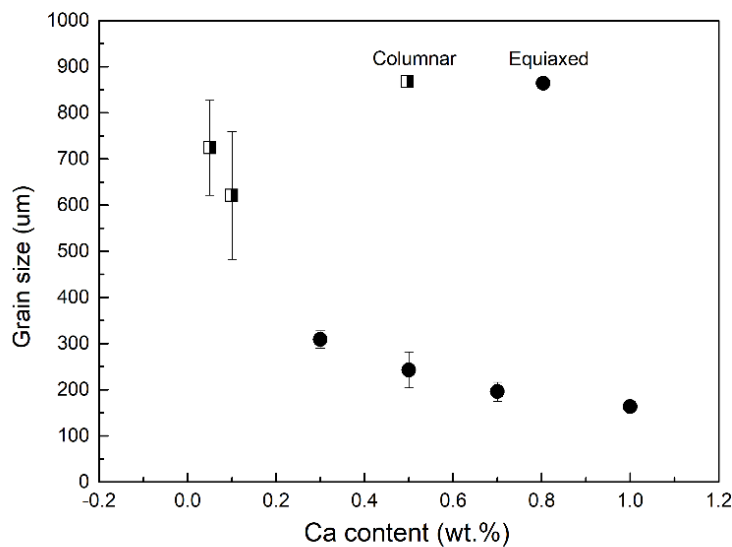


Fig. 6.3 Plot of grain size (columnar width) in a function of Ca concentration for Mg-Ca alloy without HSMC prior to casting in TP-1 mould.

As quantified in **Fig. 6.2** and **Fig. 6.3**, the average columnar width (ACW) drops from $724.2 \pm 102.7 \mu\text{m}$ to $621.4 \pm 138.5 \mu\text{m}$ when the Ca content is increased from 0.05% to 0.1%. With the addition of 0.3% Ca, the central area becomes completely equiaxed, along

with a dramatic reduction in the average grain size (AGS) ($308.8 \pm 18.6 \mu\text{m}$). The AGS decreases to $242.9 \pm 39 \mu\text{m}$, $196 \pm 20.4 \mu\text{m}$ and $163.7 \pm 11.5 \mu\text{m}$ when the Ca concentration is increased to 0.5%, 0.7% and 1%, respectively. It is noted that after the completion of CET (Mg-0.5Ca), the rate of grain size reduction is moderate. Besides, the equiaxed grains in these alloys distribute uniformly over the ingots (**Figs. 6.1(c-f)**).

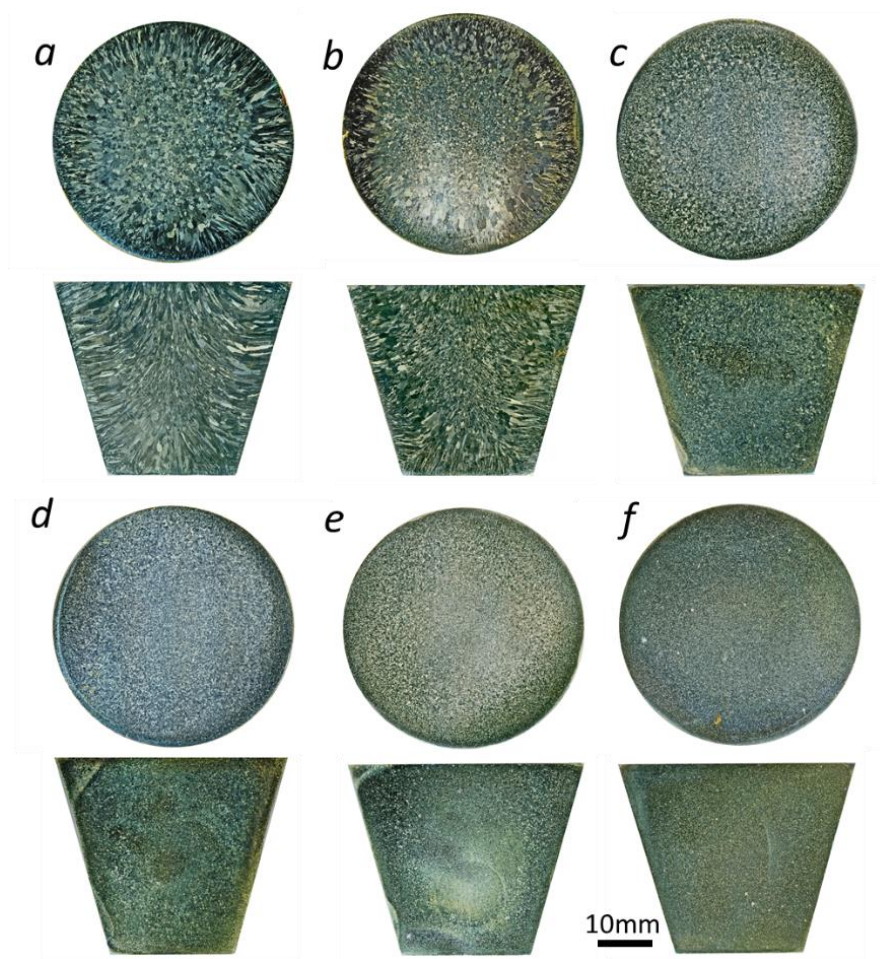


Fig. 6.4 Optical macrographs showing the grain structures of Mg-Ca binary alloys on the transverse and longitudinal sections. (a) Mg-0.05Ca-HSMC, (b) Mg-0.1Ca-HSMC, (c) Mg-0.3Ca-HSMC, (d) Mg-0.5Ca-HSMC, (e) Mg-0.7Ca-HSMC and (f) Mg-1Ca-HSMC samples with HSMC prior to casting in TP-1 mould.

6.2.2 Grain size of Mg-Ca alloys with HSMC

Figs. 6.4 to 6.6 present the as-cast grain structure and the quantified grain size of Mg-Ca alloys (Ca = 0.05, 0.1, 0.3, 0.5, 0.7, 1 wt.%) with HSMC treatment prior to casting into the TP-1 mould. Compared to the TP-1 samples of Mg-Ca alloys without HSMC (**Figs. 6.1 to 6.3**), HSMC treatment offers finer grain structures with the CET occurring earlier in the Mg-Ca-HSMC samples. A similar trend to that found in **Fig. 6.1** can be seen here as well, *i.e.*, the Ca addition firstly reduces the area of columnar grains (**Figs. 6.4(a-b)**), which finally diminishes when 0.3% Ca is added (**Fig. 6.4(c)**); further Ca addition up to

1% only leads to moderate grain size reduction in the rest samples (**Figs. 6.4(d-f)**). Although with columnar grain structures, Mg-0.05Ca-HSMC and Mg-0.1Ca-HSMC exhibit finer columnar widths than their counterparts without HSMC in **Fig. 6.1**. The cooling condition varies from the mould edge to the central area, with a cooling rate of 3.5K/s at the central area 38mm from the bottom. The variation in cooling conditions affects solidified grain structures. It is noticed that abnormally coarse grains exist in the areas a certain distance from the mould wall (**Fig. 6.4(c)**), which are replacing by fine grains with increasing Ca content (**Figs. 6.4(d-f)**).

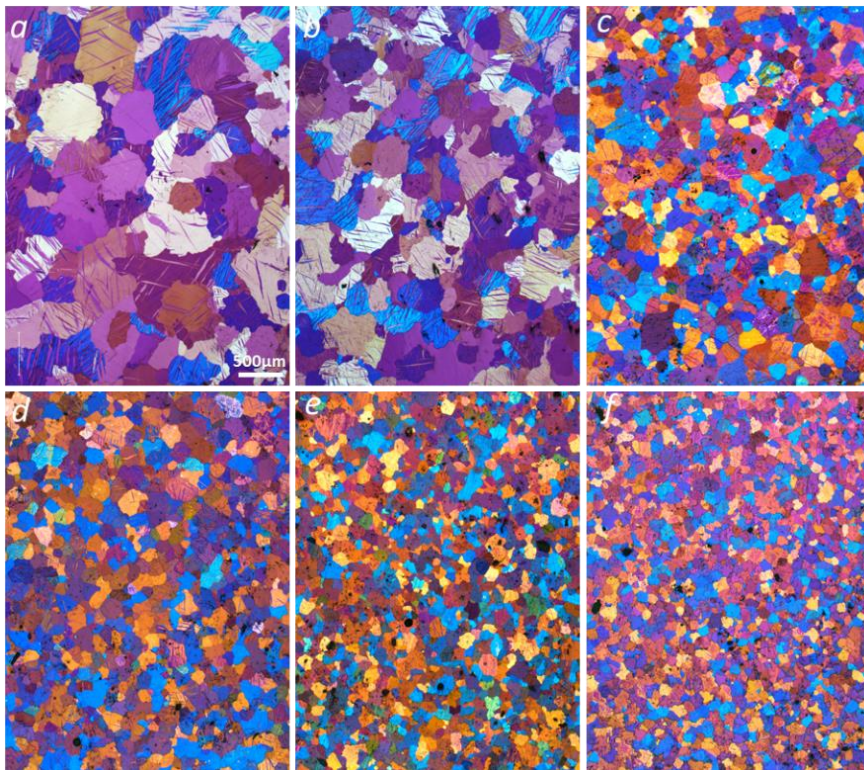


Fig. 6.5 Polarized optical micrographs showing the grain structure of (a) Mg-0.05Ca-HSMC, (b) Mg-0.1Ca-HSMC, (c) Mg-0.3Ca-HSMC, (d) Mg-0.5Ca-HSMC, (e) Mg-0.7Ca-HSMC and (f) Mg-1Ca-HSMC samples with HSMC prior to casting in TP-1 mould. Specimens were sampled from the central area of the transverse section.

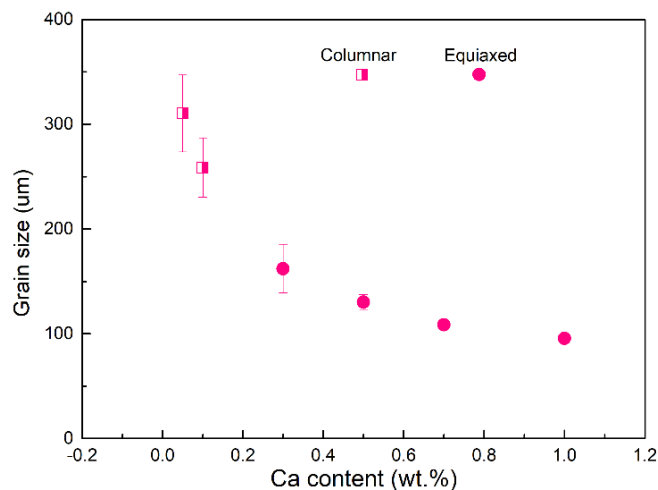


Fig. 6.6 Plot of grain size (columnar width) in a function of Ca concentration for Mg-Ca-HSMC alloys with HSMC treatment prior to casting in TP-1 mould.

The optical microstructure of the Mg-Ca alloys with HSMC is shown in **Fig. 6.5**, with the quantification of grain size (or columnar width) being plotted in **Fig. 6.6**. It is seen that 0.1% Ca addition reduces the ACW from $310.2 \pm 36.8 \mu\text{m}$ (Mg-0.05Ca-HSMC) to $258.7 \pm 28.3 \mu\text{m}$ (Mg-0.1Ca-HSMC). Accompanied by a significant reduction in grain size, CET appears in Mg-0.3Ca-HSMC that has an AGS of $162.2 \pm 23.3 \mu\text{m}$. It is followed by moderate reductions in grain size as the Ca addition keeps increasing (**Figs. 6.5(d-f)** and **6.6**), with the AGS being $130.3 \pm 7.1 \mu\text{m}$, $108.5 \pm 4.6 \mu\text{m}$, $95.5 \pm 4.7 \mu\text{m}$ in Mg-0.5Ca-HSMC, Mg-0.7Ca-HSMC and Mg-1Ca-HSMC, respectively.

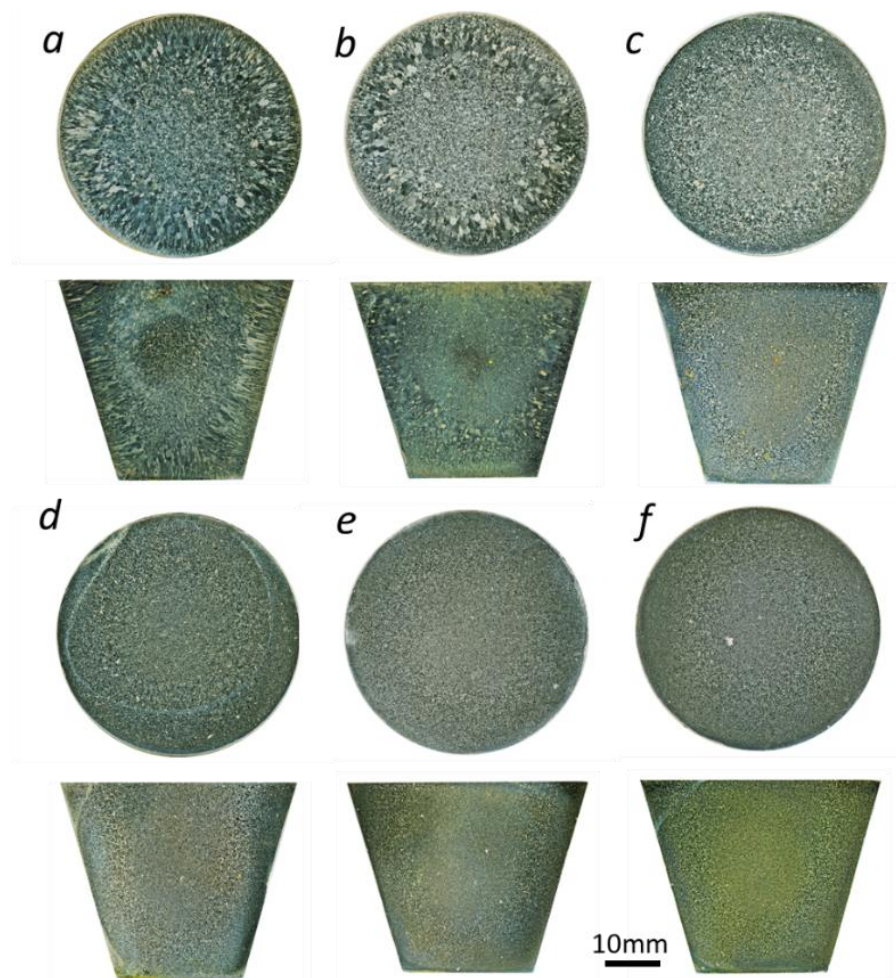


Fig. 6.7 Optical macrographs showing the grain structures on the transverse and longitudinal sections of (a) Mg-0.05Ca-HS, (b) Mg-0.1Ca-HSO, (c) Mg-0.3Ca-HSO, (d) Mg-0.5Ca-HSO, (e) Mg-0.7Ca-HSO and (f) Mg-1Ca-HSO samples treated by HSMC without protection gas prior to casting in TP-1 mould.

6.2.3 Grain size of Mg-Ca alloys with HSMC and oxidation

To generate more oxides, we deliberately removed the protecting gas during the HSMC processing (**section 3.3.3**) prior to casting. The obtained TP-1 ingot samples are referred

to as Mg-Ca-HSO. **Figs. 6.7** to **6.9** show the grain macrostructure and grain size of Mg-Ca-HSO (Ca = 0.05, 0.1, 0.3, 0.5, 0.7, 1 wt.%), where all the samples exhibit smaller columnar widths and/or finer grain sizes than their counterparts of Mg-Ca (**Fig. 6.1**) and Mg-Ca-HSMC (**Fig. 6.4**) samples. Similarly, they share a trend that more Ca content results in finer microstructures. The columnar grains with short lengths and fine widths are seen in the central area of the Mg-0.05Ca-HSO TP-1 sample, whilst the columnar grains have longer lengths, and larger widths in the areas closed to the sample edges (**Fig. 6.7(a)**). The addition of 0.1% Ca causes CET in Mg-0.1Ca-HSO (**Fig. 6.7(b)**). While a ring pattern with abnormally coarse grains near the mould wall is evident by the grain structure on the transverse section of the sample. This phenomenon is significantly weakened when 0.3% Ca is added (**Fig. 6.7(c)**), and it becomes negligible when the Ca addition is higher than 0.5% (**Figs. 6.7(d-f)**).

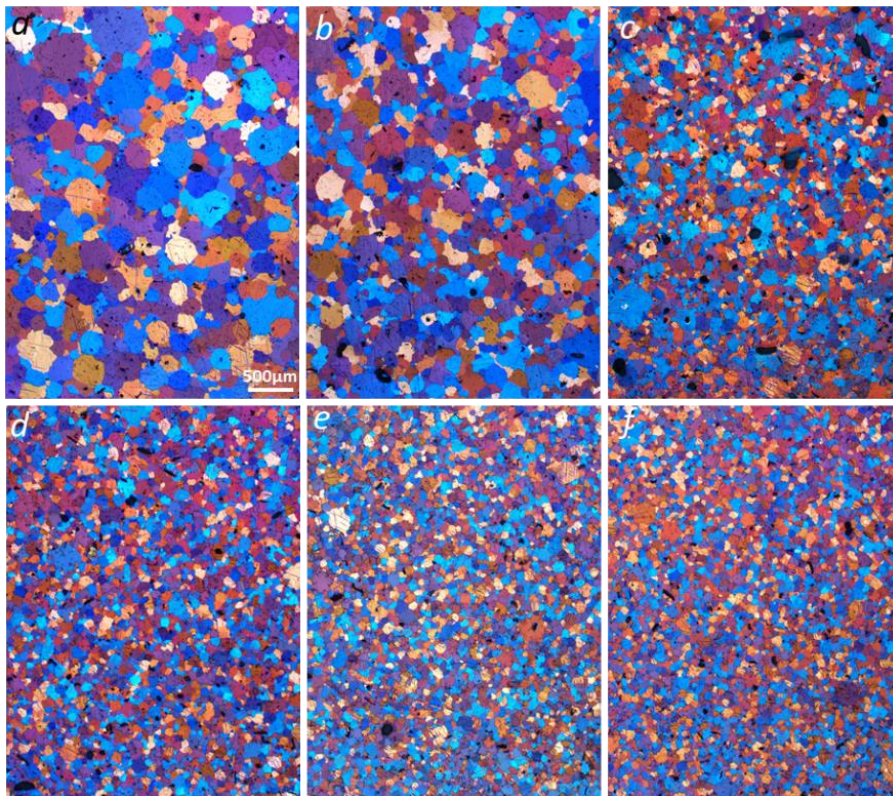


Fig. 6.8 Polarized optical micrographs showing the grain structure of (a) Mg-0.05Ca-HS, (b) Mg-0.1Ca-HSO, (c) Mg-0.3Ca-HSO, (d) Mg-0.5Ca-HSO, (e) Mg-0.7Ca-HSO and (f) Mg-1Ca-HSO samples treated by HSMC without protection gas prior to casting in TP-1 mould. Specimens were sampled from the central area of the transverse section.

The optical micrographs in **Fig. 6.8** present the detailed grain structure of Mg-Ca-HSO samples, whose declining average grain size (or average columnar width) with respect to the increasing Ca addition is plotted in **Fig. 6.9**. The ACW in the central area of Mg-0.05Ca-HSO is $200.3 \pm 17.7 \mu\text{m}$. The grain structure completely transforms from columnar

to equiaxed grains when the Ca addition is increased to 0.1%, with an AGS being $146.6 \pm 7.9 \mu\text{m}$. The AGS keeps going down to $91.3 \pm 6.9 \mu\text{m}$ as the Ca addition reaches 0.3%. Nevertheless, further Ca addition has a marginal effect on reducing grain size, with the AGS being $76.9 \pm 2.2 \mu\text{m}$, $75.2 \pm 4.2 \mu\text{m}$ and $61.4 \pm 5.6 \mu\text{m}$ for Mg-0.5Ca-HSO, Mg-0.7Ca-HSO and Mg-1Ca-HSO, respectively.

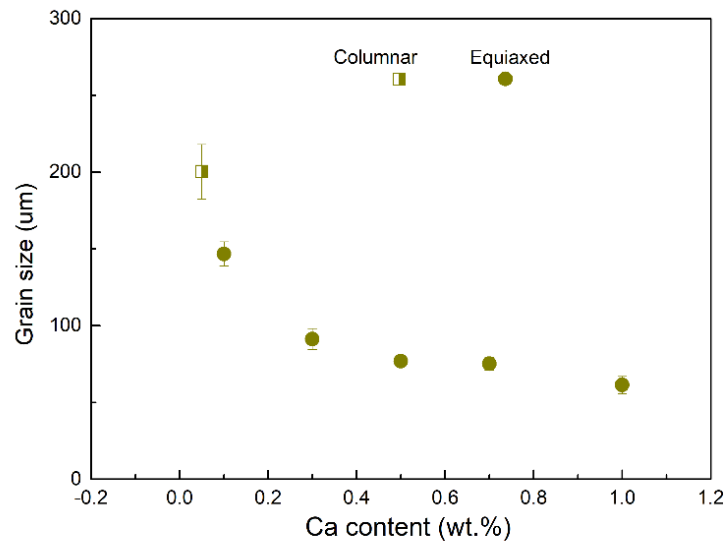


Fig. 6.9 Plot of grain size (columnar width) in a function of Ca concentration for Mg-Ca-HSO alloys treated by HSMC without protection gas prior to casting in TP-1 mould.

6.2.4 Effect of pre-cast treatments on grain size of Mg-Ca alloys

Fig. 6.10 summaries the effect of different treatments prior to casting on CET, ACW and AGS of the Mg-Ca binary alloys. It can be seen that the critical Ca content required for the formation of a fully equiaxed grain structure is affected by the pre-casting treatments. Without HSMC, some regions near the edges still have columnar grains in Mg-0.3Ca, though the central areas are fully equiaxed (**Fig. 6.1(c)**); then the critical Ca content is 0.5% where the columnar grains completely disappear (**Fig. 6.1(d)**). This critical content dramatically drops when HSMC is applied, where only 0.3% Ca is required for CET accomplishment throughout the sample (**Fig. 6.4(c)**). With both HSMC and intentional oxidation imposed, the critical Ca content falls down to 0.1% (**Fig. 6.7(b)**). It is clear that the pre-treatments have a positive effect on CET for the Mg-Ca alloys: the critical Ca addition drops following the sequence: without HSMC > HSMC > HSO.

In the Mg-Ca alloys with the different pre-treatments, another interesting point is that significant grain refinement is accompanied by CET and the grain sizes decrease only

moderately afterwards. Besides, the decreasing rate of grain size after CET is reduced in the order of: without HSMC (TP-1), HSMC, HSO. As shown in **Fig. 6.10**, the curve of Mg-Ca-HSO has the most shallow slope after CET. Other than this, the pre-treatments offer positive effects on grain refinement, either the ACW or AGS follows the sequence as: without HSMC > HSMC > HSO. For example, the average grain size of Mg-1Ca is reduced from 163.7 μm to 95.5 μm when HSMC is imposed, and it decreases further down to 61.4 μm when HSO is applied.

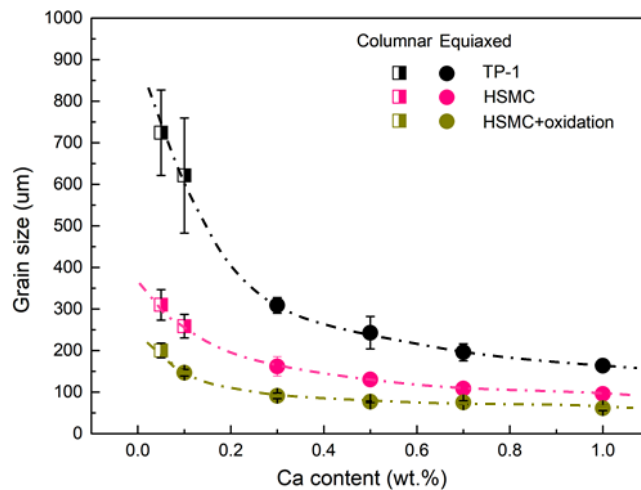


Fig. 6.10 Grain size (columnar width) of Mg-Ca binary alloys as a function of the composition of Ca.

6.2.5 Native MgO in Mg-0.5Ca alloy

Oxides and other possible inclusions were collected from the melt of Mg-0.5Ca by the pressurised filtration technique (**section 3.3.4**) and then examined by electron microscopy. As shown in **Fig. 6.11**, there exist both the {111} MgO (**Fig. 6.11(a)**) and {100} MgO (**Fig. 6.11(b)**) particles, both exhibiting similar average sizes (in a range from 50 to 200 nm) to their counterparts in CP Mg, Mg-9Al (**section 4.2.1**) and Mg-0.5Y (**section 5.2.2**). The EDS spectra in **Fig. 6.11(c)** confirm the major chemical composition of Mg and O. In the energy range 2.8 to 4 keV shown in **Fig. 6.11(d)**, the comparison of characteristic Ca K peaks from MgO particles and Mg matrix indicates that Ca was detected on both {111} and {100} MgO particles.

The BF TEM image in **Fig. 6.11(e)** shows an oxide film consisting of {111} MgO particles that are close to each other in the Mg matrix. The individual MgO particle (highlighted by an arrow) diffracts the electron beam strongly and appears in darker

contrast, exhibiting a faceted morphology. The SAED pattern taken from many oxide particles in the oxide film appears as ring-pattern reflections (**Fig. 6.11(f)**). The indexing of the patterns indicates that the constituent MgO particles are randomly orientated among the oxide film.

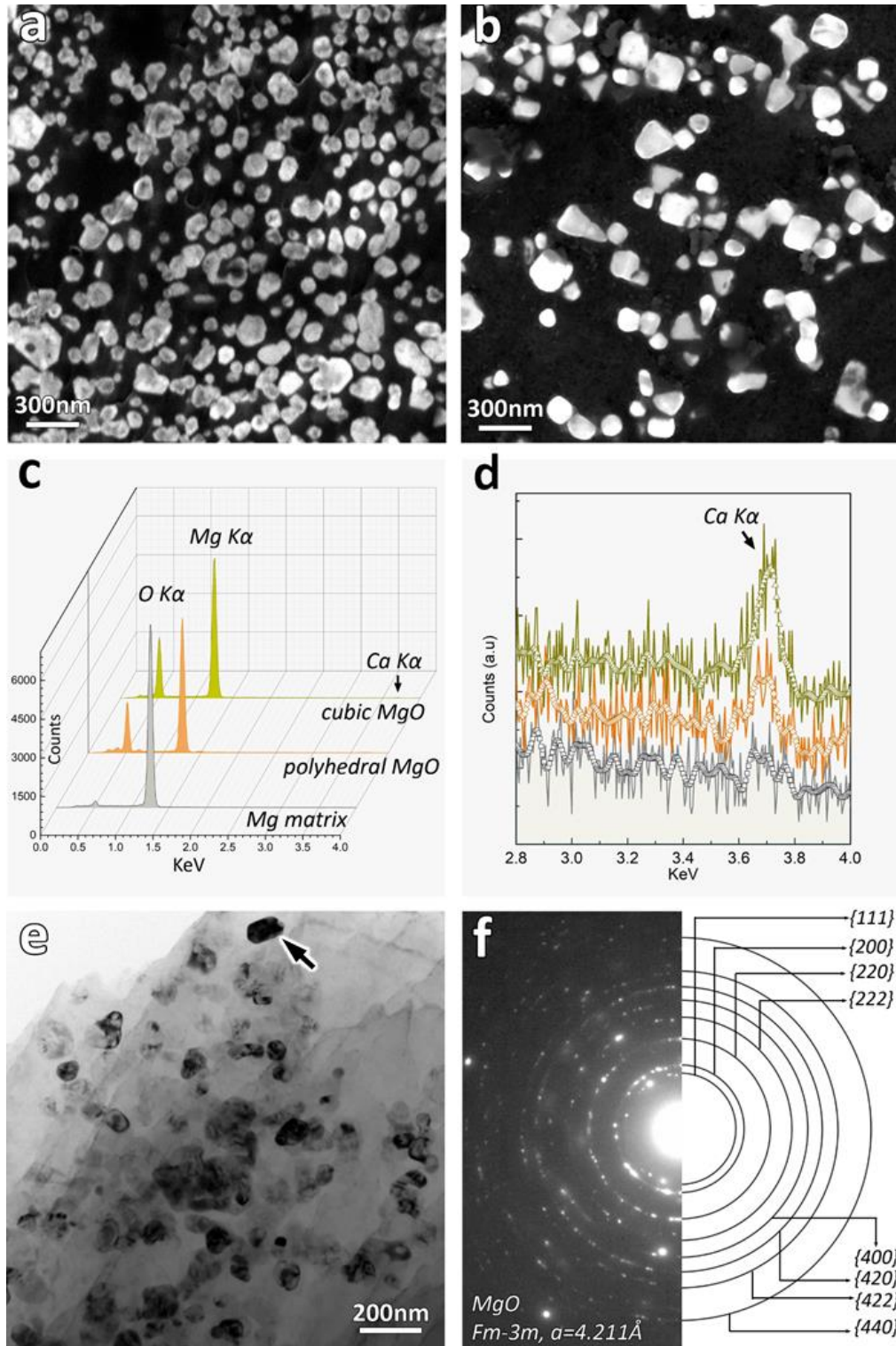


Fig. 6.11 Identification of the {111} MgO and {100} MgO particles in Mg-0.5Ca. (a, b) SEM images, (c, d) EDS spectra, (d) is the local zone of (c) in the energy range 2.8-4 KeV; (e) BF TEM

image of a MgO film and (f) the corresponding SAED pattern indicating that the particles are MgO particles randomly oriented in the film.

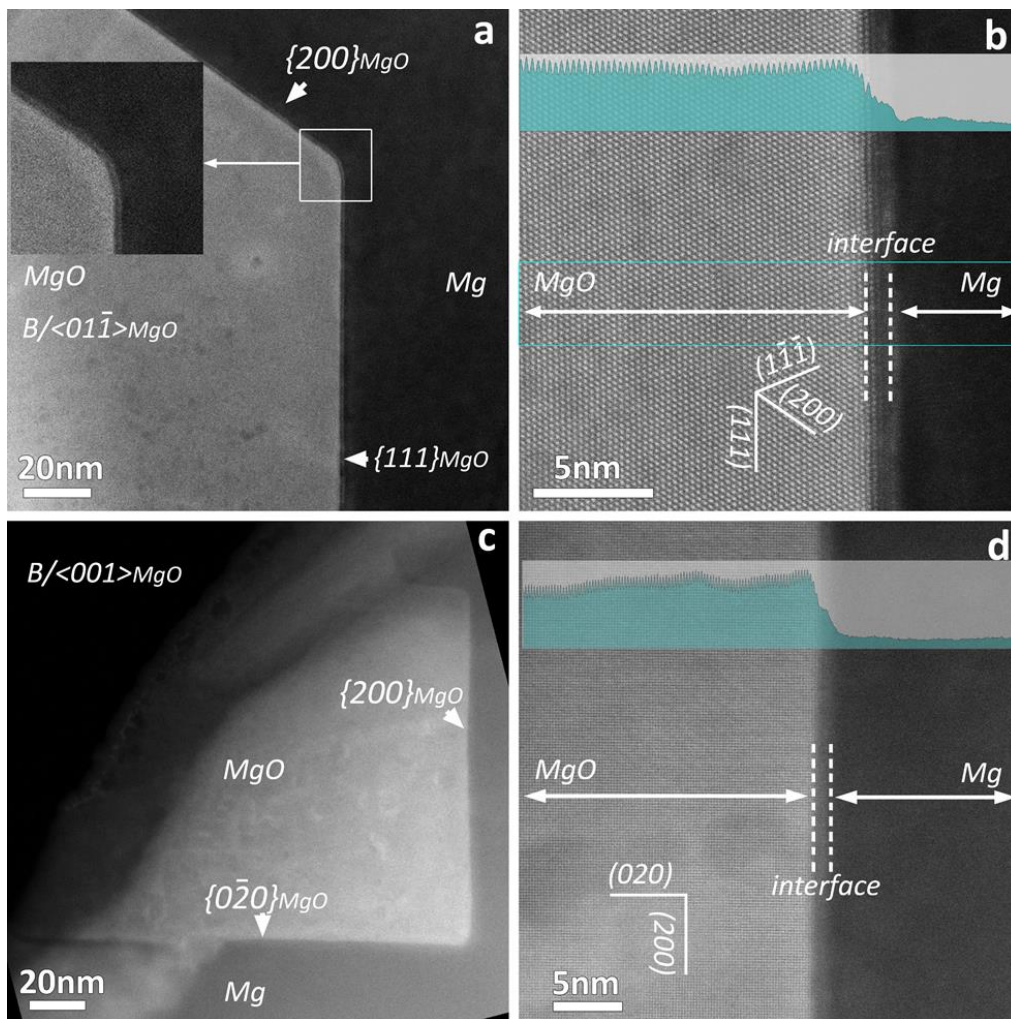


Fig. 6.12 HAADF STEM images showing the segregation layer wrapping over both (a, b) $\{111\}$ and (c, d) $\{100\}$ MgO particles in Mg-0.5Ca-prefil. It was found that the segregation layer shows lower contrast with a few atomic layers in thickness. Note that the incident beams are parallel to $\langle 011 \rangle_{\text{MgO}}$ in (a, b) and $\langle 001 \rangle_{\text{MgO}}$ in (c, d), respectively.

Characterisation of the $\{111\}$ MgO and $\{100\}$ MgO particles was further conducted by HAADF STEM imaging. **Fig. 6.12** shows the HAADF STEM images of $\{111\}$ MgO (**Figs. 6.12 (a-b)**) and $\{100\}$ MgO (**Figs. 6.12(c-d)**) from $[01\bar{1}]_{\text{MgO}}$ and $[001]_{\text{MgO}}$ zone axes, respectively. The interfacial segregation can be observed wrapping over both types of MgO particle and presenting in a relatively lower contrast than the MgO matrix, but brighter than the Mg matrix. The atomic resolution HAADF STEM images in **Figs. 6.12(b, d)** suggest that the segregation layers consist of about three atomic layers ($\sim 1\text{nm}$ in thickness), whose contrast intensity is lower than that of MgO matrix as evidenced from the associating contrast profiles (insets with cyan plots in **Figs. 6.12(b, d)**) across

the Mg/MgO interface. Such segregation layers were reproducibly observed on both $\{111\}_{\text{MgO}}$ and $\{100\}_{\text{MgO}}$ facets of 19 MgO particles in Mg-0.5Ca alloy (**Fig. A-4**, see appendix).

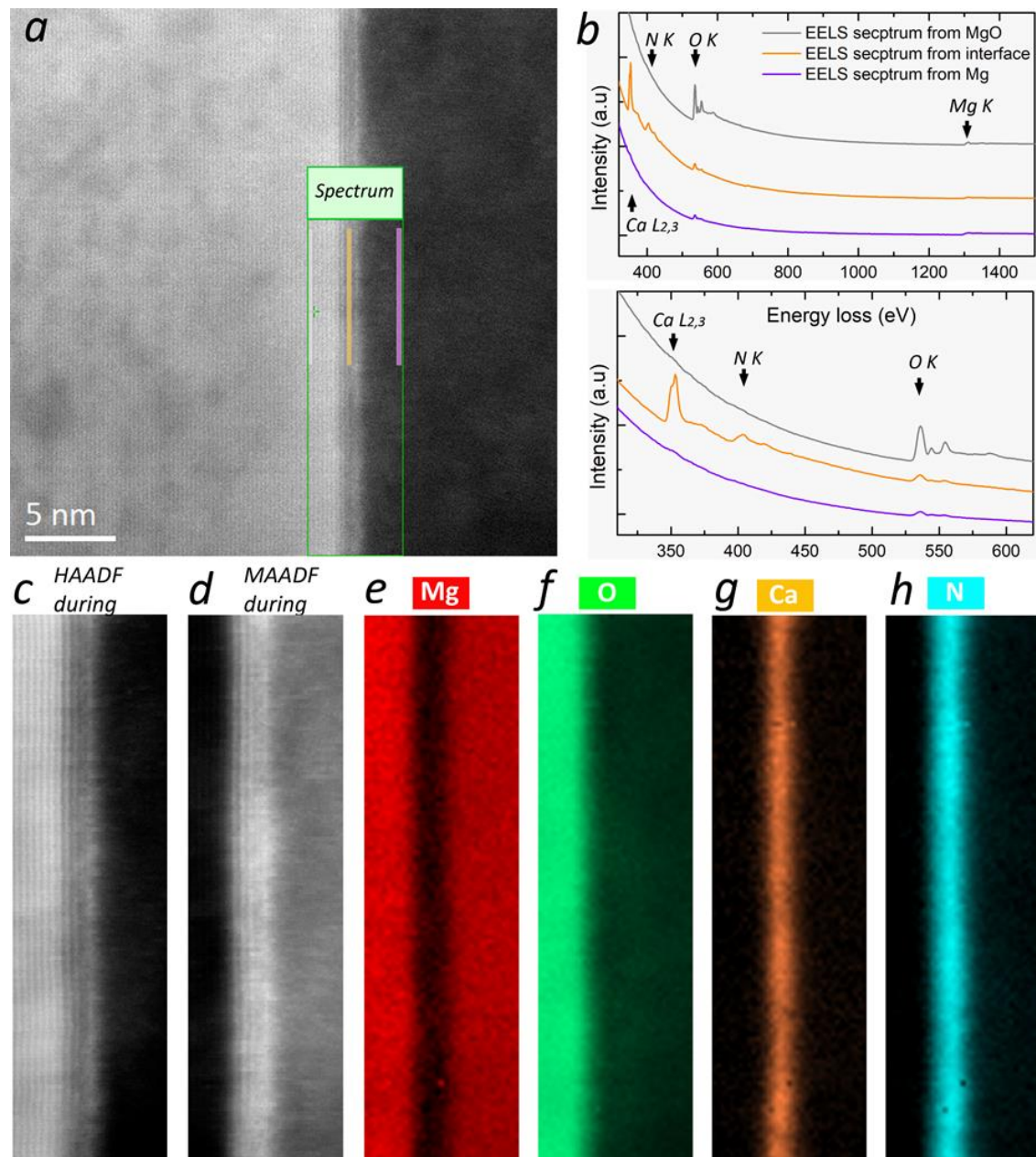


Fig. 6.13 STEM and EELS analysis at the $\{111\}_{\text{MgO}}/\text{Mg}$ interface in Mg-0.5Ca-prefil showing the existence of Ca and N. The incident beam is parallel to $\langle 112 \rangle_{\text{MgO}}$. (a) HAADF STEM image of the interface; (b) spectra extracted from the coloured rectangles in (a); (c, d) HAADF and MAADF images acquired during EELS acquisition; and (e-h) EELS elemental maps of Mg, O, Ca and N by integrating specific edges with a suitable window over the acquisition area. Ca and N can be seen concentrated in the segregation layers. (parameters: dispersion = 1eV/channel, $123 \times 35 \text{ pixel}^2$, pixel time = 0.07 s, collection angle $\beta=32\text{mrad}$).

6.2.6 Ca segregation on MgO

The chemical analysis of the segregated layer on the $\{111\}_{\text{MgO}}$ facet was undertaken by HAADF STEM and EELS analysis across the interface of MgO/Mg for the MgO particles

in Mg-Ca alloy, as shown in **Fig. 6.13**. On the $\{111\}_{\text{MgO}}$ facet of the MgO particle, which was viewed along its $\langle 112 \rangle$ direction (**Fig. 6.13(a)**), there are distinguished 3 to 4 atomic planes in lower brightness than that of the MgO matrix. **Fig. 6.13(b)** shows the EELS spectra averaged over the regions indicated by the colour-filled boxes (in **Fig. 6.13(a)**), grey for MgO, orange for MgO/Mg interface and purple for Mg). Ca and N are detected at the MgO/Mg interface. In comparison, it is seen that significant Ca $L_{2,3}$ and N K core-loss edges appear in the EELS spectrum from the interface. Therefore, Ca and N are identified as the chemical constituents in the segregation layers. The low intensity of O K edge found in the curve from the Mg matrix is the result of surface oxidation or oxygen adsorption. **Figs. 6.13(c-h)** show the HAADF image, the MAADF image, and the EELS elemental maps across the Mg/MgO interface. Ca and N are concentrated at the interface (**Figs. 6.13(e-h)**). The Ca/N co-segregation is spatially identical with the interfacial layer. As compared to the MgO matrix, the Ca/N co-segregation layer presents in a lower brightness contrast in the HAADF image (**Fig. 6.13(c)**), while it inversely exhibits a brighter contrast in the MAADF image (**Fig. 6.13(d)**). This suggests that the Ca/N co-segregation layer is highly strained.

6.2.7 Structure and chemistry of segregation layer

Systematic characterisation of the $\{111\}_{\text{MgO}}/\text{Mg}$ interface by atomic-resolution HAADF STEM imaging and the EEL spectroscopy was carried out to disclose the structural and chemical configurations of the segregation layer. A $\{111\}$ MgO particle viewed along its $\langle 112 \rangle$ direction is shown by the HAADF images in **Figs. 6.14(a-b)**, in which four atomic layers in relatively lower brightness than that of the MgO matrix are recognised at the interface. The composition analyses in **Figs. 6.14(c-f)** show the elemental distribution of Mg, O, Ca and N across the interface, respectively. It is clear that Mg and O are both deficient at the interface, where Ca and N, instead, are enriched. **Fig. 6.14(g)** presents the quantitative composition profile (in at.%) across the interface. At the MgO side, the concentration of Mg and O (~48%) are comparable with each other, additionally with a small amount of N (~4%). At the interface, the Mg curve experiences a shallow groove, but the O curve keeps declining down to ~18%. Oppositely, Ca and N are enriched at the interface appearing as bumps in their corresponding curves, with N showing a relatively higher concentration. At the Mg side, Ca and N curves both decay to a small percentage similar to that at the MgO side. O also keeps dropping gradually and becoming stable at around ~11%. The existence of N and O on the Mg side is the result of gas adsorption during sample storage and transfer.

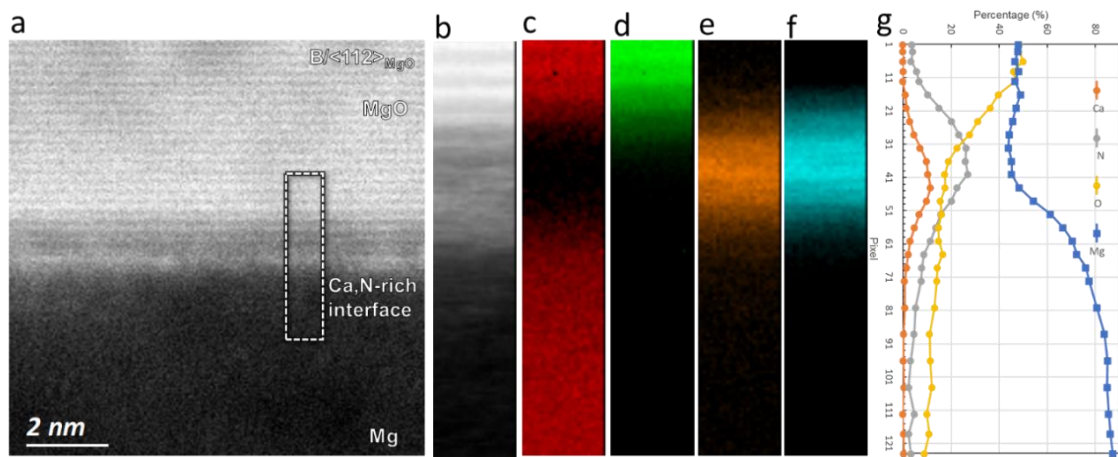


Fig. 6.14 Chemical analysis of the Ca/N co-segregation layer on the $\{111\}_{MgO}$ facet of MgO in Mg-0.5Ca-prefil by STEM and EELS technique. (a) HAADF STEM image of the MgO/Mg interface viewed along $\langle 112 \rangle$ direction, (b-f) HAADF during image and the corresponding EELS elemental maps (Mg, O, Ca, N) across the MgO/Mg interface, (g) The composition profile for each element across the interface. (parameters: dispersion = 1eV/channel, 124×25 pixel², pixel time = 0.05 s, collection angle $\beta=32$ mrad).

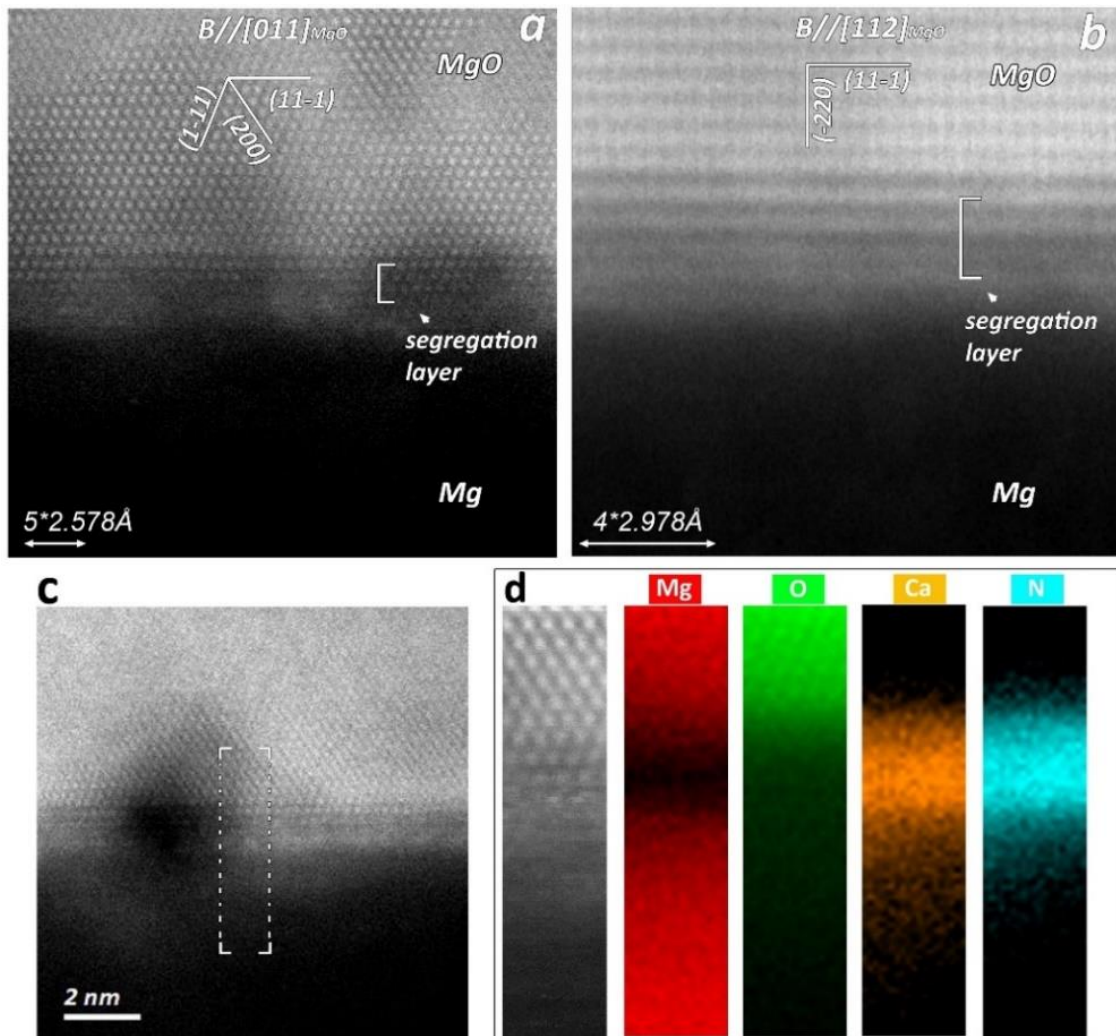


Fig. 6.15 Identification of the Ca/N co-segregation with resembling structure as MgO by the atomic-resolution HAADF and EELS analysis on the $\{111\}_{MgO}$ facet of MgO in Mg-0.5Ca-prefil. (a, b) HAADF STEM images of the MgO/Mg interface viewed along (a) $[011]_{MgO}$ and (b)

$[112]_{\text{MgO}}$, respectively; (c) HAADF image acquired before EELS acquisition; (d) HAADF during image and the corresponding EELS elemental maps of Mg, O, Ca and N by integrating specific edges with a suitable window over the acquisition area. Ca and N can be seen concentrated at the interface, where the atomic structure is identical to the MgO matrix. (parameters: dispersion = 1eV/channel, $79 \times 19 \text{ pixel}^2$, pixel time = 0.07 s, collection angle $\beta=32\text{mrad}$)

The HAADF STEM micrographs in **Figs. 6.15(a-b)** show the Ca/N co-segregation layer on the $\{111\}_{\text{MgO}}$ facets along zone axes of $[011]_{\text{MgO}}$ and $[112]_{\text{MgO}}$, respectively. The distinguishable layers in a lower brightness than that of the MgO matrix are recognised on the $\{111\}_{\text{MgO}}$ facets viewed along the $[011]_{\text{MgO}}$ direction in **Fig. 6.15(a)**, whose atomic arrangement of the segregation layers is identical to that of MgO. However, the segregation layers are blurry on the $\{111\}_{\text{MgO}}$ facets viewed along the $[112]_{\text{MgO}}$ direction in **Fig. 6.15(b)**. The EELS analysis taken across the $\{111\}_{\text{MgO}}$ /Mg interface is shown in **Figs. 6.15(c-d)** along the $[011]_{\text{MgO}}$ direction. It is seen that the segregation layer with resembling atomic structure to the MgO matrix corresponds to Mg- and O-deficient areas in the elemental maps, whereas it coincides with Ca- and N- rich areas.

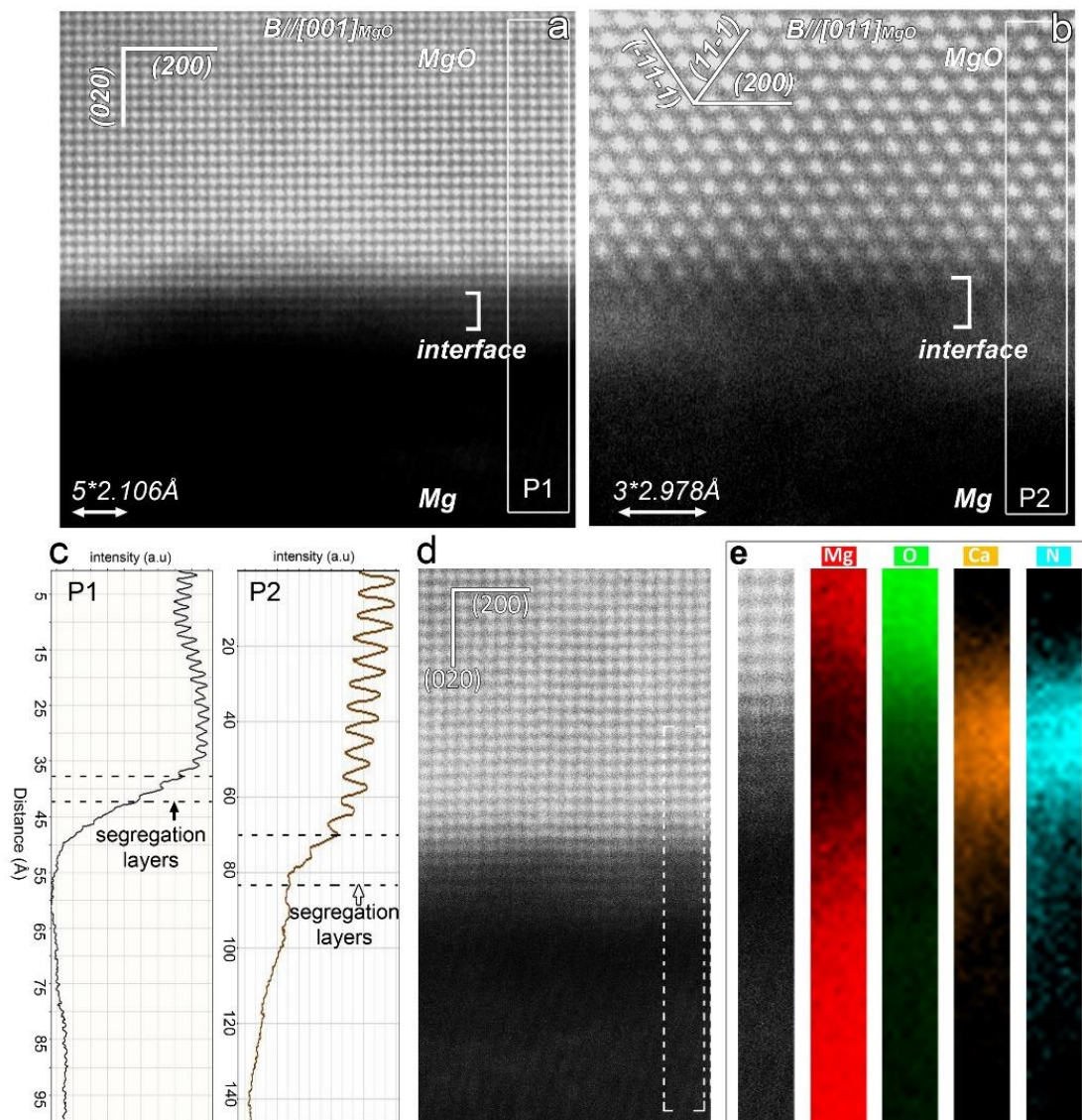


Fig. 6.16 Identification of the Ca/N segregation with resembling structure as MgO by the atomic-resolution HAADF and EELS analysis at the {001} facet of MgO in Mg-0.5Ca-prefil. (a, b) HAADF STEM images of the MgO/Mg interface viewed along (a) [001] and (b) [011] respectively, at which the segregation layers have lower contrasts, (c) contrast profiles along the labelled P1 and P2 in (a) and (b), (d) HAADF image and the corresponding EELS elemental maps of Mg, O, Ca and N by integrating specific edges with a suitable window over the acquisition area. Ca and N can be seen concentrated at the interface, where the atomic structure is identical to the MgO matrix. (parameters: dispersion = 1eV/channel, $89 \times 10 \text{ pixel}^2$, pixel time = 0.07 s, collection angle $\beta=32\text{mrad}$)

As shown in **Fig. 6.16**, similar analyses of HAADF imaging and EELS mapping were carried out to reveal the structure and chemistry of the Ca/N co-segregation layer on the $\{100\}_{\text{MgO}}$ facet of MgO particle. As projected along $[001]_{\text{MgO}}$ and $[011]_{\text{MgO}}$ zone axes, the segregation layers on the $\{100\}_{\text{MgO}}$ facet are realised from both zone axes in **Figs. 6.16(a-b)**, which are featured by the atomic layers in lower brightness contrasts than that of the MgO matrix. This is indicated by the contrast profiles in **Fig. 6.16(c)** along the ‘P1’ and ‘P2’ marked in **Figs. 6.16(a-b)**. Under both zone axes, the segregation layers show the same atomic configuration as that of MgO matrix, indicating an identical structure to MgO. The HAADF image and EELS maps in **Figs. 6.16(d-e)** show that Mg and O are deficient at the position of the segregation layer, whilst the Ca and N are concentrated.

6.2.8 Strain analysis for the segregation layer by geometric phase analysis

Based on the resultant TEM image, the primary idea of strain measurements using geometric phase analysis (GPA) is to identify the image contrast maxima as a periodic lattice, and to calculate the deviation of a real local lattice with respect to a reference crystal [243]. The HAADF STEM image in **Fig. 6.17(a)** shows the Ca/N segregation at the interface between $\{100\}_{\text{MgO}}$ and Mg. **Fig. 6.17(b)** shows the associating GPA maps of the strain component (ε_{xx}), where the $\{200\}$ reflections ($\mathbf{g}_1=(200)$ and $\mathbf{g}_2=(020)$) were chosen with Gaussians masks around $\mathbf{g}/3$ as inputs for GPA calculation. As highlighted by the dashed frame, the position of segregation layer rich in Ca and N corresponds to the location strained heavily as compared to the MgO matrix, which is clearly depicted by the strain profile along A1-A2 shown in **Fig. 6.17(c)**. The highest local strain approaches 7.2% in the segregation layer, while the average strain extent is calculated to be 3.8%.

6.2.9 Enhanced dispersity of native MgO due to segregation

The SE SEM images in **Fig. 6.18** compare the microstructures of the MgO films/particles in CP Mg and Mg-0.5Ca that experience filtration, re-melting and HSMC (**section 3.3.5**). The collected MgO particles by the melt filtration technique usually appear as films,

which can be dispersed by the shearing force introduced by HSMC. In CP Mg-prefil-HSMC, some of the MgO films (marked by the arrows in **Fig. 6.18(a)**) have size over 50 μm , while others are small clusters as the result of the HSMC dispersion. In contrast, the MgO films in Mg-0.5Ca-prefil-HSMC are better dispersed and all the MgO appears as oxide cluster (**Fig. 6.18(b)**). The individual nano MgO particles have small probabilities to be visible in 2D section at this magnification. It is noticed that the MgO particles in Mg-0.5Ca-prefil-HSMC have a qualitatively better dispersion than that in CP Mg-prefil-HSMC. With the same processes of filtration, casting and HSMC, it is suggested that the addition of 0.5Ca contributes to a better dispersion of MgO particles.

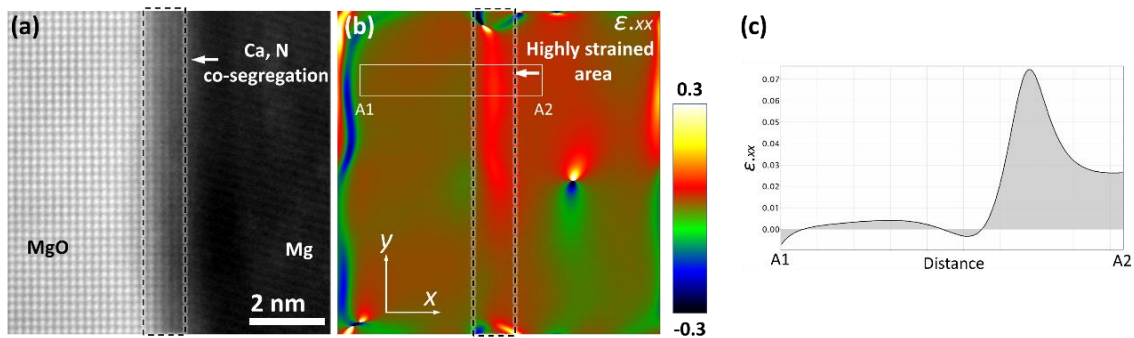


Fig. 6.17 Geometric phase analysis (GPA) of the MgO/Mg interface with Ca, N co-segregation. (a) HAADF STEM image; (b) the GPA ϵ_{xx} strain map showing the highly strained area at the position corresponding to the segregation layer; and (c) the strain profile along the A1-A2 labelled in (b).

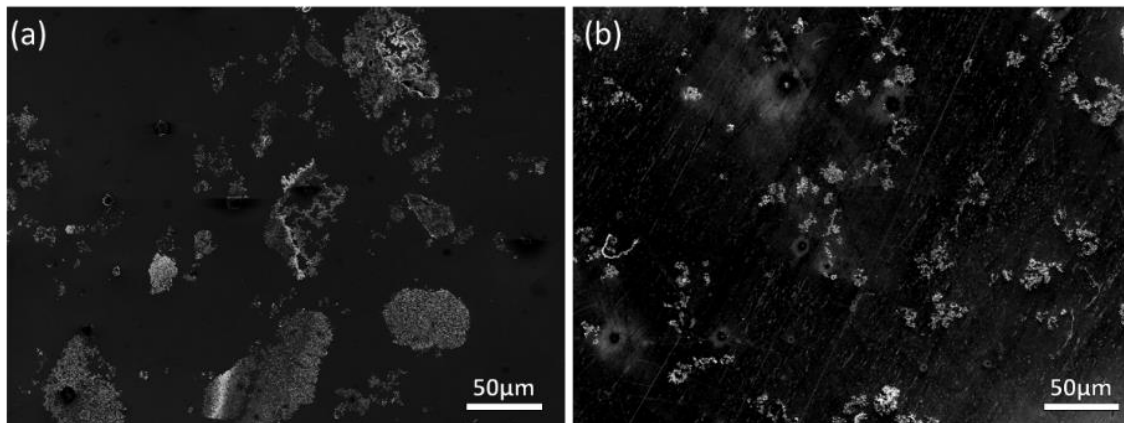


Fig. 6.18 SE SEM images of CP Mg-prefill-HSMC and Mg-0.5Ca-prefill-HSMC showing the better dispersity resulting from the Ca addition.

6.2.10 Effect of Sn addition on grain size in Mg-Sn alloys without HSMC

As shown in **Fig. 6.19**, the evolution of the as-cast macrostructure of Mg-Sn alloys in a function of Sn addition (Sn= 0.1, 0.4, 0.7, 1, 1.5, 2, 2.5 and 3%) is presented by the optical graphs taken from the transverse and longitudinal sections of TP-1 ingots. The addition of Sn has an expected positive effect on both columnar to equiaxed transition (CET) and

grain size. With the increasing Sn addition from 0.1 to 1.5%, the columnar width and length decrease, while the area of the equiaxed grains increases (**Figs. 6.19(a-e)**). The TP-1 ingot of Mg-1.5Sn is composed of equiaxed grains that uniformly distributed over the sample, expecting some elongated grains appearing in the region near the edge (**Fig. 6.19(e)**). The complete CET occurs when the Sn content reaches 2%, which is accompanied by a significant reduction in grain size (**Fig. 6.19(f)**). Further increase in Sn addition (up to 2.5% and 3%) results in little changes in the as-cast grain structure, as shown in **Figs. 6.19(g-h)**,

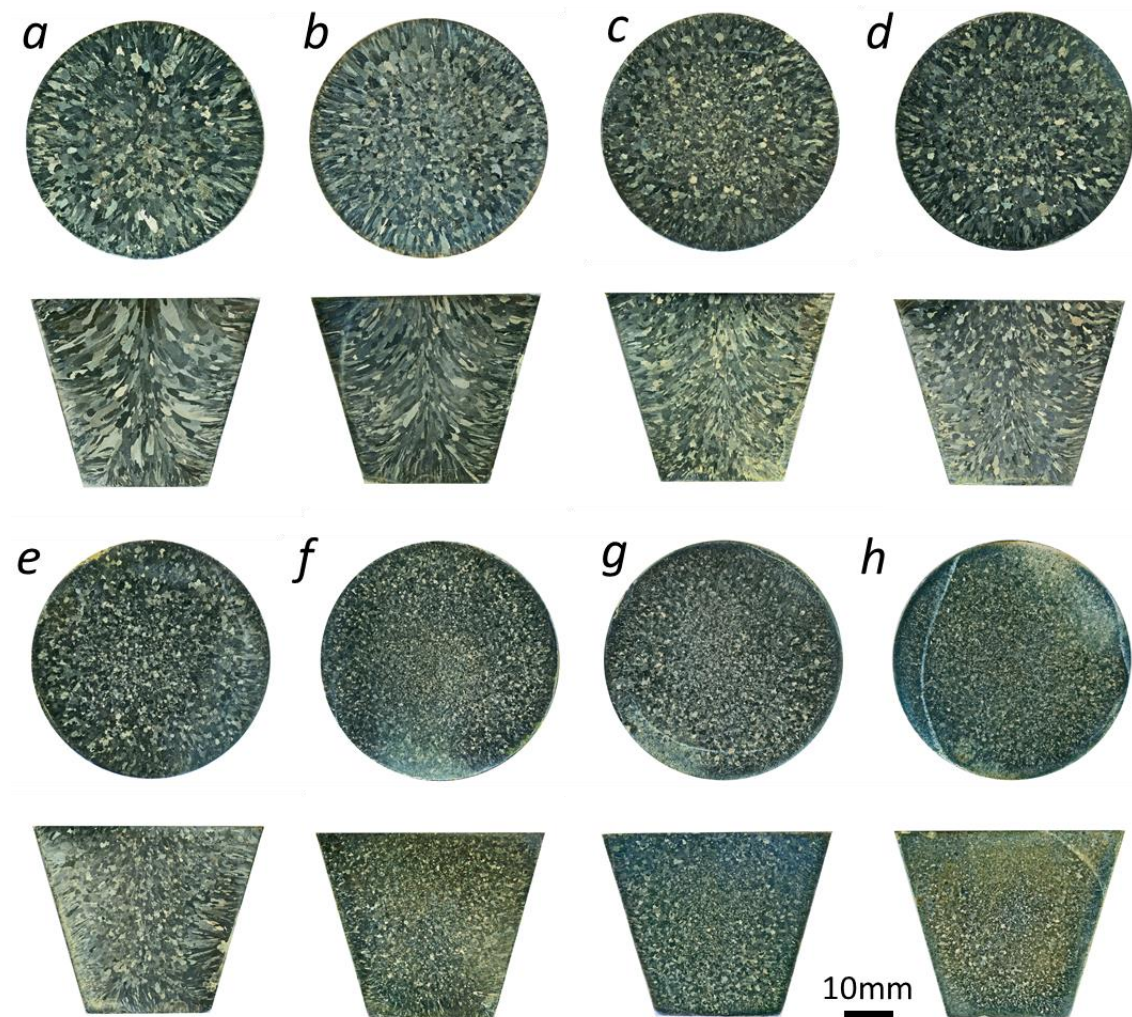


Fig. 6.19 Optical macrographs showing the grain structures on transverse and longitudinal sections of (a) Mg-0.1Sn, (b) Mg-0.4Sn, (c) Mg-0.7Sn, (d) Mg-1Sn, (e) Mg-1.5Sn, (f) Mg-2Sn, (g) Mg-2.5Sn and (h) Mg-3Sn samples cast in TP-1 mould without HSMC.

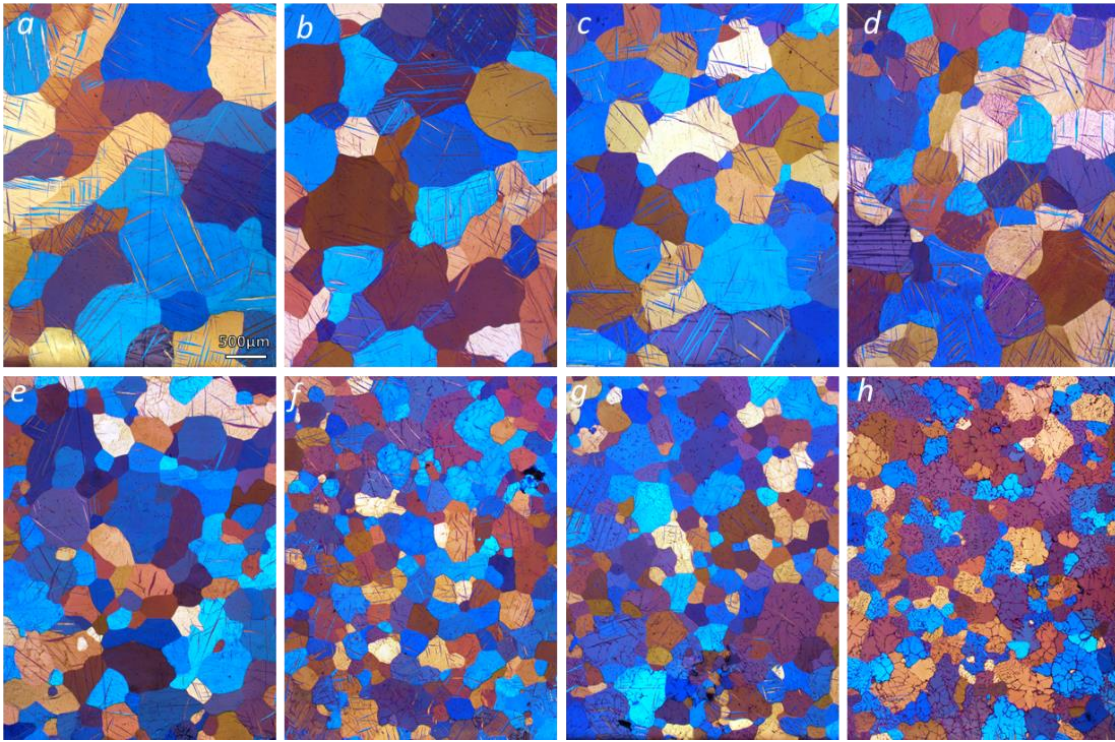


Fig. 6.20 Polarized optical micrographs showing the grain structure of (a) Mg-0.1Sn, (b) Mg-0.4Sn, (c) Mg-0.7Sn, (d) Mg-1Sn, (e) Mg-1.5Sn, (f) Mg-2Sn, (g) Mg-2.5Sn and (h) Mg-3Sn samples without HSMC prior to casting in TP-1 mould. Specimens were sampled from the central area of the transverse section. All images share the same scale bar in (a).

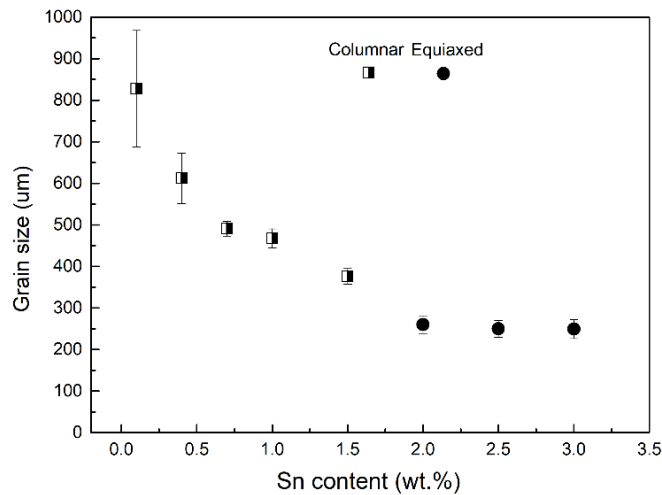


Fig. 6.21 Plot of grain size (columnar width) in a function of Sn concentration for Mg-Sn alloy cast into a TP-1 mould.

The optical microstructures of the alloys are shown in **Fig. 6.20**, with the quantified grain size being plotted in **Fig. 6.21**. The reduction in average columnar width (ACW, when $x \leq 1.5\%$) associated with the incremental Sn content follows the sequence as: $827.6 \pm 140.6 \mu\text{m}$ (Mg-0.1Sn) > $612.0 \pm 60.7 \mu\text{m}$ (Mg-0.4Sn) > $491.0 \pm 17.7 \mu\text{m}$ (Mg-0.7Sn) > $467.8 \pm 23.0 \mu\text{m}$ (Mg-1Sn) > $376.1 \pm 18.7 \mu\text{m}$ (Mg-1.5Sn). When 2% Sn is added, a fully

equiaxed grain structure occurs along with a dramatic drop in the average grain size (AGS), *i.e.*, $260.3 \pm 21.3 \mu\text{m}$ for Mg-2Sn. Moreover, the AGS experiences minor changes when the Sn content is over 2%, with AGS being $249.9 \pm 19.9 \mu\text{m}$ for Mg-2.5Sn and $249.4 \pm 23.0 \mu\text{m}$ for Mg-3Sn, respectively (**Figs. 6.20(g-h)**).

6.2.11 Grain size of Mg-Sn alloys with HSMC

Fig. 6.22 shows the variation of the as-cast macrostructure with increasing Sn content in the TP-1 samples of Mg-Sn alloys (Sn = 0.1, 0.4, 0.7, 1, 1.5 and 2%) that were treated by HSMC treatment prior to casting. In comparison to the counterparts without HSMC described above (**Figs. 6.19 to 6.21**), it is apparent that HSMC promotes CET and results in finer sizes for the alloys containing the same Sn additions. Specifically, the columnar grain structures are greatly shortened and refined as Sn increases to 0.4% (**Figs. 6.22(a-b)**) in most of the central region of the TP-1 ingot. The addition of 0.7% Sn resulted in an equiaxed grain structure for most areas, except for the region close to the edges where fine columnar grains remain (**Fig. 6.22(c)**). In Mg-1Sn-HSMC the solidified grain structure becomes fully equiaxed grains (**Fig. 6.22(d)**). More Sn addition (Sn > 1%) afterwards has a negligible effect on the grain size (**Figs. 6.22(e-f)**).

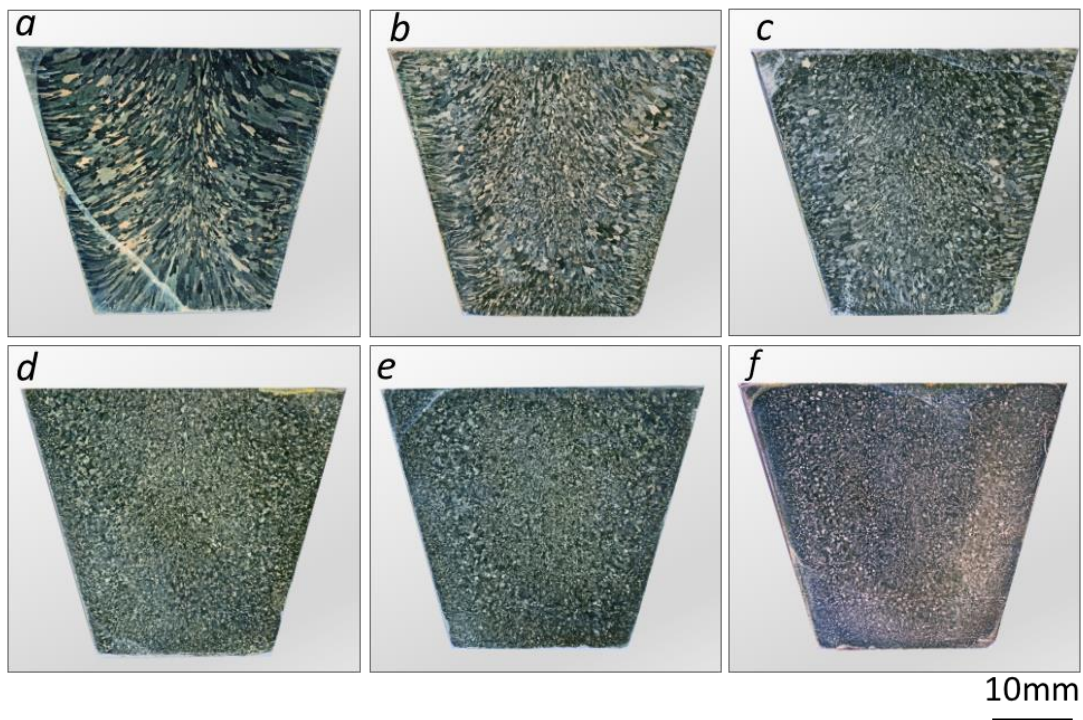


Fig. 6.22 Optical macrographs showing the grain structures on transverse and longitudinal sections of (a) Mg-0.1Sn-HSMC, (b) Mg-0.4Sn- HSMC, (c) Mg-0.7Sn- HSMC, (d) Mg-1Sn-HSMC, (e) Mg-1.5Sn- HSMC and (f) Mg-2Sn- HSMC samples with HSMC treatment prior to casting in TP-mould.

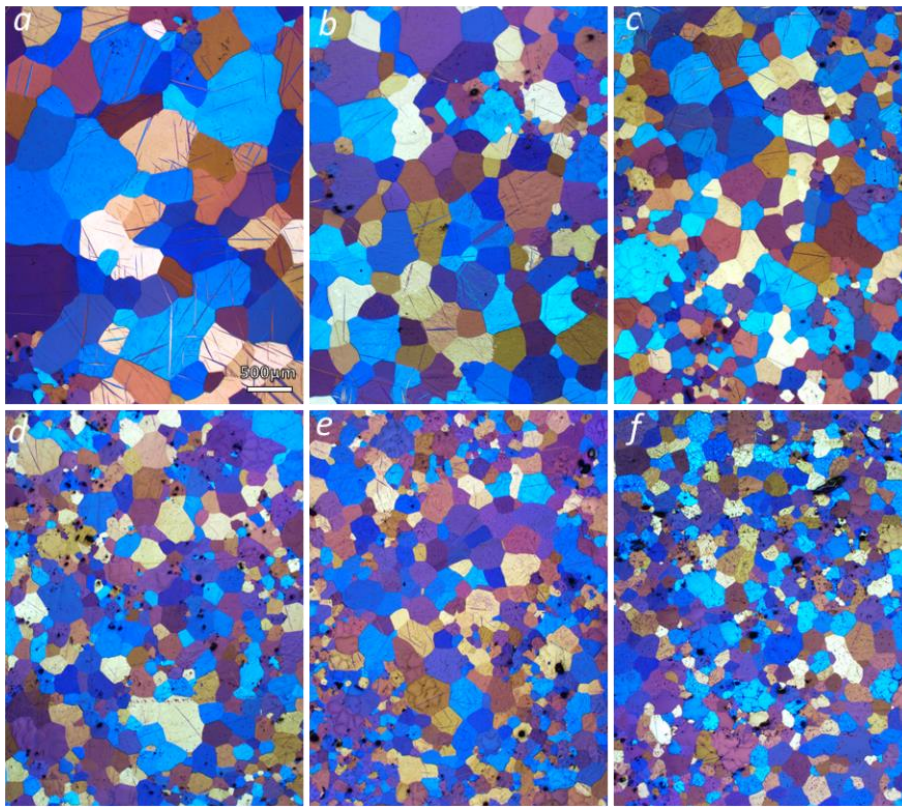


Fig. 6.23 Polarized optical micrographs showing the grain structure of (a) Mg-0.1Sn-HSMC, (b) Mg-0.4Sn-HSMC, (c) Mg-0.7Sn-HSMC, (d) Mg-1Sn-HSMC, (e) Mg-1.5Sn-HSMC and (f) Mg-2Sn-HSMC samples with HSMC prior casting in TP-1 mould. Specimens were sampled from the central area of the transverse section.

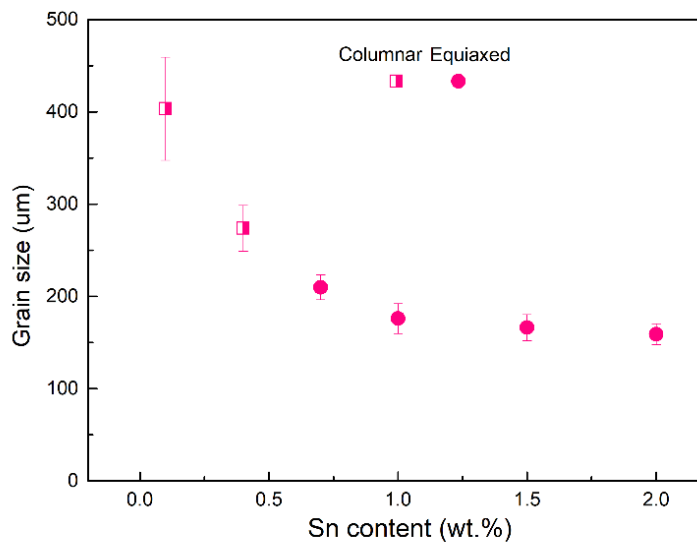


Fig. 6.24 Plot of grain size (columnar width) in a function of Sn concentration for Mg-Sn-HSMC alloy with HSMC treatment prior to casting in TP-1 mould.

The corresponding microstructure of the Mg-Sn alloys with HSMC is presented by the optical micrographs in **Fig. 6.23**, together with the quantified grain size being plotted in

Fig. 6.24. The ACW starts from $403.5 \pm 55.9 \mu\text{m}$ in Mg-0.1Sn-HSMC, and the value drops to $273.8 \pm 24.8 \mu\text{m}$ in Mg-0.4Sn-HSMC and then $209.8 \pm 13.4 \mu\text{m}$ in Mg-0.7Sn-HSMC. With more Sn addition afterwards, the average grain size is reduced in a tiny extent. The AGS values are $176.1 \pm 16.1 \mu\text{m}$, $166.3 \pm 14.2 \mu\text{m}$ and $159.0 \pm 11.5 \mu\text{m}$ in Mg-1Sn-HSMC, Mg-1.5Sn-HSMC and Mg-2Sn-HSMC, respectively. As found in **Figs. 6.23(c-e)**, some regions, which is usually associated with dark spots, have equiaxed grains in smaller size than that in the rest regions. This phenomenon is alleviated when the Sn addition is up to 2% (**Fig. 6.23(f)**).

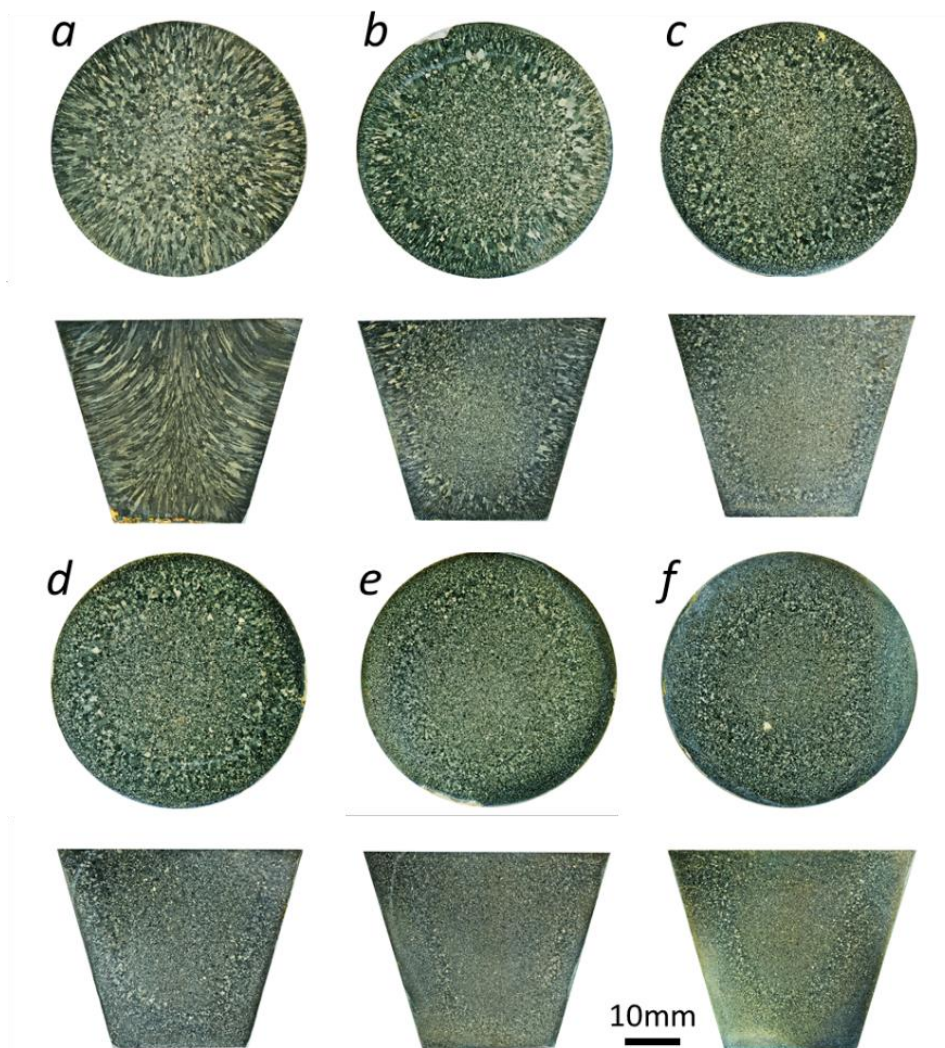


Fig. 6.25 Optical macrographs showing the grain structures on transverse and longitudinal sections of a) Mg-0.1Sn-HSO, (b) Mg-0.4Sn-HSO, (c) Mg-0.7Sn-HSO, (d) Mg-1Sn-HSO, (e) Mg-1.5Sn-HSO and (f) Mg-2Sn-HSO samples with HSMC and oxidation prior to casting in TP-1 mould.

6.2.12 Grain size of Sn Mg-Sn alloys with HSMC and oxidation

Similar to that of Mg-Ca alloys (**Fig. 6.7**), the enhancement of extra oxidation during HSMC prior to casting (**section 3.3.3**) is shown to promote the refinement of the

solidified microstructure in Mg-Sn alloys (Sn= 0.1, 0.4, 0.7, 1, 1.5, 2%). **Figs. 6.25** and **6.26** show the evolution of macro- and micro-structure as a function of Sn content for the TP-1 samples of Mg-Sn-HSO alloys, with the quantified grain size being shown in **Fig. 6.27**. Initially, the as-cast grain structure is columnar throughout the sample of Mg-0.1Sn-HSO, with an ACW of $320.6 \pm 53.1 \mu\text{m}$ (**Figs. 6.25(a)** and **6.26(a)**). Such columnar structure is nearly replaced by equiaxed one in Mg-0.4Sn-HSO, excepting for the areas near the mould wall (**Figs. 6.25(b)** and **6.26(b)**). The AGS in its central area is $169.4 \pm 14.0 \mu\text{m}$. The trend of CET and grain size reduction continue, with a complete transition to equiaxed grains being observed in Mg-0.7Sn-HSO (**Figs. 6.25(c)** and **6.26(c)**), in which the AGS is $147.0 \pm 9.1 \mu\text{m}$. After that minor changes in the grain size are observed as the Sn addition increases, with the AGS being $133.7 \pm 3.54 \mu\text{m}$, $113.3 \pm 9.4 \mu\text{m}$ and $113.4 \pm 3.7 \mu\text{m}$ for the addition of 1%, 1.5% and 2%, respectively (**Figs. 6.25(d-f)** and **6.26(d-f)**).

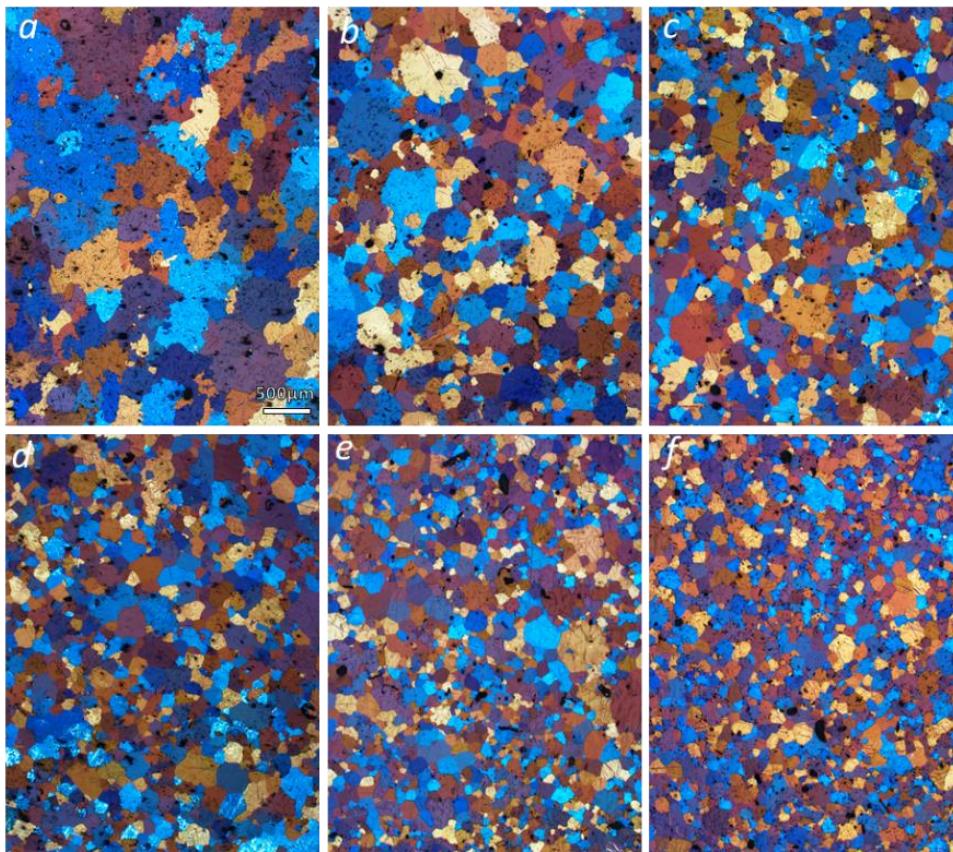


Fig. 6.26 Polarized optical micrographs showing the grain structure of (a) Mg-0.1Sn-HSO, (b) Mg-0.4Sn-HSO, (c) Mg-0.7Sn-HSO, (d) Mg-1Sn-HSO, (e) Mg-1.5Sn-HSO and (f) Mg-2Sn-HSO samples with HSMC and oxidation prior to casting in TP-1 mould. Specimens were sampled from the central area of the transverse section.

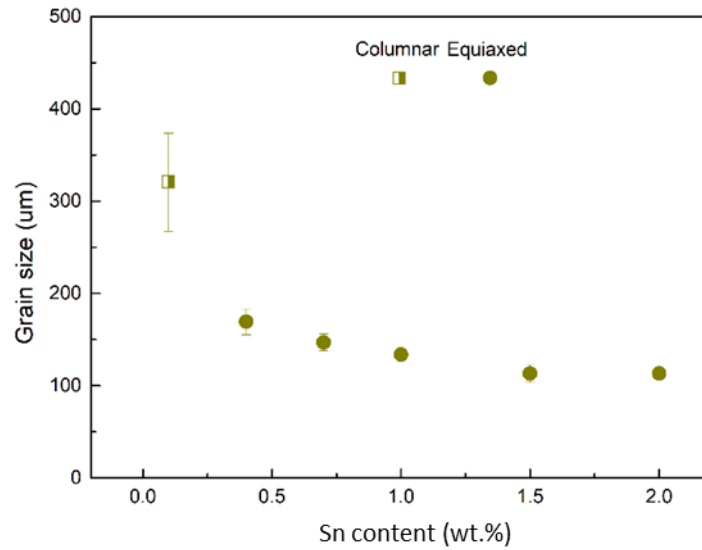


Fig. 6.27 Plot of grain size (columnar width) in a function of Sn concentration for Mg-Sn-HSO alloy with HSMC and oxidation prior to casting in TP-1 mould.

6.2.13 Effect of pre-cast treatments on grain size of Mg-Sn alloys

Fig. 6.28 summaries the effect of different treatments prior to casting on CET, ACW and AGS of the Mg-Sn binary alloys. It is found that either the Sn concentration or the pre-treatment poses positive impacts on the solidified structures. Similar to that in Mg-Ca alloys (**Fig. 6.10**), the as-cast structure of Mg-Sn alloys is refined by Sn addition. The plot of each of the Mg-Sn alloy series quickly levels as Sn content increases, especially for the Mg-Sn alloys with HSMC and HSO pre-treatments. As compared to the Mg-Sn alloys directly cast into TP-1 mould, HSMC brings further positive contribution in aspects of both CET and grain refinement. An earlier CET and finer grain sizes than the counterparts without HSMC result. Moreover, an extra positive effect is brought by the HSO treatment prior to casting. CET gets advanced with finer grain size as compared to the HSMC treated Mg-Sn alloys. By comparing the minimum grain size of each series of Mg-Sn alloys in **Fig. 6.28**, application of HSMC causes a reduction of about 100μm compared to the one without HSMC, and the HSO pre-treatment causes a further reduction of about 50μm. CET is also sensitive with the pre-treatments, and the requirement of Sn addition for CET drops in the sequence of: Mg-Sn, Mg-Sn-HSMC and Mg-Sn-HSO.

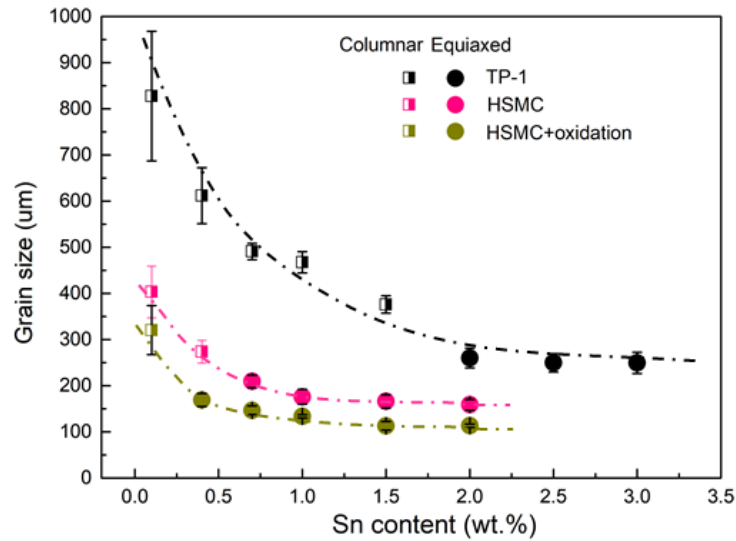


Fig. 6.28 Grain size (columnar width) of Mg-Sn binary alloys as a function of Sn composition.

6.2.14 Native MgO in Mg-2Sn alloy

Fig. 6.29 illustrates the morphology and chemistry of inclusion particles collected from the Mg-2Sn melt by melt filtration. By electropolishing, the stereo morphologies of the particles were revealed. The particles shown in **Figs. 6.29(a-c)** have sizes ranging from 50 nm to 150 nm, with some of the particles (marked by the arrows in the SEM images) in a proper projection showing faceted terminations. The faceted MgO particles are suggested to be {111} MgO based on the results and analysis in **Chapter 4**. The corresponding EDS spectrum in **Fig. 6.29(d)** confirms the chemical composition of Mg and O. Apparently, the morphology and size of the {111} MgO in Mg-2Sn are not affected by solute Sn addition.

The other type of particle is also observed in **Fig. 6.30(a)**, where a few of cubic particles about 200 nm in size are found attaching to a relatively larger one (600 nm). Smaller cubic particles around 100nm in size are seen as well. The corresponding EDS spectra in **Fig. 6.30(b)** indicate the crystal phase of MgO. Besides, the characteristic Sn L peaks are seen in the enlarged the EDS spectra in **Fig. 6.30(c)**. In spite of the low intensity, it is resolvable that characteristic Sn L peaks exist in each spectrum.

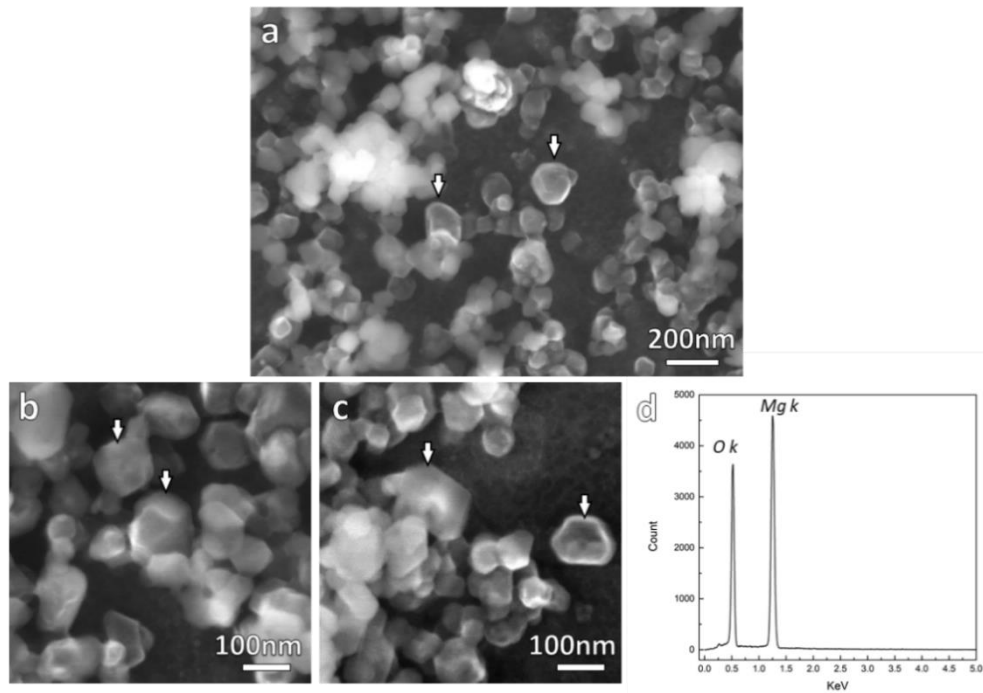


Fig. 6.29 Octahedral morphology of the native MgO particles in Mg-2Sn-prefill. (a-c) SE SEM images, and (d) EDS spectrum. Some faceted particles being well recognised as highlighted by arrows.

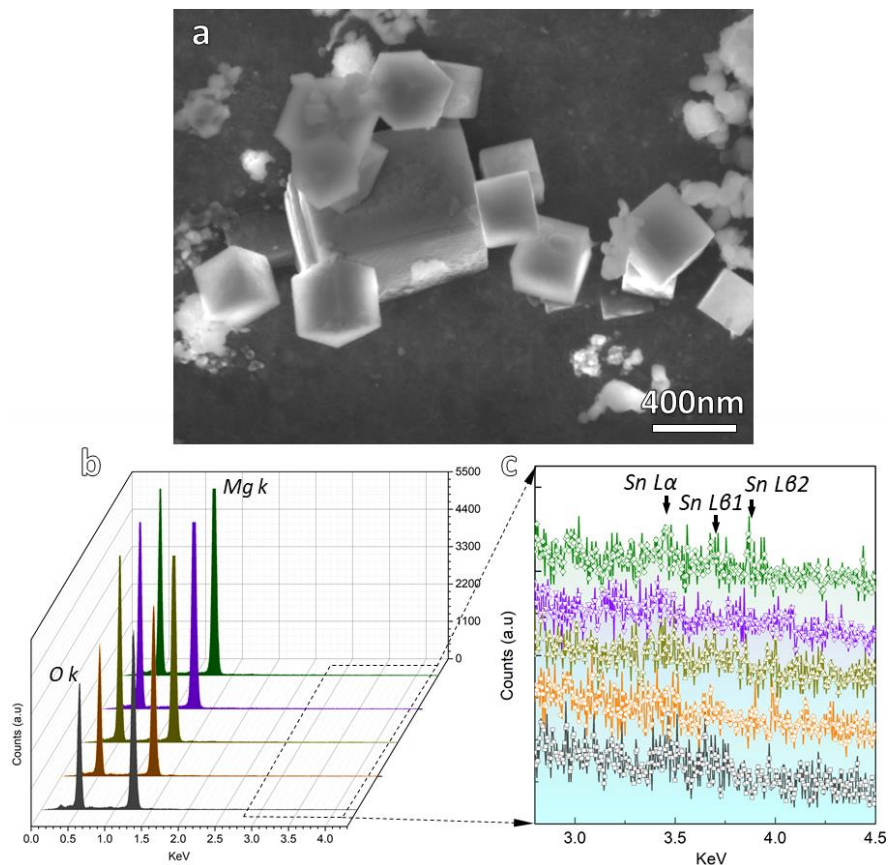


Fig. 6.30 Morphology and chemistry of $\{100\}$ MgO and in Mg-2Sn-prefil. (a) SE SEM image demonstrating the unvaried shape of cubic MgO after addition of 2Sn, (c, d) the corresponding EDS spectra showing extra Sn L peaks. Note that the deviations of Mg/O ratio away from '1' occurred in some small particles, the extra Mg signal was detected due to the interaction volume between the electron beam and MgO at accelerating voltage of 10kV.

6.2.15 Sn segregation on MgO

The weak intensity of Sn L peaks in the EDS spectra does not provide convincing information about the existence and location of Sn associated with the MgO particles. More precise examinations are required to reveal where the Sn locates and more precisely what the atomic configuration of the Sn segregation is on the MgO surface if Sn does segregate. Advanced electron microscopy analysis at the MgO/Mg interface in Mg-2Sn-prefill was conducted. **Fig. 6.31(a)** shows the ADF STEM image of a MgO particle viewed along its [001] zone axis, where the relatively brighter layer on the MgO/Mg interface suggests that the heavier Sn atoms are concentrated locally at the interface. The corresponding EDS elemental maps in **Figs. 6.31(b-e)** confirm that enrichment of Sn localises at the identical position to the brighter contrast in the ADF STEM image.

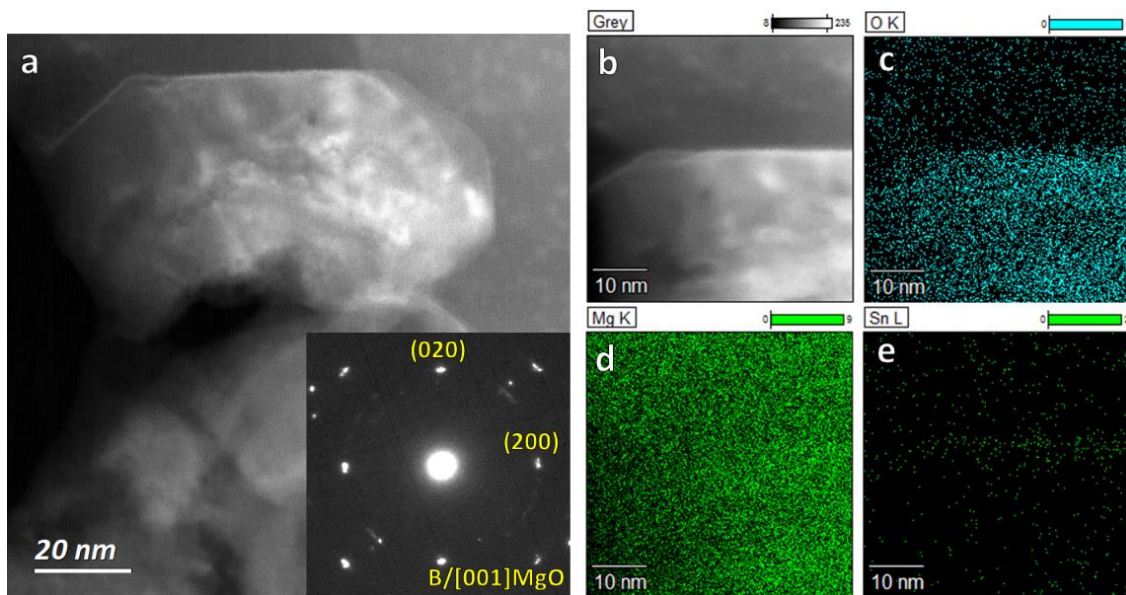


Fig. 6.31 Identification of the segregation of Sn at the $\{100\}_{\text{MgO}}$ facet of a MgO particle in Mg-2Sn-prefill. (a) ADF STEM micrograph and the corresponding SAED pattern, (b-e) the corresponding EDS elemental maps of (c) O K, (d) Mg K and (e) Sn L. Note that the beam was parallel to [001] direction of MgO.

Fig. 6.32(a) presents the BF TEM image and SAED pattern of a $\{111\}$ MgO particle with an incident beam parallel to the $[011]_{\text{MgO}}$ direction. The HRTEM image in **Fig. 6.32(b)** taken across the $\{111\}_{\text{MgO}}/\text{Mg}$ interface shows the distinguished layers at the interface. As seen from the resolvable lattice structure, the ordering of lattice planes at the interface is gradually decrease following the sequence from '0' to '3' (labelled by black arrows). Layer '0' is the $\{111\}$ terminated of MgO, and the layers '1' to '3' are suggested to be Sn segregated layers, where the lattice is not clearly resolved due to its inferior ordering than the MgO matrix. By marking four atomic layers of $\{111\}_{\text{MgO}}$ planes as a reference in **Fig. 6.32(c)** and moving them up left (labelled by the white lines and arrows), it is

recognised that positions of some lattice points in layer '2' are deviated from those of the original $\{111\}_{\text{MgO}}$ plane, with a positional protrusion towards the Mg matrix. The lattice spacing along $[2\bar{1}1]_{\text{MgO}}$ direction in layer '2' is identical to that in the MgO matrix, in spite of some lattices marked by black arrows are obscure and deviated.

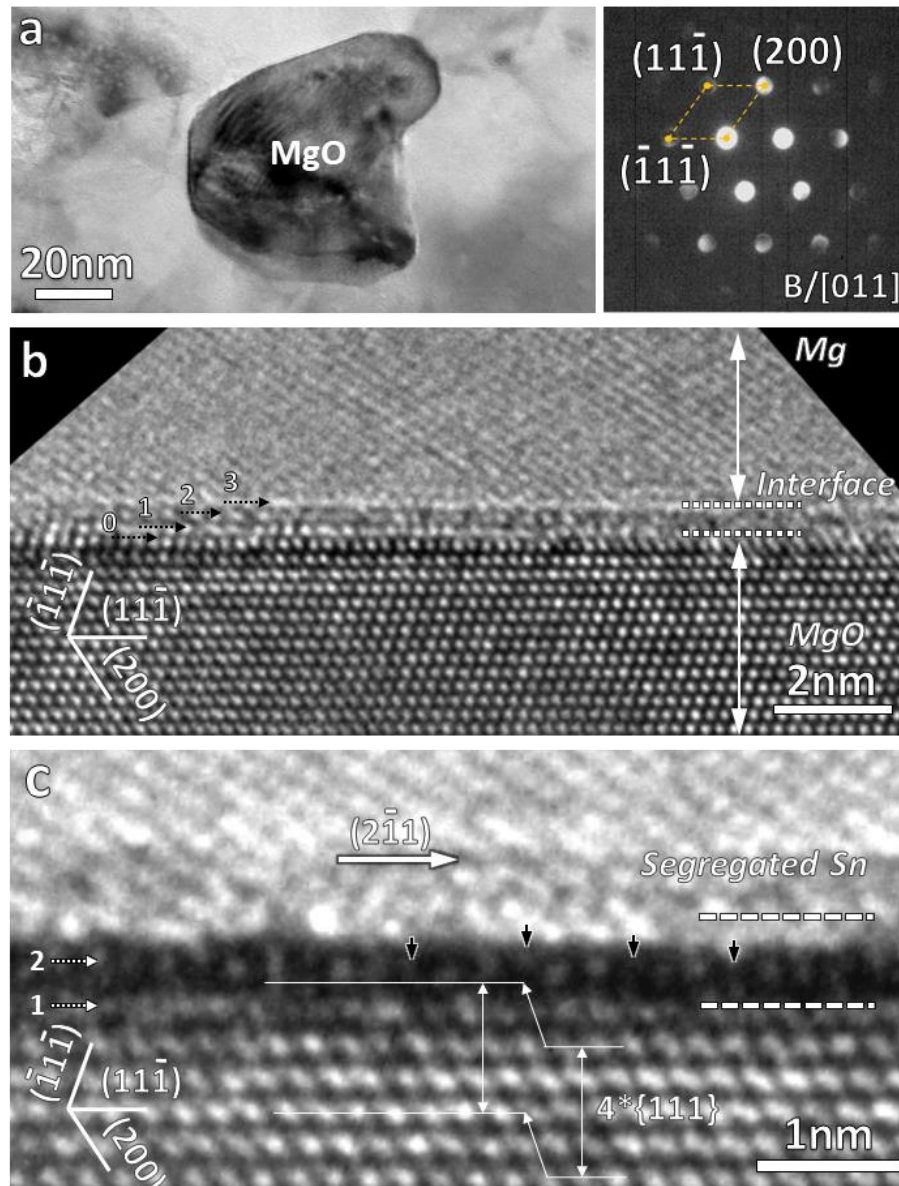


Fig. 6.32 TEM characterisation showing the Sn segregation on a $\{111\}$ MgO particle in Mg-2Sn-prefill. (a) BF TEM image and the related SAED; and (b, c) HRTEM images taken at the $\{111\}$ termination. Note that the incident beam was parallel to $[011]$ direction of MgO.

Cs-corrected STEM was further carried out to uncover the structural and chemical configurations of the Sn segregation layer on the MgO facets. The HAADF and MAADF images in **Fig. 6.33** show an example of Sn interfacial segregation on a $\{100\}$ MgO particle. The Sn segregation layers with brighter contrast in the HAADF image are seen over the MgO particle. With the intensity of MgO matrix as a reference, Sn segregation

has a higher contrast ratio in the strain sensitive MAADF STEM images than that in the HAADF images (inset in **Fig. 6.33(b)**), suggesting that the Sn segregation layer contains elastic strains. The segregation of Sn on the facets of native MgO particles has been widely observed in Mg-2Sn alloys, with 19 cases being detected (**Fig. A-5**, see appendix).

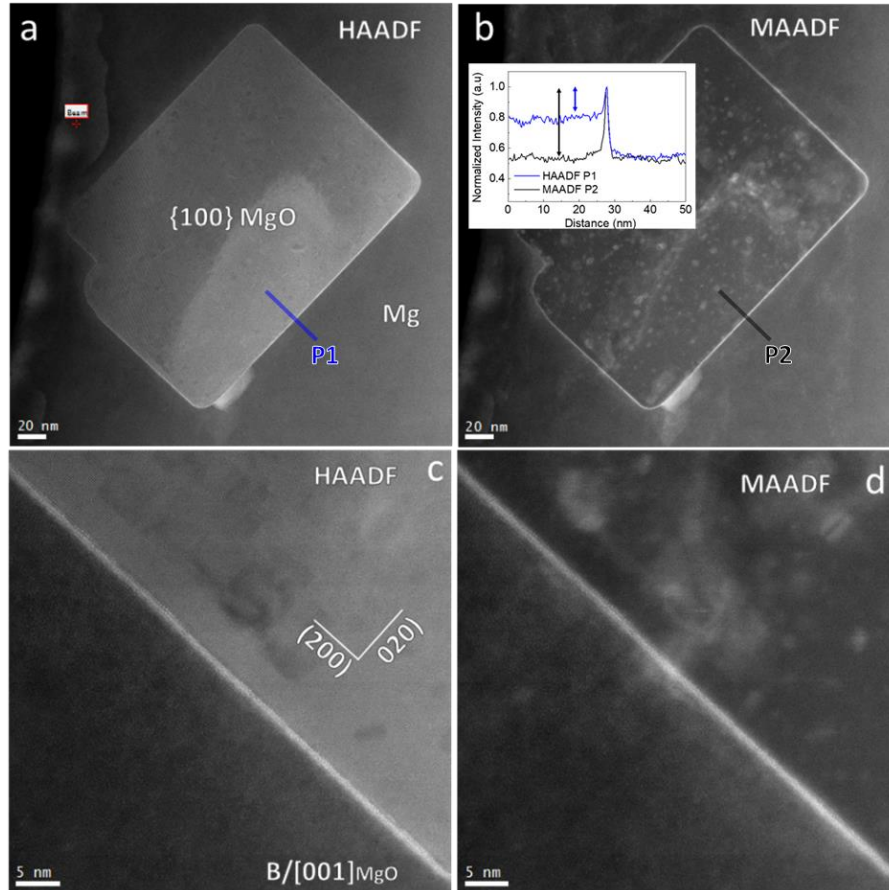


Fig. 6.33 (a, c) HAADF and (b, d) MAADF STEM images showing the segregation layer wrapping over a $\{100\}$ MgO particle in Mg-2Sn-prefill. The beam direction is parallel to the $\langle 001 \rangle_{\text{MgO}}$ zone axis. Inset in (b) shows the contrast profiles along ‘P1’ in (a) and ‘P2’ in (b).

Locally exaggerated MAADF STEM images in **Figs. 6.34(a-b)** show the $\{100\}_{\text{MgO}}/\text{Mg}$ interface with Sn segregation. The brighter Sn-rich atomic columns appear alternative along $[100]_{\text{MgO}}$ direction, and there is a shifting distance of $\frac{1}{2}[100]_{\text{MgO}}$ between the two atomic layers containing Sn-rich atomic columns. The periodic feature of the Sn-rich atomic columns is believed to be resulted from the selective substitution of some Mg atoms in the $(100)_{\text{MgO}}$ plane by Sn atoms. There are no distinct contrasts of atomic columns at the corresponding positions, indicating that both two types of interstitial sites are unoccupied in **Fig. 6.34(a)**. It can be ruled out the possibility of interstitial Sn atoms (marked by pink triangles) at the sites displayed in **Fig. 6.34(c)**, *i.e.*, body-centred site $(0.25, 0.25, 0.25)$ and face-centred site $(0.25, 0.25, 0)$. Therefore, Sn segregates onto the $\{100\}_{\text{MgO}}$ surface and preferentially substitutes the diagonal Mg sites as marked by the

red triangles in **Fig. 6.34(c)**, whereby the resultant feature is identical to that observed in the MAADF STEM image. A unit cell can be derived for the structure of Sn segregation: $a = d_{[010]_{\text{MgO}}} = 4.211 \text{ \AA}$, $b = d_{[-120]_{\text{MgO}}} = 4.708 \text{ \AA}$, $\alpha = 154.4^\circ$. In addition, atomic deviation (marked by the red arrows in **Fig. 6.34(b)**) can be discriminated by applying MgO matrix as reference.

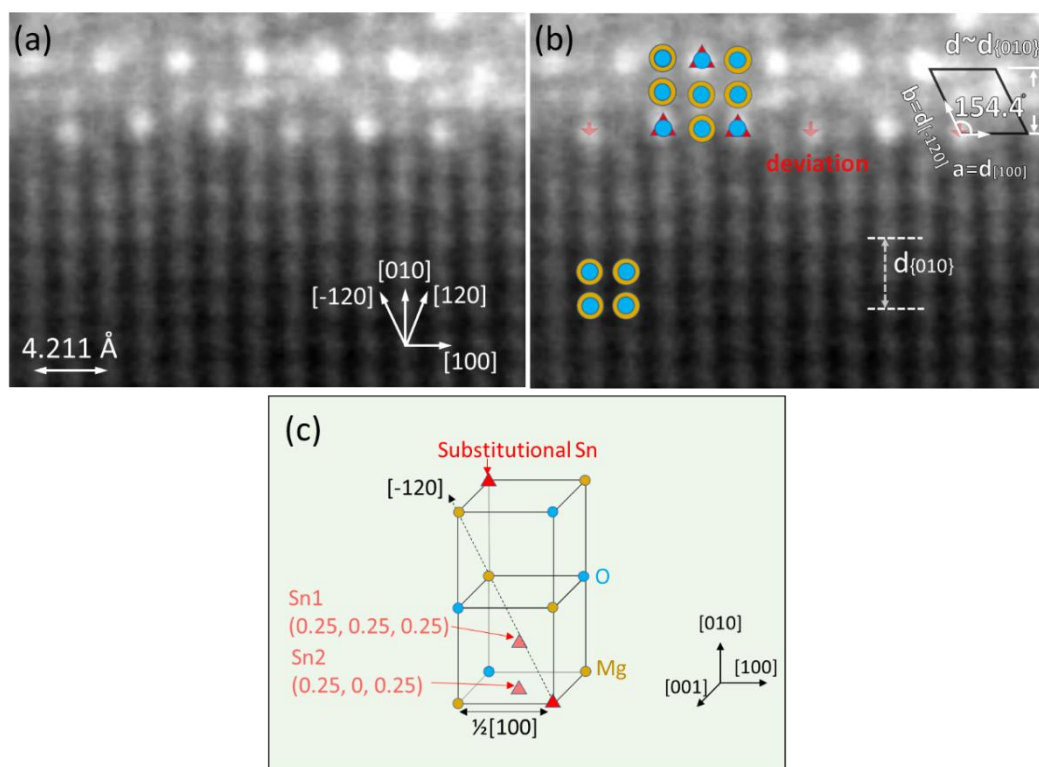


Fig. 6.34 Sn segregation layers at the $\{100\}_{\text{MgO}}/\text{Mg}$ interface in Mg-2Sn-prefill. (a) MAADF STEM image taken along $\langle 001 \rangle_{\text{MgO}}$ direction; (b) MAADF STEM image with overlapped indexing and atomic models; and (c) atomic model showing the substitutional Sn at the selective Mg lattice sites and possible interstitial sites in a $1/4$ MgO unit cell. Note that Mg, O, substitutional Sn and interstitial Sn atoms are represented by orange circles, blue circles, red triangles and pink triangle, respectively.

Fig. 6.35(a-b) show the HAADF and ABF STEM images of another $\{100\}_{\text{MgO}}/\text{Mg}$ interface acquired along the $\langle 001 \rangle_{\text{MgO}}$ direction, where a well-defined OR exists, *i.e.*, $(\bar{1}00)[001]_{\text{MgO}} // (1\bar{1}01)[10\bar{1}1]_{\text{Mg}}$. The Sn segregation layers own the same structure as that depicted in **Fig. 6.34**, whilst the feature is thicker, with 3 layers (or even 4 layers with consideration of the faded contrast towards Mg matrix) being resolved in **Fig. 6.35(a)**. Atomic occupancy in the last crystal plane ('P1') of MgO adjacent to the Sn segregation layer is affected. Comparison of the contrast profiles 'P1' (**Fig. 6.35(c)**) and 'P2' (**Fig. 6.35(d)**) illustrates that the contrast intensity in the 'P1' crystal plane is lower than that in the 'P2' crystal plane. Being adjacent to the Sn segregation layer, the atomic column in the 'P1' crystal plane is less occupied than that in the 'P2' crystal plane inside the MgO

matrix. Moreover, the occupation level (vacancy concentration) in each atomic column of the ‘P1’ plane varies alternatively as indicated by the dark-bright-dark contrast variation in **Fig. 6.35(c)**. The periodicity of contrast is the same as that of the Sn-rich columns in the Sn segregation layer. It indicates a possible connection between the variation of atomic-column occupancy in ‘P1’ and the Sn-rich columns.

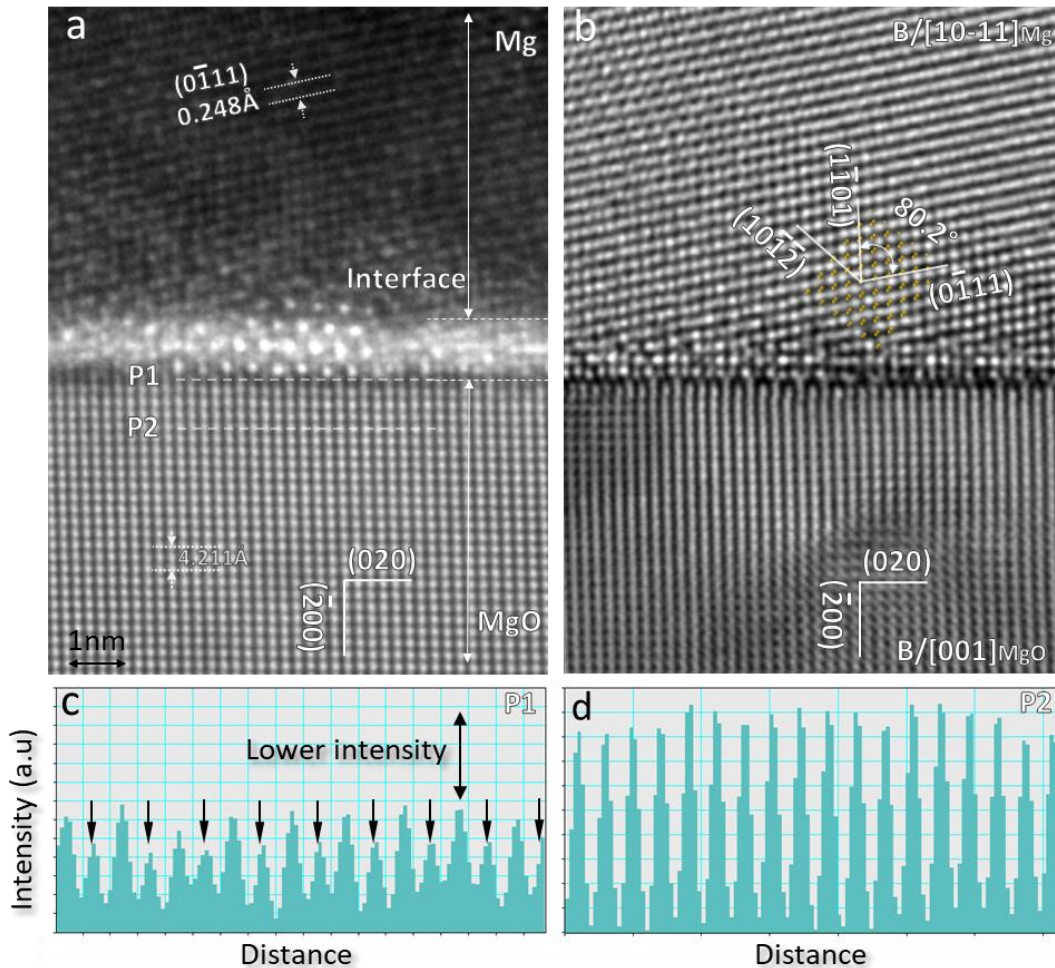


Fig. 6.35 Atomic-resolution HAADF and ABF STEM images acquired at the {100} facet of MgO in Mg-2Sn-prefill showing the Sn segregation with a specific structure and a defined OR between MgO and Mg as: $(\bar{1}00)[001]_{\text{MgO}} // (1\bar{1}01)[10\bar{1}1]_{\text{Mg}}$. (a) HAADF STEM image, (b) corresponding ABF STEM image, and (c, d) contrast profile along the labelled P1 and P2 in (a). Note that the incident beam is parallel to $\langle 001 \rangle_{\text{MgO}}$ direction.

Fig. 6.36 shows the structural and chemical analysis of the Sn interfacial segregation on the $\{100\}_{\text{MgO}}$ facet by STEM and EELS. Distinguished Sn segregation layer is shown at the $\{100\}_{\text{MgO}}/\text{Mg}$ interface in **Figs. 6.36(a-b)**. The EELS spectra image was acquired over the region marked by the white rectangle (parameters: dispersion = 1eV/channel, $181 \times 38 \text{ pixel}^2$, pixel time = 0.08 s, collection angle $\beta=32\text{mrad}$). By extracting the EELS spectra from the colour-marked areas in **Fig. 6.36(a)**, the core-loss spectra without and with background subtraction are respectively shown in **Figs. 6.36(c-d)**. Sn appears at the

interface as identified by the Sn $M_{4,5}$ edges locating on the left side of the O K edge in the spectrum from the interface. **Figs. 6.36(e-f)** present the HAADF and MAADF image taken simultaneously during the EELS acquisition, where the Sn-rich atomic columns (despite some extent of beam damage) are recognised and spatially identical to the Sn-rich area shown in **Fig. 6.36(g)**.

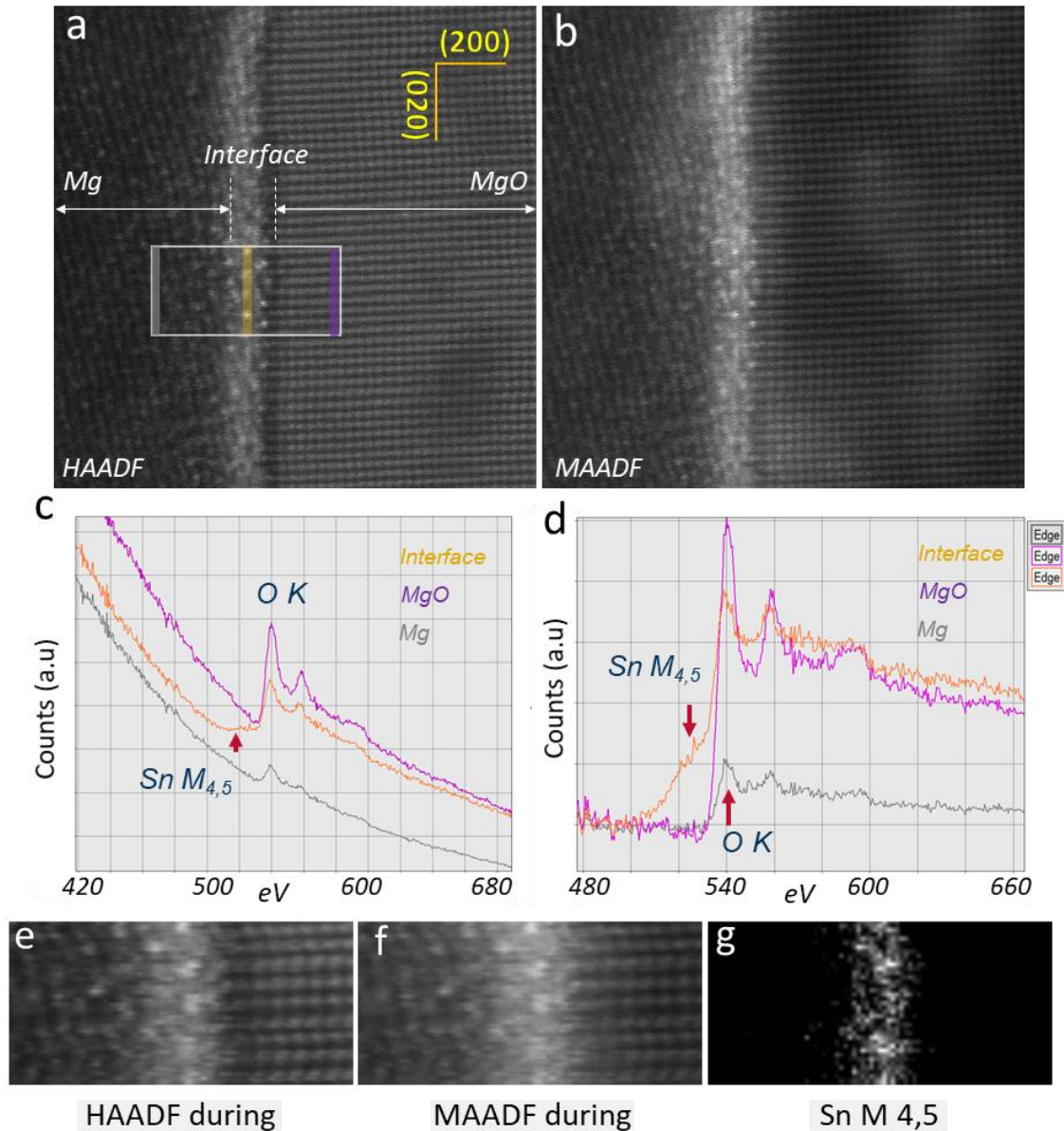


Fig. 6.36 Structural and chemical identification of the Sn segregation at a $\{100\}_{MgO}$ termination in Mg-2Sn-prefill. (a) HAADF STEM image; (b) corresponding MAADF STEM image; EELS spectra (c) without and with (d) background subtraction averaged over the labelled area in (a), suggesting that Sn exists at the interface; (e) HAADF and (f) MAADF STEM images and (g) the corresponding elemental maps showing that the bright dots at the interface are Sn-rich atomic columns.

6.3 Discussion

6.3.1 Columnar to equiaxed transition (CET)

There are generally two types of grain structures, *i.e.*, columnar and equiaxed, for solidified metallic materials. Practically, it is common to see a microstructural transition from columnar to equiaxed from the outer area to the central area of an ingot sample [11]. Achievement of columnar-to-equiaxed transition (CET) is essential for the final as-cast microstructure. For direct-chill casting, equiaxed structure is appreciated owing to the resistance to hot tearing, the better castability and the down-stream thermal processing.

As experimentally shown in **section 6.2**, the CET extent is affected by three variables. The first one is the position of the TP-1 ingot. Some samples show a mixed structure, where the columnar grains appear at the edge while equiaxed ones at the centre (see **Figs. 6.1(c), 6.4(b), 6.7(a), 6.19(e), 6.22(b) and 6.25(a)**). The second variable is the solute content. Addition of solute narrows and shortens the columnar width, and then results in a complete change of the grains from columnar to equiaxed when the solute content is above a critical value (see **Figs. 6.1(d), 6.4(c), 6.7(b), 6.19(f), 6.22(d) and 6.25(c)**). The third factor is the number density of native MgO particles, whose value increases following the sequence of TP-1 < HSMC < HSO. As shown in **Fig. 6.28**, the increment of dispersed MgO particles reduces the critical solute content required for CET. Numerical modelling will be applied to analyse how these variables affect the CET behaviour in Mg-Ca and Mg-Sn alloys.

The mechanism underlying CET has been extensively studied, which sets as the foundation to practically manipulate the as-cast microstructure. Hunt proposed the first analytical model in which the solid blocking by grains initiated ahead of the columnar front (undercooled liquid) [56]. The grain structure is equiaxed if the following equation is satisfied [56].

$$G < 0.617(N^o)^{1/3} \left\{ 1 - \frac{(\Delta T_N)^3}{(\Delta T_{tip})^3} \right\} \Delta T_{tip} \quad \text{Eq. 6-1}$$

Where G is the temperature gradient, N^o is the number density of nucleation site, ΔT_N is the undercooling for heterogeneous nucleation, ΔT_{tip} is the tip undercooling. With the understanding of nucleation and grain initiation, some modifications to **Eq. 6-1** are made. Firstly, the blocking grains should have freely grown so that N_o should be replaced by

the number density of grain initiation event N_{gi} . And correspondingly, the ΔT_N should be replaced by undercooling for grain initiation ΔT_{gi} . ΔT_{tip} is assumed to depend on growth velocity V and alloy composition C_o when the term GD/V is very small [56].

$$\Delta T_{tip} = 2 \left\{ -\frac{2mV(1-k)C_o\Gamma}{D} \right\}^{1/2} \quad \text{Eq. 6-2}$$

$$V = \frac{\Delta S_v D}{8\gamma_{LS} m (k-1) C_o} \quad \text{Eq. 6-3}$$

Where D is the diffusion coefficient of Mg, Γ is Gibbs-Thomson coefficient, ΔS_v is the entropy of fusion per unit volume, m is the slope of the liquidus line, and k is the partition coefficient. We can see that the CET criterion is the result of interplaying among the variables of G , V , C_o and N_{gi} . It has been well illustrated in Hunt's work that the CET is favoured with low thermal gradient, high growth velocity, high solute content, high grain initiation events ahead [56]. This model is applied to analyse how the aforesaid factors (position, solute and number density of MgO particles) affect the CET behaviours in Mg-Ca and Mg-Sn alloys. The CET phenomenon in current work, as a result, can be qualitatively explained. As shown in **Fig. 6.37**, the equiaxed area and columnar area can be separated by a curve (fixed C_o and N_{gi}) into two zones. A dot (d_1 , fixed G and V) locates in the columnar zone at the moment. When the N_{gi} is fixed, the addition of solute (C_o increases) can bring down the separation curve to allow involvement of the d_1 into the equiaxed zone (curve 1). While with a fixed C_o , more nucleation sites ahead (N_{gi} increases) dramatically affect the CET curve in the areas with high G . In such way, the newly generated curve 2 will move to the right and possibly engulf d_1 into the equiaxed zone. From the schematic, it can be found that the columnar structure is favoured by a high thermal gradient. In practice, as the cooling conditions may be spatially different in the melt cast in a specific mould, the dot state (V , G) varies in a function of the position ranging from the edge to the centre of the TP-1 ingot. State d_2 represents a solidifying condition with a high thermal gradient and a fast growth velocity, e.g. at positions near the mould edge; the state locates in the columnar zone.

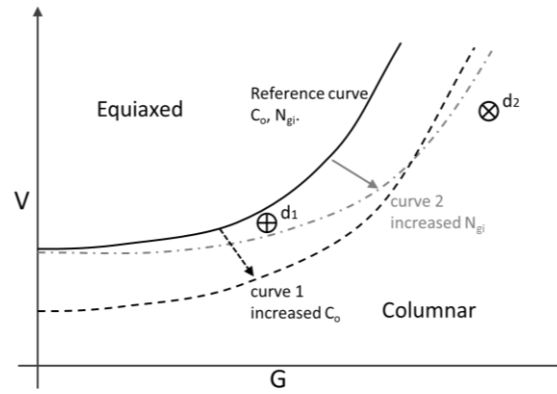


Fig. 6.37 Schematic plots showing the variation of CET curve in a function of N_o and C_o .

The TP-1 casting applied in current work provides a constant cooling of 3.5K/s at the central area 38mm away from the bottom, where the average grain size is quantified experimentally. Therefore, G and V can be notionally fixed in this area under the experimental condition applied in this work. Moreover, ΔT_N and ΔT_{gi} can be fixed when it is assumed that the sole nucleating substrate is native MgO particles with a fixed size distribution (Fig. 4.12). Therefore, the CET map for Mg-Ca and Mg-Sn alloys then can be calculated by Eq. 6-1 and Eq. 6-2 and replotted as C_o against N_{gi} . The parameters applied for the calculation are listed in Table 6-1.

Table 6-1 Physical parameters applied for numerical simulations of CET map.

| | Symbol | Unit | Mg-Ca | Mg-Sn | Reference |
|---------------------------|--------------|----------------------------------|----------|----------|-----------|
| Liquidus slop | m | $K \cdot (\text{wt.}\%)^{-1}$ | -12.67 | -2.4 | [25] |
| Partition Coefficient | k | | 0.06 | 0.39 | [25] |
| Diffusion coefficient | D | $\text{m}^2 \cdot \text{s}^{-1}$ | 2.70E-09 | 2.70E-09 | [244] |
| Gibbs-Thomson coefficient | Γ | $K \cdot \text{m}$ | 1.48E-07 | 1.48E-07 | [244] |
| Growth velocity | V | $\text{m} \cdot \text{s}^{-1}$ | 2.00E-03 | 2.00E-03 | This work |
| Thermal gradient | G | $K \cdot \text{m}^{-1}$ | 1750 | 1750 | This work |
| Nucleation undercooling | ΔT_n | K | 0.6 | 0.6 | This work |

The results are shown in Figs. 6.38(a-c), it is seen that each CET map is divided into two parts: columnar zone and equiaxed zone and CET obeys the general rule that it is favoured by a high C_o and a N_{gi} . The experimental data of C_o (Ca or Sn content) and N_{gi} (converted from AGS [17]) is also plotted on each map, showing reasonable agreements

with the calculated CET map. According to the CET maps, it is understandable to see why the solute required to achieve CET varies from different pre-casting treatments: without HSMC, HSMC and HSO. The number density of native MgO particles matters. It is well known that the HSMC can effectively tear up and disperse the native MgO films to provide a wealth of native MgO particles, which in turn serve as nucleating substrates for Mg grains ($10^{17}/\text{m}^3$ vs. $10^{14}/\text{m}^3$, three orders higher than that without HSMC [164]). The simultaneous and intentional oxidation during HSMC leads to more native MgO particles, assumed to be one order higher, *i.e.*, $10^{18}/\text{m}^3$. Although not all the particles take part in the grain initiation process, the number of initiated grains increases, which is evidenced by the as-cast grain size (Figs. 6.7 to 6.9, and 6.25 to 6.27). Therefore, with more events of grain nucleation and initiation ahead of the S/L front, less solute, of course, is required for the alloy to enter the equiaxed zone.

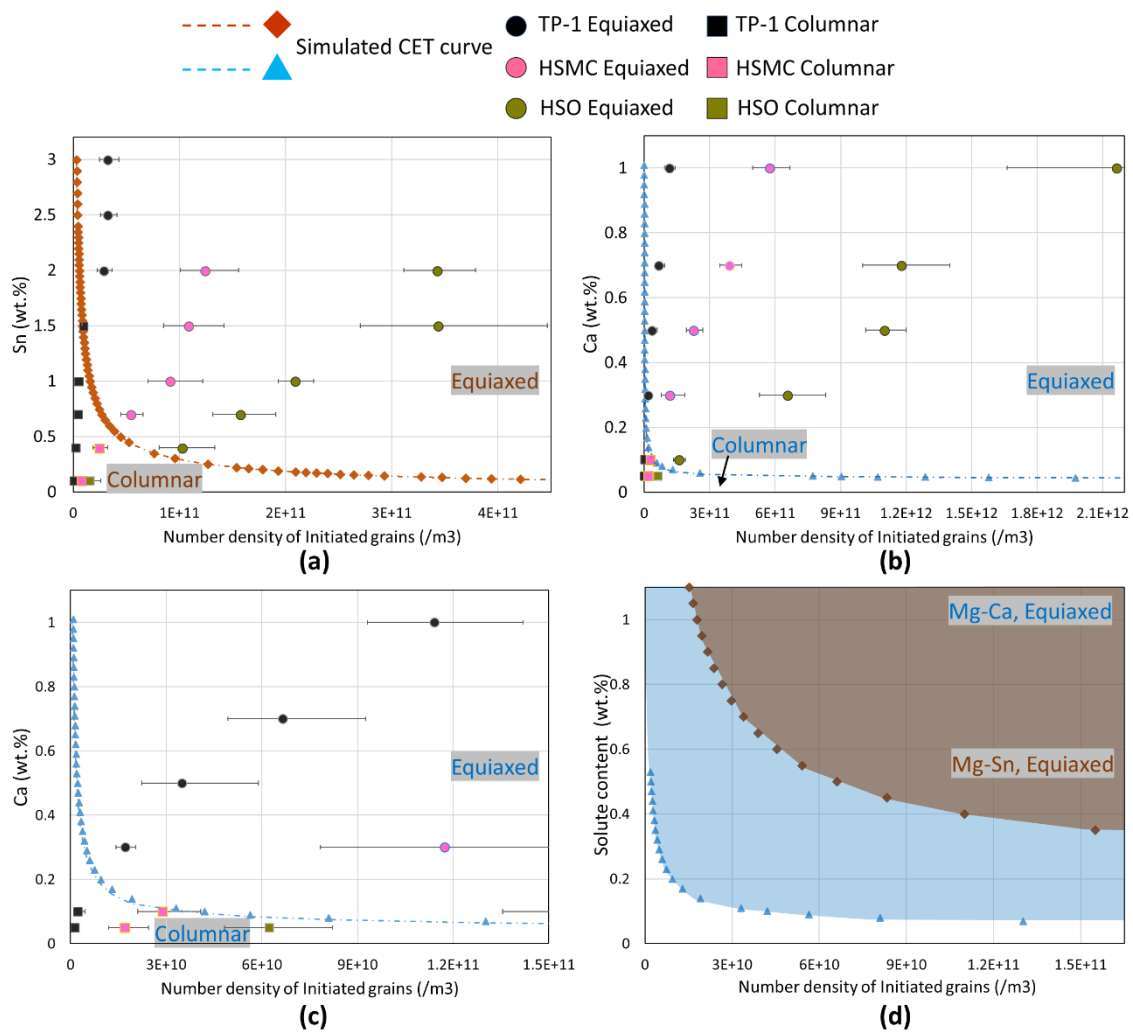


Fig. 6.38 Simulated CET curves plotted in solute content against N_o for (a) Mg-Sn alloys, (b, c) Mg-Ca alloys with different pre-treatment prior to TP-1 casting, (c) is the enlarged zone of the left part of (b). The corresponding experimental data was also plotted showing good agreements with the CET map. (d) comparison of the two simulated CET curves for Mg-Sn (brown) and Mg-

Ca alloys (blue). Note that the circle marks refer to equiaxed grain structure, while the rectangular marks refer to columnar grain structure. TP-1 data is labelled in black, HSMC in pink and HSO in brown.

The comparison of CET curves for Mg-Ca alloys and Mg-Sn alloys is presented in **Fig. 6.38(d)**, and the equiaxed zone for the former alloys is apparently larger. Owing to the higher value of the term ' $m(1-k)$ ' for Ca than that for Sn (**Eq. 6-2**), it requires less content of Ca than that of Sn to create a sufficient ΔT_c to satisfy the CET criterion (**Eq. 6-1**, with other variables kept the same). The mechanism underlying is related to the nucleating and grain initiation events ahead of the columnar front. Ca provides more growth restriction than Sn does under the same content, allowing more time for the grain initiation and growth ahead of the S/L front to block the columnar growth before recalescence. This explains our experimental results, for the samples with HSMC treatment, 0.3% Ca addition is enough for CET in Mg-Ca-HSMC alloys (**Fig. 6.4(c)**) while 0.7% Sn is required in Mg-Sn-HSMC alloy (**Fig. 6.22(c)**).

Although the cooling rate is reasonably stable at the central area 38mm away from the bottom of TP-1 sample, while in practice; variation can appear at the position close to the mould wall and diminishes towards to the centre [13]. ProCAST was employed to simulate the cooling condition of Mg-0.7Sn-HSMC cast in TP-1 method. As shown in **Figs. 6.39(a-c)**, the thermal gradient (G), cooling rate (v), and growth velocity (V) vary in a function of spatial position. All values are high at the mould edge, while they stabilise after a distance into the mould. The corresponding CET map is plotted as V against G in **Fig. 6.39(d)** with overlapping of the simulated data. It is clearly seen that after a short distance (*e.g.*, $>0.5\text{cm}$), the V/G pairs all locate in the equiaxed zone. That means the columnar structure diminishes after 0.5 cm from the edge, which is in a good agreement with the macrograph shown in **Fig. 6.22(c)**. Therefore, the variance in cooling conditions of TP-1 ingot causes the spatial differences in CET behaviour.

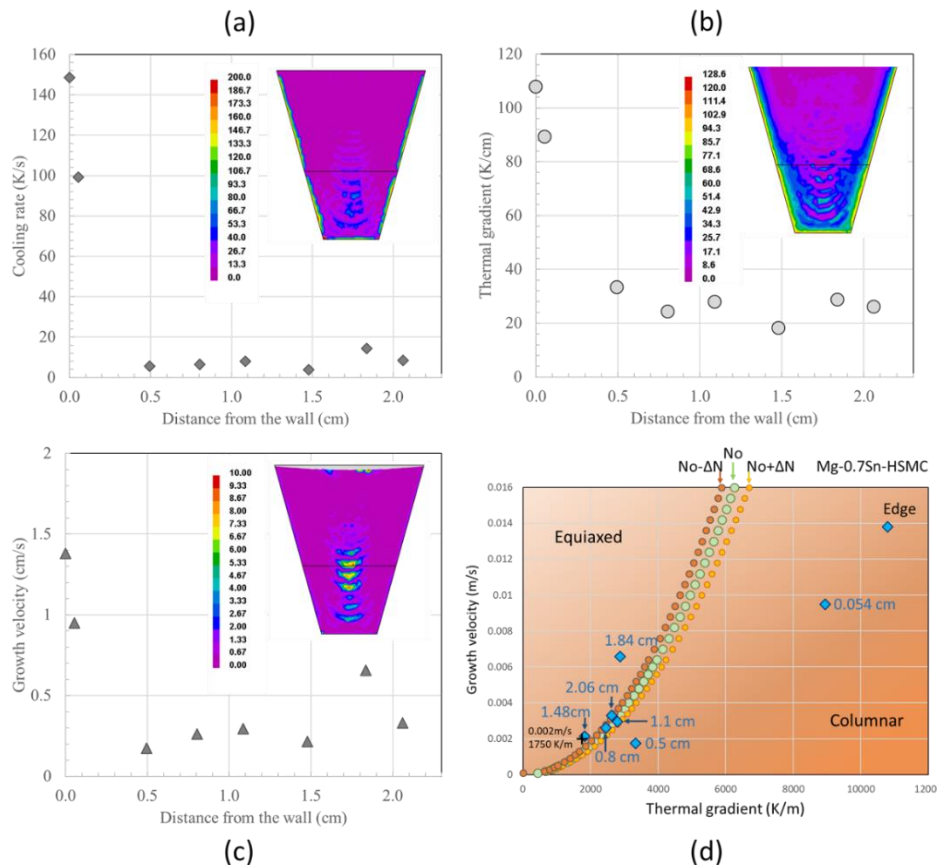


Fig. 6.39 Simulation results calculated by ProCAST software showing the cooling condition for Mg-0.7Sn-HSMC cast in TP-1 mould. (a) cooling rate profile; (b) Thermal gradient profile and (c) growth velocity profile; and (d) the corresponding CET map (plotted in V against G) overlapped with the V/G pairs.

6.3.2 Grain refinement originated from native MgO particles

It has been shown the **section 6.2** that addition of Ca or Sn to CP-Mg contribute to grain refinement (**Figs. 6.1** to **6.10**, and **6.19** to **6.28**). Without external addition of grain refiner in this work, the substrates for heterogeneous nucleation during solidification should be the internal particles, highly possible the native oxides. Due to the high affinity of Mg to O, MgO is the dominant inclusion, which is evinced by the XRD result for CP Mg (**Fig. 4.2(c)**). The introduction of more MgO particles through HSO resulted in smaller grain size than its counterparts, as demonstrated by the plots in **Figs. 6.10** and **6.28**. These native MgO particles can act as the nucleating substrate for Mg solid, as evidenced by the fact that there are well-defined ORs between MgO and α -Mg (**Figs. 4.23** and **4.24**). Other than that, the relatively smaller grain size accompanying with MgO films/particles also indicates MgO particles are closely related to the refinement of grain structure. As shown in **Figs. 6.40** and **6.41**, smaller grains appear in association with MgO films/particles in Mg-Sn or Mg-Ca alloys with HSMC, the dark contrast are induced by MgO particle agglomerates. Whilst, the larger grains are found with the absence of MgO particle

agglomerates. The relatively high number density of MgO particles in the area with MgO particle agglomerates promotes grain initiation events. Therefore, the native MgO particles contribute to the refinement the as-cast microstructure. Although it has been discussed in **section 4.3.4** that the native MgO particle has a poor potency in terms of crystallographic matching, it is applicable through the manner of explosive grain initiation (EGI).

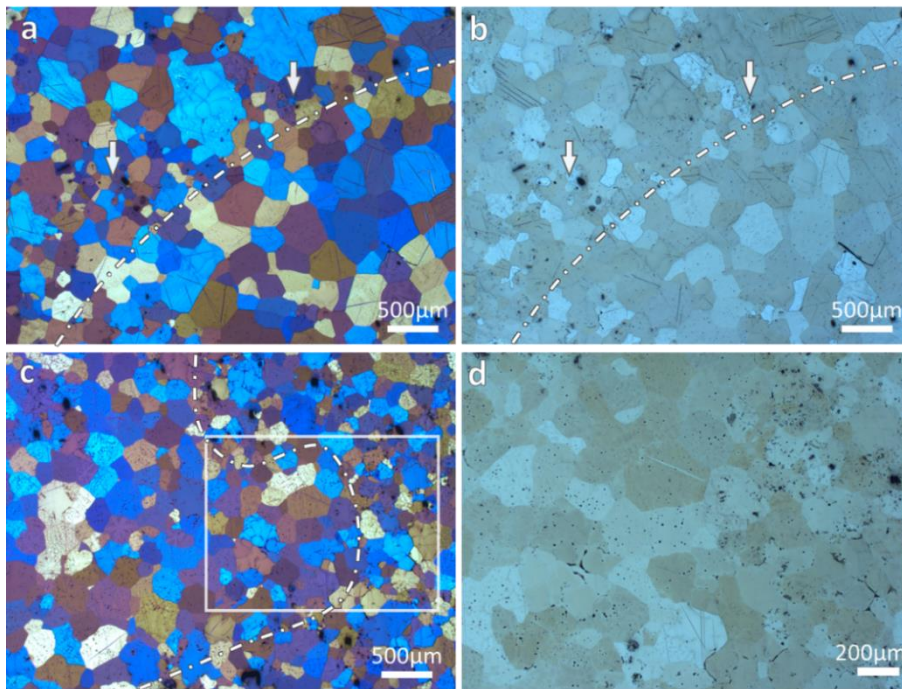


Fig. 6.40 Optical micrographs showing the finer area associated with MgO films/particles in (a, b) Mg-0.7Sn-HSMC and (c, d) Mg-2Sn-HSMC.

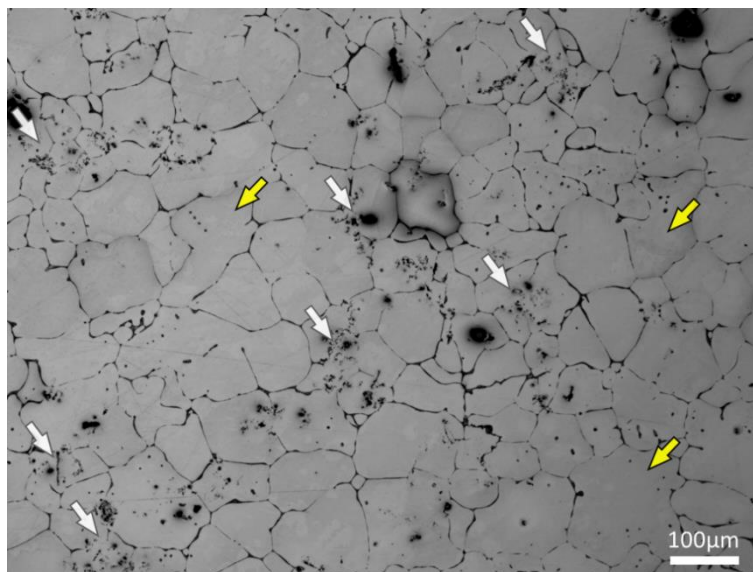


Fig. 6.41 Optical micrographs showing the finer grains associated with MgO films/particles (white arrows) and the relatively coarser grains (orange arrows) in Mg-1Ca-HSMC.

6.3.3 Modification of native MgO and its effect on heterogeneous nucleation

The nature of MgO surface can be modified by elemental segregation and/or local reaction (**section 5.3.3**) so that its potency for nucleation is modified accordingly. Experimental results in this work have shown that the elemental segregation leads to modification of atomic configuration on the MgO surface (**Figs. 6.13 to 6.16 and 6.31 to 6.36**). It is necessary to study firstly how the structural and chemical modification of MgO affect the heterogeneous nucleation of Mg solid, in order to understand the heterogeneous nucleation and grain refinement in Mg-Sn and Mg-Ca alloys,

6.3.3.1 Ca Segregation on MgO

In comparison to the native MgO particles in CP Mg (**Figs. 4.3 and 4.4**), the native {111} and {100} MgO particles in Mg-0.5Ca alloy show negligible differences in terms of their morphology and size. However, Ca/N co-segregation was detected on both types of MgO particles (**Fig. 6.11**) by the HAADF STEM images (**Figs. 6.12 to 6.16**).

Chemically, the segregation layer is concentrated with Ca and N (**Figs. 6.13 to 6.16**). The composition profiles in **Fig. 6.14** suggest that the Ca and N concentrations are increased in the segregation layer with the compensation of O and Mg reduction, with the maximum of 11 at.% of Ca and 27 at.% of N achieved in the segregation layer (**Fig. 6.14**). In terms of structure, MgO itself serves as a simple rocksalt NaCl structure, and it is feasible to determine how the external atoms entering the MgO matrix according to the STEM imaging results in **Figs. 6.13 to 6.16**. The interstitial Ca atoms in possible interstitial sites (*i.e.*, cubic-centre site (0.25, 0.25, 0.25) or the face-centred site (0.25, 0.25, 0) [245]) can be ruled out by the absence of corresponding contrast in **Fig. 6.16** when the {100}_{MgO} facet is viewed along the [001]_{MgO} direction. Ca and N atoms may segregate and partially substitute the Mg and O atoms of the atomic planes on the MgO surface, respectively. It was reported that selective substitution is a general phenomenon found in the case of doping in 2D materials [246], grain boundaries [247] and bulk crystals [248]. Moreover, Yan *et al.* found the doping of Ca on a 24°-tilted [001] grain boundary of MgO, where the atomic column is partially occupied by Ca atoms [249]. DFT calculation also has revealed that N can substitute O atoms in bulk MgO and introduced the presence of vacancies of Mg and O [250]. According to the valence electrons, N³⁻ anions and Ca²⁺ cations may respectively substitute O²⁻ anions and Mg²⁺ cations of MgO. In our case when MgO particle is involved in the Mg-Ca alloy melt, Ca and N atoms may segregate on the MgO surface and serve as substitutional atoms that partially replace the Mg and O atoms,

respectively. This atomic substitution process should be random so that a uniform contrast over the segregation layer results in the HAADF images in **Figs. 6.13** to **6.16**. Otherwise, a distinct periodic feature of the atomic columns is expected to appear in the STEM images detected along different zone axes.

According to the principle of HAADF STEM imaging, the contrast in an image is roughly proportional to the $Z^{1.7}$ [251,252]. This implies that the segregation layer that contains maximum content of 11 at.% Ca (**Fig. 6.14**) should show a higher contrast intensity than that of the MgO matrix due to its higher atomic number ($Z_{Ca} = 20$, $Mg = 12$, $O = 8$, $N = 7$). However, in the current case, the Ca segregation at the interface does not show an expected brighter contrast than that of the MgO matrix in the HAADF images (**Figs. 6.13** to **6.16**). Instead, an oppositely lower contrast appears. The structural modification should be correlated to the resultant contrast, which is discussed below.

The previous study has suggested that the doping and segregation of external element into a host crystal would lead to the modification in the atomic geometry, bonding and local electronic structure [253–256]. On the aspect of atomic geometry, the locally elemental segregation is able to introduce defects and structure transition. As one of the cases in solid state, the structural transformation from HCP stacking to FCC stacking has been found in Mg-Y-Zn alloy [254]. Schmid *et al.* found that Fe segregation at the inversion domain boundary of ZnO in forms of substitutional atoms causes planar disordering [255]. Another case was found in the grain boundary of tungsten carbide (WC), where the Co and Ti segregation respectively introduce the atomic disordering and structural transition [256]. In a case that is more related to the current study, *i.e.*, a system of alloy melt containing substrates: TiB_2 in Al-Zr melt [47], the selective substitution of Zr onto original hexagonal arranged Ti layer results in a protrusion towards Al matrix; such deviation normal to the surface leads to atomic surface roughness [47]. The local atomic geometry can be different from the origin, *i.e.*, sub-atomic deviation or structure transition, owing to the change in the coordination environment.

The substitution of Mg and O atoms by Ca and N atoms at the surface may change the atomic coordination and chemical bonding environment. The segregation structure relaxes into a stable state, during when the defects like vacancy may form. As a consequence, both the atomic deviation and the unoccupied sites reduce the atomic density along an atomic column, which in turn weakens the contrast in the Z-sensitive HAADF image (**Fig. 6.13(c)**), while enhances the contrast in the strain-sensitive MAADF

image (Fig. 6.13(d)). Fig. 6.42 verifies this assumption by comparing the MgO/Mg interfaces in CP Mg and Mg-0.5Ca. With Ca segregation in Mg-0.5Ca (Figs. 6.42(d-f)), the interfacial area of MgO is strained heavier by the MgO matrix than that in CP Mg without segregation (Figs. 6.42(a-c)).

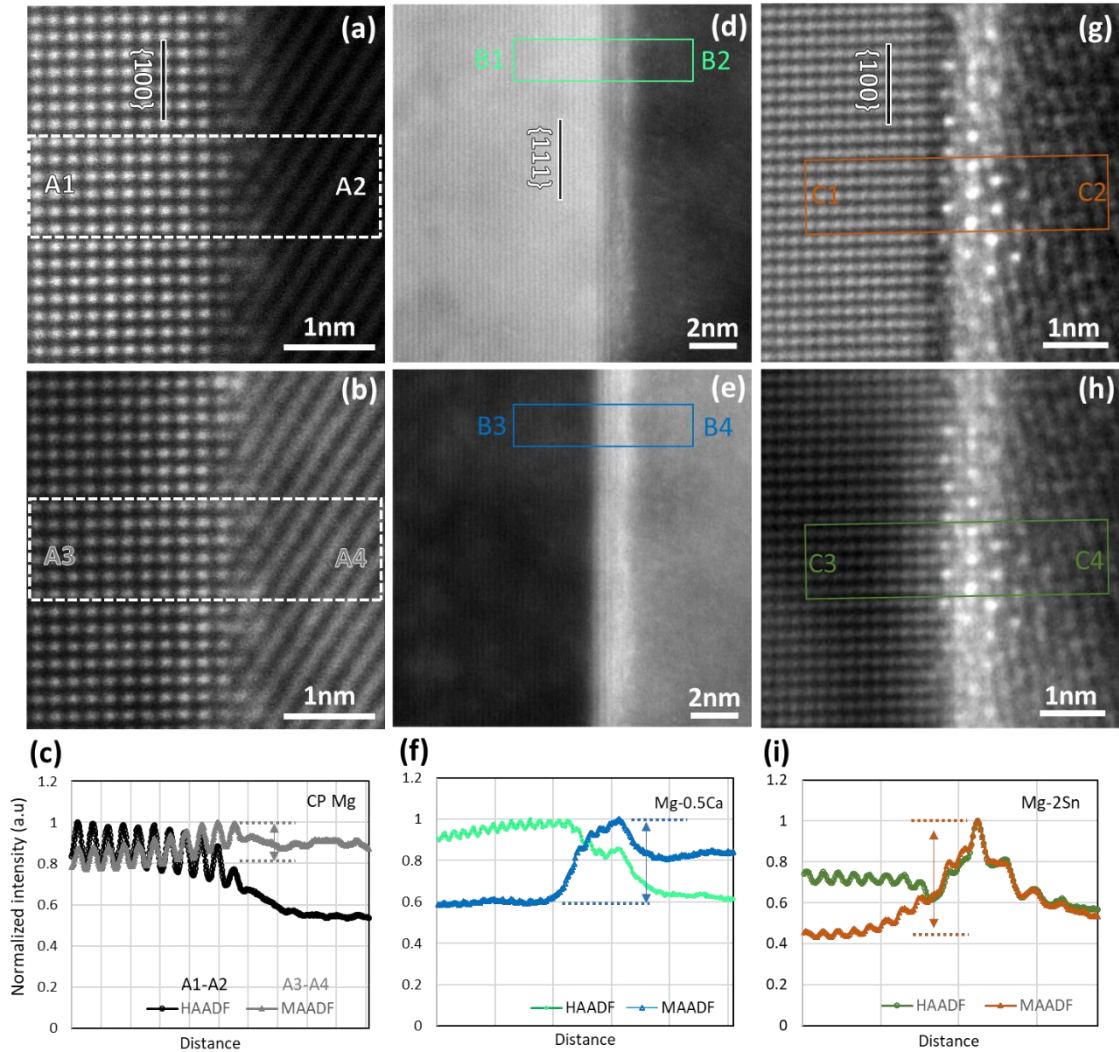


Fig. 6.42 Comparison of MgO/Mg interfacial characterisation in (a-c) CP Mg, (c-f) Mg-0.5Ca and (g-h) Mg-2Sn, suggesting locally strained area on the MgO surface caused by elemental segregation. (a, c, g) HAADF STEM images, (b, e, h) MAADF STEM images; and (c, f, i) the contrast profiles acquired along the marked areas correspondingly.

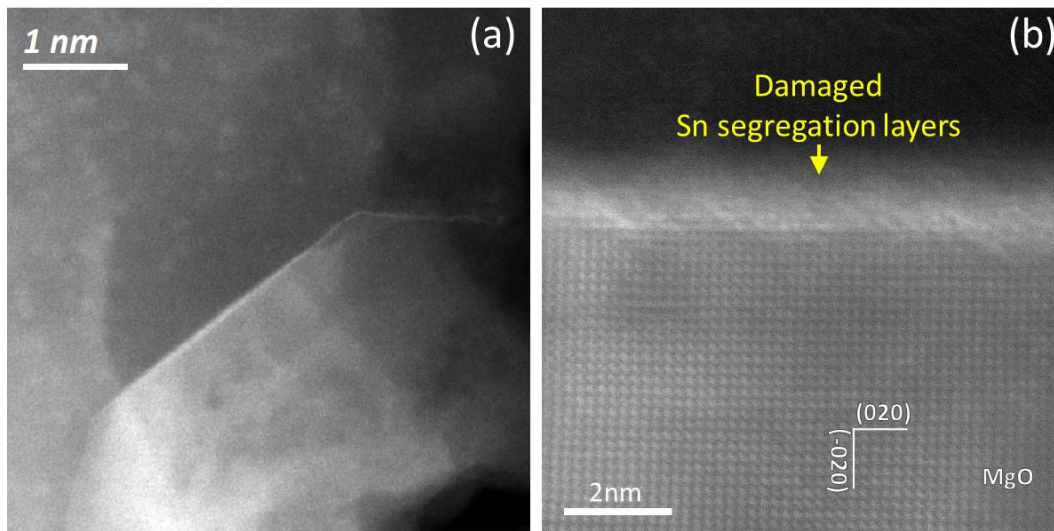


Fig. 6.43 HAADF STEM images showing the damaged Sn segregation layer at the $\{100\}$ termination of MgO in the Mg-2Sn sample prepared by PIPS at room temperature.

6.3.3.2 Sn Segregation layer on MgO

Fig. 6.43 shows the Sn segregation layer on a $\{100\}$ MgO particle in the Mg-2Sn sample that was prepared by Ar ion beam polishing under ambient temperature. It is seen that the Sn segregation layer is fuzzy due to the damages during sample preparation. In contrast, the Sn segregation exhibits as a distinct structure on the $\{100\}_{\text{MgO}}$ surface in Mg-2Sn sample that was prepared by Ar ion beam polishing at a temperature of -70°C (**Figs. 6.33 to 6.36**), which was generated and maintained by the introduction of liquid N_2 as a cooling agent. Although there still exist some a fuzzy feature without distinguished atomic structures (**Figs. 6.33 to 6.36**), the damage extent has been greatly relieved.

From the experimental STEM results (**Fig. 6.34**), the possibility of interstitial Sn atoms has been excluded due to the absent contrast at the corresponding position. The existence of Sn in the segregation layer is in the form of substitutional atoms, sharing the same mechanism as Ca segregation on both $\{111\}_{\text{MgO}}$ and $\{100\}_{\text{MgO}}$ facets (**section 6.3.3.1**) and Y on the $\{100\}_{\text{MgO}}$ facet (**section 5.3.3.3**). With the substitutional mechanism, the Sn segregation layer on the surface of MgO exhibits as a similar lattice arrangement to the MgO matrix (**Figs. 6.34 and 6.35**). On the $\{100\}$ facet, the Sn segregation layer appears as the result of selective substitution (**Fig. 6.34**). While on the $\{111\}_{\text{MgO}}$ facet, the lattice spacings in the Sn segregation layer along $[2\bar{1}1]_{\text{MgO}}$ are the same as that of MgO along the same direction (**Fig. 6.32**). This is similar to the appearance of Y substitution revealed by HRTEM imaging without Cs corrector (**Fig. 5.11**), in which only the interatomic spacing is confidently interpreted, rather than the layer thickness or the exact atomic

position. After all, more work is needed to reveal the details of Sn segregation on $\{111\}_{\text{MgO}}$ facet.

There exist some positional deviations of the Sn-rich atomic columns in the segregation layer from the MgO lattice reference (**Fig. 6.34**). The size effect is unlikely to be the reason for the deviation since Sn and Mg have a very similar atomic radius (145pm (Mg) vs. 145pm (Sn)) and ionic radius (86pm (Mg^{2+}) vs. 83pm (Sn^{4+})) [222,257]. As compared to the surrounding MgO atomic columns, the last $\{200\}_{\text{MgO}}$ crystal plane adjacent to the Sn segregation layer appears in lower brightness contrast (**Figs. 6.35 and 6.42(g)**), suggesting less atomic occupations (more vacancies) in the atomic column along viewing direction. This segregation layer is strained as shown in the strain-sensitive MAADF image in **Figs. 6.42(g-i)**. It is expected that vacancies are created due to the difference in valence electrons between Sn and Mg in the segregation layer. With the vacancies created, the positional deviation of Sn-rich columns in **Figs. 6.35 and 6.42(g-i)** may be the result of strain relaxation. While some residual strain remains as suggested by the comparison of contrast profiles in **Fig. 6.42(i)**.

Moreover, The following information can be obtained based on the EELS analysis (**Fig. 6.36**): *i*) Sn concentrates at the interface; *ii*) concentration of O is higher at the interface than that in Mg matrix and *iii*) Mg is deficient at the interface, possible Sn-O and Sn-O-Mg phases were searched in the crystal database and the literature. To the best knowledge of the author based on the thorough search of the available database and the crystallography of various phases, none of the reported Sn-O or Sn-O-Mg phases could produce the same features as detected in the STEM images in **Figs. 6.34 and 6.35**. It is, therefore, rationally concluded that the interaction between Sn solute and MgO results in atomic substitutions of Mg atoms by Sn atoms on the MgO surface, without the formation of a new phase. The introduced vacancies and variance in chemical bonding environment can give rise to the reduction of atomic occupation as well as the atomic deviation away from the original atomic position on the $\{111\}_{\text{MgO}}$ or $\{100\}_{\text{MgO}}$ crystal facet. After all, more TEM work together with DFT simulation work is still needed in order to reveal exactly how Sn segregates on the MgO surface.

6.3.3.3 Reduced potency of MgO

It is well known that the crystallographic lattice match between the nucleating substrate and solid is one of the key parameters determining the potency of heterogeneous nucleation: a better match usually corresponds to a lower undercooling for nucleation.

This suggests that, due to the unchanged lattice structure (**Figs. 6.12 to 6.16**, and **6.33 to 6.36**), segregation of Ca/N or Sn on the MgO surface should not alter the lattice misfit between MgO and with Mg. However, there are more factors affecting the potency of a substrate rather than misfit only. The introduction of vacancies and atomic deviation from the lattice position may introduce either surface roughness or in-plane disordering, which will subsequently affect the pre-nucleation and thus the heterogeneous nucleation process [31,46,233]. In terms of the Ca/N co-segregation on MgO particles in the Mg-0.5Ca alloy, vacancies and atomic deviation from the original lattice site have been supposed to exist in the segregation layer, causing the lower contrast than the MgO matrix. In the Sn segregation layer on MgO particles in the Mg-2Sn alloy, atomic protrusion of the Sn-rich atomic column and vacancies also have been recognised. Either surface roughness or in-plane disordering may be increased on the MgO surface in these two alloys, so that their potency may be reduced. This is also understandable based on the epitaxial model, where nucleation is considered as the layer-by-layer formation of the adsorbed atoms at the interface templating the atomic structure of the substrate [34]. With the existence of surface roughness or in-plane disordering at the substrate facet, it is more difficult for the adsorbed liquid atoms to mimic the atomic structure of the terminated facet as the chemical and/or structural nature has deviated from that of inside the bulk. As a result, defects like dislocation are required to compensate that effect when the PS layer increases, which will raise the undercooling required for nucleation [34]. It has also been reported that less in-plane ordering and surface roughness post a negative effect on heterogeneous nucleation [43,47,233]. Wang *et al* showed that the Ti₂Zr 2D layer impedes the pre-nucleation process as the results of the geometric protrusion of Zr-rich atomic column and the difference in the heat of mixing for Zr and Ti [47]. Fang *et al* found that the existence of vacancies in the outmost {111} crystal layer of MgO also poses a negative effect on pre-nucleation[31,233]. Molecule dynamics (MD) simulation was applied to study the pre-nucleation phenomenon above liquidus. It showed that the templating capacity decreases as the last layer has a degraded ordering extent; the near-interface solid-like layers exhibit a decay of density profile towards liquid [43]. After analysing the effects of misfit, surface roughness and in-plane ordering on nucleation potency, it is clear that the segregation of Ca or Sn will modify the surface of MgO particles, leading to a further reduced nucleating potency for the modified MgO.

6.3.4 Mechanism for grain refinement by impotent substrate

The experimental results have shown that the originally poor potency of the native MgO particles (**Table 4-3**) is further reduced by elemental segregation behaviour of Ca or Sn. This atomically modified MgO particle is straightforwardly supposed to be incompetent for grain refinement in the conventional view of point where potent nucleating particles are always favoured. Nevertheless, as discussed in **section 4.3.4**, the interplay between ΔT_n and ΔT_{gi} can lead to another grain initiation manner: explosive grain initiation (EGI), resulting in profound grain refinement [29]. This EGI scheme can be used to explain the experimental results in Mg-Ca and Mg-Sn alloys. To validate this conjecture, we carried out numerical simulations to simulate the solidification in the Mg-Ca and Mg-Sn alloys containing native MgO particles. Following the method for numerical simulation reviewed in **section 2.2.1** and **ref.** [17,30], the numerical simulation involving the nucleation, growth and heat exchange inside the Mg-Ca/Sn melts with native MgO particles was performed by a compiled Matlab code, with the parameters being listed in **Table 6-2**. The total melt volume is fixed at 1cm^3 for all simulations, the time step used is 10^{-5}s in cases of explosive grain initiation, and the size range per step was 20 nm. The numerical simulation recently has successfully demonstrated the grain initiation behaviour in Mg alloys, where impeding nucleation yields more significant grain refinement [30].

Table 6-2 Physical parameters applied for numerical simulations of the solidification processes in Mg-Ca and Mg-Sn alloys.

| Quantity | Symbol | Unit | Mg-Ca/Sn | Reference |
|------------------------------------|--------------|--|----------------------|-----------|
| Enthalpy of fusion per unit volume | ΔH_v | $\text{J}\cdot\text{m}^{-3}$ | 6.75×10^{-8} | [244] |
| Gibbs-Thomson coefficient | Γ | $\text{K}\cdot\text{m}$ | 1.48×10^{-7} | [244] |
| Heat capacity | c_{pv} | $\text{J}\cdot\text{m}^{-3}\cdot\text{K}^{-1}$ | 2.59×10^6 | [244] |
| Diffusion coefficient | D | $\text{m}^2\cdot\text{s}^{-1}$ | 2.79×10^{-9} | [244] |
| Partition coefficient | k | | 0.06/0.39 | [25] |
| Liquidus slope | m | $\text{K}\cdot(\text{wt}\cdot\%)^{-1}$ | -12.67/-2.41 | [25] |
| Log-normal distribution mean | d_0 | m | 68×10^{-9} | This work |
| Standard deviation | σ | N/A | 0.4 | This work |

All the parameters in **Table 6-2** are either quoted from reference or experimentally measured in current work. Whilst, some other values are estimated, *e.g.*, the number density of MgO particles (N_o) for alloy melts with different pre-treatments ($5 \times 10^{14}/\text{m}^3$ for TP1, $2 \times 10^{17}/\text{m}^3$ for HSMC and $2 \times 10^{18}/\text{m}^3$ for HSO), and the nucleation undercooling for MgO ($\Delta T_n = 1.2\text{K}$, which has been applied for many Mg alloy systems and shown good agreement with the experimental results [30]).

The growth restriction parameter (β) was recently developed to effectively quantify the growth restriction [54], which can be calculated by **Eq. 2-34**. Then the variations in Ca and Sn contents can be described in corresponding β values. As shown in **Fig. 6.44**, the simulated grain size is plotted against β , where the simulated curves show a good agreement with the experimental data. It is admitted that this can be obtained through the interplaying of estimated input parameters. However, the estimated parameters applied into simulation are rational as they not only predict β -grain size curves (see **Fig. 6.44**) with the reasonable fitting with measured results, but also fall in a rational range compared to the estimated values reported previously [28,29,164]. It was reported that the measured undercooling $T_R - T_{min}$ (T_R is the recalescence temperature, T_{min} is the lowest temperature before recalescence) is 0.7 K for the AZ91D alloy with HSMC treatment [164]. The liquidus temperature T_L is higher than T_R , so that the actual nucleation undercooling should be larger than 0.7 K. A rational heterogeneous nucleation undercooling of 1.2K for the native MgO particle in Mg-Al alloys has been adopted in **ref** [30], showing a good agreement between the theoretical predictions and the experimental grain size. Therefore, $\Delta T_n = 1.2\text{K}$ is adopted for the impotent MgO particles in Mg-Ca and Mg-Sn alloys. Secondly, the number density of MgO particles used for each casting process also falls in the proper range estimated in previous work: $5 \times 10^{14}/\text{m}^3$ vs. $2.1 \times 10^{14}/\text{m}^3$ [164] for TP1 without HSMC, $2 \times 10^{17}/\text{m}^3$ vs. $3.2 \times 10^{17}/\text{m}^3$ [164] with HSMC; and one order higher ($2 \times 10^{18}/\text{m}^3$) with HSMC and oxidation.

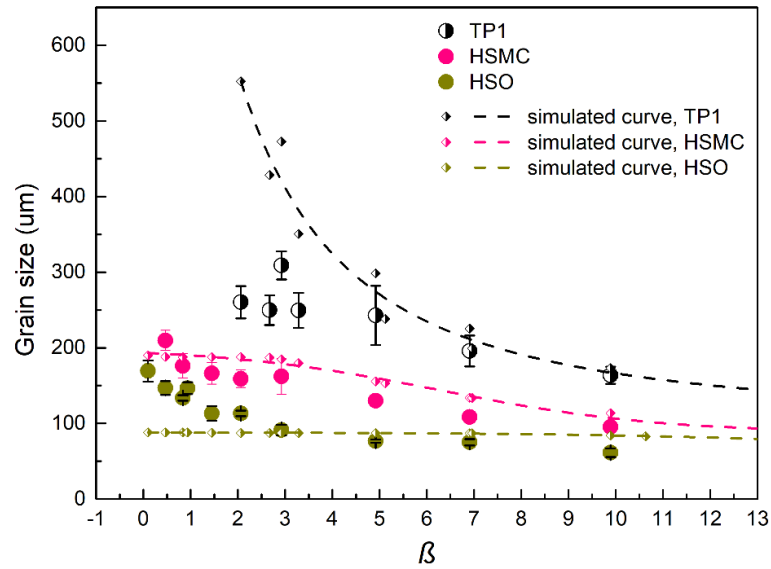


Fig. 6.44 Plots of experimental and simulated grain size against growth restriction parameter β for Mg-Ca and Mg-Sn binary alloys with different pre-treatments before TP-1 casting. Free growth model was applied to simulate the predicted values.

The corresponding evolution of EGI percentage in a function of β is shown in **Fig. 6.45**. For TP1 casting without HSMC, the grain initiation manner is found as deficient in EGI percentage that gradually drops and reaches zero as β increases. Only a marginal amount of MgO particles experience EGI due to the naturally agglomerated oxide films, and the latent heat is too small to cause recalescence. The melt can be cooled further to allow progressive grain initiation (PGI) to proceed on eligible MgO particles until recalescence. The number and proportion of PGI events increase with increasing β . When β is small, the small amount of PGI events cannot cause CET and then a coarse and columnar grain structure results (**Figs. 6.1** and **6.19**). The PGI events increase when β is increased to impeded recalescence, causing CET and refined grain size (**Figs. 6.1** and **6.19**). Similar to previous research [17,25,30,63], the effect of β on grain size gradually become minor. In contrast, the grain initiation manners are EGI dominant in the Mg alloy melt with HSMC treatment at low concentrations. EGI proportion keeps decreasing as β increases, and extra involvement of PGI events further reduces the grain size (**Figs. 6.44** and **6.45**). Besides, for the Mg alloy melts with HSO treatment, EGI manner dominates throughout the β range, despite EGI still drops little with β increment. This is because the average grain size (AGS) is proportional to the cube root of grain initiation events. When the AGS has been very small in HSO-treated alloys, an extra high proportion of PGI is required to

visibly change the as-cast AGS. Therefore, in the simulated '-HSO' curve, extra PGI event does not contribute to a distinguished reduction in grain size (Figs. 6.44 and 6.45).

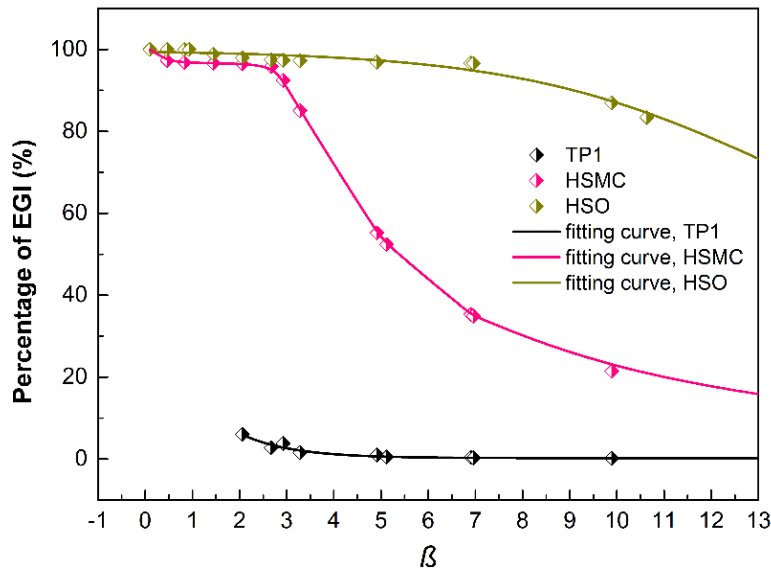


Fig. 6.45 Simulated plots of the percentage of explosive grain initiation in a function of growth restriction parameter β for Mg-Ca and Mg-Sn binary alloys with different pre-treatments before TP-1 casting. Free growth model was applied to simulate the predicted values.

The underpinning reason is the competition between heat release from growth and heat extraction by the environment. Explosive manner dominants at a low β value because the huge heat release cause recalescence immediately to stifle further progressive grain initiation. When growth restriction is enhanced, the recalescence is impeded, and the heat extraction keeps lowering the melt temperature, more particles then are further involved in grain initiation following a progressive manner. Undoubtedly, the extra contributions from PGI after EGI are beneficial for grain refinement. It is also predictable that the promoted cooling rate, which has a similar function to impede the recalescence, will play a positive role in allowing more extra PGI event and further refining the grain size.

Now it becomes clear that Mg-Ca or Mg-Sn alloys without HSMC experience a solidification behaviour dominated by PGI, the poor potency and a low number of MgO particles lead to a coarser grain size than the counterpart alloys with HSMC. The solidification behaviour in Mg-Ca or Mg-Sn alloys with HSMC is dominated by EGI when β is small, and the PGI proportion increases as β increases. With a high number density of impotent MgO particles, the number of grain initiation events in EGI and PGI manner is huge, so that fine grain sizes result. The extra oxidation introduces more

impotent MgO particle into the melts, promoting both grain initiation in EGI manner and results in a finer grain size.

Therefore, in certain conditions (a suitable number density of nucleating particle, solute concentration and cooling condition) the native MgO particles with a poor potency in Mg-Ca and Mg-Sn alloys can be harnessed to achieve grain refinement. The mechanism underlying has been demonstrated by the numerical modelling, where grain refinement is achieved by triggering more particles in the manner of explosive grain initiation, alongside with extra progressive grain initiation events under the given growth restriction.

6.4 Conclusions

1. The addition of solutes Ca/ Sn and the increased number density of MgO particles (due to pre-treatments of HSMC or HSO) promote columnar to equiaxed transition (CET) and grain refinement in Mg-Ca and Mg-Sn alloys. HSMC and/or HSO allow: *i*) CET to occur at a lower solute content; and *ii*) finer grain size of Mg-Ca and Mg-Sn alloys than that directly cast into TP-1 mould. After CET the effect of solute on grain size is minor as the solute content increases.
2. In Mg-Ca and Mg-Sn alloys, there are two types of MgO in terms of morphology: {111} MgO and {100} MgO. The morphology and size of the native MgO particles are not affected by the addition of Ca and Sn.
3. Segregation of Ca is associated with N on the surfaces of native MgO particles. The segregation layer on {111} and {100} surface of MgO has a crystal structure resembling that of bulk MgO, with Ca and N atoms selectively substitute some of the Mg and O atoms on the MgO surface, respectively. The co-segregation of Ca and N results in surface roughness and in-plane disordering, which in turn make the pre-nucleation more difficult than the unmodified MgO particle. Subsequently, the nucleation potency of the MgO modified by the co-segregation of Ca and N is reduced.
4. Segregation of Sn is observed on the surfaces of native MgO particles. Sn atoms selectively substitute some of the Mg atoms in MgO without changing the lattice structure. Sn interfacial segregation on MgO surface introduces surface roughness and thus reduces its ability for pre-nucleation and nucleation.

5. With pre-treatments of HSMC or HSO imposed to the alloy melts, the native MgO particles, which have poor potency as the result of elemental segregation in Mg-Ca and Mg-Sn alloys, can be harnessed to achieve significant grain refinement through solidification dominated by explosive grain initiation.

7 General Discussion

7.1 Morphology of native MgO particles in Mg alloys

Both the cubic and octahedral MgO particles ($\{100\}$ and $\{111\}$ MgO) have been identified in the Mg alloys studied in this work, including CP Mg, Mg-9Al, Mg-0.5Y, Mg-0.5Ca and Mg-2Sn (Figs. 4.3 to 4.5, 5.4, 5.5, 6.11, 6.29 and 6.30). According to the experimental results, it seems that the morphology of MgO particles is negligibly affected by the solutes in the alloy melts. The formation of $\{100\}$ and $\{111\}$ MgO particles may follow the same mechanism that has been proposed by analysis of thermodynamics and kinetics in section 4.3.2 and 4.3.3. $\{100\}$ MgO is the oxidation product of Mg vapour, and $\{100\}_{\text{MgO}}$ faceted plane has the lowest surface energy. While $\{111\}$ MgO is the product of oxidation on the melt surface, under which condition the polar $\{111\}_{\text{MgO}}$ faceted is kinetically favoured and stabilised by the Mg-screening effect. Although the conditions of oxidation reaction are different, the morphologies of MgO products are both thermodynamic- and kinetic-controlled.

Being the oxidation product of Mg, the native MgO can be either the oxidation product during casting practice or the inclusions inherently present inside the raw materials. To understand why both $\{100\}$ and $\{111\}$ MgO particles are not affected by solutes in the melt. It is necessary to consider the possible effect of solutes on its morphology during the growth stage for the MgO particles formed during casting, and the effect of solutes on the inherent MgO particles through solute/MgO interaction.

The morphology of a crystal can be affected significantly by the involvement of foreign atoms. They may serve as adsorbed substance during growth on the facet of a crystal at different sites: kinks, step ledges and surface terraces to kinetically alter the growth rate on specific directions [165,258,259]. This has set the basis for the modification of eutectic Si in Al-Si alloys by the addition of modifier elements, which can adsorb at the intersection of Si twins to modify its growth pattern and the ultimate morphology [260,261]. Besides, it has been reported that KCl crystal, one of the alkali halides, change its morphology from cubic to octahedral in the presence of Pb ion in the aqueous solution [262]. The preferential precipitation of PbCl_2 on the $\langle 110 \rangle_{\text{KCl}}$ steps causes the pile-up of the steps on $\{100\}_{\text{KCl}}$ surface, which was proposed as the mechanism for the appearance of $\{111\}_{\text{KCl}}$ facet. In this study, the alloying elements Al, Y, Ca or Sn do not participate

in the growth process of MgO particles according to the experimental results. With the assistance of advanced electron microscopy to trace any composition variance inside the MgO particles, none of the solutes (Al, Y, Ca and Sn) has been detected inside the MgO crystals in all the binary alloys by HAADF imaging and/or EELS spectroscopy (**Figs. 4.15 to 4.17, 5.13 to 5.19, 6.13 to 6.16, and 6.33 to 6.36**). Therefore, it is less likely that the solutes applied in this work take part into the MgO growth during oxidation.

The impurities may also thermodynamically change the surface energy of the crystal facets by adsorption, which in turn may alter the ultimate morphology of a crystal [165,258,259]. When the integral MgO particles are placed into a solution, their morphologies are able to be altered through the modification of surface energies of specific crystal planes by interacting with the substance in the solution [168–172]. For example, dissolution of cubic MgO particles in aqueous solutions is a general phenomenon that agrees well with the theoretical calculation of surface energy [171,211]. The $\{111\}_{\text{MgO}}$ facet can be stabilised by the adsorption of ‘-OH’ groups, leading to the reduction of surface energy [172]. Similarly, doping of Li [263] ion or Fe ion [264] onto the cubic MgO particles were also found to change their morphology. In this study, the solutes of Y, Ca or Sn do segregate onto the surface of MgO particles, forming distinct segregation layers that are different from MgO in terms of composition and/or structure (**sections 5.2.3, 6.2.6, and 6.2.15**). However, the macro morphology of both $\{111\}$ and $\{100\}$ MgO particles remains. It is understood that the elemental segregation is driven by the decrease of interfacial energy [32,184,185,188]. The elemental segregation layers on the surface of MgO particles maintain the parallelism to the original $\{100\}_{\text{MgO}}$ and $\{111\}_{\text{MgO}}$ facets, and they confine within atomic thicknesses ranging from one atomic layer to a few. As a result, the interaction between both the $\{111\}$ and $\{100\}$ MgO particles and solutes in this work stabilises the original facets by the atomic-thickness elemental segregation, leaving the ultimate morphology unchanged.

However, the interaction between Y and MgO is intensified to micron scale in Mg-Y alloys when Y content is sufficiently high (*e.g.*, Y=3%) (see **Figs. 5.23 and 5.24**). According to the Ellingham diagram as well as the recent thermodynamic calculation [227,228], the transformation of MgO into Y_2O_3 is possible in Mg-Y alloy melts when the Y content allows the entry to Y_2O_3 -containing zone in the phase diagram. As validated by experimental observations in this work, the formation of C- Y_2O_3 particles and dissolution of native MgO particles occur in Mg-3Y alloy melt (**Figs. 5.23 and 5.24**).

7.2 Modification of MgO and its nucleation potency

Nucleation potency is an index to evaluate the capability of a substrate for nucleation of a solid phase. The structural matching between the substrate and the solid at the interface is closely correlated with the nucleation potency, with a number of theories and models applying the lattice misfit under a specific matching OR as an indicator for the nucleation capacity [14,16,34,71]. This can be referred to as a structural factor. Recent studies advance our understanding of nucleation by taking two more factors into account: chemical factor [45] and surface roughness [46]. Generally, a chemical affinity between substrate surface atoms and the adjacent liquid atoms promotes the atomic ordering of liquid atoms closely above the substrate (*i.e.*, pre-nucleation), which in turn promotes heterogeneous nucleation. On the other hand, a chemical repulsiveness between them at the substrate/liquid interface degraded the ability of pre-nucleation. Also, the surface roughness of a substrate is closely related to both atomic layering and in-plane atomic ordering in the liquid adjacent to the substrate during pre-nucleation [46]. An atomically rough surface of substrate impedes prenucleation and in turn inhibits the subsequent nucleation process, reducing the substrate's potency for nucleation.

The affecting factors mentioned above raise the importance of the atomic configuration on the surface of a substrate. With the assistance of advanced electron microscopy, the variance of atomic configuration at the surface of native MgO particles was identified. There are three situations for the native MgO particles in various Mg alloys.

(1) There is no preferential segregation of elements on the MgO surface as those in the Mg-9Al melt (**Figs. 4.15 to 4.17**). The segregation of Al at the interface of MgO/Mg melt is energetically unfavourite as it will raise the interfacial energy γ_{LN} , *i.e.*, $\frac{\partial \gamma_{LN}}{\partial X} > 0$. This results in a constant lattice parameter and therefore an unchanged potency in terms of lattice misfit (f). However, atomic interaction may occur between the Mg and/or O atoms on the MgO surface and the surrounding Mg and/or Al liquid atoms without segregation. A recent study using *ab initio* molecular dynamics simulation revealed a hexagonal atomic configuration of Mg atoms together with vacancies on both the O-terminated or Mg-terminated $\{111\}_{\text{MgO}}$ surfaces of MgO [31]. The $\{111\}_{\text{MgO}}$ surface therefore becomes rough at the atomic scale. At the $\{100\}_{\text{MgO}}$ surface, the difference in chemical bonding for Mg-Mg and Mg-O also introduces surface roughness. Due to the surface roughness introduced by defects (vacancies) or chemical-bonding difference, the nucleation potency

of both types of MgO substrate is degraded. A simulation work studying the interaction between Al liquid atoms and MgO substrate indicates a similar effect [265]. How the interaction between the native MgO and relevant solute atoms proceeds in an Mg-Al melt warrants further investigations.

(2) Element segregation on the MgO surface is energetically favoured, *i.e.*, $\frac{\gamma_{LN}}{\partial X} < 0$, and the lattice misfit between the modified MgO and Mg decreases *i.e.*, $\frac{\partial f}{\partial X} < 0$, heterogeneous nucleation is promoted. As shown by HAADF images, the {111} MgO particles in Mg-Y alloys interact with Y solute, forming Y₂O₃ 2DC on its {111}_{MgO} plane obeying a certain OR (**Fig. 5.26**). Such intermediate phase significantly reduces the lattice misfit f from 7.86% between MgO and Mg down to 1.71% between Y₂O₃ 2DC and Mg (**Fig. 5.28** and **Table 5-2**), indicating a higher potency than the original {111}_{MgO} substrate (**Table 4-3**).

(3) The element segregation modifies the MgO surface with an invariant lattice structure, *i.e.*, an unchanged lattice misfit, $\frac{\partial f}{\partial X} = 0$, while it associates with defects like vacancies or dislocations that introduce surface roughness of the substrate. The nucleation potency of MgO therefore degrades as compared to the original MgO without segregation. This has been experimentally demonstrated by the co-segregation of Ca and N on the MgO surface in Mg-0.5Ca alloy (**Figs. 6.15** to **6.17**), where an isostructural Ca segregation layer with high strain extent was formed. The degraded nucleation potency of MgO particles is verified by explosive grain initiation (EGI) manner, resulting in finer grain size than that achieved in Mg-0.1Y and Mg-0.5Y alloys which experienced PGI manner.

It can be concluded that the potency of native MgO for nucleating primary Mg solid can be modified by tuning the atomic configurations at the terminated surface. An analogous case is noticed in TiB₂/Al systems [47,189], where the lattice misfit of TiB₂ ($f_{TiB_2}^0 = -4.2\%$) decrease to $f_{TiB_2}^{Al_3Ti}^{2DC} = 0.09\%$ by the formation of a Al₃Ti 2DC monolayer on its {0001}_{TiB₂} plane, or it is reset back to -4.2% through the formation of Ti₂Zr 2DC monolayer on the {0001}_{TiB₂} plane. It is believed that the modification of nucleation potency of substrates is a general phenomenon, which is probably the reason why it is less likely to have a universal grain refiner for a specific metallic system. Such statement, as least, is true for Al and Mg alloys.

7.3 Nucleation, grain initiation and grain refinement in Mg alloys

Solidification involves two distinct stages: nucleation and growth. The former is determined by nucleation undercooling (ΔT_n) and the latter is determined by the grain initiation undercooling (ΔT_{gi}). Following the time sequence, nucleation of solid usually occurs before growth on a substrate with high potency ($\Delta T_n < \Delta T_{gi}$). While nucleation and growth can proceed simultaneously on a substrate if $\Delta T_n \geq \Delta T_{gi}$. The incorporation of the deterministic nucleation process into the numerical modelling for solidification reveals two kinds of distinguished grain initiation manners: *i*) progressive grain initiation (PGI); and *ii*) explosive grain initiation (EGI) [28–30]. In a Mg alloy only containing MgO particles with a fixed size distribution, the nucleation and grain initiation manner can be affected by the factors including: potency; number density of MgO particles; solute concentration (growth restriction); and cooling rate [28–30]. Their effects will be discussed one by one with the rest parameters being constant.

In a Mg alloy with a certain number density of native MgO particles, manipulation of their potency for nucleating Mg solid through elemental segregation could alter the nucleation and grain initiation behaviour of the alloy melt. The native MgO particles without elemental segregation have a lattice misfit of 7.86% with Mg (**section 4.3.4.1**), indicating a large ΔT_n required for heterogeneous nucleation of Mg solid on the MgO particles. The particles that satisfy $\Delta T_n \geq \Delta T_{gi}$ undergo simultaneous nucleation and initiation of Mg grains, *i.e.*, EGI manner. The nucleation potency of the MgO particles can be changed due to elemental segregation on their surface (**section 7.2**), which in turn affects the nucleation and grain initiation behaviour. For instance, the nucleation potency of {111} MgO particles is enhanced by the formation of Y₂O₃ 2DC on the MgO surface to reduce its lattice misfit with Mg down to 1.71% (**section 5.3.3.2**). A small ΔT_n is expected. The MgO particles that satisfy $\Delta T_n < \Delta T_{fg} \leq \Delta T$ then undergo grain initiation of Mg progressively from the largest particle to the smaller ones, *i.e.*, PGI manner.

The number density of native MgO particles can be manipulated by the application of high shearing melt conditioning (HSMC) or HSMC plus extra oxidation (HSO). With a fixed large ΔT_n , MgO particles that satisfy $\Delta T_n \geq \Delta T_{gi}$ experience nucleation and grain initiation of Mg grains simultaneously. The number of these EGI events on the MgO particle is affected by the number density of native MgO particles. There exists a critical number density of MgO particles, where a large latent heat released by the nucleation and

the initial free growth of EGI events will cause an immediate recalescence to stifle extra PGI events on smaller MgO particles. Then the grain initiation behaviour is completely explosive (see HSMC and HSO curves in **Fig. 6.45** at low β). However, if the number density of native MgO particles is below the critical value, for instance in Mg alloys without HSMC/HSO, smaller MgO particles are able to grain initiate Mg grain in PGI manner (see TP1 curve in **Fig. 6.45**). A certain proportion of PGI events occurs. Apparently, EGI is favoured with a high number density of impotent MgO particles, as demonstrated in **Fig. 6.45**, where the proportion of EGI in HSO-treated samples prevails over that in samples treated by HSMC. Moreover, HSO-treated samples show resistance to growth restriction on EGI transition.

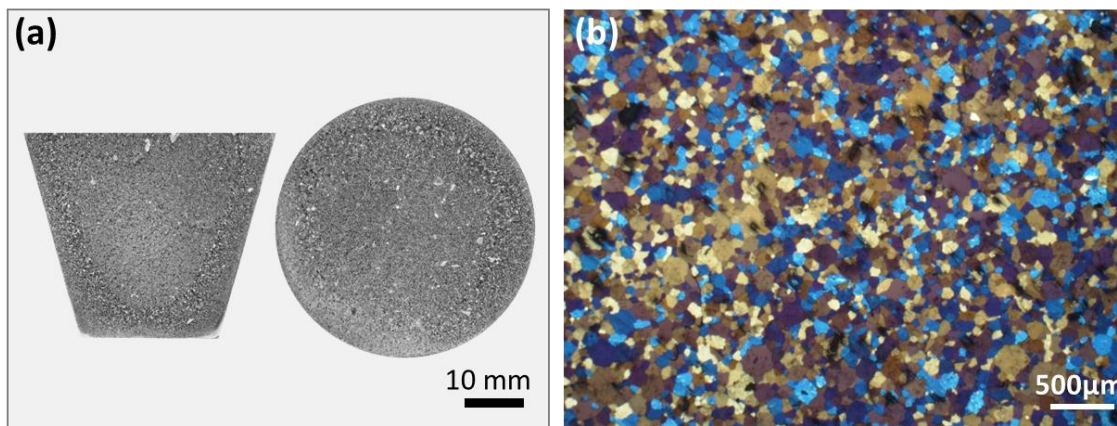


Fig. 7.1 Optical photographs showing the (a) macro and (b) grain structures of the Mg-0.2Al alloys with HSMC prior to casting.

Growth restriction and rapid cooling are able to impede recalescence respectively by hindering grain growth and enhancing heat extraction. When the other parameters are fixed in a Mg alloy containing MgO particles without elemental segregation, they could change the number of EGI events on eligible MgO particles ($\Delta T_n \geq \Delta T_{gi}$). It is expected that further cooling of the melt is allowed if the heat extraction is larger than the latent heat released from the initial growth of EGI events. Therefore, extra grain initiations on smaller MgO particles are allowed to proceed in PGI manner when they satisfy $\Delta T > \Delta T_{gi} \geq \Delta T_n$. The more growth restriction and higher cooling rate applied, the larger proportion of PGI events will be. Apparently, these extra PGI events contribute to grain refinement as well. As demonstrated in **Fig. 6.45**, PGI proportion is increased by the increment of growth restriction for the HSMC curve, causing the reduction of grain size. Same statement can be seen in **ref [30]**. In addition, the cooling rate was verified to have the same effect on the PGI proportion [30]. These extra PGI events offer further grain refinement (see **Fig. 6.45** and [30]).

With the understanding of how each factor affects heterogeneous nucleation and grain initiation on MgO particles in Mg alloys, it is able to promote grain refinement in Mg alloys containing MgO particles with a fixed size distribution. The corresponding solidification process can be: *i*) EGI dominated or *ii*) PGI dominated, with dependence on the proportion of EGI and PGI. But first of all, columnar to equiaxed transition (CET) is essential before the discussion about grain refinement. Solute addition is critical to provide growth restriction for CET in a given Mg alloy (**Fig. 6.38**), no matter it is EGI dominated or PGI dominated. The EGI events on the MgO particles in CP Mg-HSMC results in a fine but columnar grain structure (**Fig. 4.28**), and the addition of 0.2% Al (which shows no segregation on MgO particles, see **Figs. 4.15 to 4.17**) into CP Mg-HSMC causes a completely CET, as shown in **Fig. 7.1**. Additionally, together with enhanced PGI events on MgO particles modified by Y₂O₃ 2DC, the presences of 0.1/0.5% Y solute in Mg-0.1/0.5Y-HSMC alloys are essential for the fine and equiaxed grains (**Figs. 5.2 and 5.3**).

When EGI is dominant in a Mg alloy, grain refinement can be promoted by the reduction of nucleation potency and the increased number density of MgO particles. The reduced potency of MgO particle causes the increase in nucleation undercooling ΔT_n , the size range of MgO particles that meet the criterion for EGI ($\Delta T_n \geq \Delta T_{gi}$) is enlarged, so that more particles can nucleate and grain initiate Mg grain in the EGI manner. In this way, more grain initiation events occur and result in a finer grain size. When ΔT_n is fixed, the increase of number density of MgO particles does not change the size range, but it increases the number of MgO particles inside the size range. Therefore, grain initiation events increase and lead to further grain refinement. It can be verified by the comparison of the HSMC curve and the HSO curve in **Figs. 6.44 and 6.45**, where the HSO curve has a smaller grain size than the HSMC curve has in the EGI-dominant region. Moreover, as shown in the EGI-dominant regions for both curves, growth restriction and cooling rate have limited effect on grain refinement. Although the growth restriction and cooling rate have no effect on increasing the EGI events, they are able to add extra PGI events on smaller MgO particles in PGI manner by delaying recalescence. But the grain size can be reduced limitedly before the grain initiation behaviour becomes PGI dominant. This is also validated in the HSMC curve in **Figs. 6.44 and 6.45**, in the EGI-dominant range from 50% to 100%, the corresponding grain sizes reduce marginally when the growth restriction increases.

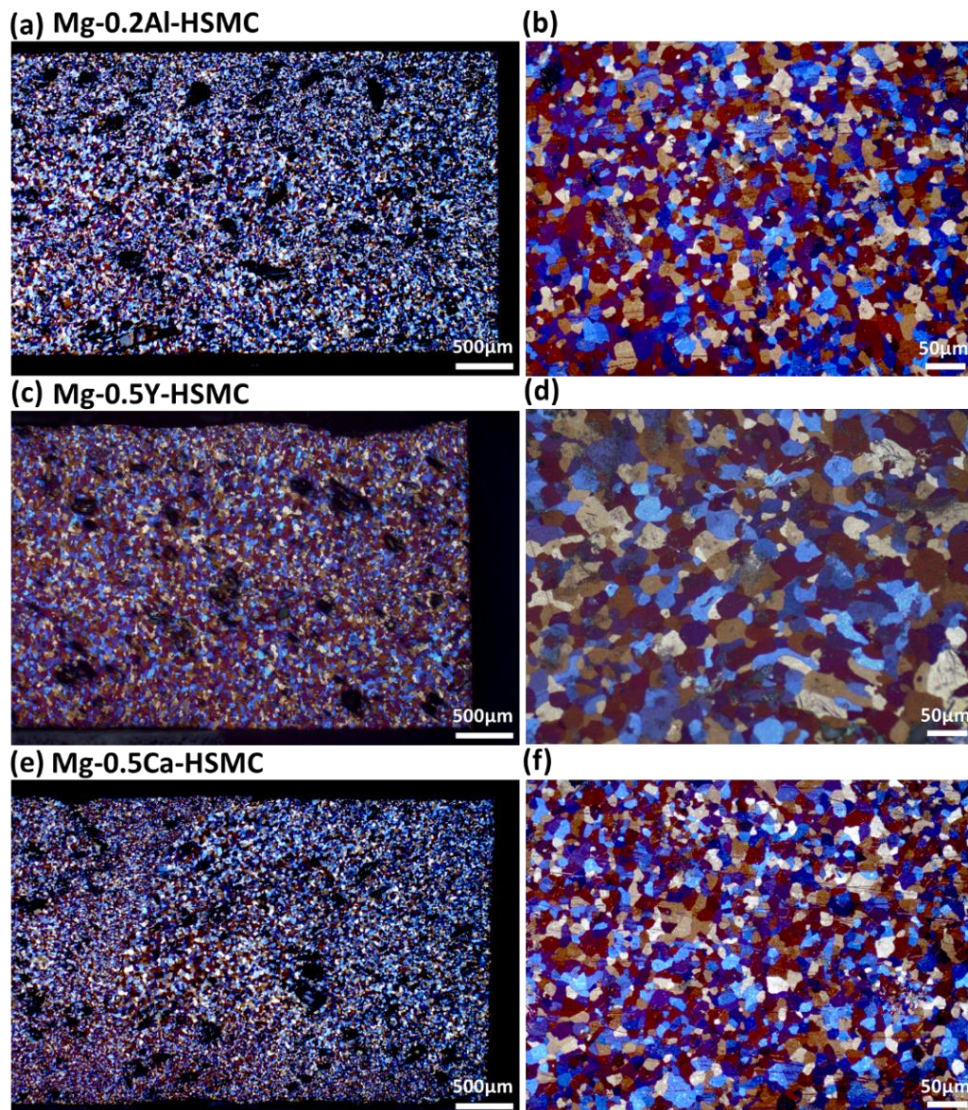


Fig. 7.2 Optical photographs showing the micron grain structures of (a, b) Mg-0.2Al-HSMC, (c, d) Mg-0.5Y-HSMC and (e, f) Mg-0.5Ca-HSMC cast by vacuum suction casting into a 3mm diameter copper mould.

When PGI is dominant in the Mg alloy, grain refinement is enhanced by the growth restriction, a fast cooling rate and the increased number density of MgO particles. Owing to the impedance of recalescence by growth restriction and fast cooling rate, smaller MgO particles are able to nucleate and grain initiate Mg grains progressively [17,63]. The number and proportion of PGI are increased to further reduce grain size. Besides, the increased number density can maximise the progressive grain initiation of Mg grains on MgO particles, promoting grain refinement. It can also be verified by the experiment and simulation results in **Figs. 6.44** and **6.45**, where the HSMC curve has a finer grain size than the TP1 curve has in the PGI dominant range. In addition, the grain size reduces with the increased growth restriction for both curves, with the TP1 curve having a faster reduction rate.

It was reported that the impotent particle has a more powerful effect on grain refinement than that of the potent particles [28–30]. The modifiable potency of MgO particles in Mg alloys provides an excellent case to verify this statement. **Fig. 7.2** shows the grain structure of Mg-0.2Al-HSMC, Mg-0.5Y-HSMC and Mg-0.5Ca-HSMC solidified in an ultrafast cooling rate ($\approx 1000 \text{ K}\cdot\text{s}^{-1}$) by application of vacuum suction casting in a 3mm copper mould. It is seen that Mg-0.2Al-HSMC and Mg-0.5Ca-HSMC with impotent MgO have smaller grain size than that of the Mg-0.5Y-HSMC containing potent MgO with Y_2O_3 2DC modification. With the assuming that these alloys have the same number density of MgO particles, the higher potential of impotent MgO particle on refining grain size than that of potent particles is verified. In addition, a rapid cooling rate contributes to further grain refinement because the grain size of each alloy decreases dramatically as compared to that cast in TP-1 mould (**Figs. 5.3, 6.2 and 7.1**).

Overall, the heterogeneous nucleation, grain initiation and grain refinement in Mg alloys with native MgO particles have been clarified in terms of theoretical understanding and experimental evidence. Experimentally, the performances of native MgO particles in CP Mg, AZ series [134,136,207], Mg-Zr [90], Mg-Y, Mg-Ca and Mg-Sn alloys have verified their grain refining ability, either following PGI or EGI dominant solidification behaviour. It is suggested that the native MgO particles can be a universal grain refiner for Mg alloys to get a fine grain structure. The boosting of MgO particles into grain initiation through either PGI or EGI manner is the principle to achieve and maximise the grain refinement in Mg alloys.

8 Conclusions

In this thesis, the nature of native MgO particles present in Mg alloy melt, their interactions with solute elements and corresponding grain refinement of CP Mg, Mg-Al, Mg-Y, Mg-Ca and Mg-Sn alloys have been comprehensively studied through casting experiment, optical microscopy and advanced electron microscopy. Heterogeneous nucleation and grain initiation behaviour of Mg grains have been extensively analysed in terms of the crystallography, morphology, size distribution and number density of the MgO particles as well as their interaction with the relevant solute element.

1. The native MgO in CP Mg and Mg-9Al exists as three distinct types of oxide films: young film, old film and old skin. The films/skins consist of discrete and densely populated MgO particles which have nano size and follow log-normal size distribution. The individual MgO particles have two morphologies: octahedral MgO with mainly $\{111\}_{\text{MgO}}$ facets and cubic MgO with $\{100\}_{\text{MgO}}$ facets. The cubic MgO is the product of oxidation of Mg in vapour phase, where the $\{100\}_{\text{MgO}}$ terminations are favourable in terms of thermodynamics and kinetics. The octahedral MgO particles are originated from the oxidation of liquid Mg on the melt surface. The polar $\{111\}_{\text{MgO}}$ facet can be stabilised by an Mg screening effect, and its continued existence through the particle growth is kinetically favoured. Although both types of MgO particle are impotent substrates for heterogeneous nucleation of α -Mg in terms of lattice misfit (7.86%), they offer significant grain refinement of Mg alloys via explosive grain initiation (EGI) scheme.
2. Interfacial segregation of Y is observed on both the $\{111\}_{\text{MgO}}$ and $\{100\}_{\text{MgO}}$ surfaces of the native MgO particles collected from Mg-0.5Y alloy melt. A Y_2O_3 2-dimensional compound (2DC) is found on the $\{111\}$ termination of MgO, resulting in a promotion of heterogeneous nucleation by the reduced lattice misfit with Mg (1.71%) and enhanced chemical interaction between Y and Mg atoms. Y segregates on the $\{100\}$ terminated surface of MgO by partially substituting the Mg atoms of MgO on the surface. With an unchanged misfit as compared to MgO without Y segregation (7.86%), the substitutional Y atoms introduce atomic roughness on the $\{100\}$ surface to a reduced pre-nucleation ability, then the subsequent nucleation is impeded.

3. With an impeded nucleation potency, the {100} MgO particles with Y segregation do not participate in the nucleation and grain initiation processes. In contrast, the formation of Y_2O_3 2DC on {111} MgO particles that account for the dominant population of native MgO particles results in enhancements in nucleation potency and particle dispersion. Thereby, nucleation of Mg on the modified {111} MgO particles is promoted and more {111} MgO particles are participated in the grain initiation process in a progressive manner, contributing to the grain refinement in Mg-0.1Y-HSMC and Mg-0.5Y-HSMC alloys.
4. Bulk C- Y_2O_3 ($Ia\bar{3}$, $a=1.06nm$) particles form in the Mg-Y alloy melt when Y content is sufficiently high, *e.g.*, 3% Y. The C- Y_2O_3 particles have a smaller lattice misfit (thus more potent), a larger particle size and a lower number density than that of the MgO particles with Y_2O_3 2DC. The C- Y_2O_3 particles dominate both nucleation and grain initiation processes in Mg-Y-HSMC ($Y \geq 1\%$ or HSMC=15mins). However, the insufficient Y solute and low number density of C- Y_2O_3 particles will not be adequate to cause CET, resulting in a columnar grain structure.
5. Segregation of Ca on the surfaces of native MgO particles in Mg-0.5Ca is associated with N. The co-segregation layer of Ca and N has a similar structure to that of the MgO matrix on both $\{111\}_{MgO}$ and $\{100\}_{MgO}$ facets, with the Mg and O atoms on the MgO surface being substituted by Ca and N atoms, respectively. Such substitutional process leads to the formation of vacancy and local atomic re-configuration, resulting in the surface roughness and in-plane disordering which in turn make the pre-nucleation more difficult than pure MgO, so does the heterogeneous nucleation.
6. Segregation of Sn is observed on the surfaces of native MgO particles. Sn atoms selectively substitute partial Mg atoms on the $\{100\}_{MgO}$ faceted surface of MgO without changes in lattice structure. Nevertheless, Sn segregation causes surface roughness to reduce the ability of MgO particle for pre-nucleation, which in turn impede nucleation.
7. The nucleation potency of the native MgO particles is reduced further as the result of elemental segregation of Ca or Sn. With the pre-treatments of high shear melt conditioning (HSMC) and HSMC plus extra oxidation (HSO) to the alloy melt, the modified MgO due to segregation of Ca or Sn still offers significant grain refinement of the alloys through the solidification dominated by explosive grain initiation process.

8. Grain refinement of the Mg alloys is enhanced by the pre-treatments (HSMC or HSO) before casting due to the increased number density of MgO particles.
9. Significant grain refinement is associated with columnar to equiaxed transition (CET), after that the effect of solute on grain size becomes minor. Pre-treatment of HSMC or HSO allow CET to occur earlier in Mg-Ca and Mg-Sn alloys than that directly cast into TP-1 mould without the pre-treatment.
10. Either potent or impotent particles can be utilised for grain refinement through the promotion of grain initiation in the manner of EGI or/and PGI. For a Mg alloy with MgO particles in a fixed size distribution, grain refinement is promoted by increasing growth restriction, cooling rate and number density of MgO particles when the grain initiation behaviour is progressive dominant; while grain refinement is also enhanced by increasing number density of impotent MgO particles when the grain initiation behaviour is explosively dominant.
11. Overall, it is demonstrated in this study that the native MgO is effective for grain refining CP Mg, Mg-Y, Mg-Ca, Mg-Sn and Mg-Al alloys.

9 Future work

- Quantitative measurement of the MgO particles and other possible particles inside the melt of Mg alloys is required to be studied through direct or indirect methods. A uniformly particle-distributed bulk of Mg alloy is required in the first instance for the direct measurement. Experimental imaging techniques can be potentially applied, such as high-resolution synchrotron, FIB 3D reconstruction, 3D tomography in S/TEM, *etc.* More easily, a proper solution that can easily dissolve Mg but unreacted with MgO will make the weight proportion of MgO accessible. Indirect methods also require a good sample with a homo-distribution of MgO and minimised defects, and the parameters like density, electron resistance/conductivity, young's modulus, *etc.* can be applied.
- Minimise the interference from other impurities during solidification. Design a researching prototype system containing Mg and native MgO without or with marginal interferences from other inclusions to study the grain refinement behaviours. In this way, the experimental condition may approach the assumption used for numerical simulation. Therefore, solidification behaviour becomes directly interpretable.
- More dedicated electron microscopy work is required to precisely reveal the atomic configuration of segregation layer at the MgO/Mg interface in Mg-Ca and Mg-Sn binary alloys.
- It is necessary to do an extensional study of the application of native MgO particles into other binary Mg alloys on grain refinement, and to investigate the interaction between more solutes and the native MgO particles, as well as the following impact on the potency of MgO and the solidification behaviours.
- Based on the systems we have studied, *e.g.*, Mg-Y-Ca, Mg-Y-Sn, Mg-Ca-Sn and Mg-Y-Ca-Sn systems, the study of the elemental segregation behaviour can be extended into ternary, quaternary systems, or new alloy systems. The outcome results and analysis would be beneficial for the proposal of a principle to understand how elements segregate/adsorb onto a substrate.

- Find out the effect of variables like solute content, shearing time, temperature, *etc.* on the elemental segregation in a given binary Mg alloy, Mg-Y alloys for instance. To figure out the critical parameters for the elemental segregation as well as the kinetics process.
- The experimentally observed elemental segregation on MgO can be understood by simulation work using density functional theory (DFT) or molecular dynamics (MD) which may provide: *i)* understanding of the atomic configuration of MgO with segregation; *ii)* underlying principle how the stable segregation forms; and moreover *iii)* the following effect on nucleation.
- With a large experimental database and the theoretical assistance, it may become possible to understand the correlation of heterogeneous nucleation potency with lattice misfit, surface roughness and chemical interaction in a certain substrate/liquid system. Hopefully, a general equation can be generated.
- With the advanced *in-situ* technique in electron microscopy, as well as the dedicated sample preparation methods, it is possible to conduct and observe the single solidification event under the atomic scale. The dynamic solidification process and the associated measured parameters will absolutely improve our understanding of solidification.

10 Appendix

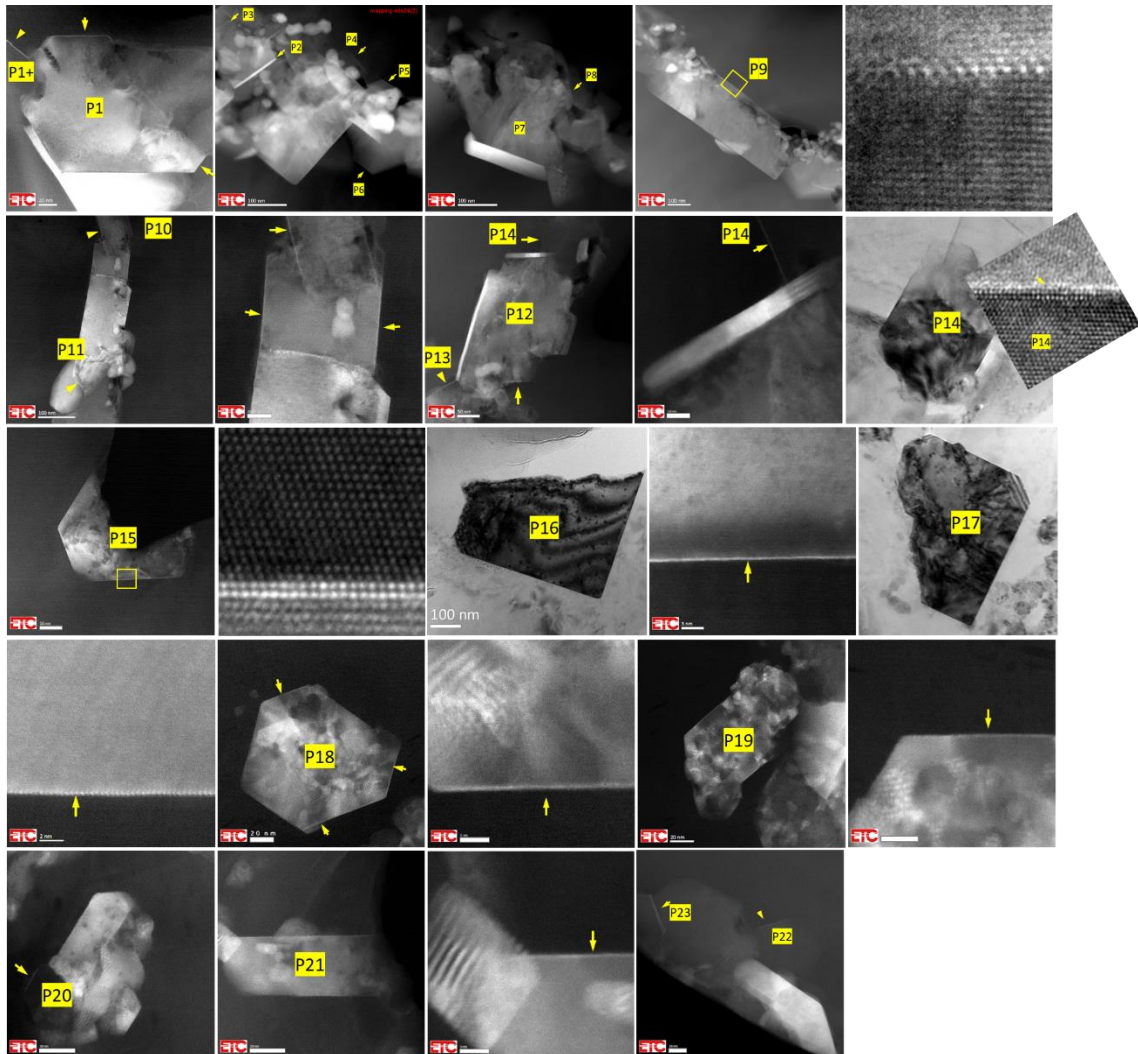


Figure A-1 TEM images showing the observation of Y segregation on 23 MgO particles in Mg-0.5Y-prefil sample. Among them, Y segregations on P2, P7 and P12 exhibit as nano-size layers having thickness way larger than mono (Substitutional Y on {100} facet) or two-atomic layers (Y_2O_3 2DC on {1011} facet) for the rest particles.

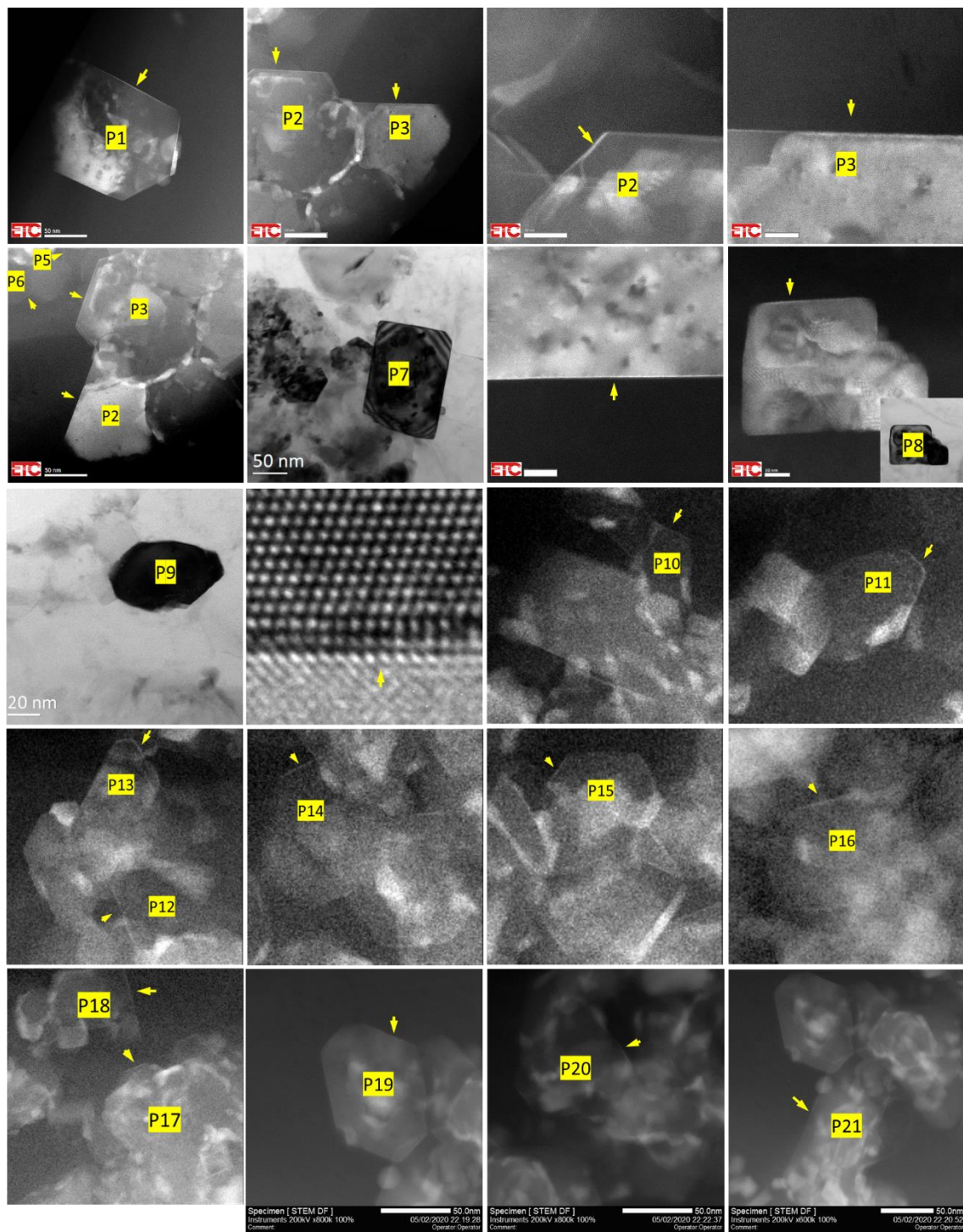


Figure A-2 TEM images showing the observation of Y segregation on 41 MgO particles (1st to 21st) in Mg-3Y-prefil sample.

Characterisation of native MgO and its roles in solidification of Mg alloys

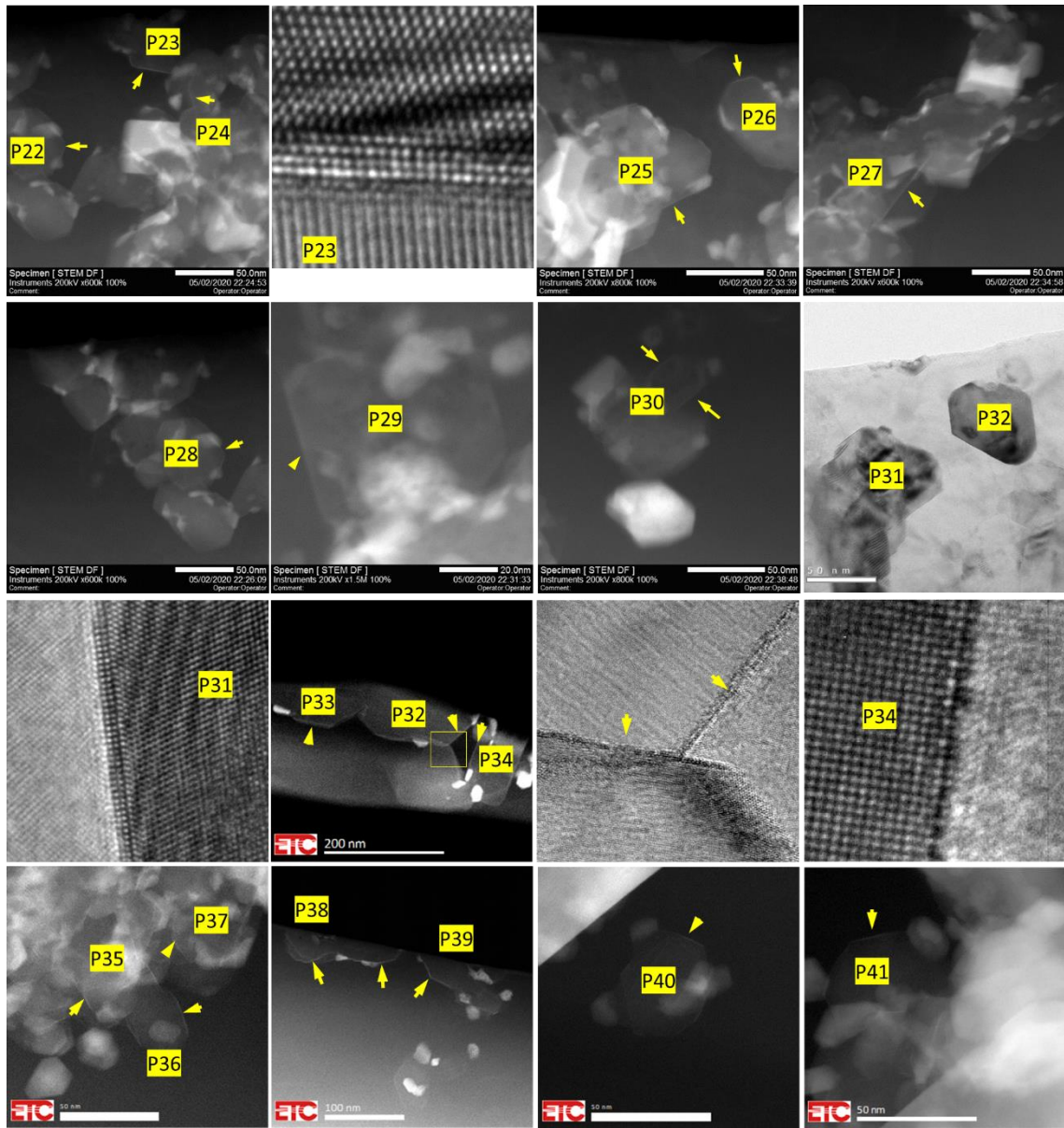


Figure A-3 TEM images showing the observation of Y segregation on 41 MgO particles (22nd to 41st) in Mg-3Y-prefil sample.

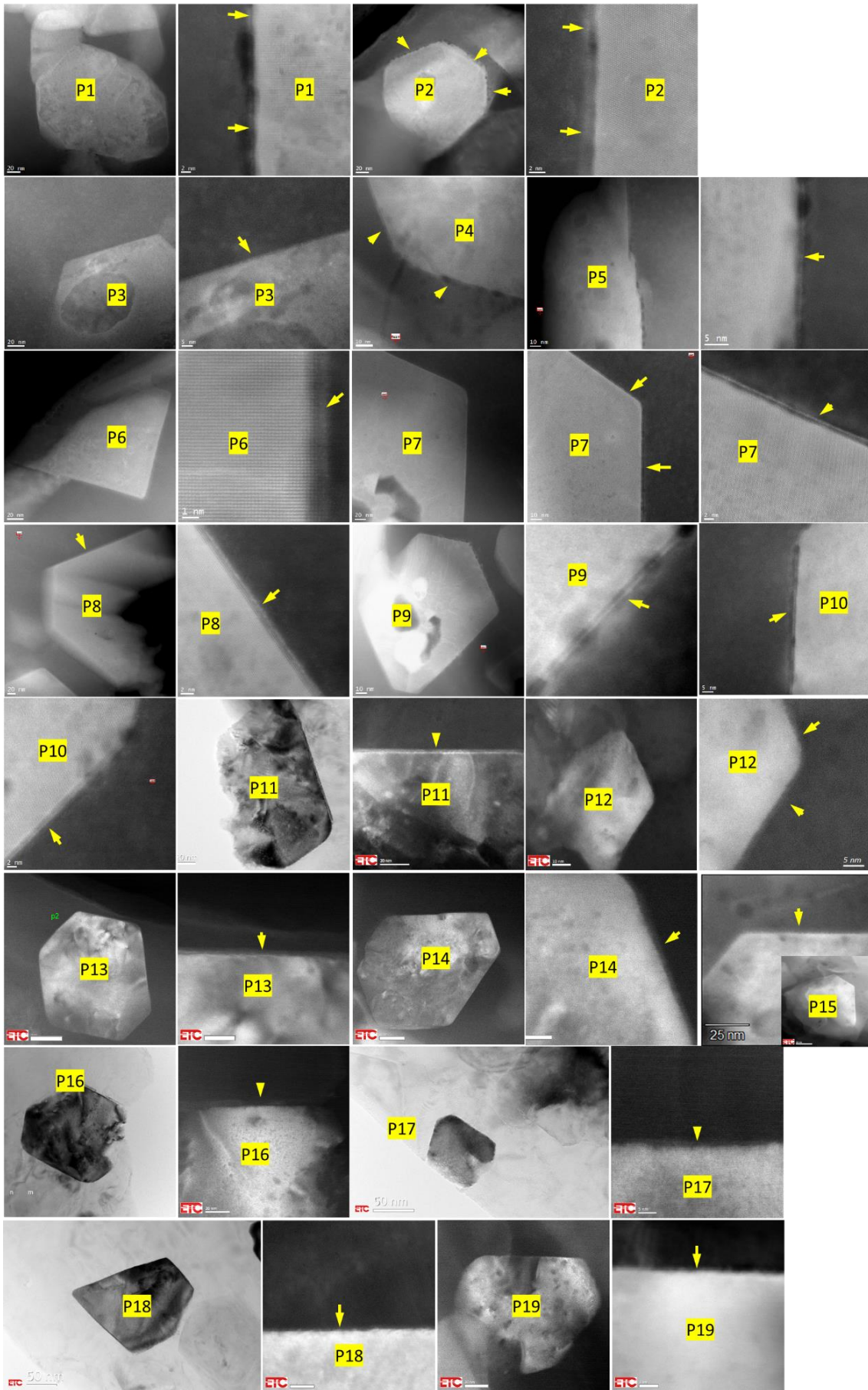


Figure A-4 TEM images showing the observation of Ca segregation on 19 MgO particles in Mg-0.5Ca-prefil sample.

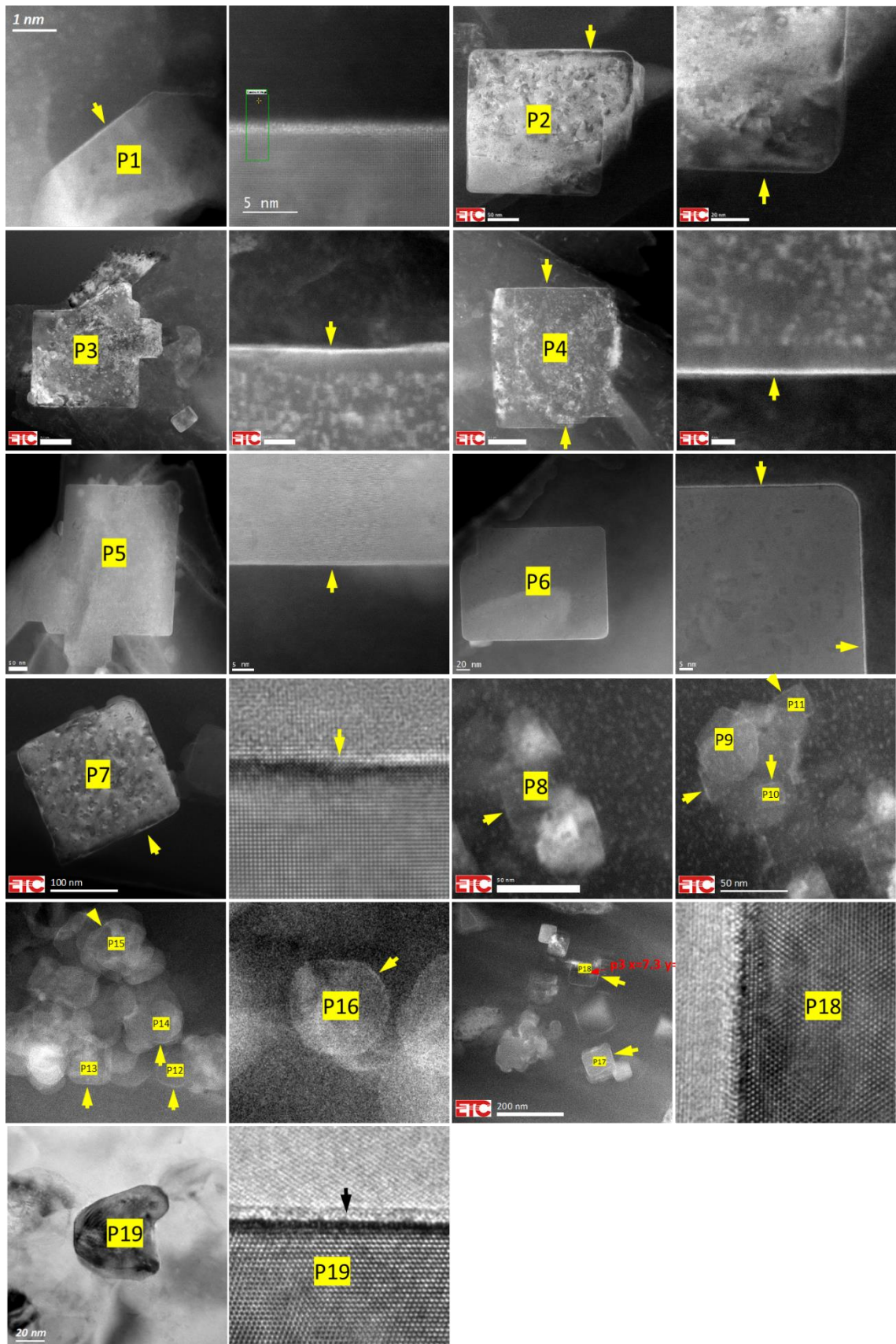


Figure A-5 TEM images showing the observation of Sn segregation on 18 MgO particles in Mg-2Sn-prefil sample.

11 References

- [1] A.A. Luo, Applications: aerospace, automotive and other structural applications of magnesium, in: M. Pekguleryuz, A. Kainer, KU, Kaya (Eds.), *Fundam. Magnes. Alloy Metall.*, Woodhead Publishing Limited, London, 2013: pp. 266–316.
- [2] N. Li, Y. Zheng, Novel Magnesium Alloys Developed for Biomedical Application : A Review, *J. Mater. Sci. Technol.* 29 (2013) 489–502.
- [3] A.A. Luo, Magnesium: Current and potential automotive applications, *JOM.* 54 (2002) 42–48.
- [4] M. Alderman, A Perspective: Potential Growth in The Global Magnesium Industry - Where is Our Research Leading US?, in: A. Singh, K. Solanki, M. V Manuel, N.R. Neelameggham (Eds.), *Magnes. Technol.* 2016, Springer, Cham, 2016: pp. 59–60.
- [5] G. Mann, J.R. Griffiths, C.H. Cáceres, Hall-Petch parameters in tension and compression in cast Mg–2Zn alloys, *J. Alloys Compd.* 378 (2004) 188–191.
- [6] C.J. Bettles, M.A. Gibson, S.M. Zhu, Microstructure and mechanical behaviour of an elevated temperature Mg-rare earth based alloy, *Mater. Sci. Eng. A.* 505 (2009) 6–12.
- [7] J. Song, F. Pan, B. Jiang, A. Atrens, M.X. Zhang, Y. Lu, A review on hot tearing of magnesium alloys, *J. Magnes. Alloy.* 4 (2016) 151–172.
- [8] K.D. Ralston, N. Birbilis, Effect of grain size on corrosion: a review, *Corrosion.* 66 (2010) 75005.
- [9] W.J. Kim, S.W. Chung, C.S. Chung, D. Kum, Superplasticity in thin magnesium alloy sheets and deformation mechanism maps for magnesium alloys at elevated temperatures, *Acta Mater.* 49 (2001) 3337–3345.
- [10] H. Gjestland, H. Westengen, Advancements in high pressure die casting of magnesium, *Adv. Eng. Mater.* 9 (2007) 769–776.
- [11] M.C. Flemings, *Solidification processing*, McGraw-Hill Education, 1974.
- [12] K.F. Kelton, *Crystal Nucleation in Liquids and Glasses*. In *Solid state physics*, Vol. 45, Academic Press, London, 1991.
- [13] J.A. Dantzig, M. Rappaz, *Solidification*, EPFL Press, Lausanne, Switzerland, 2009.
- [14] D. Turnbull, B. Vonnegut, Nucleation Catalysis, *Ind. Eng. Chem.* 44 (1952) 1292–1298.
- [15] F.J. Bradshaw, M.E. Gasper, S. Pearson, The Supercooling of Gold as Affected by Some Catalysts, *J. Inst. Met.* 87 (1958) 15–18.
- [16] M.X. Zhang, P.M. Kelly, Crystallographic features of phase transformations in solids, *Prog. Mater. Sci.* 54 (2009) 1101–1170.
- [17] A.L. Greer, A.M. Bunn, A. Tronche, P. V Evans, D.J. Bristow, Modelling of inoculation of metallic melts: application to grain refinement of aluminium by Al–Ti–B, *Acta Mater.* 48 (2000) 2823–2835.

- [18] D.H. StJohn, M. Qian, M.A. Easton, P. Cao, The Interdependence Theory: The relationship between grain formation and nucleant selection, *Acta Mater.* 59 (2011) 4907–4921.
- [19] I.G. Farbenindustrie, British patent, GB359,425, 1931.
- [20] C.E. Nelson, Grain size behavior in magnesium casting alloys, *Charles Edgar Hoyt Annu. Lect.* (1948) 1–4.
- [21] J.A. Davis, L.W. Eastwood, J.C. DeHaven, Grain refinement in magnesium casting alloys, *AFS Trans.* 53 (1945) 352–362.
- [22] I.G. Farbenindustrie, Belgian Patent, 444,757, 1942.
- [23] D.H. StJohn, M.A. Easton, M. Qian, J.A. Taylor, Grain Refinement of Magnesium Alloys: A Review of Recent Research, Theoretical Developments, and Their Application, *Metall. Mater. Trans. A.* 44 (2013) 2935–2949.
- [24] E. Karakulak, A review: Past, present and future of grain refining of magnesium castings, *J. Magnes. Alloy.* 7 (2019) 355–369.
- [25] D.H. StJohn, M. Qian, M. Easton, P. Cao, Z. Hildebrand, Grain Refinement of Magnesium Alloys, *Metall. Mater. Trans. A.* 36A (2005) 1669–1679.
- [26] E.F. Emley, *Principles of magnesium technology*, Pergamon Press, New York, London, 1966.
- [27] M. Qian, D.H. StJohn, M.T. Frost, A New Zirconium-Rich Master Alloy for the Grain Refinement of Magnesium Alloys, in: K.U. Kainer (Ed.), *Magnes. Proc. 6th Int. Conf. Magnes. Alloy. Their Appl.*, Weinheim, FRG: Wiley-VCH Verlag GmbH & Co. KGaA., 2003: pp. 706–712.
- [28] B. Jiang, Z. Fan, Grain Initiation: Progressive vs. Explosive, in: *Proc. 6th Decenn. Int. Conf. Solidif. Process.*, 2017: pp. 61–65.
- [29] Z. Fan, Heterogeneous Nucleation, Grain Initiation and Grain Refinement of Mg-Alloys, in: Z. Fan, C. Mendis (Eds.), *Magnes. 2018 Proc. 11th Int. Conf. Magnes. Alloy. Their Appl.*, Brunel University Press, Beaumont Estate, Old Windsor, UK, 2018: pp. 7–16.
- [30] Z. Fan, F. Gao, B. Jiang, Z. Que, Impeding Nucleation for More Significant Grain Refinement, *Sci. Rep.* 10 (2020) 1–11.
- [31] C.M. Fang, Z. Fan, Prenucleation at the Interface between MgO and Liquid Magnesium: An ab initio Molecular Dynamics Study, *Metall. Mater. Trans. A.* 51 (2020) 788–797.
- [32] W.T. Kim, B. Cantor, An adsorption model of the heterogeneous nucleation of solidification, *Acta Metall. Mater.* 42 (1994) 3115–3127.
- [33] P. Wynblatt, Interfacial Segregation Effects in Wetting Phenomena, *Annu. Rev. Mater. Res.* 38 (2008) 173–196.
- [34] Z. Fan, An epitaxial model for heterogeneous nucleation on potent substrates, *Metall. Mater. Trans. A.* 44 (2013) 1409–1418.

- [35] W.D. Callister, D. Rethwisch, *Fundamentals of materials science and engineering: an integrated approach*, 5th Editio, John Wiley & Sons, 2015.
- [36] D.A. Porter, K.E. Easterling, M. Sherif, *Phase Transformations in Metals and Alloys*, (Revised Reprint), CRC press, 2009.
- [37] D. Turnbull, Formation of crystal nuclei in liquid metals, *J. Appl. Phys.* 21 (1950) 1022–1028.
- [38] O.M. Magnussen, B.M. Ocko, M.J. Regan, K. Penanen, P.S. Pershan, M. Deutsch, X-Ray Reflectivity Measurements of Surface Layering in Liquid Mercury, *Phys. Rev. Lett.* 74 (1995) 4444–4447.
- [39] M.J. Regan, E.H. Kawamoto, S. Lee, P.S. Pershan, N. Maskil, M. Deutsch, O.M. Magnussen, B.M. Ocko, L.E. Berman, Surface layering in liquid gallium: An x-ray reflectivity study, *Phys. Rev. Lett.* 75 (1995) 2498–2501.
- [40] S.H. Oh, Y. Kauffmann, C. Scheu, W.D. Kaplan, M. Rühle, Ordered liquid aluminum at the interface with sapphire, *Science* (80-.). 310 (2005) 661–663.
- [41] W.D. Kaplan, Y. Kauffmann, Structural Order in Liquids Induced By Interfaces With Crystals, *Annu. Rev. Mater. Res.* 36 (2006) 1–48.
- [42] M. Asta, F. Spaepen, J.F. Van Der Veen, Solid-liquid interfaces: Molecular structure, thermodynamics, and crystallization, *MRS Bull.* 29 (2004) 920–926.
- [43] H. Men, Z. Fan, Prenucleation induced by Crystalline Substrates, *Metall. Mater. Trans. A.* 49 (2018) 2766–2777.
- [44] H. Men, Z. Fan, Atomic ordering in liquid aluminium induced by substrates with misfits, *Comput. Mater. Sci.* 85 (2014) 1–7.
- [45] C.M. Fang, H. Men, Z. Fan, Effect of Substrate Chemistry on Prenucleation, *Metall. Mater. Trans. A.* 49 (2018) 6231–6242.
- [46] B. Jiang, H. Men, Z. Fan, Atomic ordering in the liquid adjacent to an atomically rough solid surface, *Comput. Mater. Sci.* 153 (2018) 73–81.
- [47] Y. Wang, C.M. Fang, L. Zhou, T. Hashimoto, X. Zhou, Q.M. Ramasse, Z. Fan, Mechanism for Zr poisoning of Al-Ti-B based grain refiners, *Acta Mater.* 164 (2019) 428–439.
- [48] J.A. Marcantonin, L.F. Mondolfo, Grain refinement in aluminum alloyed with Ti and some other elements, *Met. Trans.* 2 (1971) 465–471.
- [49] D.H. StJohn, A. Prasad, M.A. Easton, M. Qian, The Contribution of Constitutional Supercooling to Nucleation and Grain Formation, *Metall. Mater. Trans. A.* 46 (2015) 4868–4885.
- [50] L.A. Tarshis, J.L. Walker, J.W. Rutter, Experiments on the solidification structure of alloy castings, *Metall. Trans.* 2 (1971) 2589–2597.
- [51] J.A. Spittle, S. Sadli, The influence of zirconium and chromium on the grain-refining efficiency of Al-Ti-B inoculants, *Cast Met.* 7 (1995) 247–253.

- [52] I. Maxwell, A. Hellawell, A simple model for grain refinement during solidification, *Acta Metall.* 23 (1975) 229–237.
- [53] H.B. Aaron, D. Fainstein, G.R. Kotler, Diffusion-limited phase transformations: a comparison and critical evaluation of the mathematical approximations, *J. Appl. Phys.* 41 (1970) 4404–4410.
- [54] Z. Fan, F. Gao, L. Zhou, S.Z. Lu, A new concept for growth restriction during solidification, *Acta Mater.* 152 (2018) 248–257.
- [55] J.C. Fisher, B. Chalmers, *Principles of Solidification*, Wiley New York, 1964.
- [56] J.D. Hunt, Steady state columnar and equiaxed growth of dendrites and eutectic, *Mater. Sci. Eng.* 65 (1984) 75–83.
- [57] M. Vandyoussefi, A.L. Greer, Application of cellular automaton–finite element model to the grain refinement of directionally solidified Al–4.15 wt% Mg alloys, *Acta Mater.* 50 (2002) 1693–1705.
- [58] K.F. Kelton, A.L. Greer, *Nucleation in Condensed Matter Applications in condensed matter: applications in materials and biology*, Elsevier, 2010.
- [59] J.D. Hunt, Z. Fan, A simple model for the nucleation and growth of equiaxed grains, in: *John Hunt Int. Symp.*, 2011: pp. 59–78.
- [60] J.C. Fisher, J.H. Hollomon, D. Turnbull, Nucleation, *J. Appl. Phys.* 19 (1948) 775–784.
- [61] D. Turnbull, Theory of catalysis of nucleation by surface patches, *Acta Metall.* 1 (1953) 8–14.
- [62] T.E. Quested, A.L. Greer, Athermal heterogeneous nucleation of solidification, *Acta Mater.* 53 (2005) 2683–2692.
- [63] T.E. Quested, A.L. Greer, The effect of the size distribution of inoculant particles on as-cast grain size in aluminium alloys, *Acta Mater.* 52 (2004) 3859–3868.
- [64] R. Günther, C. Hartig, R. Bormann, Grain refinement of AZ31 by (SiC)P: Theoretical calculation and experiment, *Acta Mater.* 54 (2006) 5591–5597.
- [65] J. Lelito, P.L. Zak, A.A. Shirzadi, A.L. Greer, W.K. Krajewski, J.S. Suchy, K. Haberl, P. Schumacher, Effect of SiC reinforcement particles on the grain density in a magnesium-based metal-matrix composite: Modelling and experiment, *Acta Mater.* 60 (2012) 2950–2958.
- [66] M. Easton, D. Stjohn, Grain Refinement of Aluminum Alloys : Part II . Confirmation of , and a Mechanism for , the Solute Paradigm, *Metall. Mater. Trans. A.* 30 (1999) 1625–1633.
- [67] M. Easton, D. Stjohn, Grain refinement of aluminum alloys: Part I. The nucleant and solute paradigms - a review of the literature, *Metall. Mater. Trans. A.* 30 (1999) 1613–1623.
- [68] M. Easton, D. StJohn, An analysis of the relationship between grain size, solute content, and the potency and number density of nucleant particles, *Metall. Mater. Trans. A.* 36

- (2005) 1911–1920.
- [69] P. Cao, M. Qian, D.H. StJohn, Mechanism for grain refinement of magnesium alloys by superheating, *Scr. Mater.* 56 (2007) 633–636.
- [70] M. Sun, M.A. Easton, D.H. Stjohn, G. Wu, T.B. Abbott, W. Ding, Grain refinement of magnesium alloys by Mg-Zr master alloys: The role of alloy chemistry and Zr particle number density, *Adv. Eng. Mater.* 15 (2013) 373–378.
- [71] B.L. Bramfitt, The effect of carbide and nitride additions on the heterogeneous nucleation behavior of liquid iron, *Metall. Trans.* 1 (1970) 1987–1995.
- [72] M.X. Zhang, P.M. Kelly, M. Qian, J.A. Taylor, Crystallography of grain refinement in Mg-Al based alloys, *Acta Mater.* 53 (2005) 3261–3270.
- [73] M.X. Zhang, P.M. Kelly, Edge-to-edge matching and its applications: Part II. Application to Mg-Al, Mg-Y and Mg-Mn alloys, *Acta Mater.* 53 (2005) 1085–1096.
- [74] D. Qiu, M. Zhang, H. Fu, P.M. Kelly, J.A. Taylor, M. Zhang, H. Fu, P.M. Kelly, J.A. Taylor, Crystallography of recently developed grain refiners for Mg–Al alloys, *Philos. Mag. Lett.* 87 (2007) 505–514.
- [75] F. Wang, Role of the peritectics in grain refinement of cast aluminium alloys, PhD thesis, The university of queensland, 2013.
- [76] F. Wang, D. Eskin, J. Mi, T. Connolley, J. Lindsay, M. Mounib, A refining mechanism of primary Al₃Ti intermetallic particles by ultrasonic treatment in the liquid state, *Acta Mater.* 116 (2016) 354–363.
- [77] W.Z. Zhang, G.C. Weatherly, On the crystallography of precipitation, *Prog. Mater. Sci.* 50 (2005) 181–292.
- [78] M.X. Zhang, S.Q. Chen, H.P. Ren, P.M. Kelly, Crystallography of the simple HCP/FCC system, *Metall. Mater. Trans. A.* 39 A (2008) 1077–1086.
- [79] S. Housh, B. Mikucki, A. Stevenson, Selection and application of magnesium and magnesium alloys, *ASM Int. Met. Handbook*, Tenth Ed. 2 (1990) 455–479.
- [80] Y.C. Lee, Grain refinement of magnesium, PhD thesis, The University of Queensland, 2002.
- [81] F. Sauerwald, U.D.B.D.E. Von, Magnesiumlegierungen Durch Zirkonium Und Einige Eigenschaften Von Gegossenen Magnesium-Legierungen Mit Zirkonium, *Zeitschrift Fur Met.* 40 (1949) 41–46.
- [82] Y.C. Lee, A.K. Dahle, D.H. StJohn, The role of solute in grain refinement of magnesium, *Metall. Mater. Trans. A.* 31 (2000) 2895–2906.
- [83] Y. Tamura, Grain refining mechanism and casting structure of Mg-Zr alloy, *Keikinzoku.* 48 (1998) 185–189.
- [84] M. Qian, L. Zheng, D. Graham, M.T. Frost, D.H. StJohn, Settling of undissolved zirconium particles in pure magnesium melts, *J. Light Met.* 1 (2001) 157–165.
- [85] M. Qian, Z.C.G. Hildebrand, D.H. St. John, The loss of dissolved zirconium in

- zirconium-refined magnesium alloys after remelting, *Metall. Mater. Trans. A.* 40 (2009) 2470–2479.
- [86] M. Qian, Heterogeneous nuclei size in magnesium – zirconium alloys, *Scr. Mater.* 50 (2004) 1115–1119.
- [87] M. Qian, D.H. StJohn, M.T. Frost, M.R. Barnett, Grain refinement of pure magnesium using rolled Zirmax® Master alloy (MG-33.3ZR), in: H.I. Kaplan (Ed.), *Magnesium Technol. 2003*, San Diego, California, USA, 2003: pp. 215–220.
- [88] P. Saha, S. Viswanathan, Grain Refinement of Magnesium by Zirconium : Characterization and Analysis, in: W.H. Sillekens, S.R. Agnew, N.R. Neelameggham, S.N. Mathaudhu (Eds.), *Magnes. Technol. 2011*, Schaumburg, IL USA, 2011.
- [89] W. Yang, L. Liu, J. Zhang, S. Ji, Z. Fan, Heterogeneous nucleation in Mg-Zr alloy under die casting condition, *Mater. Lett.* 160 (2015) 263–267.
- [90] G.S. Peng, G.S. Song, Y. Wang, K.H. Chen, S.Y. Chen, Intensive melt shearing and calcium concentration effects on grain refinement of commercial purity Mg, *Int. J. Cast Met. Res.* 31 (2018) 99–107.
- [91] N. Tiner, Superheating of magnesium alloys, *AIME, Tech Pub.* 12 (1945) 1–19.
- [92] Y. Tamura, T. Haitani, E. Yano, T. Motegi, N. Kono, E. Sato, Grain refinement of high-purity Mg-Al alloy ingots and influences of minor amounts of iron and manganese on cast grain size, *Mater. Trans.* 43 (2002) 2784–2788.
- [93] Y. Tamura, T. Motegi, N. Kono, E. Sato, Effect of minor elements on grain size of Mg-9%Al alloy, in: *Mater. Sci. Forum*, Trans Tech Publications Ltd., 2000: pp. 199–204.
- [94] K. Achenbach, Contribution to the Question of Melting Practice for Casting Magnesium, *Die Giesserer.* 26 (1939) 597–604.
- [95] P. Cao, M. Qian, D. StJohn, Grain refinement of commercial purity Mg-9%Al alloys by superheating, in: N.R. Neelameggham, H.I. Kaplan, B.R. Powell (Eds.), *Magnes. Technol. 2005*, Minerals, Metals & Materials Society (TMS), San Francisco, CA, U.S.A., 2005: pp. 297–302.
- [96] P. Cao, M. Qian, D.H. StJohn, Effect of iron on grain refinement of high-purity Mg-Al alloys, *Scr. Mater.* 51 (2004) 125–129.
- [97] F.A. Fox, E. Lardner, H. Sutton, An Exploration of the Problem of Superheating in Magnesium-Base Alloys, *J. Inst. Met.* 71 (1945) 455–456.
- [98] J. Byun, S. Il Kwon, H.P. Ha, J. Yoon, A Manufacturing Technology of AZ91-Alloy Slurry for Semi Solid Forming, in: K.U. Kainer (Ed.), *Magnes. Proc. 6th Int. Conf. Magnes. Alloy. Their Appl.*, Weinheim, FRG: Wiley-VCH Verlag GmbH & Co. KGaA., 2003: pp. 713–718.
- [99] P. Cao, D.H. StJohn, M. Qian, The effect of manganese on the grain size of commercial AZ31 alloy, in: *Mater. Sci. Forum*, Trans Tech Publ, 2005: pp. 139–142.
- [100] D. Qiu, M.X. Zhang, J.A. Taylor, H.M. Fu, P.M. Kelly, A novel approach to the

- mechanism for the grain refining effect of melt superheating of Mg-Al alloys, *Acta Mater.* 55 (2007) 1863–1871.
- [101] P. Cao, M. Qian, D.H. Stjohn, Native grain refinement of magnesium alloys, *Scr. Mater.* 53 (2005) 841–844.
- [102] M. Qian, P. Cao, Discussions on grain refinement of magnesium alloys by carbon inoculation, *Scr. Mater.* 52 (2005) 415–419.
- [103] C.H. Mahoney, A.L. Tarr, P.E. LeGrand, A study of factors influencing grain size in magnesium alloys and a carbon inoculation method for grain refinement, *Trans Am Inst Min Met. Pet Eng Inc.* 1892 (1945) 1–20.
- [104] L. Lu, A.K. Dahle, D.H. Stjohn, Grain refinement efficiency and mechanism of aluminium carbide in Mg-Al alloys, *Scr. Mater.* 53 (2005) 517–522.
- [105] S. Liu, Y. Chen, H. Han, Grain refinement of AZ91D magnesium alloy by a new Mg-50%Al₄C₃ master alloy, *J. Alloys Compd.* 624 (2015) 266–269.
- [106] M.A. Easton, A. Schiffl, J.Y. Yao, H. Kaufmann, Grain refinement of Mg-Al(-Mn) alloys by SiC additions, *Scr. Mater.* 55 (2006) 379–382.
- [107] Y. Huang, K.U. Kainer, N. Hort, Mechanism of grain refinement of Mg – Al alloys by SiC inoculation, *Scr. Mater.* 64 (2011) 793–796.
- [108] X. Yang, F. Wang, Z. Fan, Crystallographic study of nucleation in SiC particulate reinforced magnesium matrix composite, *J. Alloys Compd.* 706 (2017) 430–437.
- [109] D. Qiu, M.X. Zhang, J.A. Taylor, P.M. Kelly, A new approach to designing a grain refiner for Mg casting alloys and its use in Mg-Y-based alloys, *Acta Mater.* 57 (2009) 3052–3059.
- [110] D. Qiu, M.X. Zhang, P.M. Kelly, Crystallography of heterogeneous nucleation of Mg grains on Al₂Y nucleation particles in an Mg-10 wt.% Y alloy, *Scr. Mater.* 61 (2009) 312–315.
- [111] D. Qiu, M.X. Zhang, The nucleation crystallography and wettability of Mg grains on active Al₂Y inoculants in an Mg-10 wt% y Alloy, *J. Alloys Compd.* 586 (2014) 39–44.
- [112] D. Qiu, M.X. Zhang, Effect of active heterogeneous nucleation particles on the grain refining efficiency in an Mg-10 wt.% Y cast alloy, *J. Alloys Compd.* 488 (2009) 260–264.
- [113] J. Dai, M. Easton, S. Zhu, G. Wu, W. Ding, Grain refinement of Mg-10Gd alloy by Al additions, *J. Mater. Res.* 27 (2012) 2790–2797.
- [114] C. Wang, J. Dai, W. Liu, L. Zhang, G. Wu, Effect of Al additions on grain refinement and mechanical properties of Mg-Sm alloys, *J. Alloys Compd.* 620 (2015) 172–179.
- [115] Z. Jiang, B. Jiang, Y. Zeng, J. Dai, F. Pan, Role of Al modification on the microstructure and mechanical properties of as-cast Mg – 6Ce alloys, *Mater. Sci. Eng. A.* 645 (2015) 57–64.
- [116] D. Liu, J. Song, B. Jiang, Y. Zeng, Q. Wang, Z. Jiang, B. Liu, G. Huang, F. Pan, Effect

- of Al content on microstructure and mechanical properties of as-cast Mg-5Nd alloys, *J. Alloys Compd.* 737 (2018) 263–270.
- [117] H.M. Fu, D. Qiu, M.X. Zhang, H. Wang, P.M. Kelly, J.A. Taylor, The development of a new grain refiner for magnesium alloys using the edge-to-edge model, *J. Alloys Compd.* 456 (2008) 390–394.
- [118] H.M. Fu, M.X. Zhang, D. Qiu, P.M. Kelly, J.A. Taylor, Grain refinement by AlN particles in Mg-Al based alloys, *J. Alloys Compd.* 478 (2009) 809–812.
- [119] Y. Ali, D. Qiu, B. Jiang, F. Pan, M.X. Zhang, The influence of CaO addition on grain refinement of cast magnesium alloys, *Scr. Mater.* 114 (2016) 103–107.
- [120] C.J. Deng, M.L. Wong, M.W. Ho, P. Yu, D.H.L. Ng, Formation of MgO and Mg-Zn intermetallics in an Mg-based composite by in situ reactions, *Compos. Part A Appl. Sci. Manuf.* 36 (2005) 551–557.
- [121] S. Saha, C. Ravindran, Effects of zinc oxide addition on the microstructure and mechanical properties of AZ91E Mg alloy, *Int. J. Met.* 9 (2015) 39–48.
- [122] X. Liu, Z. Zhang, Q. Le, L. Bao, The Effects of ZnO Particles on the Grain Refinement and Mechanical Properties of AZ31 Magnesium Alloys, *Trans. Indian Inst. Met.* 69 (2016) 1911–1918.
- [123] S.J. Huang, Z.W. Chen, Grain refinement of AlNp/AZ91D magnesium metal-matrix composites, *Kov. Mater.* 49 (2011) 259–264.
- [124] C. Yang, B. Zhang, D. Zhao, H. Lü, T. Zhai, F. Liu, Microstructure and mechanical properties of AlN particles in situ reinforced Mg matrix composites, *Mater. Sci. Eng. A.* 674 (2016) 158–163.
- [125] H. Dieringa, L. Katsarou, R. Buzolin, G. Szakács, M. Horstmann, M. Wolff, C. Mendis, S. Vorozhtsov, D. StJohn, Ultrasound assisted casting of an AM60 based metal matrix nanocomposite, its properties, and recyclability, *Metals (Basel)*. 7 (2017) 388–401.
- [126] B.S. You, W.W. Park, I.S. Chung, Effect of calcium additions on the oxidation behavior in magnesium alloys, *Scr. Mater.* 42 (2000) 1089–1094.
- [127] S. Ha, J.-K. Lee, H.-H. Jo, S. Jung, S.K. Kim, Behavior of CaO and Calcium in pure Magnesium, *Rare Met.* 25 (2006) 150–154.
- [128] I. Barin, O. Knacke, O. Kubaschewski, Thermochemical properties of inorganic substances: supplement, Springer Science & Business Media, 2013.
- [129] B. Wiese, C.L. Mendis, D. Tolnai, A. Stark, N. Schell, H.P. Reichel, R. Brückner, K.U. Kainer, N. Hort, CaO dissolution during melting and solidification of a Mg-10 wt.% CaO alloy detected with in situ synchrotron radiation diffraction, *J. Alloys Compd.* 618 (2015) 64–66.
- [130] J. Jeong, J. Im, K. Song, M. Kwon, S. Kwang, Transmission electron microscopy and thermodynamic studies of CaO-added AZ31 Mg alloys, *Acta Mater.* 61 (2013) 3267–3277.

- [131] S.M. Liang, R. Schmid-Fetzer, Complete thermodynamic description of the Mg-Ca-O phase diagram including the Ca-O, Mg-O and CaO-MgO subsystems, *J. Eur. Ceram. Soc.* 38 (2018) 4768–4785.
- [132] H.J.T. Ellingham, Reducibility of oxides and sulfides in metallurgical processes, *J Soc Chem Ind.* 63 (1944) 125–133.
- [133] Y. Wang, Z. Fan, X. Zhou, G.E. Thompson, Characterisation of magnesium oxide and its interface with α -Mg in Mg–Al-based alloys, *Philos. Mag. Lett.* 91 (2011) 516–529.
- [134] Z. Fan, Y. Wang, M. Xia, S. Arumuganathar, Enhanced heterogeneous nucleation in AZ91D alloy by intensive melt shearing, *Acta Mater.* 57 (2009) 4891–4901.
- [135] B. Jiang, Solidification Behaviour of Magnesium Alloys, PhD thesis, Brunel University, 2013.
- [136] S. Das, N.S. Barekar, O. El Fakir, L. Wang, A.K. Prasada Rao, J.B. Patel, H.R. Kotadia, A. Bhagurkar, J.P. Dear, Z. Fan, Effect of melt conditioning on heat treatment and mechanical properties of AZ31 alloy strips produced by twin roll casting, *Mater. Sci. Eng. A.* 620 (2015) 223–232.
- [137] H. Hall, A Note on Attempts to Produce Superheating Effect by Addition of Alumina to Electron A-8, *Magnes. Rev. Abs.* 3 (1945) 68.
- [138] Z. Fan, B. Jiang, Y.B. Zuo, Apparatus and method for liquid metals treatment, GB2011/051744, 2011.
- [139] Y. Wang, Z. Fan, X. Zhou, G.E. Thompson, Characterisation of magnesium oxide and its interface with α -Mg in Mg–Al-based alloys, *Philos. Mag. Lett.* 91 (2011) 516–529.
- [140] Y. Wang, G. Peng, Z. Fan, Grain Refinement of Mg and Its Alloy by Inoculation of In Situ MgO Particles, in: K.N. Solanki, D. Orlov, S. Alok, N.R. Neelameggham (Eds.), *Magnes. Technol.* 2017, Springer, 2017: pp. 99–106.
- [141] M. Boiocchi, F. Caucia, M. Merli, D. Prella, L. Ungaretti, Crystal-chemical reasons for the immiscibility of periclase and wüstite under lithospheric P,T conditions, *Eur. J. Mineral.* 13 (2001) 871–881.
- [142] T. Marker, Evaluating the flammability of various magnesium alloys during laboratory- and full-scale aircraft fire test, US Dep. Transp. Fed. Aviat. Adm. Atl. City, New Jersey, DOT/FAA/AR-11/3. (2013) 15. <https://www.fire.tc.faa.gov/pdf/AR11-13.pdf>.
- [143] F. Czerwinski, The oxidation behaviour of an AZ91D magnesium alloy at high temperatures, *Acta Mater.* 50 (2002) 2639–2654.
- [144] G. Song, A. Atrens, Understanding magnesium corrosion. A framework for improved alloy performance, *Adv. Eng. Mater.* 5 (2003) 837–858.
- [145] J. Campbell, An overview of the effects of bifilms on the structure and properties of cast alloys, *Metall. Mater. Trans. B.* 37 (2006) 857–863.
- [146] J. Campbell, *Complete Casting Handbook: Metal Casting Processes, Metallurgy, Techniques and Design: Second Edition*, Butterworth-Heinemann, 2015.

- [147] C.F. Baker, Molten Magnesium Operations: Establishing and Maintaining Quality, No. 900787. (1990) SAE Technical Papers.
- [148] P. Bakke, D.O. Karlsen, Inclusion assessment in magnesium and magnesium base alloys, SAE Trans. (1997) 314–326.
- [149] H.S. Tathgar, P. Bakke, T.A. Engh, Impurities in Magnesium and Magnesium Based Alloys and their Removal, in: K.U. Kainer (Ed.), *Magnesium Alloy. Their Appl.*, Wiley-VCH Verlag GmbH, 2006: pp. 767–779.
- [150] W.D. Griffiths, N.W. Lai, Double oxide film defects in cast magnesium alloy, *Metall. Mater. Trans. A.* 38 (2007) 190–196.
- [151] H. Jafari, M.H. Idris, A. Ourdjini, High temperature oxidation of AZ91D magnesium alloy granule during in-situ melting, *Corros. Sci.* 53 (2011) 655–663.
- [152] M.J. Balart, Z. Fan, Surface oxidation of molten AZ91D magnesium alloy in air, *Int. J. Cast Met. Res.* 27 (2014) 167–175.
- [153] S.J. Splinter, N.S. McIntyre, W.N. Lennard, K. Griffiths, G. Palumbo, An AES and XPS study of the initial oxidation of polycrystalline magnesium with water vapour at room temperature, *Surf. Sci.* 292 (1993) 130–144.
- [154] V. Fournier, P. Marcus, I. Olefjord, Oxidation of magnesium, *Surf. Interface Anal.* 34 (2002) 494–497.
- [155] E.A. Gulbransen, The Oxidation and Evaporation of Magnesium at Temperatures from 400° to 500° C, *Trans. Electrochem. Soc.* 87 (1945) 589.
- [156] C. Lea, C. Molinari, Magnesium diffusion, surface segregation and oxidation in Al-Mg alloys, *J. Mater. Sci.* 19 (1984) 2336–2352.
- [157] N. Cabrera, N.F. Mott, Theory of the oxidation of metals, *Reports Prog. Phys.* 12 (1949) 163–184.
- [158] N.B. Pilling, R.E. Bedworth, The oxidation of metals at high temperatures, *J. Inst. Met.* 29 (1923) 529–582.
- [159] O. Kubaschewski, B.E. Hopkins, *Oxidation of metals and alloys*, Academic Press, 1962.
- [160] J.R. Liu, H.K. Chen, L. Zhao, W.D. Huang, Oxidation behaviour of molten magnesium and AZ91D magnesium alloy in 1,1,1,2-tetrafluoroethane/air atmospheres, *Corros. Sci.* 51 (2009) 129–134.
- [161] W.W. Smeltzer, Oxidation of An Aluminum-3 Per Cent Magnesium Alloy in the Temperature Range 200°–550°C, *J. Electrochem. Soc.* 105 (1958) 67–71.
- [162] C.J. Simensen, Sedimentation analysis of inclusions in aluminium and magnesium, *Metall. Trans. B.* 12 (1981) 733–743.
- [163] L. Wang, H. Rhee, S.D. Felicelli, A.S. Sabau, J.T. Berry, Oxide film and porosity defects in magnesium alloy AZ91, in: J. Campbell, P.N. Crepeau, M. Tiryakioglu (Eds.), *Shape Cast. 3rd Int. Symp. 2009*, Warrendale, Pa. : TMS, ©2009, 2009: pp. 123–130.
- [164] H. Men, B. Jiang, Z. Fan, Mechanisms of grain refinement by intensive shearing of

- AZ91 alloy melt, *Acta Mater.* 58 (2010) 6526–6534.
- [165] M.I. Vesselinov, *Crystal growth for beginners: fundamentals of nucleation, crystal growth and epitaxy*, World scientific, 2016.
- [166] G. Wulff, On the question of speed of growth and dissolution of crystal surfaces, *Z. Krist.* 34 (1901) 449.
- [167] J. Zhang, Q. Kuang, Y. Jiang, Z. Xie, Engineering high-energy surfaces of noble metal nanocrystals with enhanced catalytic performances, *Nano Today.* 11 (2016) 661–677.
- [168] R.D. Heidenreich, Electron Reflections in MgO Crystals with the Electron Microscope, *Phys. Rev.* 62 (1942) 291–292.
- [169] M. Peter, Chemisorption states, *J. Phys. Chem. Solids.* 29 (1968) 689–697.
- [170] F. Finocchi, J. Goniakowski, The effects of exchange and correlation on the computed equilibrium shapes of wet MgO crystallites, *Surf. Sci.* 601 (2007) 4144–4148.
- [171] K. Refson, R.A. Wogelius, D.G. Fraser, M.C. Payne, M.H. Lee, V. Milman, Water Chemisorption and Reconstruction of the MgO Surface, *Phys. Rev. B.* 52 (1995) 10823.
- [172] R. Hacquart, J. Jupille, Hydrated MgO smoke crystals from cubes to octahedra, *Chem. Phys. Lett.* 439 (2007) 91–94.
- [173] P. Chaudhari, J.W. Matthews, Coincidence twist boundaries between crystals of MgO smoke, *Appl. Phys. Lett.* 17 (1970) 115–117.
- [174] V.E. Henrich, Thermal faceting of (110) and (111) surfaces of MgO, *Surf. Sci.* 57 (1976) 385–392.
- [175] R. Huang, A.H. Kitai, Temperature-dependence of the growth orientation of atomic layer growth MgO, *Appl. Phys. Lett.* 61 (1992) 1450–1452.
- [176] W. Mader, B. Maier, TEM investigation of metal/MgO interfaces produced by precipitation, *J. Phys. Colloq. C1* (1990) 867–872.
- [177] P. Lu, F. Cosandey, Electron microscopy studies of metal / MgO interfaces, *Ultramicroscopy.* 40 (1992) 271–280.
- [178] D. Shashkov, M. Chisholm, D. Seidman, Atomic-scale structure and chemistry of ceramic/metal interfaces—I. Atomic structure of {222} MgO/Cu (Ag) interfaces, *Acta Mater.* 47 (1999) 3939–3951.
- [179] M.W. Finnis, A.M. Stoneham, P.W. Tasker, *Metal-Ceramic Interfaces*, Oxford: Pergamon) p, 1990.
- [180] J. Goniakowski, L. Giordano, C. Noguera, Polarity compensation in low-dimensional oxide nanostructures: The case of metal-supported MgO nanoribbons, *Phys. Rev. B - Condens. Matter Mater. Phys.* 87 (2013) 1–10.
- [181] G.S. Peng, Y. Wang, K.H. Chen, S.Y. Chen, Improved Zr grain refining efficiency for commercial purity Mg via intensive melt shearing, *Int. J. Cast Met. Res.* 30 (2017) 374–378.
- [182] G.S. Peng, Y. Wang, Z. Fan, Competitive Heterogeneous Nucleation Between Zr and

- MgO Particles in Commercial Purity Magnesium, *Metall. Mater. Trans. A.* 49 (2018) 2182–2192.
- [183] L. Rogal, L. Litynska-Dobrzynska, Effect of in-situ formed MgO on the microstructure of thixomolded AZ91 magnesium alloy, *Mater. Sci. Technol. (United Kingdom)*. 35 (2019) 349–360.
- [184] P.A. Dowben, A. Miller, *Surface Segregation phenomena*, CRC Press, 1990.
- [185] W.D. Kaplan, D. Chatain, P. Wynblatt, W.C. Carter, A review of wetting versus adsorption, complexions, and related phenomena: The rosetta stone of wetting, *J. Mater. Sci.* 48 (2013) 5681–5717.
- [186] J.P. Hirth, Thermodynamics of surfaces, *Struct. Prop. Met. Surfaces.* (1973) 10–33.
- [187] J.W. Gibbs, *The collected works of JW Gibbs*, Longmans, Green, 1928.
- [188] H. Men, Z. Fan, An Analytical Model for Solute Segregation at Liquid Metal/Solid Substrate Interface, *Metall. Mater. Trans. A.* 45 (2014) 5508–5516.
- [189] Z. Fan, Y. Wang, Y. Zhang, T. Qin, X.R. Zhou, G.E. Thompson, T. Pennycook, T. Hashimoto, Grain refining mechanism in the Al/Al-Ti-B system, *Acta Mater.* 84 (2015) 292–304.
- [190] A. Arjuna Rao, B.S. Murty, M. Chakraborty, Influence of chromium and impurities on the grain-refining behavior of aluminum, *Metall. Mater. Trans. A.* 27 (1996) 791–800.
- [191] M.E.J. Birch, Grain refining of aluminium-lithium based alloys with titanium boron aluminium, *Alum. Alloy. III.* (1986) 152–158.
- [192] P.S. Mohanty, Grain refinement mechanisms of hypoeutectic Al-Si alloys, *Acta Mater.* 44 (1996) 3749–3760.
- [193] Y. Liu, X. Liu, X. Bian, Grain refinement of Mg-Al alloys with Al₄C₃-SiC/Al master alloy, *Mater. Lett.* 58 (2004) 1282–1287.
- [194] T.J. Chen, X.D. Jiang, Y. Ma, Y.D. Li, Y. Hao, Grain refinement of AZ91D magnesium alloy by SiC, *J. Alloys Compd.* 496 (2010) 218–225.
- [195] S. Wang, F. Wang, Y. Wang, Q. Ramasse, Z. Fan, Segregation of Ca at the Mg/MgO interface and its effect on grain refinement of Mg alloys, in: *IOP Conf. Ser. Mater. Sci. Eng.*, IOP Publishing, 2019: p. 012048.
- [196] A. Bogner, P. Jouneau, G. Thollet, D. Basset, C. Gauthier, A history of scanning electron microscopy developments : Towards “ wet-STEM ” imaging, *Micron.* 38 (2007) 390–401.
- [197] C.B. Carter, D.B. Williams, *Transmission electron microscopy: Diffraction, imaging, and spectrometry*, Springer, 2016.
- [198] M. Han, X. Zhu, T. Gao, X. Liu, Revealing the roles of Al₄C₃ and Al₈Mn₅ during α -Mg nucleation in Mg-Al based alloys, *J. Alloys Compd.* 705 (2017) 14–21.
- [199] K. Nogita, S.D. McDonald, K. Tsujimoto, K. Yasuda, A.K. Dahle, Aluminium phosphide as a eutectic grain nucleus in hypoeutectic Al-Si alloys, *J. Electron Microsc.*

- (Tokyo). 53 (2004) 361–369.
- [200] F. Wang, D. Qiu, Z.L. Liu, J.A. Taylor, M.A. Easton, M.X. Zhang, The grain refinement mechanism of cast aluminium by zirconium, *Acta Mater.* 61 (2013) 5636–5645.
- [201] J.G. Jung, T.Y. Ahn, Y.H. Cho, S.H. Kim, J.M. Lee, Synergistic effect of ultrasonic melt treatment and fast cooling on the refinement of primary Si in a hypereutectic Al–Si alloy, *Acta Mater.* 144 (2018) 31–40.
- [202] C.R. Ho, B. Cantor, Heterogeneous nucleation of solidification of Si in Al–Si and Al–Si–P alloys, *Acta Metall. Mater.* 43 (1995) 3231–3246.
- [203] B. Cantor, Heterogeneous nucleation and adsorption, *Philos. Trans. R. Soc. London. Ser. A Math. Phys. Eng. Sci.* 361 (2003) 409–417.
- [204] P. Schumacher, A.L. Greer, Heterogeneously nucleated α -Al in amorphous aluminium alloys, *Mater. Sci. Eng. A.* 178 (1994) 309–313.
- [205] Z. Fan, Y.B. Zuo, B. Jiang, A new technology for treating liquid metals with intensive melt shearing, in: *Mater. Sci. Forum*, Trans Tech Publ, 2011: pp. 141–144.
- [206] A.A. Association, Standard test procedure for aluminum alloy grain refiners, *Alum. Assoc.* (2012).
- [207] J. Patel, Y. Zuo, Z. Fan, Liquid metal engineering by application of intensive melt shearing, in: M. Krane, A. Jardy, R. Williamson, J. Beaman (Eds.), *Proc. 2013 Int. Symp. Liq. Met. Process. Cast.*, Springer, 2013: pp. 291–299.
- [208] A. Ul-Hamid, *A Beginners' Guide to Scanning Electron Microscopy*, Springer, 2018.
- [209] M. Watanabe, M. Kanno, D. Ackland, C. Kiely, D. Williams, Applications of Electron Energy-Loss Spectrometry and Energy Filtering in an Aberration-Corrected JEM-2200FS STEM/TEM, *Microsc. Microanal.* 13 (2007) 2006–2007.
- [210] F. Finocchi, A. Barbier, J. Jupille, C. Noguera, Stability of rocksalt (111) polar surfaces: Beyond the octopole, *Phys. Rev. Lett.* 92 (2004) 136101.
- [211] P. Geysmans, F. Finocchi, J. Goniakowski, R. Hacquart, J. Jupille, Combination of (100), (110) and (111) facets in MgO crystals shapes from dry to wet environment, *Phys. Chem. Chem. Phys.* 11 (2009) 2228–2233.
- [212] B. Predel, K. Hülse, Metastable phases of the aluminium-magnesium system, *Chem. Informationsd.* 10 (1979) 690–696.
- [213] J. Goldak, L.T. Lloyd, C.S. Barrett, Lattice parameters, thermal expansions, and Grüneisen coefficients of zirconium, 4.2 to 1130°K, *Phys. Rev.* 144 (1966) 478–484.
- [214] R.S. Krishnan, R. Srinivasan, S. Devanarayanan, *Thermal expansion of crystals: international series in the science of the solid state*, 1st ed., Pergamon Press, Oxford, 1979.
- [215] M.A. Durand, The coefficient of thermal expansion of magnesium oxide, *Physics (College. Park. Md.)* 7 (1936) 297–298.
- [216] M. Suzuki, H. Sato, K. Maruyama, H. Oikawa, Creep behavior and deformation

- microstructures of Mg-Y alloys at 550 K, *Mater. Sci. Eng. A.* 252 (1998) 248–255.
- [217] S.R. Agnew, M.H. Yoo, C.N. Tomé, Application of texture simulation to understanding mechanical behavior of Mg and solid solution alloys containing Li or Y, *Acta Mater.* 49 (2001) 4277–4289.
- [218] N. Žaludová, Mg-RE Alloys and Their Applications, in: J. Safrankova (Ed.), WDS'05 Proc. Contrib. Pap. Part III-Physics, Prague, Matfyzpress, 2005: pp. 643–648.
- [219] A.S.M.H. Committee, Properties and Selection: Nonferrous Alloys and Special-Purpose Materials, (1990).
- [220] R. Schmid-Fetzer, F. Zhang, The light alloy Calphad databases PanAl and PanMg, *Calphad Comput. Coupling Phase Diagrams Thermochem.* 61 (2018) 246–263.
- [221] S. Katagiri, N. Ishizawa, F. Marumo, A new high temperature modification of face-centered cubic Y₂O₃, *Powder Diffr.* 8 (1993) 60.
- [222] E. Clementi, D.L. Raimondi, W.P. Reinhardt, Atomic screening constants from SCF functions. II. Atoms with 37 to 86 electrons, *J. Chem. Phys.* 47 (1967) 1300–1307.
- [223] M.G. Paton, E.N. Maslen, A refinement of the crystal structure of yttria, *Acta Crystallogr.* 19 (1965) 307–310.
- [224] T.E. Quested, A.L. Greer, Grain refinement of Al alloys: Mechanisms determining as-cast grain size in directional solidification, *Acta Mater.* 53 (2005) 4643–4653.
- [225] C.T. Koch, Determination of core structure periodicity and point defect density along dislocations, PhD thesis, Arizona State University, 2002.
- [226] E. Withey, A. Kruiženga, C. Andraka, P. Gibbs, Plasma sprayed coatings for containment of Cu-Mg-Si metallic phase change material, *Surf. Coatings Technol.* 304 (2016) 117–124.
- [227] H.S.C. Outotec, Chemistry 8, (n.d.). <http://www.outotec.com/en/Products--services/HSC-Chemistry/>.
- [228] R. Schmid-fetzer, Recent progress in development and applications of mg alloy thermodynamic database, in: V. V Joshi, J.B. Jordon, D. Orlov, N.R. Neelamegham (Eds.), *Magensium Technol.* 2019, 2019: pp. 249–255.
- [229] W. Xu, R. Zheng, K.J. Laws, S.P. Ringer, M. Ferry, In situ formation of crystalline flakes in Mg-based metallic glass composites by controlled inoculation, *Acta Mater.* 59 (2011) 7776–7786.
- [230] A. Takeuchi, Classification of Bulk Metallic Glasses by Atomic Size Difference, Heat of Mixing and Period of Constituent Elements and Its Application to Characterization of the Main Alloying Element, *Mater. Trans.* 41 (2005) 846–2829.
- [231] O. Dyck, M. Ziatdinov, D.B. Lingerfelt, R.R. Unocic, B.M. Hudak, A.R. Lupini, S. Jesse, S. V. Kalinin, Atom-by-atom fabrication with electron beams, *Nat. Rev. Mater.* 4 (2019) 497–507.
- [232] T. Kizuka, N. Tanaka, Atomic desorption process in nanometre-scale electron-beam

- drilling of MgO in high-resolution transmission electron microscopy, *Philos. Mag. Lett.* 76 (1997) 289–297.
- [233] C. Fang, Z. Fan, A first-principles study of the formation of atomically rough { 111 } MgO surface and its effect on prenucleation of Mg A first-principles study of the formation of atomically rough { 111 } MgO surface and its effect on prenucleation of Mg, in: 11th Int. Conf. Magnes. Alloy. Their Appl., 2018: pp. 107–111.
- [234] B.S. Murty, S.A. Kori, M. Chakraborty, Grain refinement of aluminium and its alloys by heterogeneous nucleation and alloying, *Int. Mater. Rev.* 47 (2002) 3–29.
- [235] T.F. Tadros, *Dispersion of Powders: in Liquids and Stabilization of Suspensions*, John Wiley & Sons, 2012.
- [236] A.M. Bunn, P. Schumacher, M.A. Kearns, C.B. Boothroyd, A.L. Greer, Grain refinement by Al–Ti–B alloys in aluminium melts: a study of the mechanisms of poisoning by zirconium, *Mater. Sci. Technol.* 15 (1999) 1115–1123.
- [237] D.L. Zhang, B. Cantor, Effect of Ge on the heterogeneous nucleation of Pb solidification by Al, *J. Cryst. Growth.* 104 (1990) 583–592.
- [238] C.R. Ho, B. Cantor, Effect of Ge on the heterogeneous nucleation of Cd solidification by Al, *Philos. Mag. A.* 66 (1992) 141–149.
- [239] B. Jiang, Y. Zeng, M. Zhang, J. Liao, F. Pan, The effect of addition of cerium on the grain refinement of Mg–3Al–1Zn cast alloy, *J. Mater. Res.* 28 (2013) 2694–2700.
- [240] X. Gao, S.M. Zhu, B.C. Muddle, J.F. Nie, Precipitation-hardened Mg–Ca–Zn alloys with superior creep resistance, *Scr. Mater.* 53 (2005) 1321–1326.
- [241] Z. Li, X. Gu, S. Lou, Y. Zheng, The development of binary Mg–Ca alloys for use as biodegradable materials within bone, *Biomaterials.* 29 (2008) 1329–1344.
- [242] G. Derge, A.R. Kommel, R.F. Mehl, Studies upon the Widmanstätten structure IX—the Mg–Mg₂Sn and Pb–Sb systems, *Trans. AIME.* 124 (1937) 367–378.
- [243] M.J. Hÿtch, E. Snoeck, R. Kilaas, Quantitative measurement of displacement and strain fields from HREM micrographs, *Ultramicroscopy.* 74 (1998) 131–146.
- [244] M.M. Avedesian, H. Baker, *ASM specialty handbook: magnesium and magnesium alloys*, ASM international, 1999.
- [245] T. Brudevoll, E. Kotomin, Interstitial-oxygen-atom diffusion in MgO, *Phys. Rev. B.* 53 (1996) 7731–7735.
- [246] P. Luo, F. Zhuge, Q. Zhang, Y. Chen, L. Lv, Y. Huang, H. Li, T. Zhai, Doping engineering and functionalization of two-dimensional metal chalcogenides, *Nanoscale Horizons.* 4 (2019) 26–51.
- [247] P.R. Cantwell, M. Tang, S.J. Dillon, J. Luo, G.S. Rohrer, M.P. Harmer, Grain boundary complexions, *Acta Mater.* 62 (2014) 1–48.
- [248] M. Cargnello, A.C. Johnston-Peck, B.T. Diroll, E. Wong, B. Datta, D. Damodhar, V.V.T. Doan-Nguyen, A.A. Herzing, C.R. Kagan, C.B. Murray, Substitutional doping in

- nanocrystal superlattices, *Nature*. 524 (2015) 450–453.
- [249] Y. Yan, M.F. Chisholm, G. Duscher, S.J. Pennycook, Atomic structure of a Ca-doped [001] tilt grain boundary in MgO, *J. Electron Microsc. (Tokyo)*. 47 (1998) 115–120.
- [250] M. Pesci, F. Gallino, C. Di Valentin, G. Pacchioni, Nature of defect states in nitrogen-doped MgO, *J. Phys. Chem. C*. 114 (2010) 1350–1356.
- [251] B.M. Siegel, D.R. Beaman, *Physical aspects of electron microscopy and microbeam analysis*, Wiley, 1975.
- [252] M.M.J. Treacy, Z dependence of electron scattering by single atoms into annular dark-field detectors, *Microsc. Microanal.* 17 (2011) 847–858.
- [253] B.I. Shklovskii, A.L. Efros, *Electronic properties of doped semiconductors*, Springer Science & Business Media, 2013.
- [254] Y.M. Zhu, A.J. Morton, J.F. Nie, The 18R and 14H long-period stacking ordered structures in Mg-Y-Zn alloys, *Acta Mater.* 58 (2010) 2936–2947.
- [255] H. Schmid, E. Okunishi, T. Oikawa, W. Mader, Structural and elemental analysis of iron and indium doped zinc oxide by spectroscopic imaging in Cs-corrected STEM, *Micron*. 43 (2012) 49–56.
- [256] Z. Luo, C. Hu, L. Xie, H. Nie, C. Xiang, X. Gu, J. He, W. Zhang, Z. Yu, J. Luo, A highly asymmetric interfacial superstructure in WC: expanding the classic grain boundary segregation and new complexion theories, *Mater. Horizons*. 7 (2020) 173–180.
- [257] R.D. Shannon, Revised effective ionic radii and systematic studies of interatomic distances in halides and chalcogenides, *Acta Crystallogr. Sect. A*. 32 (1976) 751–767.
- [258] Y. Yoshioka, T. Matsui, M. Kasuga, T. Irisawa, Effects of impurities on lateral growth of crystals, *J. Cryst. Growth*. 198–199 (1999) 71–76.
- [259] K. Sangwal, Effects of impurities on crystal growth processes, *Prog. Cryst. Growth Charact. Mater.* 32 (1996) 3–43.
- [260] R.S. Wagner, On the growth of germanium dendrites, *Acta Met.* 8 (1960) 57–60.
- [261] S.-Z. Lu, A. Hellawell, The mechanism of silicon modification in aluminum-silicon alloys: impurity induced twinning, *Metall. Trans. A*. 18 (1987) 1721–1733.
- [262] L. Lian, K. Tsukamoto, I. Sunagawa, Impurity adsorption and habit changes in aqueous solution grown KCl crystals, *J. Cryst. Growth*. 99 (1990) 150–155.
- [263] U. Zavyalova, M. Geske, R. Horn, G. Weinberg, W. Frandsen, M. Schuster, R. Schlögl, Morphology and Microstructure of Li/MgO Catalysts for the Oxidative Coupling of Methane, *ChemCatChem*. 3 (2011) 949–959.
- [264] M. Niedermaier, T. Schwab, P. Kube, G.A. Zickler, A. Trunschke, O. Diwald, Catalytic activity, water formation, and sintering: Methane activation over Co- and Fe-doped MgO nanocrystals, *J. Chem. Phys.* 152 (2020) 74713.
- [265] C. Fang, Z. Fan, Atomic ordering at the interfaces between liquid Al and solid MgO: An Ab Initio molecular dynamics study, *Philos. Mag. Lett.* 100 (2020) 1–10.

Characterisation of Native MgO and Its Roles in Solidification of Mg Alloys

Brunel Centre for Advanced Solidification Technology
Brunel University London
Kingston Lane
Uxbridge, Middlesex, United Kingdom
UB8 3PH

Shihao Wang



Brunel
University
London